AD-A166 575 CREEP AND FRACTURE CHARACTERISTICS OF MATERIALS AND STRUCTURES AT ELEVATED TEMPERATURES(U) GEORGE WASHINGTON UNIV WASHINGTON DC SCHOOL OF ENGINEERING AN 1/4

UNCLASSIFIED .. H LIEBOWITZ 14 FEB 86 N00014-84-K-0027 F/G 20/11 NL

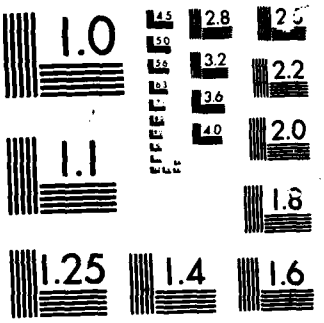

MICROCOPY CHART

CREEP AND FRACTURE CHARACTERISTICS OF MATERIALS AND STRUCTURES [redacted] AT ELEVATED TEMPERATURES

THE GEORGE WASHINGTON UNIVERSITY

STUDENTS FACULTY STUDY R
ESEARCH DEVELOPMENT FUT
URE CAREER CREATIVITY CC
MMUNITY LEADERSHIP TECH
NOLOGY FRONTIE ESIGN
ENGINEERING APP ENC
GEORGE WASHIN NIV

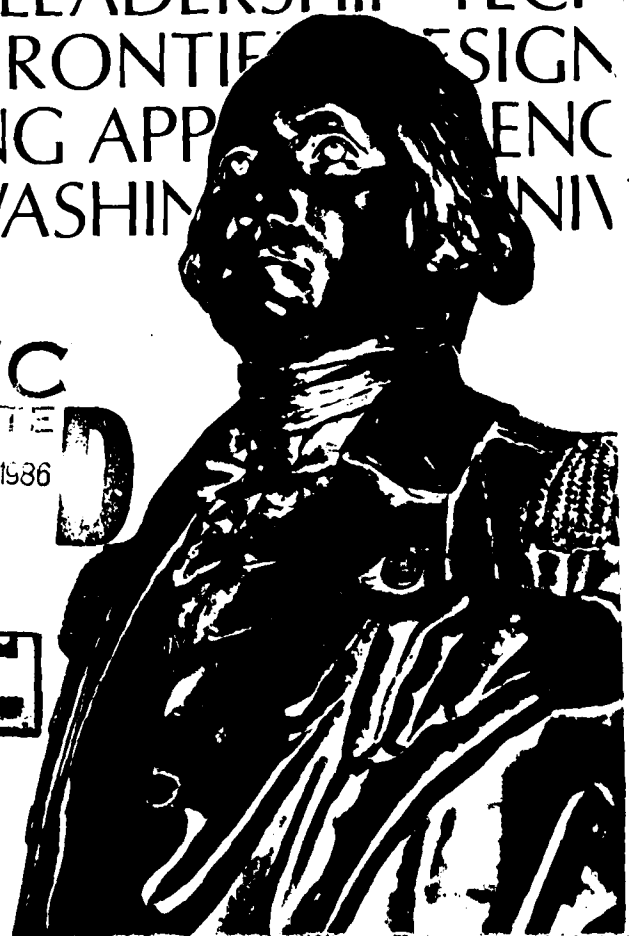

SCHOOL OF ENGINEERING AND APPLIED SCIENCE

(4)

CREEP AND FRACTURE CHARACTERISTICS OF MATERIALS AND STRUCTURES [redacted] AT ELEVATED TEMPERATURES

TECHNICAL PROGRESS REPORT

ONR CONTRACT NUMBER: N00014-84-K-0027

ONR WORK UNIT NUMBER: NR: 064738

Principal Investigator: Dr. Harold Liebowitz

Technical Director: Dr. E. Thomas Moyer, Jr.

ONR SCIENTIFIC OFFICER: Dr. Yapa Rajapakse

February 14, 1986

School of Engineering and Applied Science
The George Washington University
Washington, D.C. 20052

The work on ONR Contract #N00014-84-K-0027 has progressed steadily during the first year of the contract. A major focus of the first year was on the mixed-mode fracture problem. Theoretical work on the computational methodology for the calculation of mixed-mode stress intensity factors was performed. The convergence properties of several algorithms were delineated and guidelines for the accurate calculation of mixed-mode stress intensity factors were established. This study also investigated the effects and influence of loading holes on the calculations, (loading holes are usually ignored in theoretical studies, if they are modeled, they are usually modeled poorly). While previous studies have investigated the accurate modeling of loading holes, their influence on fracture specimens had not been sufficiently explored. In addition to these fundamental studies, a proposed mixed-mode specimen was carefully analyzed. This specimen (originally designed by Professor H. Richard) has been proposed for studies near the range of pure Mode II loading (so-called "pure shear"). The calculations demonstrated the utility of the specimen for measuring critical shear conditions for pure Mode II failure. This study was performed in conjunction with an exchange student to The George Washington University (Mr. Peter Bäuerle). His final report carefully documents the work performed and is included as Appendix A of this report.

Concurrent with the theoretical work, independent experimental verification of this fracture specimen was per-

formed. Several refinements were made to the original design. This design (which involves a very specialized grip configuration) was constructed and tested. PMMA specimens were tested to determine the failure envelope under the full range of mixed-mode loading. In addition, uncracked specimens were tested to determine their resistance to shear loading. The results demonstrate the ability of this loading grip system to accurately induce the full range (from pure Mode I to pure Mode II) of planer mixed-mode loading conditions. This study was also performed in conjunction with an exchange student to The George Washington University (Mr. Roland Gerstner). His final report completely covers the work performed and is included as Appendix B of this report.

Most of the previous recent fracture research sponsored by ONR focused on studying the nature of plastic deformation in the vicinity of three-dimensional crack fronts. These studies were completed during this contract year. Experimental surface contractions were measured and compared with finite element predictions. For the worst cases, the results agreed within 4%. The plasticity model employed and the finite element grid convergence were, therefore demonstrated. In addition, several global response parameters were compared with an experiment. It was shown that global parameter agreement does not guarantee accurate local modeling. The results of this study are included in a paper entitled "Prediction of Plasticity Characteristics for Three-Dimensional Fracture Specimens -

Comparison with Experiment" which has been accepted for publication in Engineering Fracture Mechanics. This paper is included as Appendix C of this report.

The three-dimensional plasticity studies have also demonstrated many of the local response characteristics near a crack front. Having established the accuracy of the modeling, the response of the interior of the specimen can now be accurately predicted. The influence of hardening, specimen thickness, local relaxation, crack growth, etc., was accurately predicted and investigated for straight crack, Mode I specimens. While no conclusions regarding appropriate failure criteria have been drawn, it was demonstrated that the failure was definitely governed by a local parameter and it should be related to the local deformation response. Previous studies have indicated the inadequacy of a global failure parameter, however, the local deformation characteristics have only now been delineated and verified. The results were presented as an invited paper at the American Society of Metals meeting held in Salt Lake City, Utah (December, 1985). This paper is included as Appendix D of this report. This paper will subsequently be published in the proceedings of this conference by the American Society of Metals.

The major focus of this contract has been to develop the methodology and to begin a systematic study into the fracture behavior of specimens subjected to high temperatures. To this end, a test system for the high temperature and mechanical

loading of specimens was procured, installed and tested. After verifying the instrumentation, preliminary studies were performed to delineate the constitutive behavior of Inconel 718 when loaded at elevated temperatures (temperatures above 500°C). Uniaxial tests were performed and the data was "fit" with several constitutive models. Upon the completion of uniaxial testing, the experimental work focused on establishing the instrumentation necessary to study crack growth phenomena. Attention is focusing on accurate measurement of crack mouth opening behavior for modeling purposes. In addition, preliminary tests are being run to determine the requisite loading to produce different crack growth rates of importance for application. The experimental work to date is summarized in Appendix E of this report. This Appendix also covers the constitutive modeling being done.

Concurrent with the experimental and constitutive modeling, work has focused on developing and testing a finite element code to perform fracture analyses. The preliminary code using a simple constitutive model has been completed and tested. Work is underway to build in crack growth capabilities, large strain modeling and alternative constitutive models with mixed hardening properties. The formulations being employed are discussed in Appendix F of this report.

In addition to the work discussed above, two other publications were produced which summarized and concluded previous

work performed under ONR support. These papers: "Finite Element Methodology for Elastic-Plastic Fracture Problems in 3-Dimensions" and "Effect of Specimen Thickness on Crack Front Plasticity Characteristics in Three-Dimensions" are included as Appendices G and H of this report.

As is evident from this report and the publications included, much has been accomplished in the first year of this contract. The next year will be spent establishing the basic experimental and numerical approaches for accurate modeling and investigation of creep fracture processes. While our efforts are producing useful and informative results, we have only scratched the surface of this problem.

APPENDICES

APPENDIX A:

Appendices Contained in this report refer to:

Determination of Two-Dimensional Stress Intensity;

By: Peter Bäuerle.

Final Report, June 1985.

DETERMINATION OF TWO DIMENSIONAL STRESS INTENSITY

By

Peter Bäuerle

June 1985

Under the Guidance of
Dr. E. Thomas Moyer, Jr.
School of Engineering and Applied Science
The George Washington University
Washington, D.C. 20052

ABSTRACT

Stress intensity factors are material independent parameters which measure the stress and strain distribution at the tip of a crack in a loaded solid body. These stress intensity factors contain the geometry of the crack. They enable to predict if a prescribed load can be applied to a damaged material without losing the required safety.

In this research all calculations were done with the finite element program APES which uses 12-node quadrilateral isoparametric elements. In order to obtain the singularities at the crack tip, the following two crack tip elements were utilized:

- enriched elements
- collapsed cubic isoparametric elements

  ($\frac{1}{9}$ & $\frac{4}{9}$ point elements)

Since the stiffness matrix of the enriched elements already contains the singularity functions, K_I and K_{II} can be calculated together with the displacements by the computer program. Using the collapsed cubic isoparametric elements, the stress intensity factors K_I and K_{II} have to be determinated with the aid of crack border displacement functions after the run of the program.

These calculations were done for a special specimen developed by H. A. Richard for mixed mode problems. Also, the influence of the holes where the forces are applied was studied.

TABLE OF CONTENTS

TABLE OF CONTENTS (Continued)

1. INTRODUCTION

During the last 20 years many investigations have been done to determine the stress intensity factor K_I (Mode I) where the forces are applied perpendicular to the crack. However, most cracks lead to mixed mode problems where also the stress intensity factor K_{II} (Mode II, see Figure 1) has to be taken into consideration. For this case it is important to develop methods which allow to determine both, K_I and K_{II}, more accurately. Only dependable stress intensity factors allow an engineer to decide whether a damaged part of a machine or a building can be used without losing the required safety.

In this paper, the finite element program APES will be utilized to determine the two-dimensional stress intensity factors K_I and K_{II}. The 12-node quadrilateral isoparametric elements of this program already lead to a high accuracy with a relative small number of elements, compared to lower order elements of other finite element programs.

On the following pages, only plane strain will be taken into consideration. Plane strain means that along the z-axis (third dimension) no strains are allowed according to the Poisson's ratio. Therefore, in addition to the stresses in x- and y-direction also stresses in z-direction have to come into being. In reality, this state of stress can just be realized in the middle of the crack tip of a Compact Tension Shear

specimen if the specimen is thick enough. Plane strain represents the crucial load case of a CTS specimen which leads to cleavage fracture without any prior plastic deformation.

2. INTRODUCTION TO THE 12-NODE QUADRILATERAL ISOPARAMETRIC ELEMENT

The APES program, with which this research was done, utilizes the 12-node cubic isoparametric element (shown in Figure 2). One 12-node element, given in the x,y coordinate system, can be transformed into the natural ξ, η coordinate system where the element is mapped to a square and the coordinates are dimensionless [1].

The displacement components can be written in the form

$$u = \sum_{i=1}^{12} N_i(\xi,\eta)\, u_i \tag{1}$$

$$v = \sum_{i=1}^{12} N_i(\xi,\eta)\, v_i \tag{2}$$

u,v are the components of the displacements of a point with the coordinates ξ, η, whereas u_i, v_i are the displacement components of the node i. $N_i(\xi, \eta)$ represent the shape functions or interpolation functions at the node i which are given by

$$\begin{aligned} N_i(\xi,\eta) = {} & \frac{1}{256}(1 + \xi\xi_i)(1 + \eta\eta_i)[-10 + 9(\xi^2 + \eta^2)]\cdot \\ & [-10 + 9(\xi_i^2 + \eta_i^2)] \\ & + \frac{81}{256}(1 + \xi\xi_i)(1 + 9\eta\eta_i)(1 - \eta^2)(1 - \eta_i^2) \\ & + \frac{81}{256}(1 + \eta\eta_i)(1 + 9\xi\xi_i)(1 - \xi^2)(1 - \xi_i^2) \end{aligned} \tag{3}$$

where ξ_i, η_i are the coordinates of the point i. It has to be mentioned as the important feature of the cubic isoparametric elements, that the same shape functions are utilized to describe the geometry of the 12-node elements in the x, y coordinate system.

$$x = \sum_{i=1}^{12} N_i(\xi,\eta)\ x_i \tag{4}$$

$$y = \sum_{i=1}^{12} N_i(\xi,\eta)\ x_i \tag{5}$$

where x_i, y_i represent the nodes of the element in the x, y coordinate system. Evaluating the shape functions at each node i, $N(\xi, \eta\ )$ becomes:

$$N_1 = \frac{1}{32}(1 - \eta)(1 - \xi)[- 10 + 9(\xi^2 + \eta^2)]$$

$$N_2 = \frac{9}{32}(1 - \eta)(1 - \xi^2)(1 - 3\xi)$$

$$N_3 = \frac{9}{32}(1 - \eta)(1 - \xi^2)(1 + 3\xi)$$

$$N_4 = \frac{1}{32}(1 - \eta)(1 + \xi)[- 10 + 9(\xi^2 + \eta^2)]$$

$$N_5 = \frac{9}{32}(1 + \xi)(1 - \eta^2)(1 - 3\eta)$$

$$N_6 = \frac{9}{32}(1 + \xi)(1 - \eta^2)(1 + 3\eta)$$

$$N_7 = \frac{1}{32}(1 + \eta)(1 + \xi)[- 10 + 9(\xi^2 + \eta^2)]$$

$$N_8 = \frac{9}{32}(1 + \eta)(1 - \xi^2)(1 + 3\xi)$$

$$N_9 = \frac{9}{32}(1 + \eta)(1 - \xi^2)(1 - 3\xi)$$

$$N_{10} = \frac{1}{32}(1 + \eta)(1 - \xi)[-10 + 9(\xi^2 + \eta^2)]$$

$$N_{11} = \frac{9}{32}(1 - \xi)(1 - \eta^2)(1 + 3\eta)$$

$$N_{12} = \frac{9}{32}(1 - \xi)(1 - \eta^2)(1 - 3\eta)$$

The element stiffness matrix [K] can be written in the form

$$[K] = \int_{-1}^{1}\int_{-1}^{1} [B]^T[D][B] \det |J| \, d\xi \, d\eta \qquad (6)$$

where [B] is given by

$$[\varepsilon] = [B][u] \qquad \begin{matrix}[\varepsilon]: & \text{strain field} \\ [u]: & \text{displacement field}\end{matrix} \tag{7}$$

$$[B] = [\ldots, B_i, \ldots.]$$

$$[B_i] = \begin{bmatrix} \frac{\partial N_i}{\partial x} & 0 \\ 0 & \frac{\partial N_i}{\partial y} \\ \frac{\partial N_i}{\partial y} & \frac{\partial N_i}{\partial x} \end{bmatrix}$$

[D] is the material stiffness matrix for plane stress:

$$[D] = \frac{E}{1-\nu^2} \begin{bmatrix} 1 & \nu & 0 \\ \nu & 1 & 0 \\ 0 & 0 & \frac{(1-\nu)}{2} \end{bmatrix} \tag{8}$$

for plane strain [2]:

$$[D] = \frac{E}{(1+\nu)(1-2\nu)} \begin{bmatrix} (1-\nu) & \nu & 0 \\ \nu & (1-\nu) & 0 \\ \nu & \nu & 0 \\ 0 & 0 & \frac{(1+\nu)(1-2\nu)}{2(1+\nu)} \end{bmatrix}$$

[J] represents the Jacobian matrix (transformation matrix)

$$[J] = \begin{bmatrix} \frac{\partial x}{\partial \xi} & \frac{\partial y}{\partial \xi} \\ \frac{\partial x}{\partial \eta} & \frac{\partial y}{\partial \eta} \end{bmatrix} = \begin{bmatrix} \ldots, \frac{\partial N_i}{\partial \xi}, \ldots \\ \ldots, \frac{\partial N_i}{\partial \eta}, \ldots \end{bmatrix} \tag{9}$$

If det $|J|$ is zero, stress and strains become singular.

The advantages of the 12-node quadrilateral isoparametric elements are [3]:

- the edges of the elements can take the shape of a cubic function. Therefore, the 12-node elements can be easily adapted to many practical problems.
- strains and stresses vary cubically over the element, which means that only a few elements are sufficient to simulate the required stress and strain distribution in a solid.

3. CRACK-TIP ELEMENTS

In order to simulate the nodal crack tip singularity in a proper way, the finite elements around the crack tip have to reproduce the strain singularity. The finite element program APES already contains enriched elements which take the strain singularity into account with the aid of specific singular assumptions.

3.1 Enriched Elements

3.1.1 Introduction to the Enriched Elements

The enriched elements have the same shape like the ordinary cubic isoparametric elements and they can be adapted to the required geometry of the specimen in the same way. In order to simulate the strain singularity at the crack tip special singular functions are utilized.

S. E. Benzley describes the displacement assumptions for enriched elements with 4 nodes [4]. For 12-node elements these displacement functions can be written as follows:

$$u_i = \sum_{k=1}^{12} f_k \, u_{ik} + R \{K_I(Q_{1i} - \sum_{k=1}^{12} f_k \, \bar{Q}_{1ik}) + K_{II}(Q_{2i} - \sum_{k=1}^{12} f_k \, \bar{Q}_{2ik})\} \tag{10}$$

where u_{ik} = nodal displacements

f = shape functions

Q_{1i}, Q_{2i} = special singular assumptions

$\bar{Q}_{1ik}, \bar{Q}_{2ik}$ = the value of Q_{1i}, Q_{2i} evaluated at node k

R = correction function.

The correction function R provides for a disappearance of the singular assumptions at the borders where both, enriched and 12-node cubic isoparametric elements, have to fit together. However, these compatibility conditions are just satisfied directly at the nodes. Between the nodes, the displacements of these two different elements are not coincident.

Strains are obtained by the derivation of the displacements and they are not continuous at the border of enriched and ordinary 12-node elements. Therefore, strains and stresses are not correct close to the crack tip and they can not be utilized for the determination of the stress intensity factors. The stiffness matrix of the enriched elements becomes [4]:

$$\begin{bmatrix} K^{11} & | & K^{12} \\ \cdots & | & \cdots \\ \cdots & & \cdots \\ K^{21} & | & K^{22} \end{bmatrix} \begin{Bmatrix} \bar{u} \\ \cdots \\ \cdots \\ K_I \\ K_{II} \end{Bmatrix} = \begin{Bmatrix} F \\ \cdots \\ \cdots \\ \bar{F} \end{Bmatrix} \qquad (11)$$

where $\bar{u}$ = element nodal displacements

K^{11} = regular

K^{22} = stiffness matrix from enriched terms

K^{12} = coupled stiffness matrix from regular and enriched terms

$\bar{F}$ = singular load vector which becomes a null vector if no enriched element is on a loaded boundary.

The equation system (11) points out that all singular assumptions of the enriched elements are contained in the stiffness matrix and that the stress intensity factors K_I and K_{II} can be evaluated directly by the program with the displacements.

Furthermore, it is advantageous that the size of the enriched elements can be quite large without losing considerable accuracy. Therefore, complete problems can be solved quite easily within a short data preparation time. Usually, enriched elements are working within an accuracy of about 5%.

However, it has to be noted that smaller enriched elements need not necessarily lead to a higher accuracy which is the case for $\frac{1}{9}$ & $\frac{4}{9}$ point elements.

3.1.2 Application of the Enriched Elements

The determination of the stress intensity factors K_I and K_{II} was done using a special specimen developed by H. A. Richard for mixed mode problems [5], shown in Figure 3.

First, a modified compact tension shear specimen was studied, where the influence of the holes was neglected (Figure 4). Equally distributed stresses were applied.

With the aid of the sinus/cosinus relationship each applied force F under the load angle α can be decomposed to the forces F_z and F_s where

F_z leads to pure Mode I

F_s leads to pure Mode II

It should be mentioned that, in order to obtain pure shear stress on the elongated crack line for case Mode II, also a moment M with

$$M = F_s \cdot c$$

has to be applied in opposite direction of F_s. Applied tensile and shear stresses:

for Mode I: $\sigma_z = \frac{F_z}{wt}$

for Mode II: $\tau_o = \frac{F_s}{wt}$ $\quad \sigma_{bmax} = \frac{M}{W} = \frac{6M}{tw^2}$

The shear stress distribution was chosen in the form of a parabola where

$$\tau_{max} = 1.5\ \tau_o \quad \text{(Figure 5)}$$

Figure 6 and 7 point out the finite element grid of the compact tension shear specimen with the ideal force application. Altogether, 20 finite elements are used, whereas 4 enriched elements are arranged around the crack tip.

In Figure 6, the boundary conditions for pure shear are used: all nodes on the x-axis are constrained in x- and y-direction. It should be added that for pure shear, according to the Moor's strain circle (Figure 8), ε vanishes in shear direction, whereas γ reaches its maximum. However, because of the bending moment M there exist tensile and compressive stresses along the x-axis (Figure 4) which should allow some displacements of the nodes at the boundaries in x-direction. This is not possible. Since the maximal tensile and compressive stresses exist at the corners and since the boundaries are far away from the crack line, these effects can be neglected.

In Figure 7, the boundary conditions for pure tension are shown. Only one node on the x-axis has to be constrained in x- and y-direction, whereas all other nodes on the boundaries can move in x-direction. This takes the Poisson's effect into consideration.

Chart 1, Figure 9 and 10 point out the dimensionless stress intensity factors K_I and K_{II} for load application angles changing from 0 to 90 degrees. $\frac{a}{w}$ was 0.6.

3.2 $\frac{1}{9}$ & $\frac{4}{9}$ Point Elements

3.2.1 Introduction to the $\frac{1}{9}$ & $\frac{4}{9}$ Point Elements

In order to achieve the stress and strain singularity at the crack tip, collapsed cubic isoparametric 12-node elements can be utilized (Figure 11)[7]. These crack-tip elements have to be distorted as follows:

- all nodes lying on the side of the crack tip have to overlap (nodes 1,10,11,12).
- the nodes lying on the sides close to the crack tip are placed on the points with the distances $\frac{1}{9}\ell$, $\frac{4}{9}\ell$ and ℓ away from the tip (therefore the name $\frac{1}{9}$ & $\frac{4}{9}$ point elements).

The mathematical proof of the singularity for these elements is given in [7].

The advantages if these $\frac{1}{9}$ & $\frac{4}{9}$ point elements are:

- one does not need special crack tip elements. Ordinary 12-node elements can be utilized.
- smaller $\frac{1}{9}$ & $\frac{4}{9}$ point elements will lead to a higher accuracy, which is not necessarily the case for enriched elements.

However, these have to be noted as disadvantages:

- because of the higher number of elements, the $\frac{1}{9}$ & $\frac{4}{9}$ point element method is more time consuming than the enriched element method.
- the stress intensity factors K_I and K_{II} have to be calculated in post-process.

The stress intensity factors K_I and K_{II} can be obtained by using the following displacement equations at the crack tip (Figure 12)[8]:

$$u_x \simeq \frac{K_I}{\mu}\sqrt{\frac{r}{2\pi}}\cos\frac{\theta}{2}\left[\frac{1}{2}(k-1) + \sin^2\frac{\theta}{2}\right] + \frac{K_{II}}{\mu}\sqrt{\frac{r}{2\pi}}\sin\frac{\theta}{2}\left[\frac{1}{2}(k+1) + \cos^2\frac{\theta}{2}\right] \quad (13)$$

$$u_y \simeq \frac{K_I}{\mu}\sqrt{\frac{r}{2\pi}}\sin\frac{\theta}{2}\left[\frac{1}{2}(k+1) - \cos^2\frac{\theta}{2}\right] + \frac{K_{II}}{\mu}\sqrt{\frac{r}{2\pi}}\cos\frac{\theta}{2}\left[\frac{1}{2}(1-k) + \sin^2\frac{\theta}{2}\right] \quad (14)$$

provided that $0 < r << 1$

μ = elastic shear modulus

$$k = \begin{cases} 3 - 4\nu & \text{for plane strain} \\ \dfrac{3 - \nu}{1 + \nu} & \text{for plane stress} \end{cases}$$

ν = Poisson's ratio ($\nu = 0.3$)

For $\theta = 90°$ and $\theta = 180°$ K_I and K_{II} become $\theta = 90°$:

$\theta = 90°$:

$$K_I = \frac{u_x + \frac{(\frac{k}{2} + 1)}{(\frac{k}{2} - 1)} u_y}{\sqrt{\frac{r}{4\pi}}\frac{(\frac{k}{2})}{\mu}\left[1 + \frac{(\frac{k}{2} + 1)}{(\frac{k}{2} - 1)}\right]} \tag{15}$$

$$K_{II} = \frac{\mu(u_x - u_y)}{\sqrt{\frac{r}{4\pi}}\, k} \tag{16}$$

$\theta = 180°$:

$$K_I = \frac{\mu\, u_x}{\sqrt{\frac{2r}{\pi}}\,(1 - \nu)} \tag{17}$$

$$K_{II} = \frac{\mu\, u_y}{\sqrt{\frac{2r}{\pi}}\,(1 - \nu)} \tag{18}$$

3.2.2 Optimum Size of the $\frac{1}{9}$ & $\frac{4}{9}$ Point Elements

In order to find out the optimum size of the $\frac{1}{9}$ & $\frac{4}{9}$ point elements, the problem shown in Figure 13 was studied with the appropriate boundary conditions.

Figure 14 points out the finite element grid for shear with which the best results could be obtained. Altogether, 30 finite elements were used, 6 crack tip elements were arranged around the crack tip. The length ℓ of the $\frac{1}{9}$ & $\frac{4}{9}$ point elements was 1.23% of the length of the crack a.

For shear, the stress intensity factors K_I and K_{II} were evaluated along the $\theta = 180°$ line, since this is the only line where the tensile stresses vanish. The equations (17) and (18) were utilized. The results can be seen in Figure 15.

Because the nodes of the crack tip are constrained in both directions the stress intensity factors calculated very close to the tip have to be neglected (about first two elements). The stress intensity factors K_I and K_{II} directly at the crack tip were obtained graphically.

Figure 16 shows the results of a 12 element mesh using 4 crack-tip elements (shear). The length of the $\frac{1}{9}$ & $\frac{4}{9}$ point elements was 1% of the crack length. This grid turns out to be too rigid.

Figure 17 points out the results of a 36 element grid using 6 $\frac{1}{9}$ & $\frac{4}{9}$ point elements around the crack tip. It turns out that just increasing the elements without using more crack tip elements need not necessarily lead to a higher accuracy (Length of the crack-tip elements: 0.667% of the length of the crack.).

For pure tension, the best results could be obtained along the $\theta = 90°$ line where the equations (15) and (16) were used (Figure 18).

The dimensionless K_I and K_{II} factors are ($\frac{a}{w} = 0.6$):

The dimensionless K_I and K_{II} factors are ($\frac{a}{w}$ = 0.6):

α [°]	0	90
$\frac{K_I}{\frac{F}{wt}\sqrt{\pi a}}$	3.99 (4.12)	0 (- 0.01)
$\frac{K_{II}}{\frac{F}{wt}\sqrt{\pi a}}$	(-) 0.11 ((-)0.05)	1.57 (1.63)

For α equal to zero degree, the dimensionless K_I factor becomes 3.99, whereas K_{II} turns out to be - 0.11. Usually K_{II} should vanish for this loading case. However, this discrepancy should not be overevaluated, since for Mode I, all nodes at the crack tip are constrained in both directions. This restriction can lead to different results.

For α equal to 90 degrees, the dimensionless K_{II} factor turns out to be 1.57, whereas K_I vanishes.

The values in parentheses show the results of the enriched element method.

3.2.3 Application of the $\frac{1}{9}$ & $\frac{4}{9}$ Point Elements to the CTS Specimen

Now, the $\frac{1}{9}$ & $\frac{4}{9}$ point elements are applied to the compact tension shear specimen. The stress intensity factors of the CTS specimen are determined with the aid of the finite element grid of Figure 19. Twelve $\frac{1}{9}$ & $\frac{4}{9}$ point elements are arranged around the crack tip. This grid is utilizing the boundary

conditions already shown in Figure 6 and 7. Ideal distributed forces are applied to the specimen.

There are several reasons why the whole finite element grid of the CTS spcimen (Figure 19) has to be used and why it can not be replaced by the grid shown in Figure 14.

First, in Figure 14 all nodes at the crack tip are constrained in x- and y-direction. This leads to restrictions which need not represent the reality. All nodes at the crack tip should be able to move in all directions in order to adapt to the required situation. This restriction can be the reason for the inaccurate stress intensity factors close to the crack tip in Figures 15-18.

Secondly, the boundary conditions of Figure 14 (shear) do not simulate the boundary conditions for pure shear. According to equation (14), all nodes along the boundaries should be able to move in y-direction ($\theta = 0°$, $K_I = 0$, $K_{II} = 0$) except for the nodes at the crack tip. In Figure 14, this would lead to instabililty and could not be realized.

The finite element grid of Figure 19 does not use any boundary conditions at and around the crack tip.

In Figure 20 and 21, it can be seen how the stress intensity factors are evaluated. For pure tension (Figure 20a,b), the stress intensity factors were determined along the $\theta = 90°$ line (Figure 12, equations 15 and 16), whereas for pure shear (Figure 21a,b), the $\theta = 180°$ line was utilized along the upper crack surface (equations 17 and 18). The calculations

along the upper and lower crack surface lead to identical results. In Figure 20 and 21, the k factors of all nodes along the $\theta = 90°$ or $\theta = 180°$ line could be used in order to determine the stress intensity factors at the crack tip. For all calculations, the nodal displacements relative to the crack tip were taken into consideration. Since all nodes of the crack tip are allowed to move separately, only that crack tip node was chosen as the reference point which was laying on the $\theta = 90°$ or $\theta = 180°$ line of the respective $\frac{1}{9}$ & $\frac{4}{9}$ point element.

In Chart 3, Figure 22 and 23, the dimensionless stress intensity factors are shown for $\frac{a}{w} = 0.6$. For pure tension, the dimensionless K_I factor turns out to be 3.98, whereas K_{II} vanishes. For pure shear, the dimensionless stress intensity factor K_{II} becomes 1.56, whereas K_I is zero.

The results of the $\frac{1}{9}$ & $\frac{4}{9}$ point elements are compared with those of the enriched elements and of Richard [9]. Richard used a superelement in order to simulate the crack tip singularity. In general, the stress intensity factor of the $\frac{1}{9}$ & $\frac{4}{9}$ point elements and the results of Richard are laying very close together. The differences are equal to or smaller than 1% and can be neglected. The enriched elements are a little bit more inaccurate.

Figure 24 and 25 point out the location of the crack-tip

nodes after applied shearing and tensile stresses. For shear, the nodes are more distributed in direction of the x-axis, whereas for Mode I, the crack tip nodes are more arranged along the y-axis. Unfortunately, it is not possible to find out in which direction the crack will propagate. The nodes of the crack-tip elements are randomly distributed.

Figure 26 and 27 show how the crack will behave for the loading cases tension and shear. For pure tension (Figure 26), the nodes on the upper crack surface undergo larger displacements than the nodes of the lower crack surface. However, in the vicinity of the crack tip, the displacement of the corresponding nodes on both surfaces are identical. Figure 27 shows the behavior of both crack surfaces for pure shear. Along the whole crack line, both surfaces are sliding against each other as expected. Away from the crack tip, both crack surfaces are penetrating slightly. This penetration is very small compared with the displacements in x-direction or the displacements in Figure 26. It lies within the accuracy of the program and should not be overevaluated. It can be said that for pure shear, no penetration occurs along the crack surface.

4. LOADED HOLES WITHIN A PLATE

4.1 Modelling of the Holes

Up to now, just the ideal force application to the compact tension shear specimen has been taken into consideration. In reality, the forces are applied with the aid of bolts which could lead to a different stress and strain distribution around the crack tip.

In most of the previous examinations just a nodal force was assumed in the middle of the holes. Also Richard [10] was working with single nodal forces when he was studying the stress intensity factors of his CTS specimen.

However, there are required so huge forces in order to be able to tear apart a CTS specimen that a plastic deformation comes into being. This plastic deformation leads to a force application over a broader cross section at the holes. No one knows how broad this plastic zone will be.

In this research another approach was done. It was assumed that the bolts fit exactly into the holes of the CTS specimen and that the forces can be applied over the hole cross section of the holes. All calculations were done for the pure elastic case.

Figure 28 and 29 point out the finite element grids of a arbitrary plate and a bolt. The boundary conditions of the bolt are imitating the hole of the plate: the points 1-7 of the bolt can just move along the tangent of the hole. For

both, hole and plate, the symmetry could be used.

When the bolt is loaded, a nodal force F is applied in the center of the bolt in negative y-direction which leads to an elastic deformation and to reaction forces in the nodes 1-7 in y-direction. These forces (F_1 - F_7) are applied at the nodes 1* - 7* of the plate. The displacements of these nodes (1* - 7*) can be taken as prescribed displacements for the nodes 1-7 of the bolt. After 9 iterations, the changes of the forces in the nodes 1-7 of the bolt were less than 1%. The obtained forces and displacements are given in Chart 2.

It should be mentioned that

$$\sum_{i=1}^{13} F_i = 1.3873 = 1.3873\ F$$

The reason is that the finite element method is based on the principle of virtual displacements which leads to

δW_E: work done by external forces

$$\delta W_E = \delta W_i \tag{19}$$

δW_i: work done by internal forces

$$\int_V (\underset{\sim}{\sigma}^T \delta \underset{\sim}{\varepsilon})\ dV = \int_V (\underset{\sim}{b}^T \Delta \underset{\sim}{u})\ dV + \int_A (\underset{\sim}{p}^T \Delta \underset{\sim}{u})\ dA \tag{20}$$

$\underset{\sim}{\sigma}$ = stress matrix

$\underset{\sim}{\varepsilon}$ = strain matrix

$\underset{\sim}{b}$ = body force matrix

$\underset{\sim}{p}$ = exterior surface force matrix

$\underset{\sim}{u}$ = displacement matrix

A = surface area

V = volume

Because of the separation of bolt and plate, for the plate, just the nodal forces $F_1 \ldots F_{13}$ have to be taken into consideration. Therefore, the resultive force which is applied to the hole of a plate is

$$F_{res} = 1.3873\ F = \sum_{i=1}^{13} F_i \qquad (21)$$

Figure 30 shows the deformation of the bolt and the plate under the influence of the applied force F.

Figure 31 and 32 point out the dimensionless stress distribution around the bolt and the hole of the plate.

4.2 Application of the Holes to the Simplified Compact Tension Shear Specimen

First, the holes are applied to the simplified CTS specimen of Figure 12 which leads to Figure 33 ($\frac{a}{w} = 0.6$).

In Figure 34 it can be seen how the stress intensity factors K_I and K_{II} are evaluated for shear. It turns out

that the difference between the stress intensity factors using a CTS specimen with and without holes is less than 0.2%. For both cases K_I is pretty exactly zero (shear).

The dimensionless K_{II} factors are:

including the holes: $$K^*_{II_1} = \frac{K_{II_1}}{\frac{F}{tw}\sqrt{\pi a}} = 1.573$$

without the holes: $$K^*_{II_2} = \frac{K_{II_2}}{\frac{F}{tw}\sqrt{\pi a}} = 1.576$$

$$\left| \frac{K^*_{II_2} - K^*_{II_1}}{K^*_{II_2}} \right| = 0.19\%$$

which lies within the accuracy of the procedure and can be neglected. Since for pure shear, the shear force is applied to a single hole and the other two holes are utilized to apply the bending moment, this case can be considered as the extreme loading case. For all other loading cases the difference of the stress intensity factors using specimen with and without holes will not be more than 0.2%. Therefore, for the following problems the influence of the holes can be neglected and only CTS specimen with the application of equally distributed forces will be used.

4.3 Application of the Holes to a CTS Specimen

Figure 35 shows the CTS specimen with enriched elements including the holes. In this grid the ideal boundary conditions could be utilized (statically stable):

- at the upper three holes the required forces are applied
- the nodes of the lower holes are fixed in the shown way: they can move in one direction. In the direction perpendicular to it prescribed displacements are used in order to achieve the same force distribution which is applied to the upper three holes.

With this grid, the boundary conditions of Figure 6 should be tested which are not 100% correct. Unfortunately, this mesh does not work because the allowed bandwidth of the program was exceeded.

5. EXAMINATION OF DIFFERENT CRACK LENGTHS

Up to now, only one crack length ($\frac{a}{w} = 0.6$) has been studied. In this chapter, also two other crack lengths ($\frac{a}{w} = 0.5$ and $\frac{a}{w} = 0.7$) will be examined with the aid of a finite element grid similar to that one of Figure 19. Equally distributed forces are applied to the specimen.

In Figure 36a-39b, it can be seen how the stress intensity factors are evaluated for pure tension and pure shear. All results are put together in Chart 4, Figure 40, 41 and 42.

For pure shear, the dimensionless K_{II} factors are $1.37(\frac{a}{w} = 0.5)$, $1.56(\frac{a}{w} = 0.6)$ and $1.74(\frac{a}{w} = 0.7)$. Except for $\frac{a}{w} = 0.5$, all K_I factors vanish. For $\frac{a}{w} = 0.5$, K_I is slightly negative (- 0.02), which would lead to a penetration of the crack surfaces. For this loading case,

$\left| \frac{K_I}{K_{II}} \right|$ is equal to 1.4% which lies within the accuracy of the program and should not be overevaluated.

All obtained stress intensity factors are compared with the results of Richard [9]. The differences between the results of the $\frac{1}{9}$ & $\frac{4}{9}$ point element method and the results of Richard are small, except for the crack length $\frac{a}{w} = 0.5$ ($\alpha = 90^\circ$) where

Richard obtains a K_I factor of + 0.08. The $\frac{1}{9}$ & $\frac{4}{9}$ point elements lead to $|K_I|$ = + 0.02 which is smaller.

For pure tension, the dimensionless K_I factors become 2.81($\frac{a}{w}$ = 0.5), 3.98($\frac{a}{w}$ = 0.6) and 6.19($\frac{a}{w}$ = 0.7). All stress intensity factors K_{II} are zero.

6. SUMMARY

In this research, the stress intensity factors K_I and K_{II} were evaluated for a special compact tension shear specimen developed by Richard. Two different crack-tip elements were utilized: enriched elements and $\frac{1}{9}$ & $\frac{4}{9}$ point elements. The finite element grid using enriched elements leads to quite accurate results with a relative low number of elements. In order to obtain more accurate results, $\frac{1}{9}$ & $\frac{4}{9}$ point elements have to be used. For this case, the size of the finite elements arranged around the crack tip has to be very small. The optimum results could be achieved for $\frac{1}{9}$ & $\frac{4}{9}$ point elements with an element length of about 1.23% of the crack length.

Furthermore, the holes were examined where the forces are applied to the compact tension shear specimen. Two different finite element grids were compared: one mesh with a force concentration around the holes and another finite element grid with equally distributed forces at the whole cross section. Both finite element grids led to the same results which means that the CTS specimen is so well designed that the holes do not have an influence on the stress intensity factors.

Altogether, the stress intensity factors were evaluated for three different crack lengths. For pure shear, the dimensionless stress intensity factors K_{II} become

1.37($\frac{a}{w}$ = 0.5), 1.56($\frac{a}{w}$ = 0.6) and 1.74($\frac{a}{w}$ 0.7). K_I is pretty exactly zero for all three crack lengths.

For pure tension, the dimensionless stress intensity factors K_I turn out to be 2.81($\frac{a}{w}$ = 0.5), 3.98($\frac{a}{w}$ = 0.6) and 6.19($\frac{a}{w}$ = 0.7), whereas the K_{II} factors vanish.

REFERENCES

[1] S. L. Pu, M. A. Hussain and W. E. Lorensen, "The Collapsed Cubic Isoparametric Element as a Singular Element for Crack Problems," in International Journal for Numerical Methods in Engineering, Vol. 12, pp. 1728-1730, 1978.

[2] K. Kussmaul, "Festigkeitslehre I," Vorlesungsmanuskript, MPA Stuttgart, p. 169, 1982.

[3] L. N. Gifford, "APES - Second Generation Two-Dimensional Fracture Mechanics and Stress Analysis by Finite Elements," DTNSRDC Report #4799, p. 12, December 1975.

[4] S. E. Benzley, "Representation of Singularities with Isoparametric Finite Elements," in International Journal for Numerical Methods in Engineering, Vol. 8, pp. 538--542, 1974.

[5] H. A. Richard, "Einleitung von überlagerter Normal- und Scherbeanspruchung in Bruchmechanikproben," University of Kaiserslautern, 1981.

[6] M. M. Filonenko-Boroditsch, "Festigkeitslehre Band I," VEB Verlag Technik Berlin, p. 191, 1954.

[7] M. M. Pu, M. A. Hussain and W. E. Lorensen, "The Collapsed Cubic Isoparametric Element as a Singular Element for Crack Problems," in International Journal for Numerical Methods in Engineering, Vol. 12, pp. 1730-1734, 1978.

[8] J. Eftis, N. Subramonian and H. Liebowitz, "Crack Border Stress and Displacement Equations Revisited," in Journal Fracture Mechanics, Vol. 9, p. 189, 1977.

[9] H. A. Richard, Habilitationsschrift, University of Kaiserslautern, p. 213, Chart 15, 1984.

[10] H. A. Richard, Habilitationsschrift, University of Kaiserslautern, p. 168, 1984.

A P P E N D I X A

MEASUREMENTS AND CONVERSION FACTORS

MEASUREMENTS

Length	INCH	IN.
Force	kilo pound	kip(1000 lb.)
Stress σ, τ)	pound/inch^2	psi = $\frac{\text{lb.}}{\text{in.}^2}$
Young's Modulus (E)		3×10^7 psi(metals)
Poisson's Ratio (ν)		0.3(metals)
Stress Intensity Factor (K)		psi $\sqrt{\text{in.}}$

CONVERSION FACTORS

1 in. = 2.54cm = 2.54×10^{-2} m

1 lb. = 453.6g = 0.4536 kg

1 psi = 6.8948×10^{-3} $\frac{\text{N}}{\text{mm}^2}$

A P P E N D I X B

CHARTS

CHART 1: Dimensionless K_I and K_{II} Factors for Enriched Elements (Ideal Force Application)

$\frac{a}{w} = 0.6$

α [°]	$\frac{K_I}{\frac{F}{tw}\sqrt{\pi a}}$	$\frac{K_{II}}{\frac{F}{tw}\sqrt{\pi a}}$
0	4.12	- 0.05
15	3.98	0.37
30	3.56	0.77
45	2.91	1.11
60	2.05	1.38
75	1.06	1.56
90	- 0.01	1.63

CHART 2: Equivalent Forces and Displacements Due to Bolt Loading

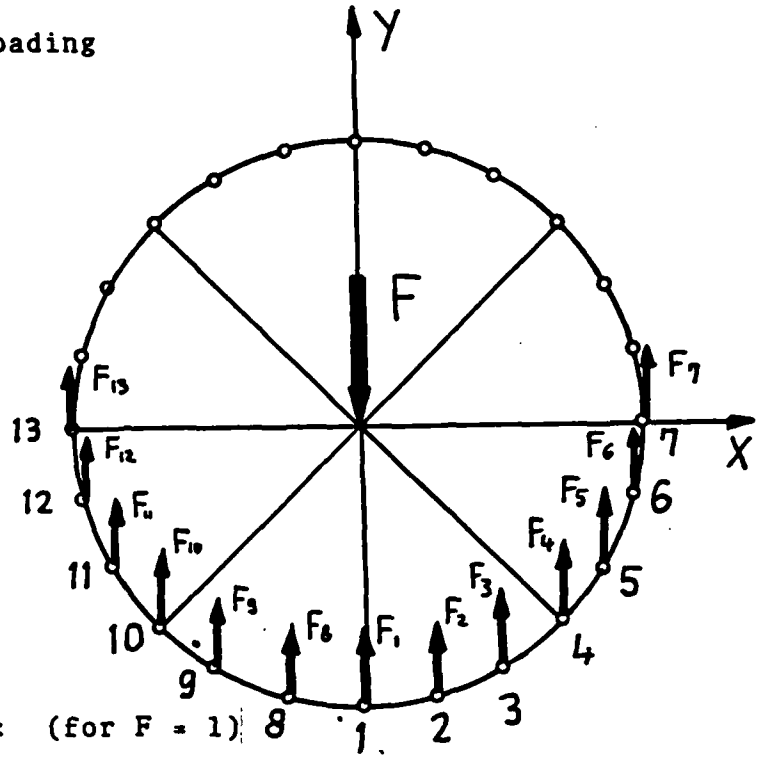

Obtained forces:

$F = +1$

$F_1 = 0.12489$

$F_2 = F_8 = 0.14789$

$F_3 = F_9 = 0.14274$

$F_4 = F_{10} = 0.08601$

$F_5 = F_{11} = 0.12535$

$F_6 = F_{12} = 0.12076$

$F_7 = F_{13} = 0.00844$

Obtained displacements: (for F = 1)

Node #	y [x 10^{-11}]	x [x 10^{-11}]
1	- 361.9	0.
2	- 375.8	13.5
3	- 334.5	23.6
4	- 278.3	7.7
5	- 216.9	18.6
6	- 131.7	- 52.1
7	0.	- 60.2
8	- 375.8	- 13.4
9	- 334.5	- 23.6
10	- 278.3	- 7.7
11	- 216.9	18.6
12	- 131.7	52.1
13	0.	60.2

CHART 3: Dimensionless Stress Intensity Factors for $\frac{a}{w} = 0.6$

α [°]	$\frac{1}{9}$ & $\frac{4}{9}$ Point Elements		Richard		Enriched Elements	
	$\frac{K_I}{\frac{F}{wt}\sqrt{\pi a}}$	$\frac{K_{II}}{\frac{F}{wt}\sqrt{\pi a}}$	$\frac{K_I}{\frac{F}{wt}\sqrt{\pi a}}$	$\frac{K_{II}}{\frac{F}{wt}\sqrt{\pi a}}$	$\frac{K_I}{\frac{F}{wt}\sqrt{\pi a}}$	$\frac{K_{II}}{\frac{F}{wt}\sqrt{\pi a}}$
0	3.98	0.00	4.02	0.00	4.12	- 0.05
15	3.84	0.40	3.89	0.41	3.98	0.37
30	3.45	0.78	3.49	0.78	3.56	0.77
45	2.81	1.10	2.86	1.11	2.91	1.11
60	1.99	1.35	2.03	1.36	2.05	1.38
75	1.03	1.51	1.06	1.52	1.06	1.56
90	0.00	1.56	0.02	1.57	- 0.01	1.63

CHART 4: Dimensionless Stress Intensity Factors for Different Crack Lengths

α (°)	$\frac{a}{w} = 0.5$				$\frac{a}{w} = 0.6$				$\frac{a}{w} = 0.7$			
	$\frac{K_I}{\frac{F}{wt}\sqrt{\pi a}}$		$\frac{K_{II}}{\frac{F}{wt}\sqrt{\pi a}}$		$\frac{K_I}{\frac{F}{wt}\sqrt{\pi a}}$		$\frac{K_{II}}{\frac{F}{wt}\sqrt{\pi a}}$		$\frac{K_I}{\frac{F}{wt}\sqrt{\pi a}}$		$\frac{K_{II}}{\frac{F}{wt}\sqrt{\pi a}}$	
	$\frac{1}{9}$ & $\frac{4}{9}$ Point Elements	Richard	$\frac{1}{9}$ & $\frac{4}{9}$ Point Elements	Richard	$\frac{1}{9}$ & $\frac{4}{9}$ Point Elements	Richard	$\frac{1}{9}$ & $\frac{4}{9}$ Point Elements	Richard	$\frac{1}{9}$ & $\frac{4}{9}$ Point Elements	Richard	$\frac{1}{9}$ & $\frac{4}{9}$ Point Elements	Richard
0	2.81	2.84	0.00	0.00	3.98	4.02	0.00	0.00	6.19	6.26	0.00	0.00
15	2.71	2.76	0.35	0.36	3.84	3.89	0.40	0.41	5.78	6.05	0.45	0.46
30	2.42	2.50	0.68	0.69	3.45	3.49	0.78	0.78	5.36	5.42	0.87	0.88
45	1.97	2.06	0.97	0.98	2.81	2.86	1.10	1.11	4.38	4.43	1.23	1.25
60	1.39	1.49	1.19	1.20	1.99	2.03	1.35	1.36	3.09	3.13	1.51	1.53
75	0.71	0.81	1.32	1.34	1.03	1.06	1.51	1.52	1.60	1.62	1.68	1.71
90	- 0.02	0.08	1.37	1.39	0.00	0.02	1.56	1.57	0.00	0.00	1.74	1.77

A P P E N D I X C

FIGURES

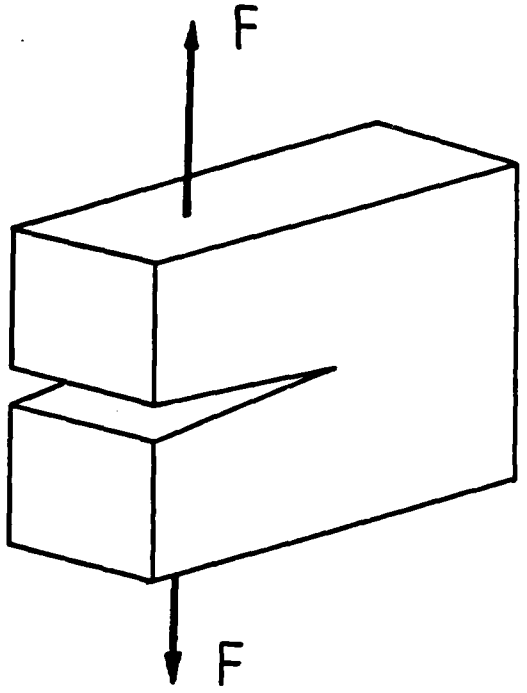

Mode I

Opening Mode

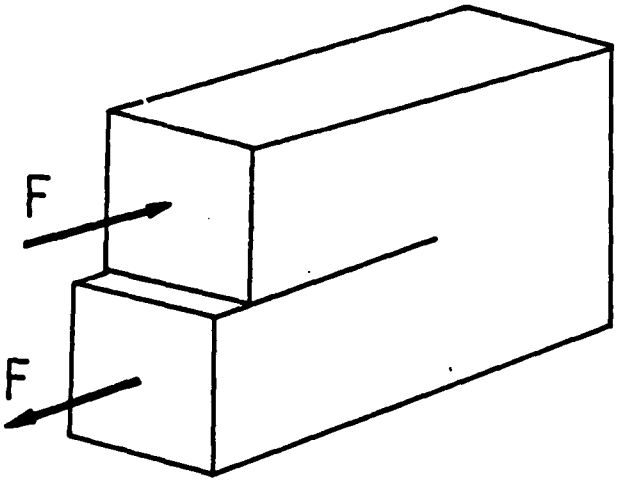

Mode II

Sliding Mode

Figure 1: Mode I and Mode II

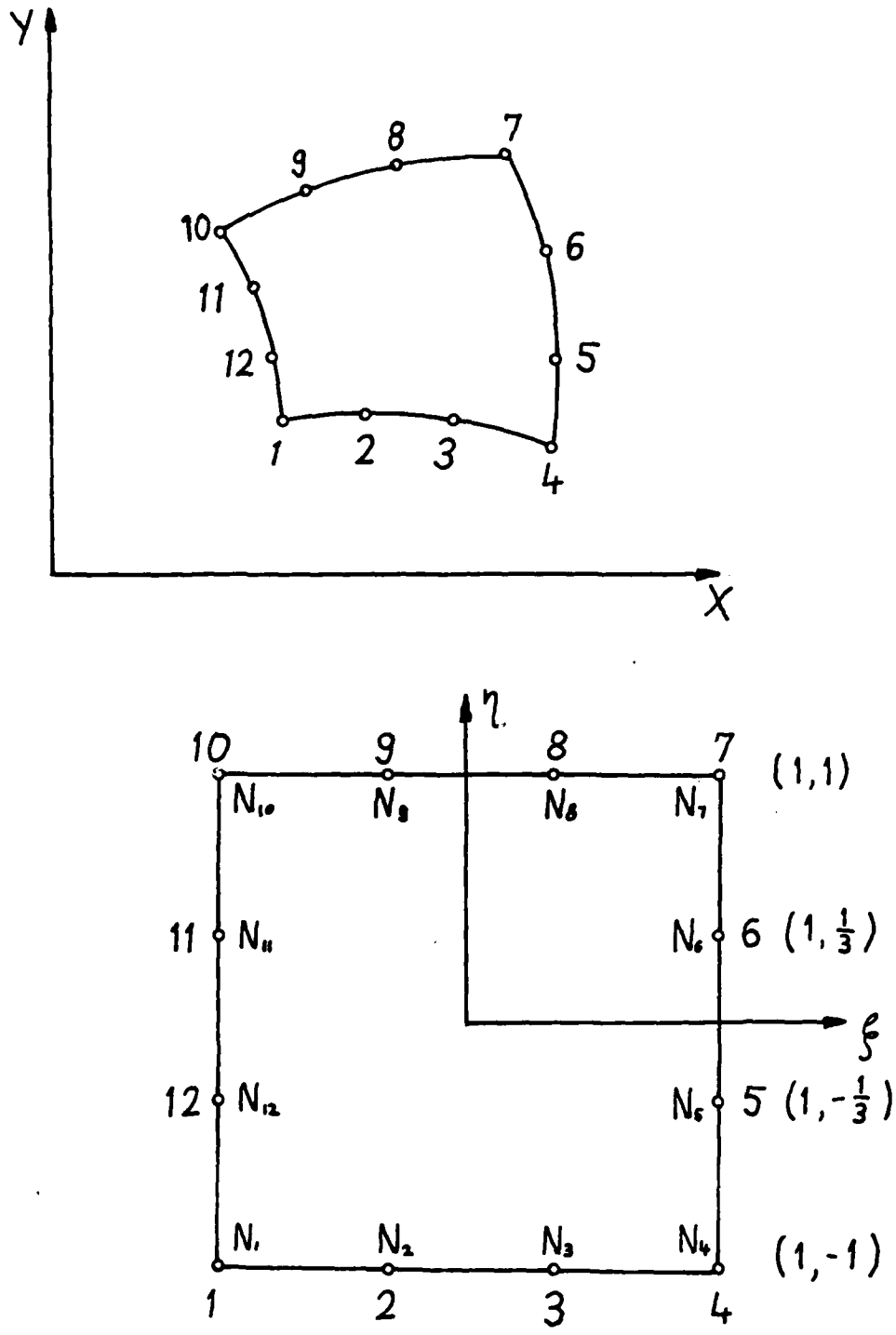

Figure 2: 12-Node Quadrilateral Isoparametric Element

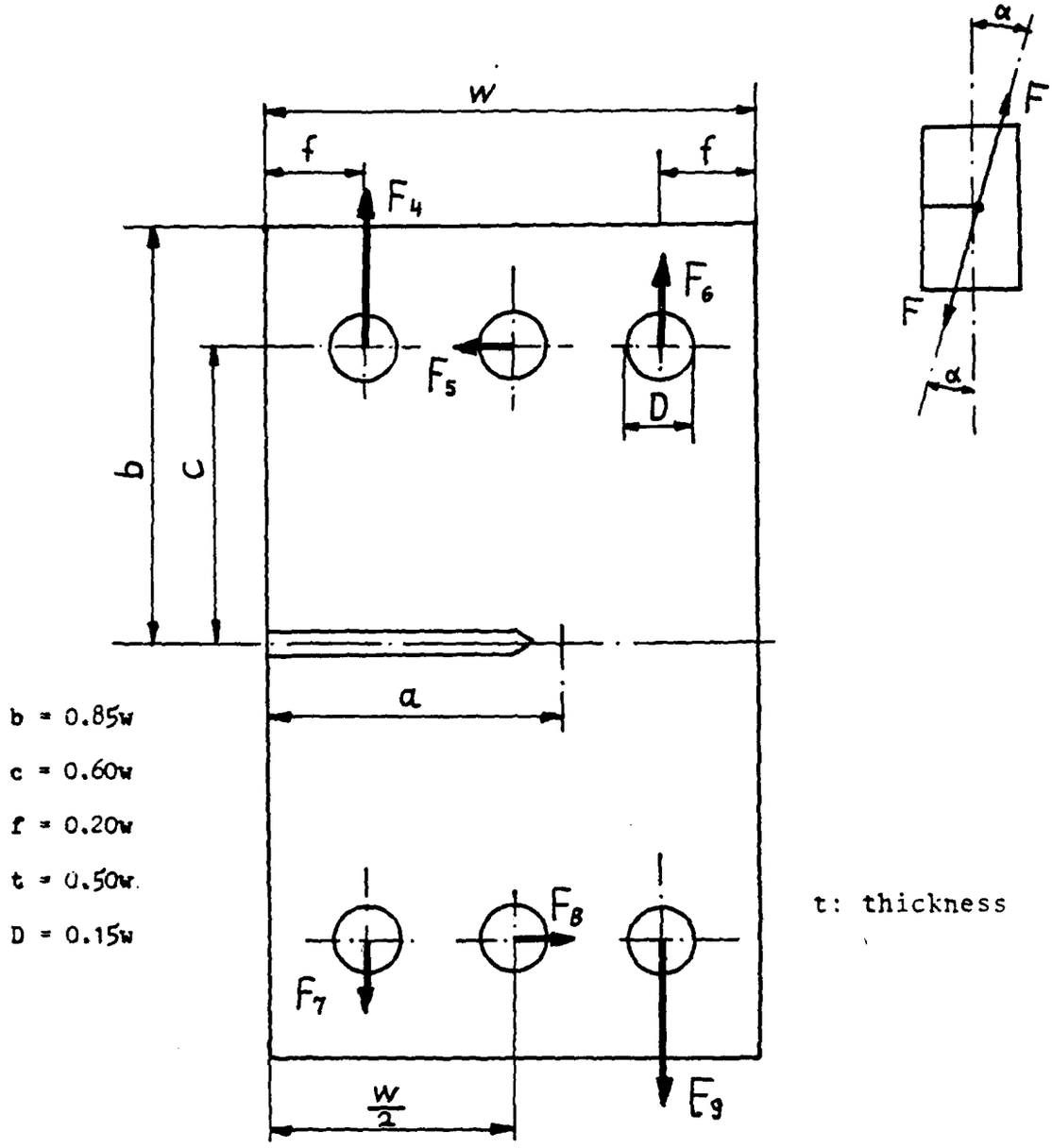

b = 0.85w

c = 0.60w

f = 0.20w

t = 0.50w

D = 0.15w

t: thickness

$$F_4 = F_9 = F\left(\frac{1}{2}\cos\alpha + \frac{c}{w-2f}\sin\alpha\right)$$

$$F_5 = F_8 = F\sin\alpha$$

$$F_6 = F_7 = F\left(\frac{1}{2}\cos\alpha - \frac{c}{w-2f}\sin\alpha\right)$$

Figure 3: Compact Tension Shear Specimen

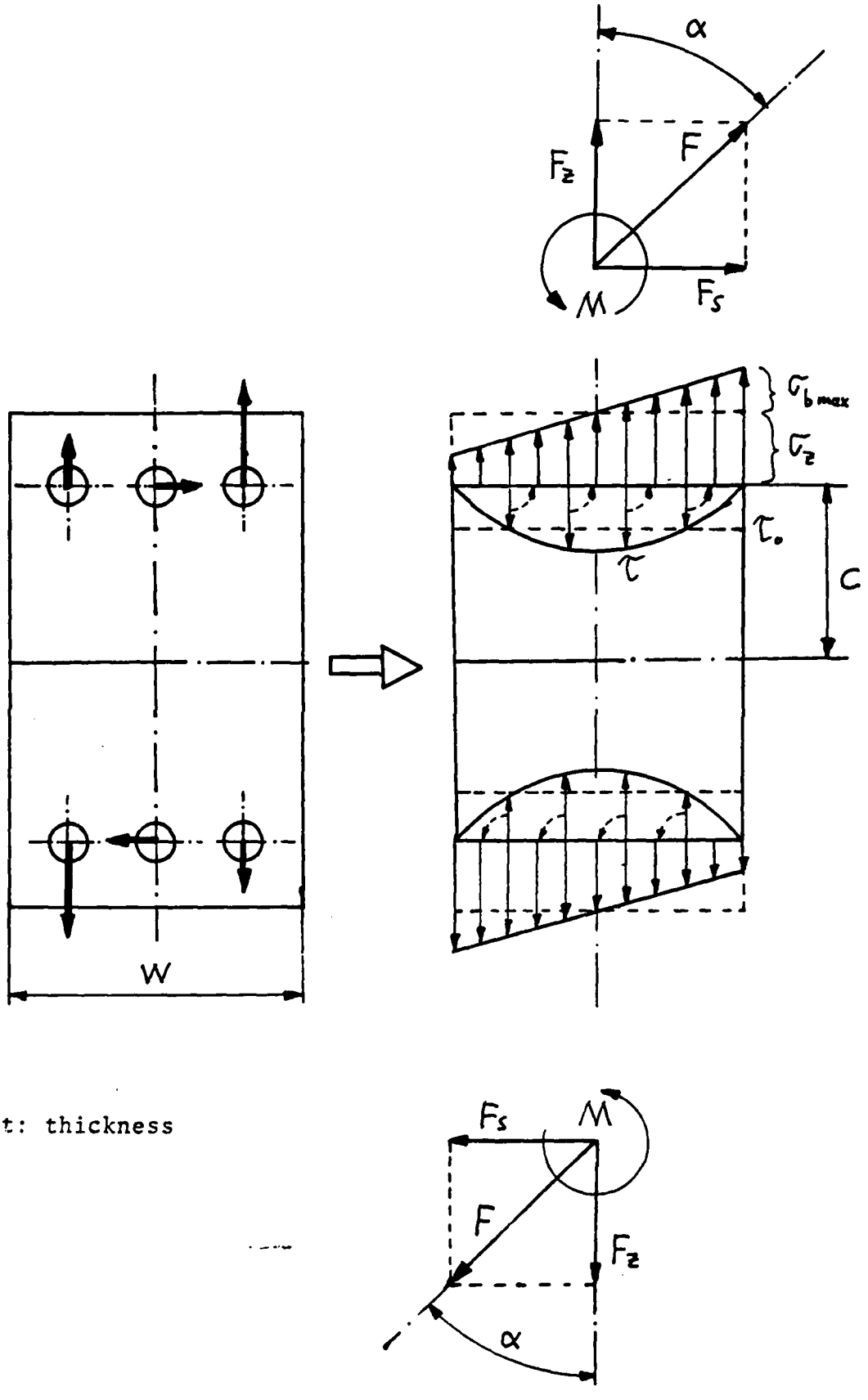

Figure 4: Ideal Force Application

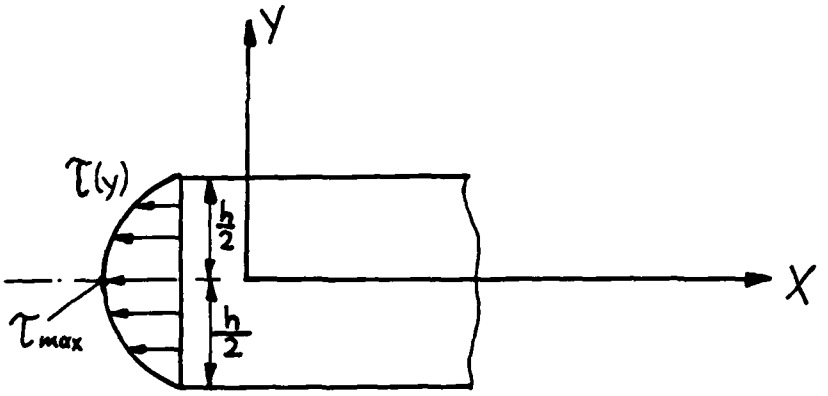

$$\tau = \frac{6Q}{bh^3}\left(\frac{h^2}{4} - y^2\right)$$

$$y = 0: \tau_{max} = \frac{3Q}{bh} = \frac{3}{2}\frac{Q}{F}$$

b: thickness

Q: shearing force

F: cross section

Coordinate Transformation:

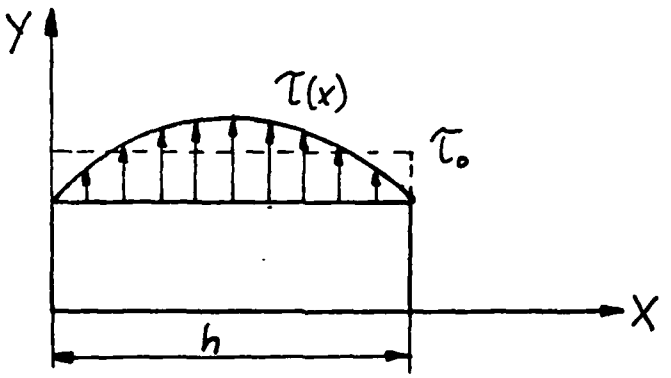

$$\tau = 6\tau_o\left(\frac{1}{4} - \left(\frac{x-h/2}{h}\right)^2\right)$$

Figure 5: Shear Stress Distribution

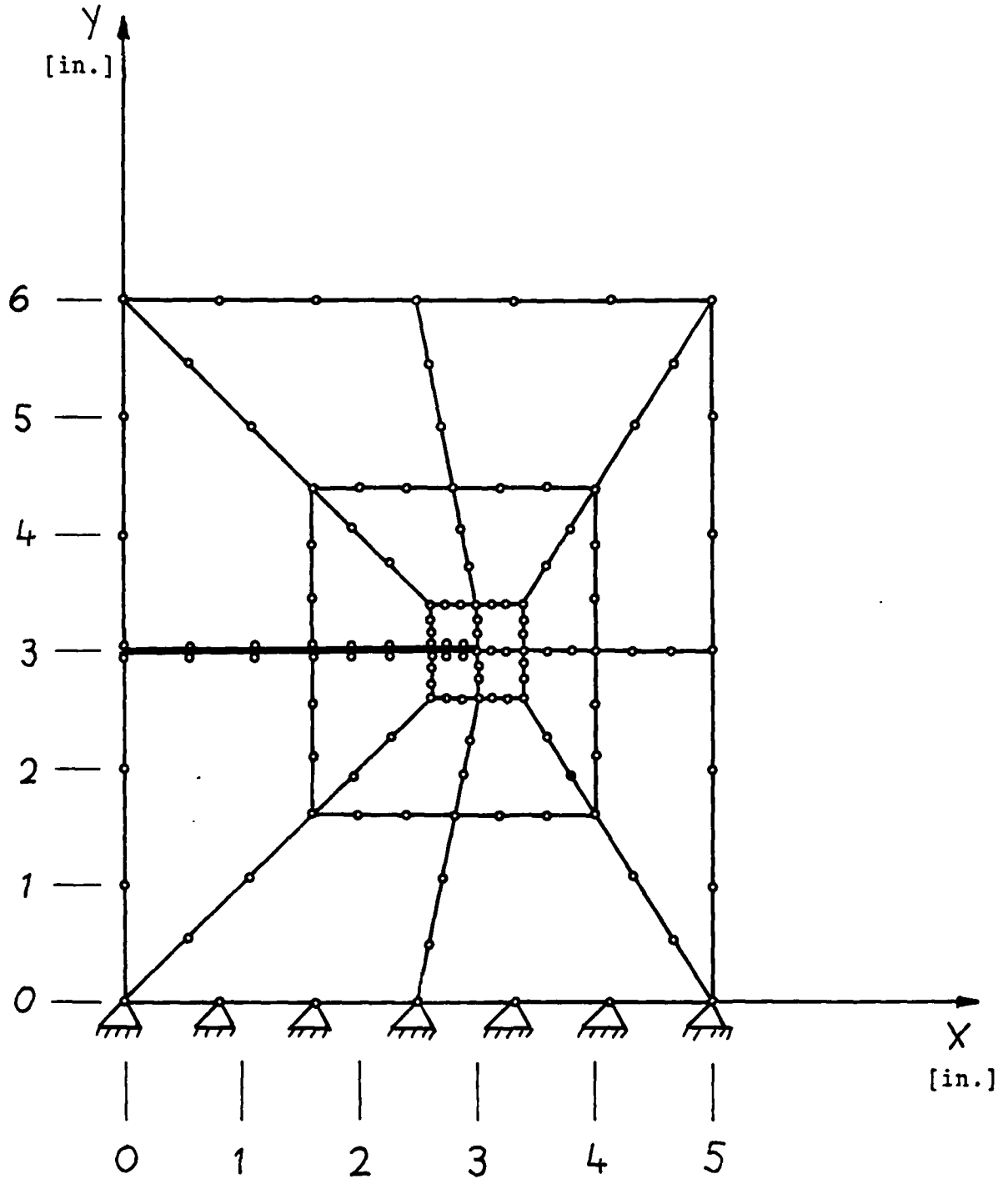

Figure 6: 20 Element Grid with 4 Enriched Elements Using the Boundary Conditions for Mode II

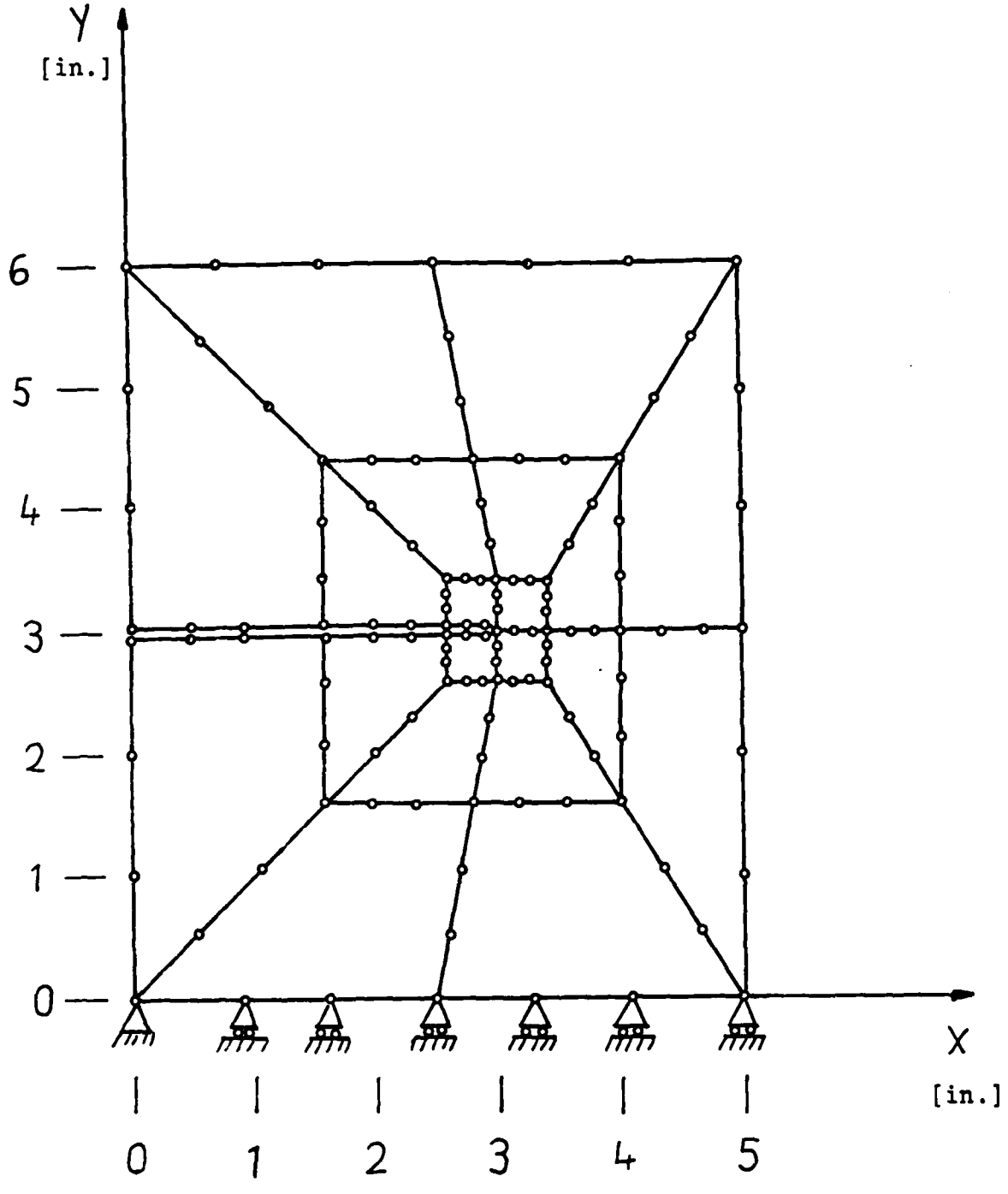

Figure 7: 20 Element Grid with 4 Enriched Elements Using the Boundary Conditions for Mode I

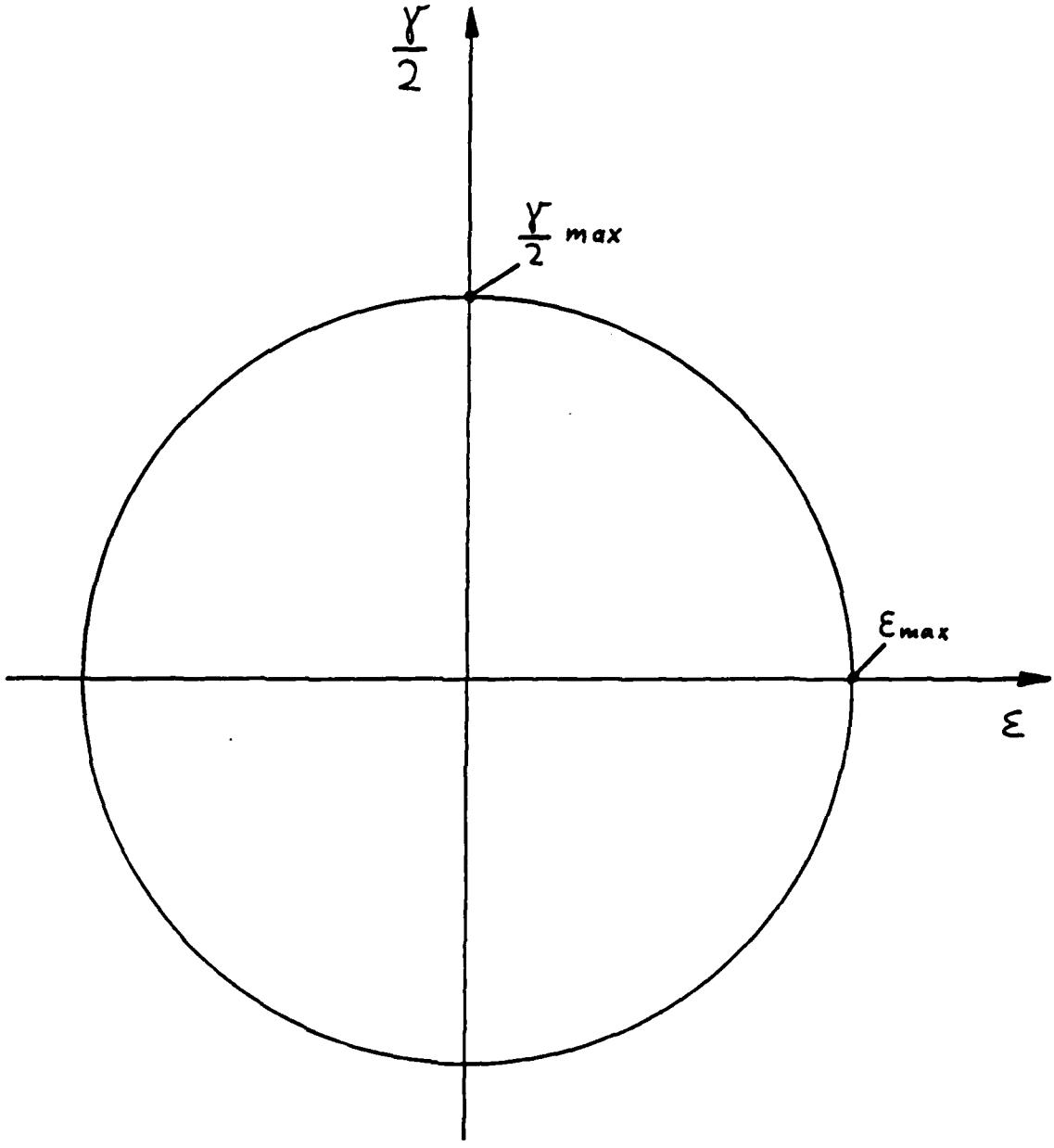

Figure 8: Moor's Strain Circle

Figure 9: Dimensionless K_I-Factors for Enriched Elements

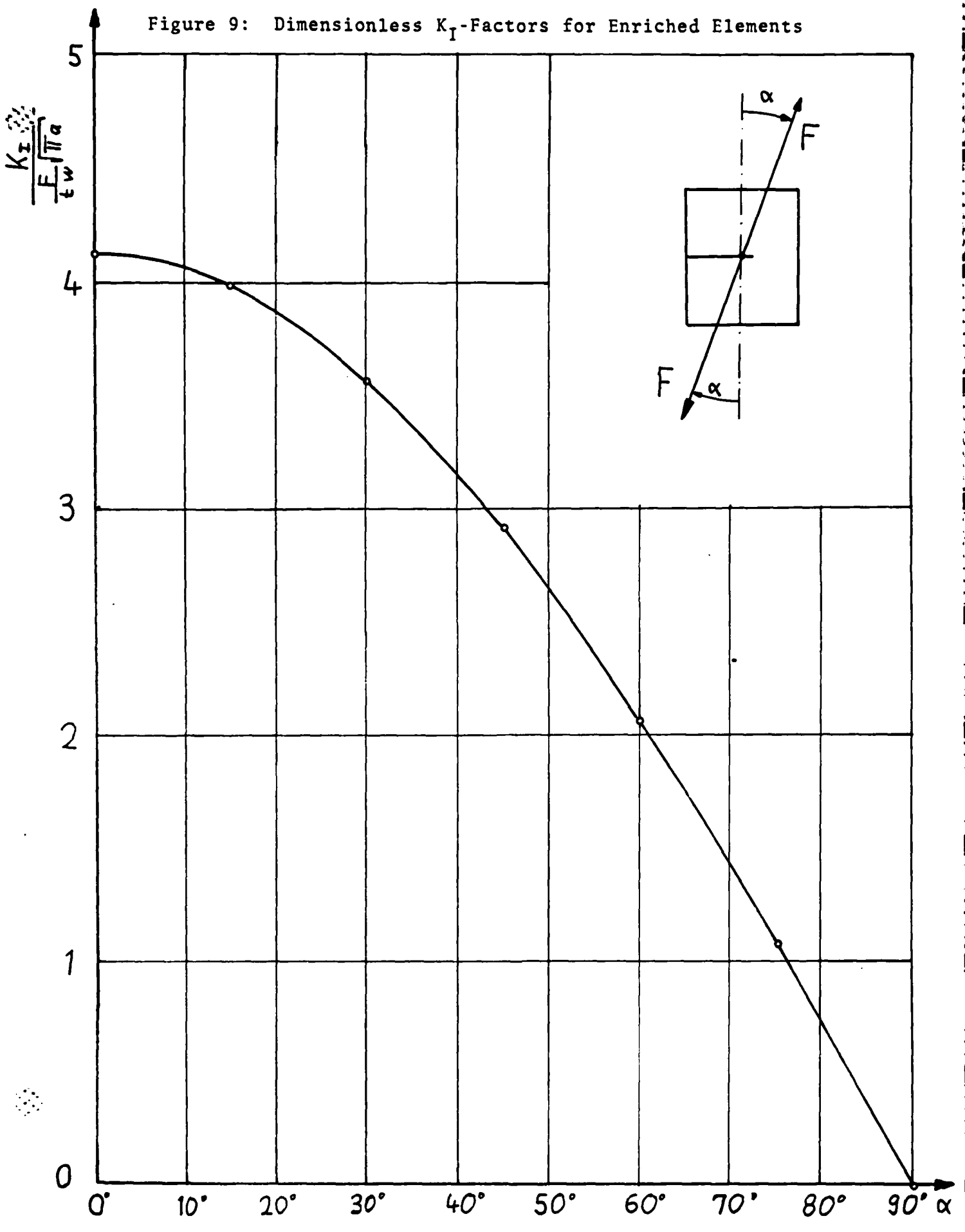

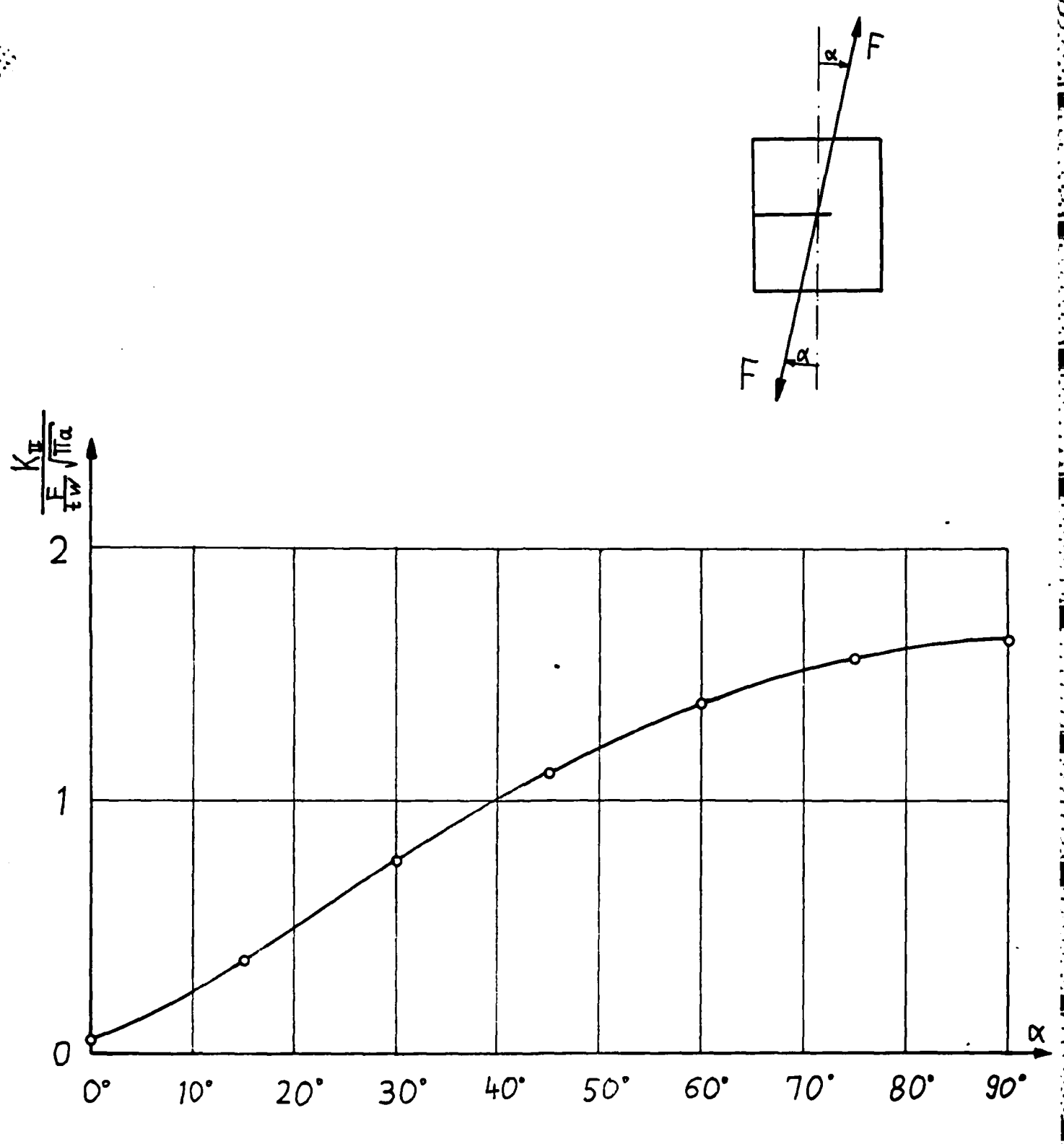

Figure 10: Dimensionless K_{II}-Factors for Enriched Elements

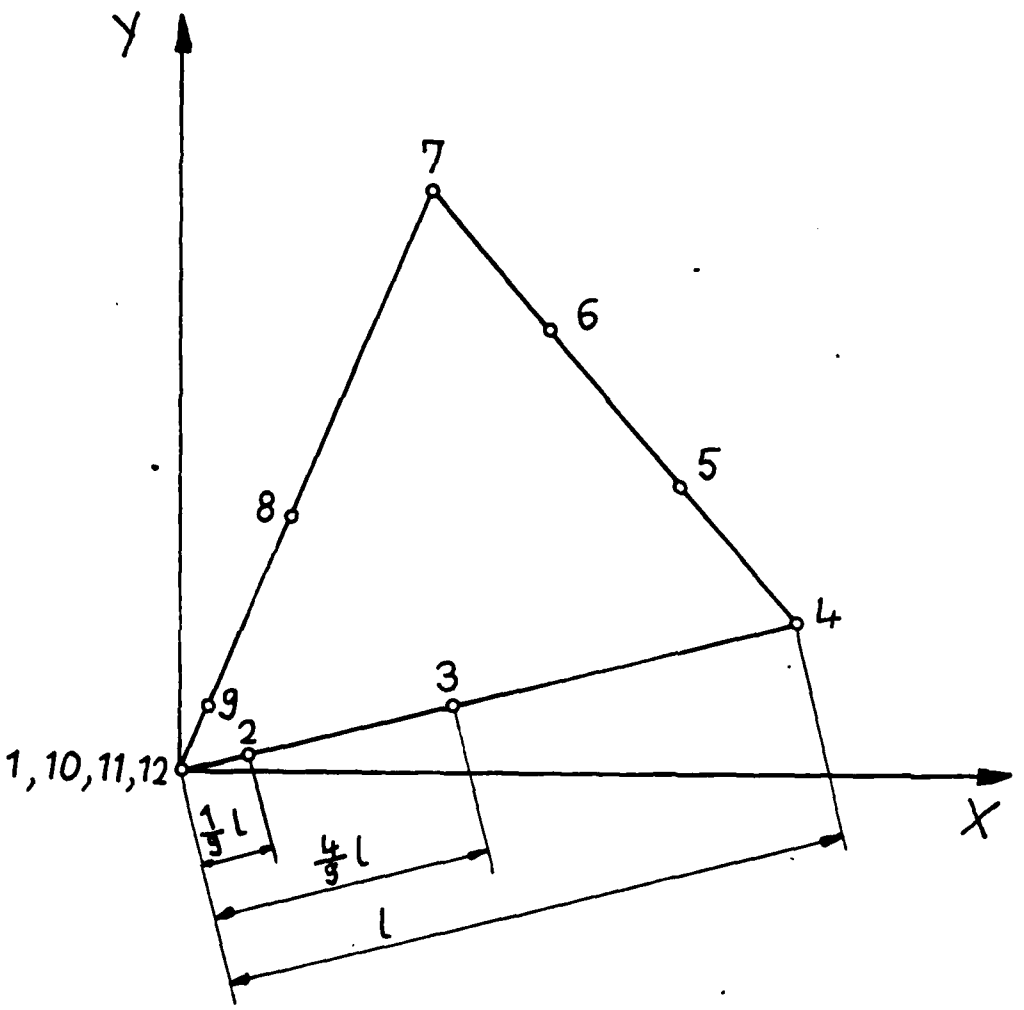

Figure 11: $\frac{1}{9}$ & $\frac{4}{9}$ Point Element

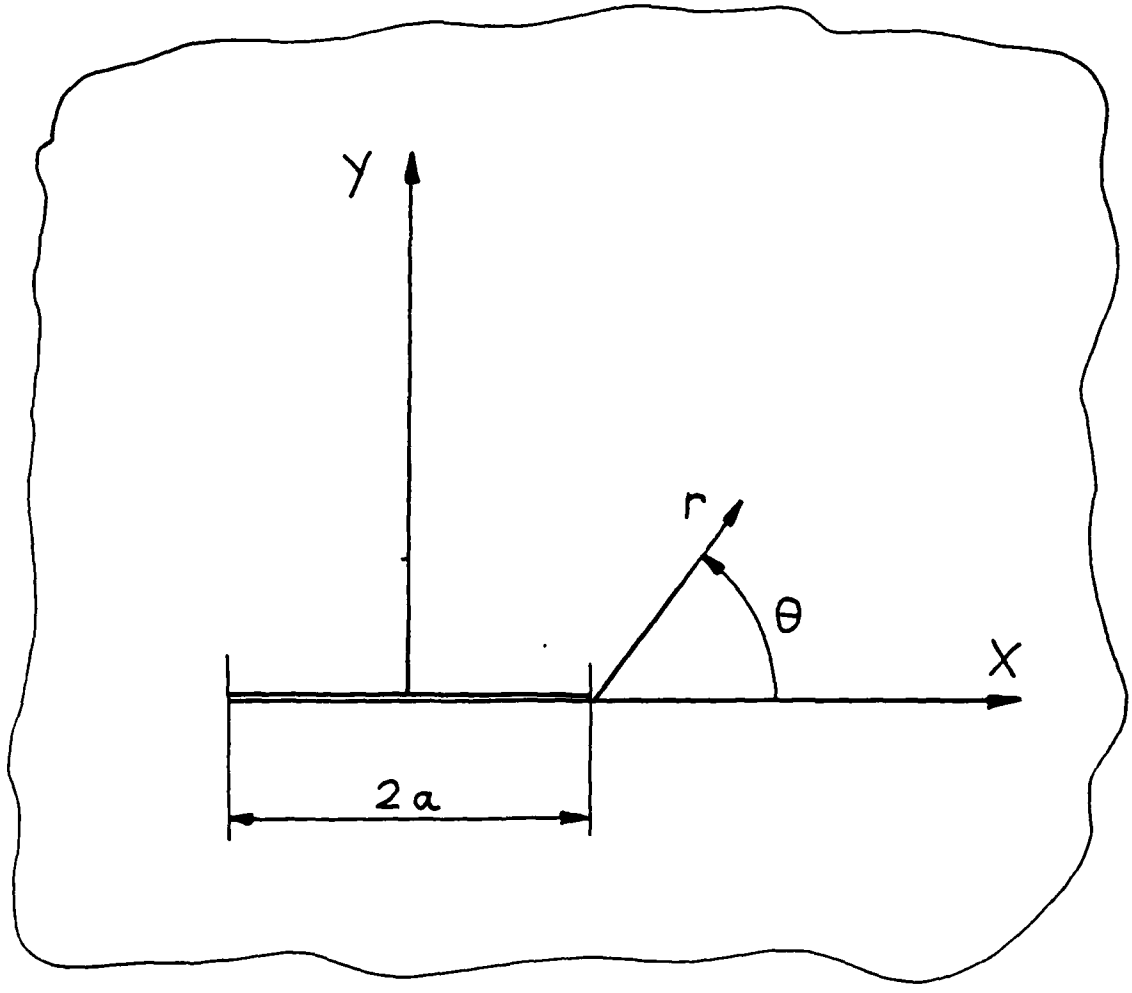

Figure 12: General Fracture Mechanics Geometry

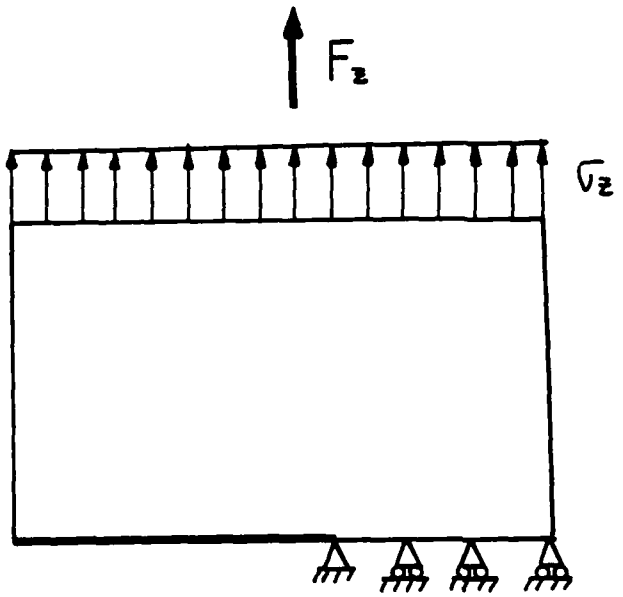

Pure Tension

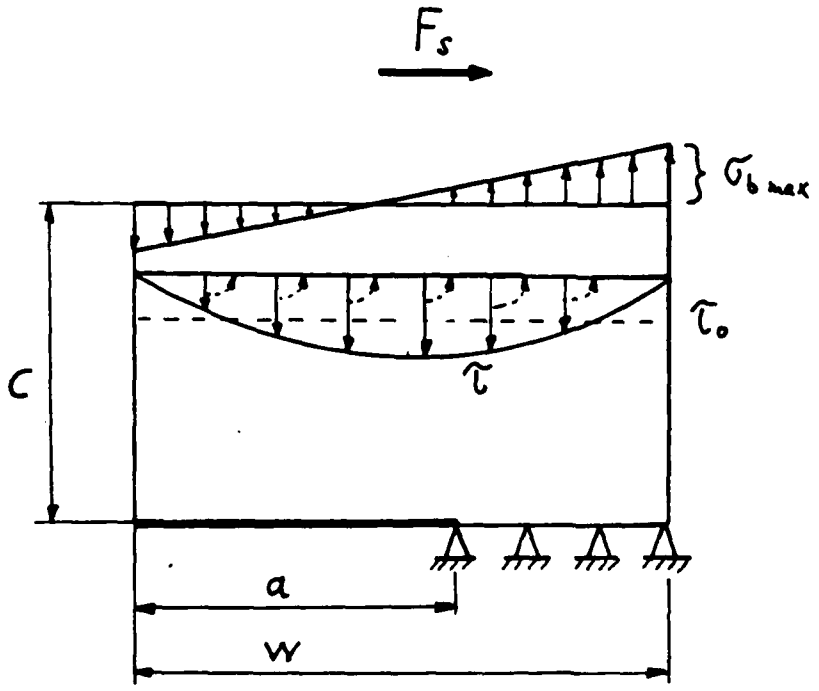

Pure Shear

Figure 13: Simplified CTS Specimen

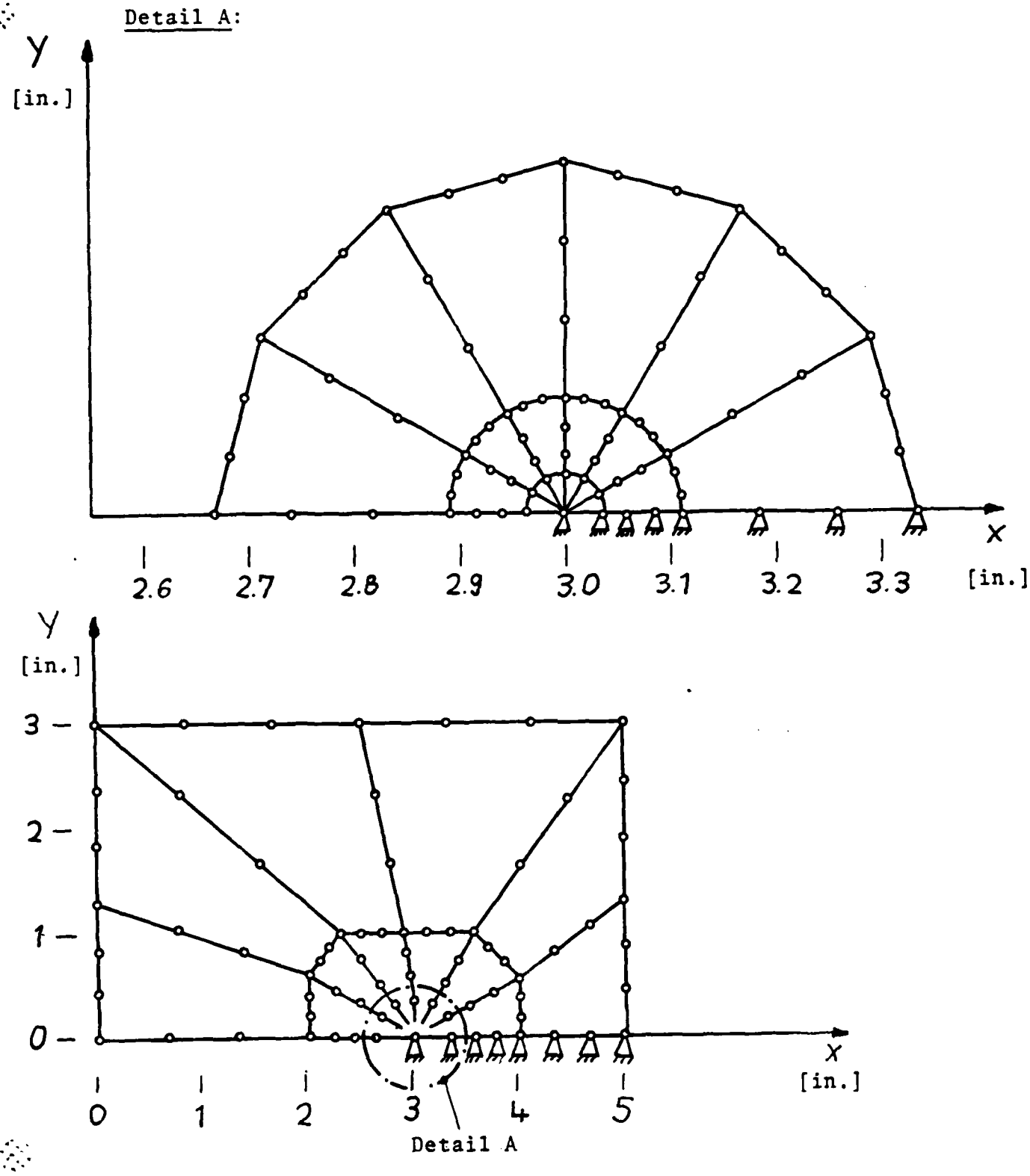

Figure 14: 30 Element Mesh, 6 $\frac{1}{9}$ & $\frac{4}{9}$ Point Elements, Shear

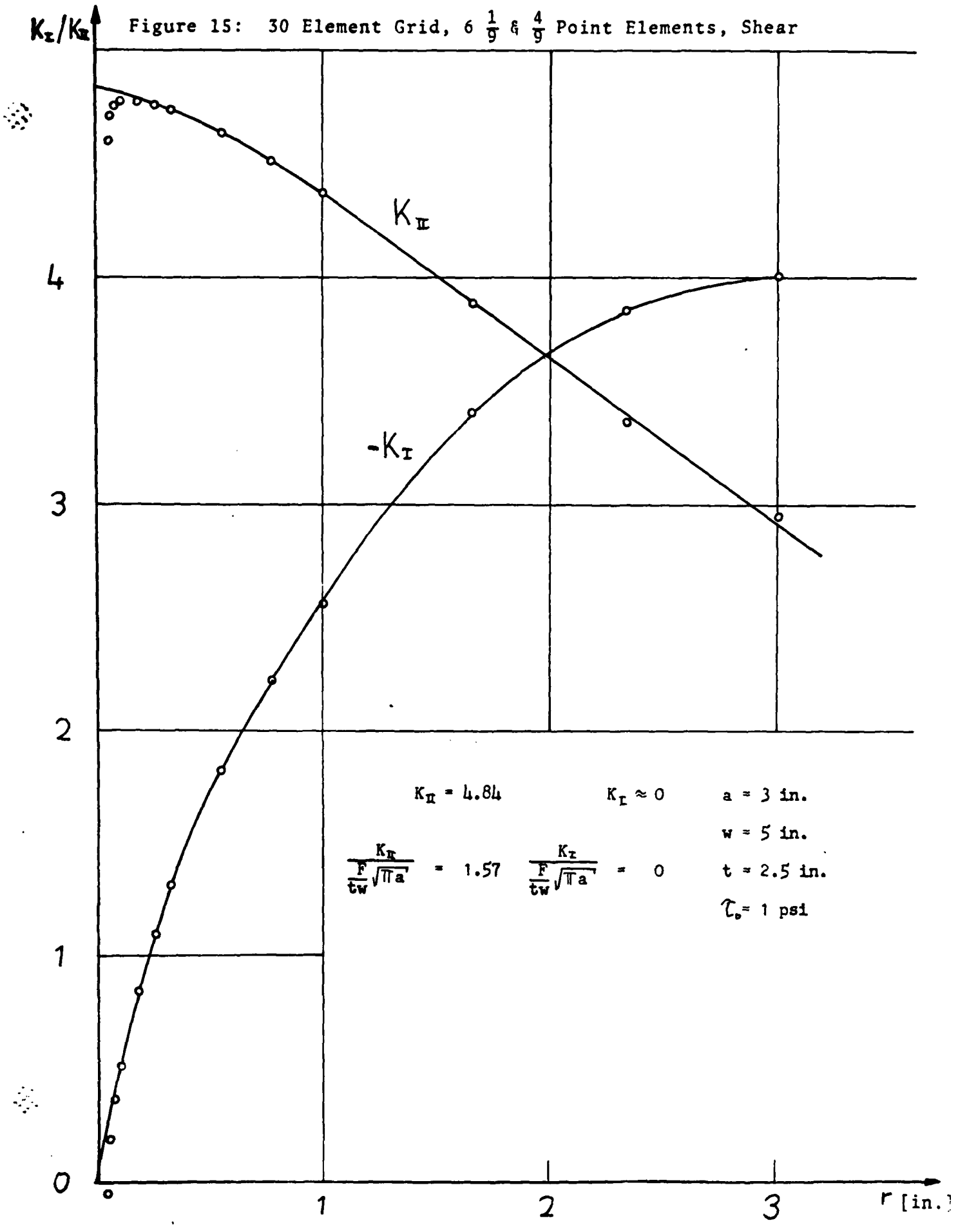
K_I/K_{II}
Figure 15: 30 Element Grid, 6 $\frac{1}{9}$ & $\frac{4}{9}$ Point Elements, Shear
K_{II}
$-K_I$
4
3
2
1
0
1
2
3
r [in.]
K_{II} = 4.84
$K_I \approx 0$
a = 3 in.
w = 5 in.
t = 2.5 in.
τ_o = 1 psi
$\frac{K_{II}}{\frac{F}{tw}\sqrt{\pi a}}$ = 1.57
$\frac{K_I}{\frac{F}{tw}\sqrt{\pi a}}$ = 0

Figure 16: 12 Element Grid, 4 $\frac{1}{9}$ & $\frac{4}{9}$ Point Elements, Shear

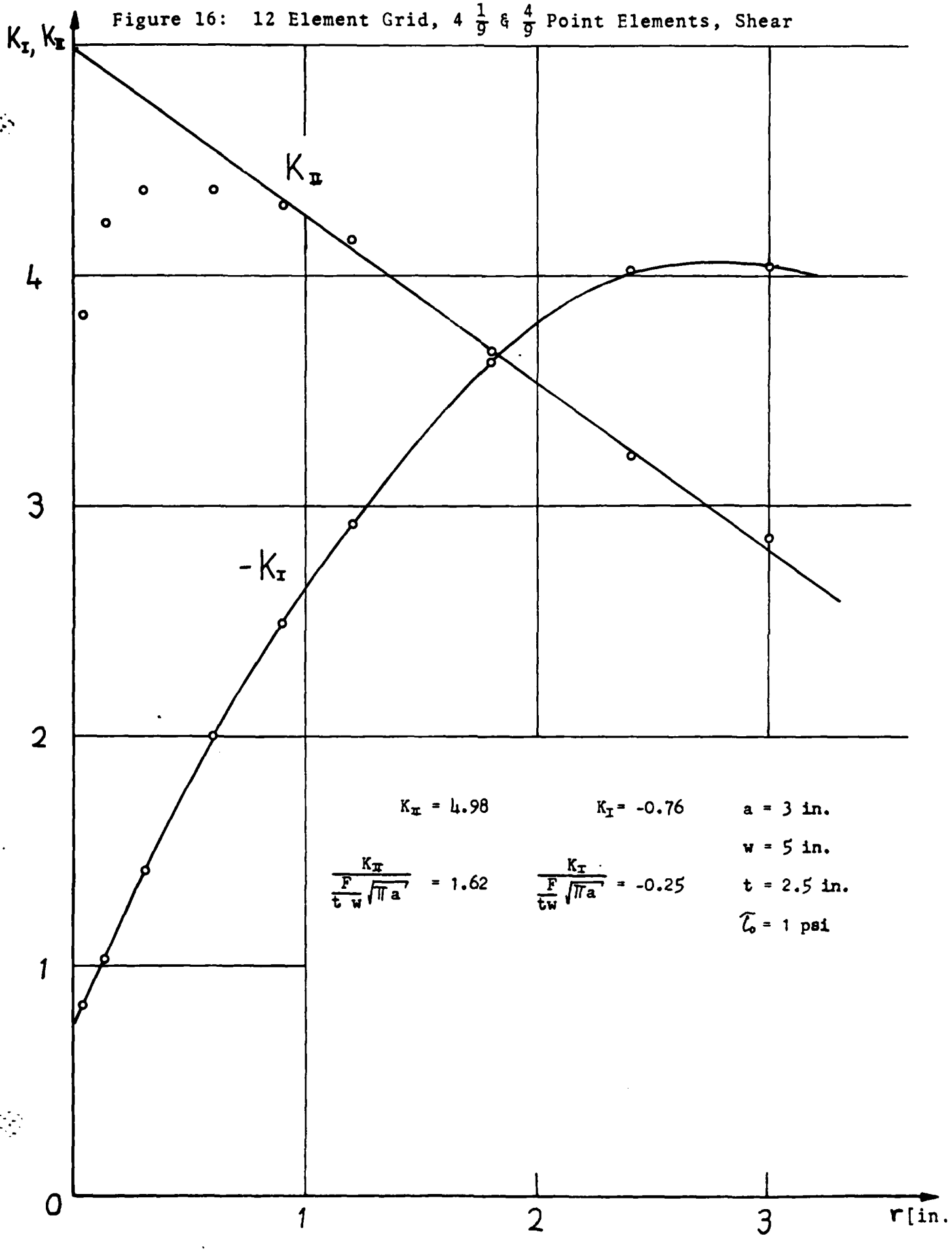

$K_{II} = 4.98$ $\quad K_I = -0.76$ $\quad a = 3$ in.

$w = 5$ in.

$\frac{K_{II}}{\frac{F}{t\,w}\sqrt{\pi a}} = 1.62$ $\quad \frac{K_I}{\frac{F}{tw}\sqrt{\pi a}} = -0.25$ $\quad t = 2.5$ in.

$\tau_o = 1$ psi

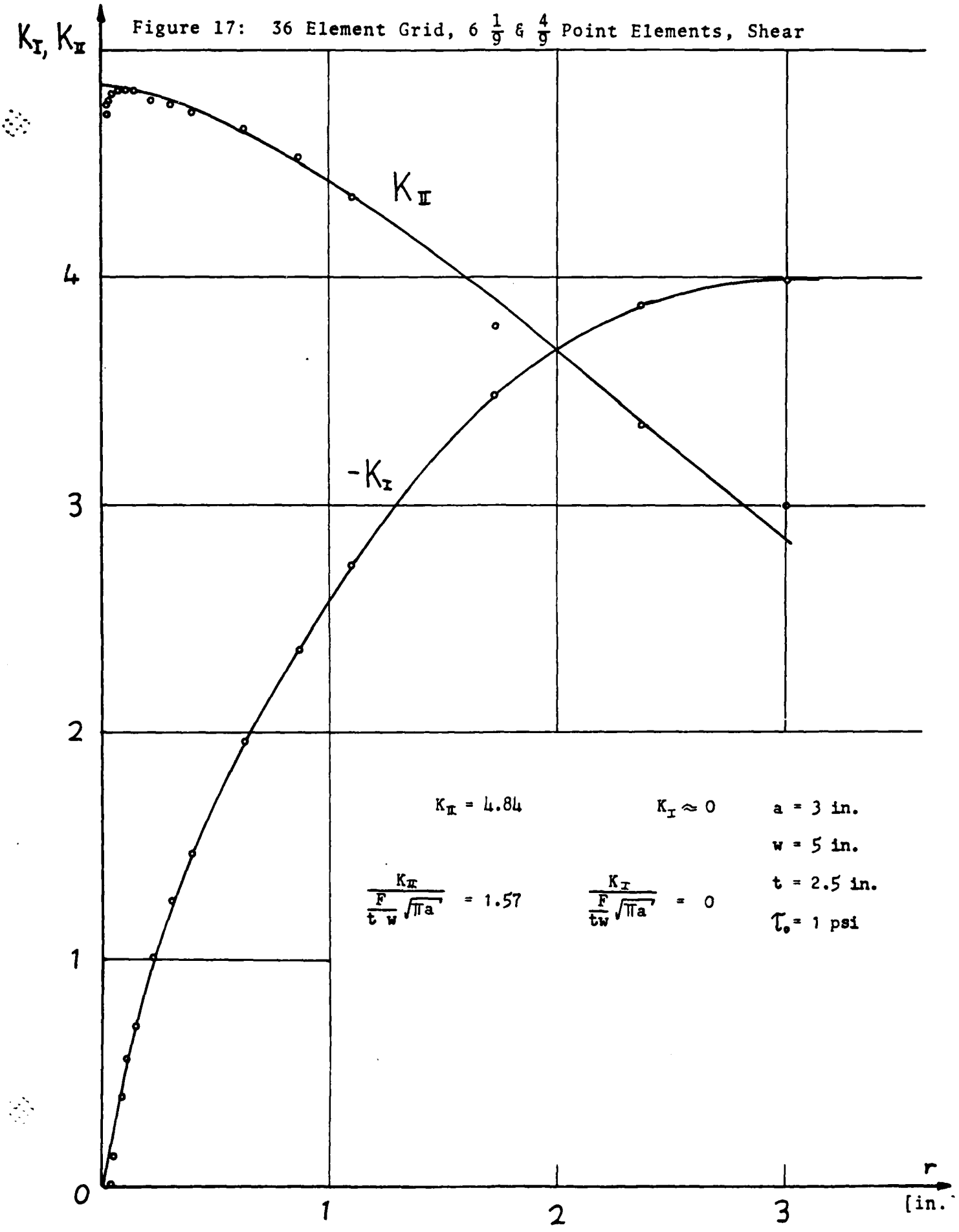
Figure 17: 36 Element Grid, 6 1/9 & 4/9 Point Elements, Shear
K_I, K_{II}
K_{II}
$-K_I$
4
3
2
1
0
1
2
3
r
[in.
$K_{II} = 4.84$
$K_I \approx 0$
a = 3 in.
w = 5 in.
t = 2.5 in.
τ_o = 1 psi
$\frac{K_{II}}{\frac{F}{t\,w}\sqrt{\pi a}} = 1.57$
$\frac{K_I}{\frac{F}{tw}\sqrt{\pi a}} = 0$

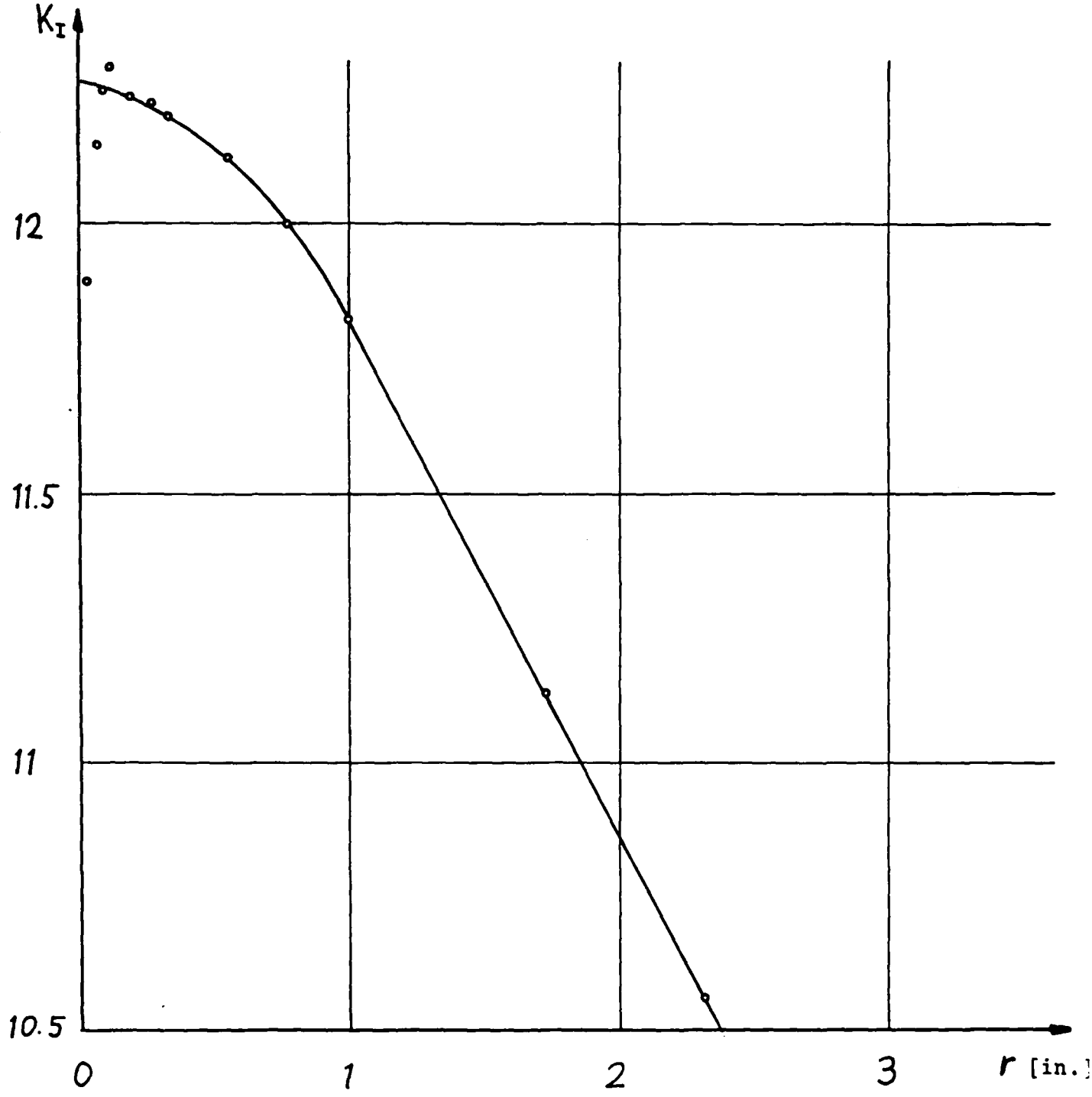

$K_I = 12.26$

$\frac{K_I}{\frac{F}{t\,w}\sqrt{\pi a}} = 3.99$

a = 3 in.
w = 5 in.
t = 2.5 in.
σ = 1 psi

Figure 18a: 30 Element Grid, 6 $\frac{1}{9}$ & $\frac{4}{9}$ Point Elements, Tension

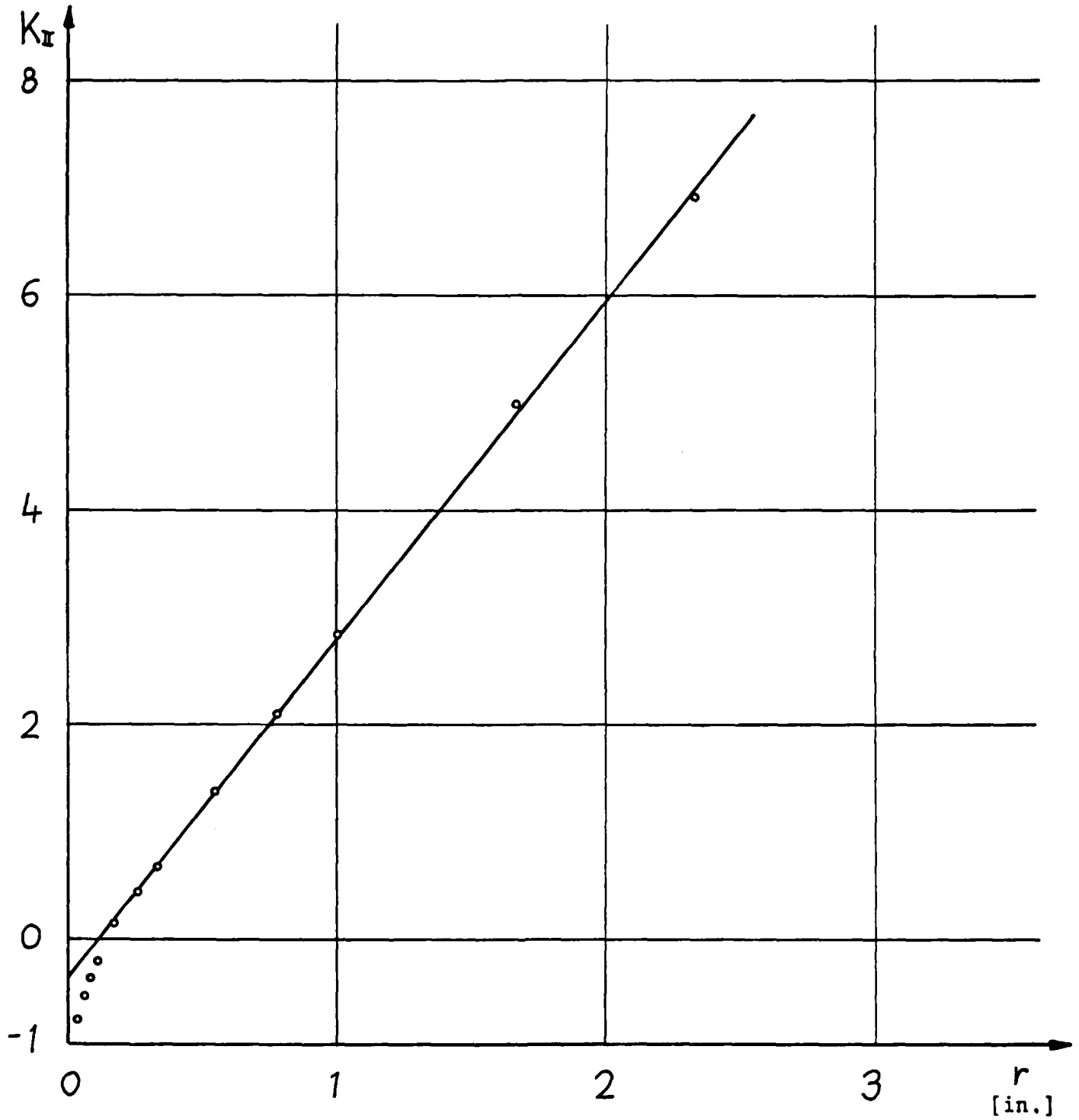

$K_{II} = -0.35$ $\qquad \frac{K_{II}}{\frac{F}{t_w}\sqrt{\pi a}} = -0.11$

Figure 18b: 30 Element Grid, 6 $\frac{1}{9}$ ¢ $\frac{4}{9}$ Point Elements, Tension

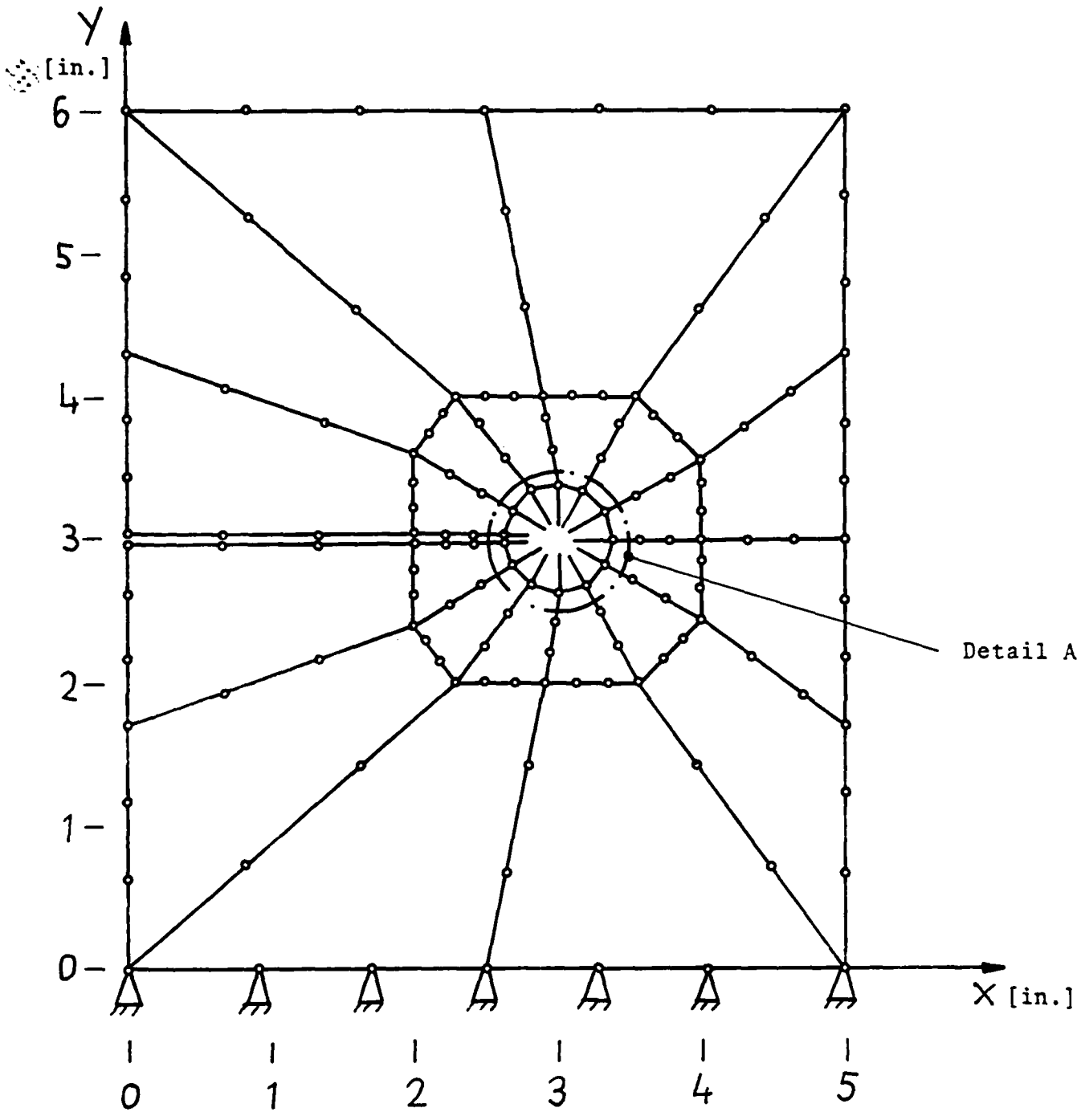

Figure 19a: CTS Specimen Using $\frac{1}{9}$ & $\frac{4}{9}$ Point Elements

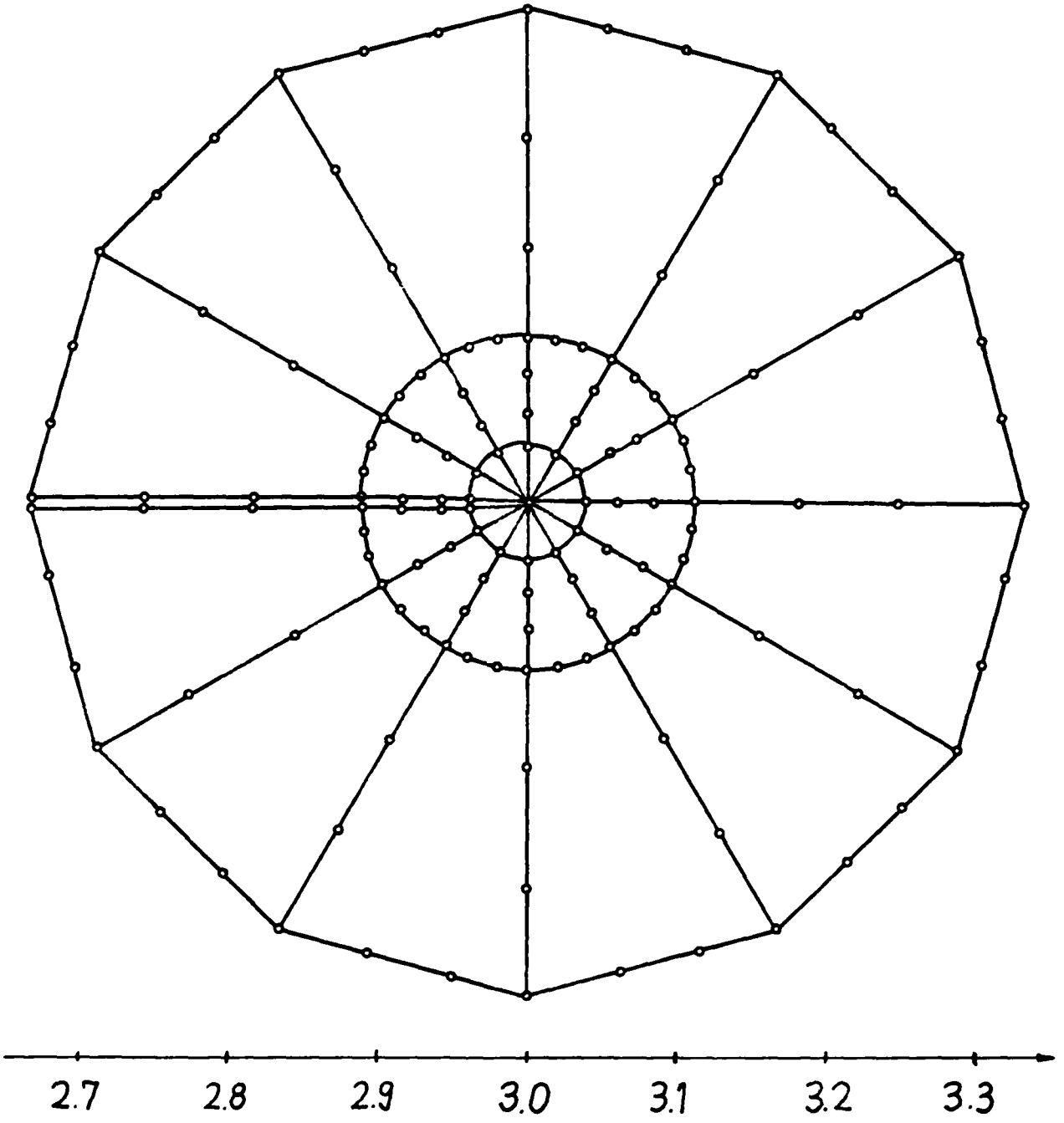

Figure 19b: Detail A

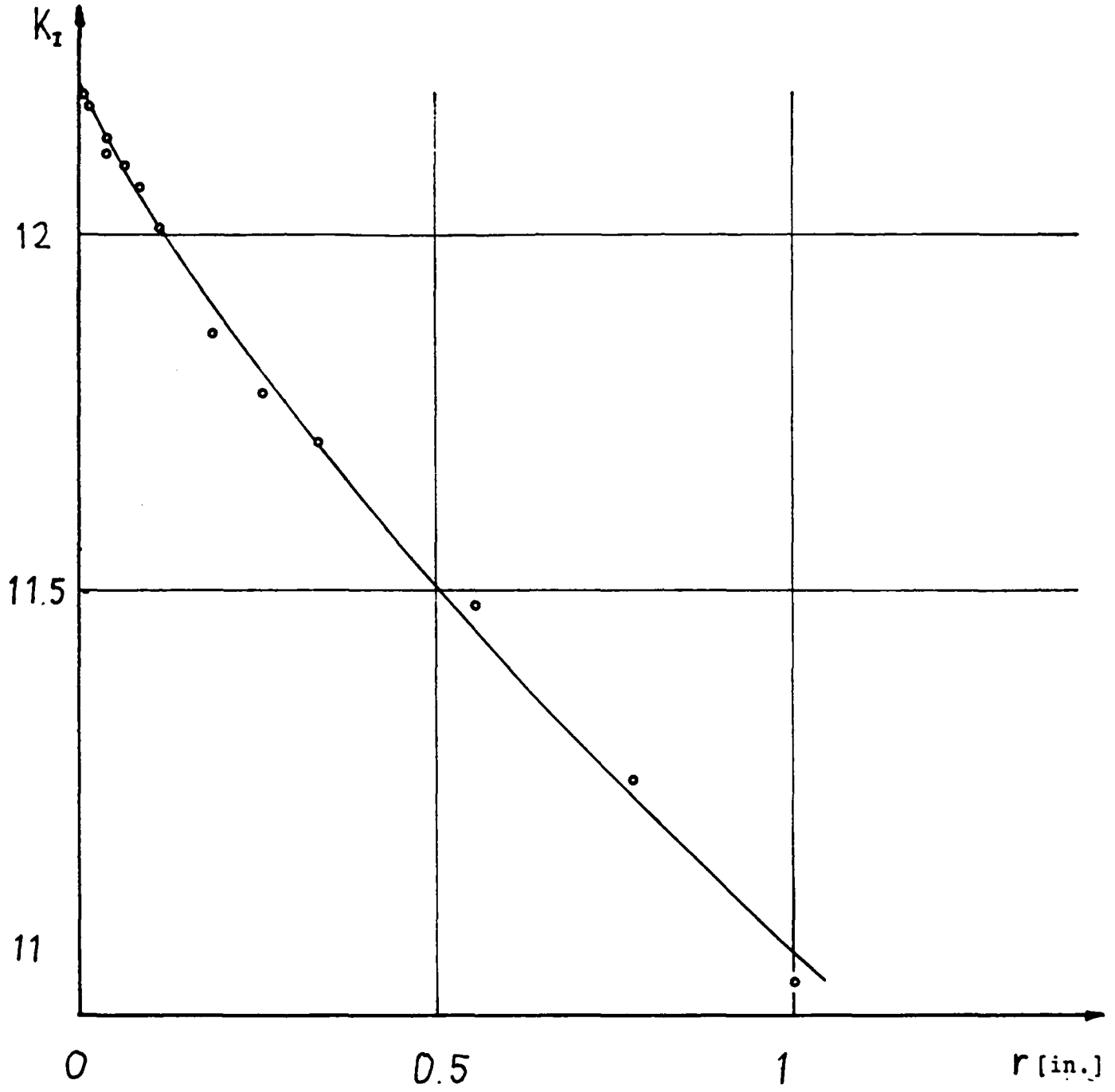

$K_I = 12.21$

$\frac{K_I}{\frac{F}{wt}\sqrt{\pi a}} = 3.98$

a = 3 in.
w = 5 in.
t = 2.5 in.
σ = 1 psi

Figure 20a: K_I Factor for Pure Tension and $\frac{a}{w} = 0.6$

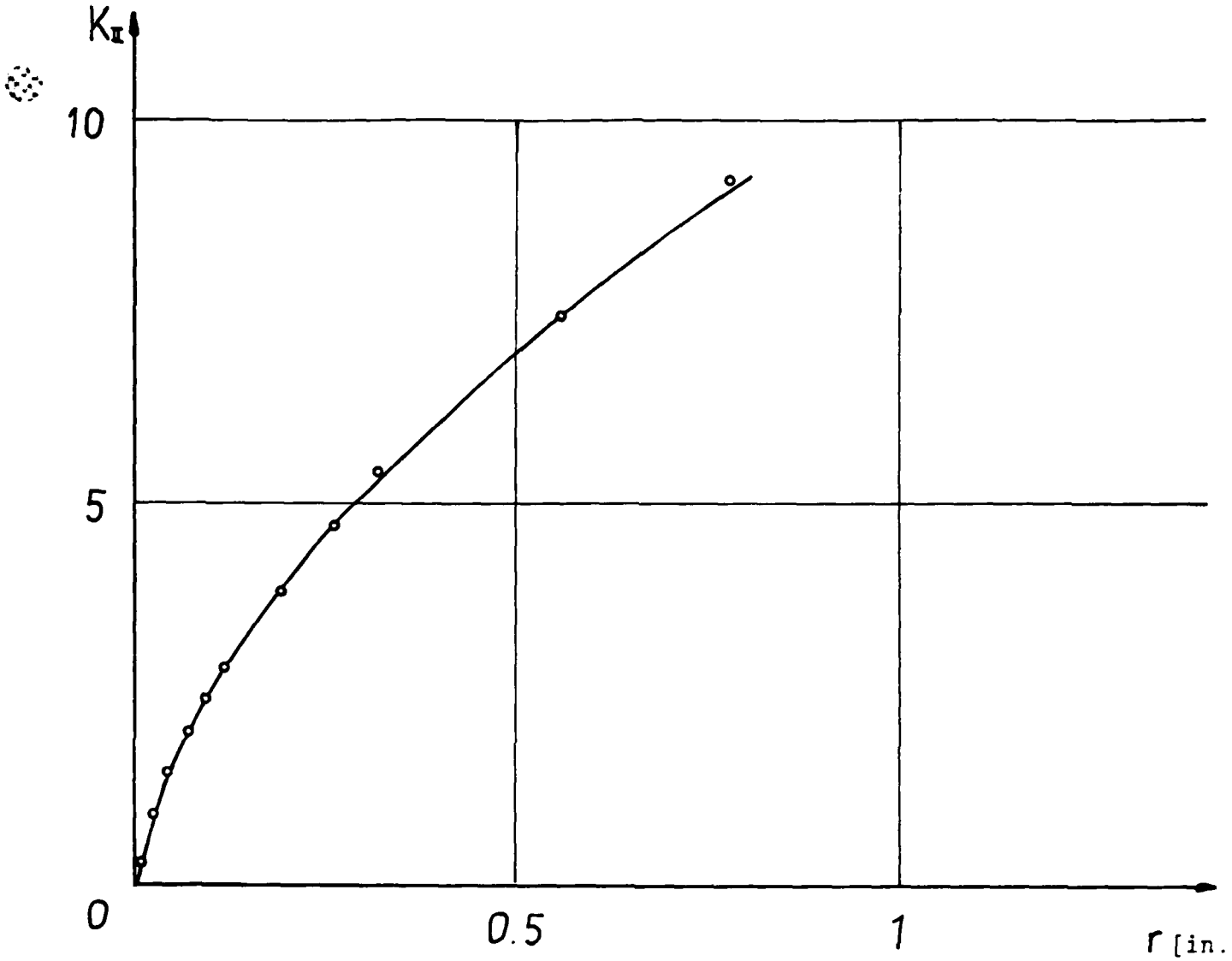

$K_{II} = 0$

$\frac{K_{II}}{\frac{F}{wt}\sqrt{\pi a}} = 0$

a = 3 in.
w = 5 in.
t = 2.5 in.
σ = 1 psi

Figure 20b: K_{II} Factor for Pure Tension and $\frac{a}{w} = 0.6$

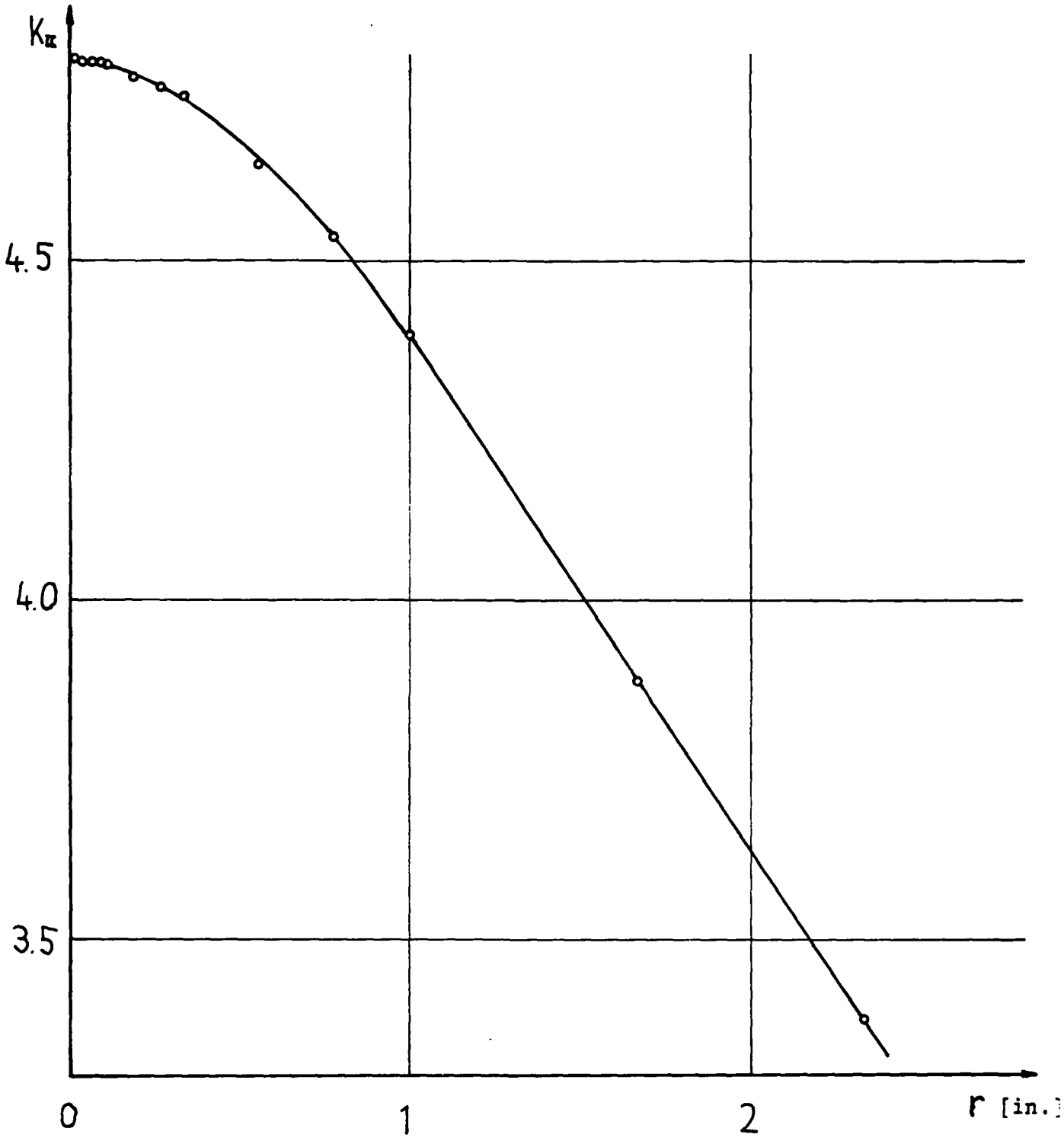

$K_{II} = 4.79$ $\quad \frac{K_{II}}{\frac{F}{wt}\sqrt{\pi a}} = 1.56$ $\quad a = 3$ in. $\quad t = 2.5$ in. $\quad w = 5$ in. $\quad \tau_o = 1$ psi

Figure 21a: K_{II} Factor for Pure Shear ($\frac{a}{w} = 0.6$)

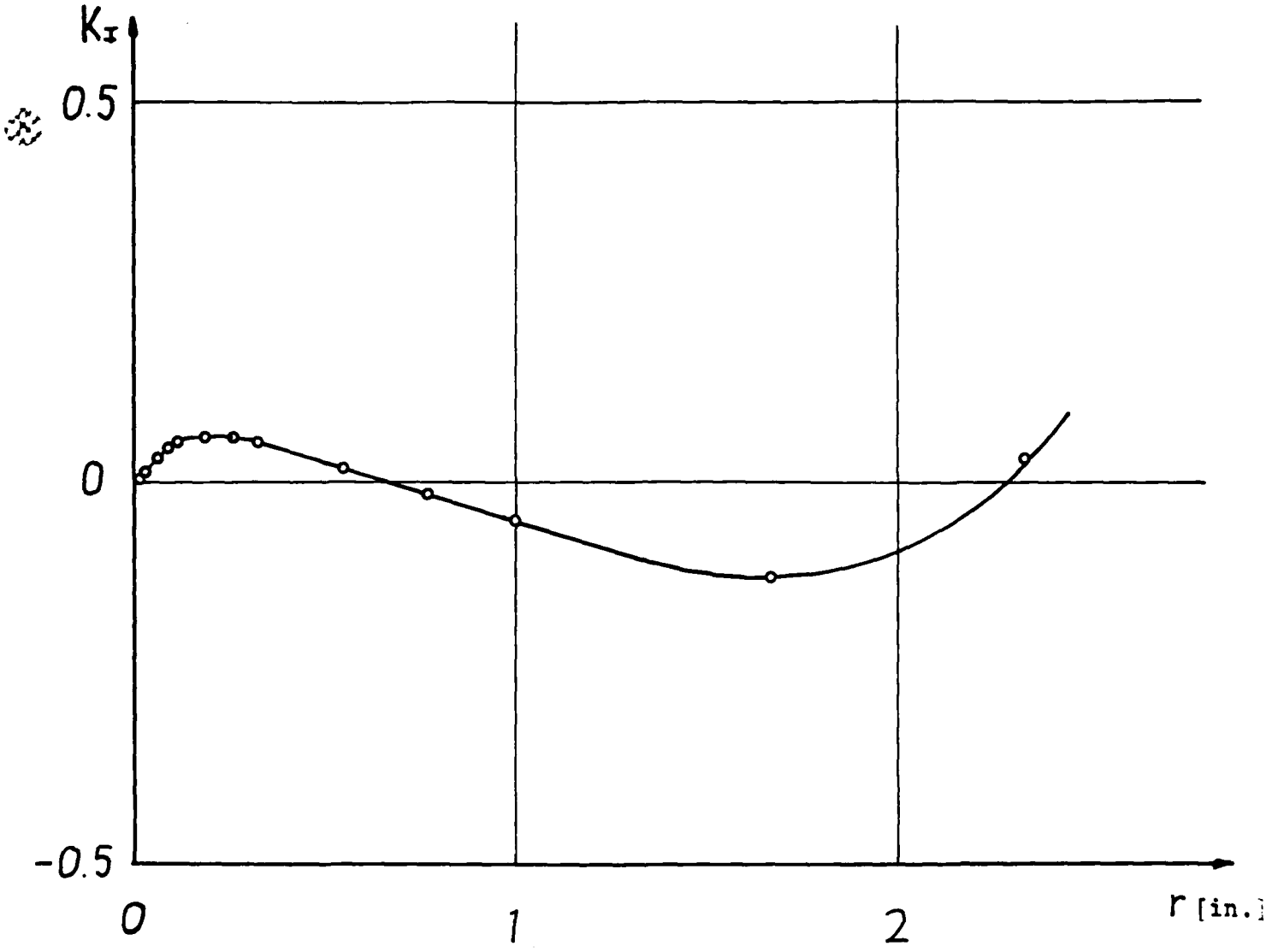

$K_I = 0$

$\frac{K_I}{F\sqrt{\pi a}} = 0$

$a = 3$ in.
$w = 5$ in.
$t = 2.5$ in.
$\tau_o = 1$ psi

Figure 21b: K_I Factor for Pure Shear and $\frac{a}{w} = 0.6$

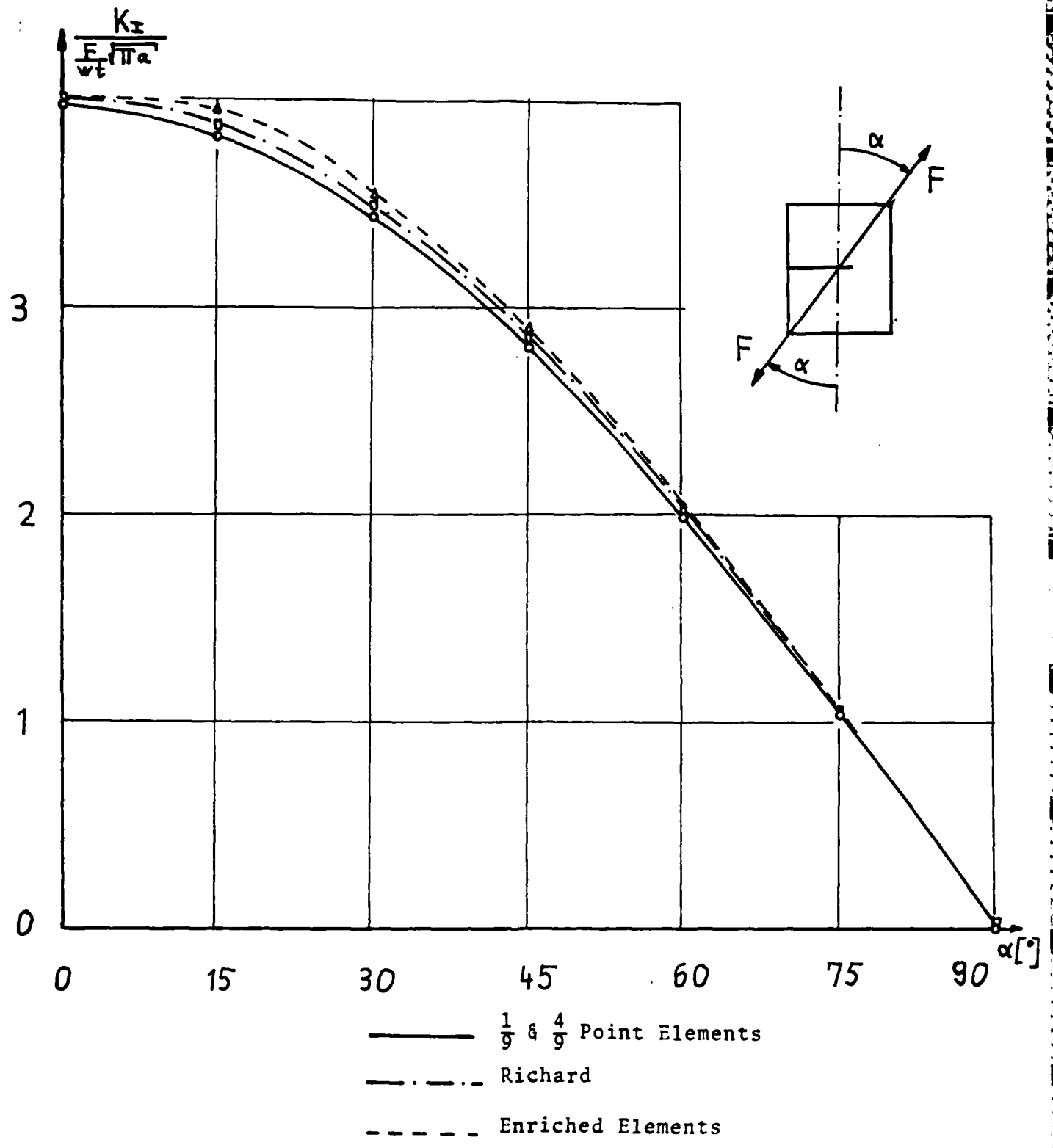

Figure 22: Dimensionless K_I Factors for $\frac{a}{w} = 0.6$

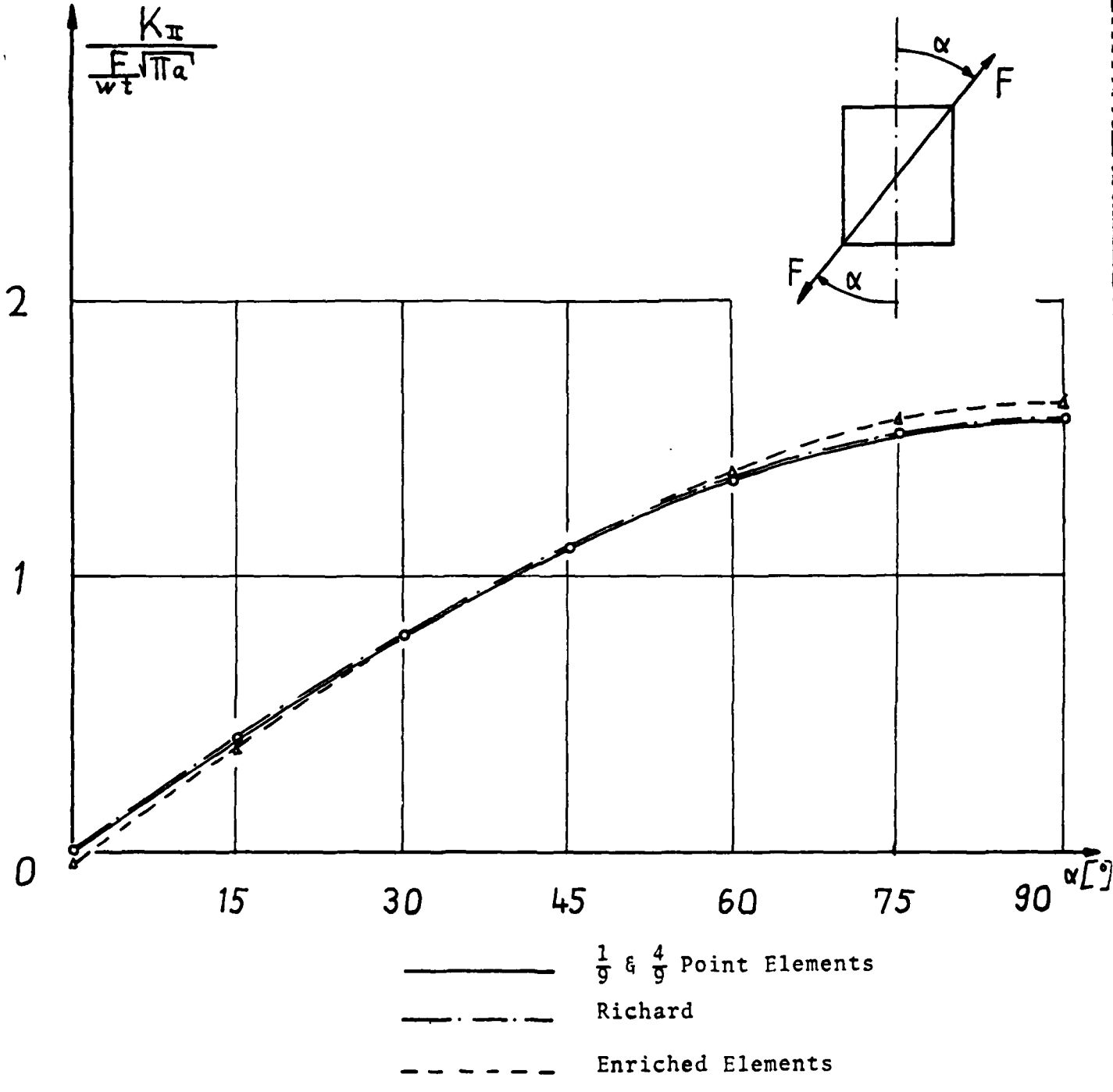

Figure 23: Dimensionless K_{II} Factors for $\frac{a}{w} = 0.6$

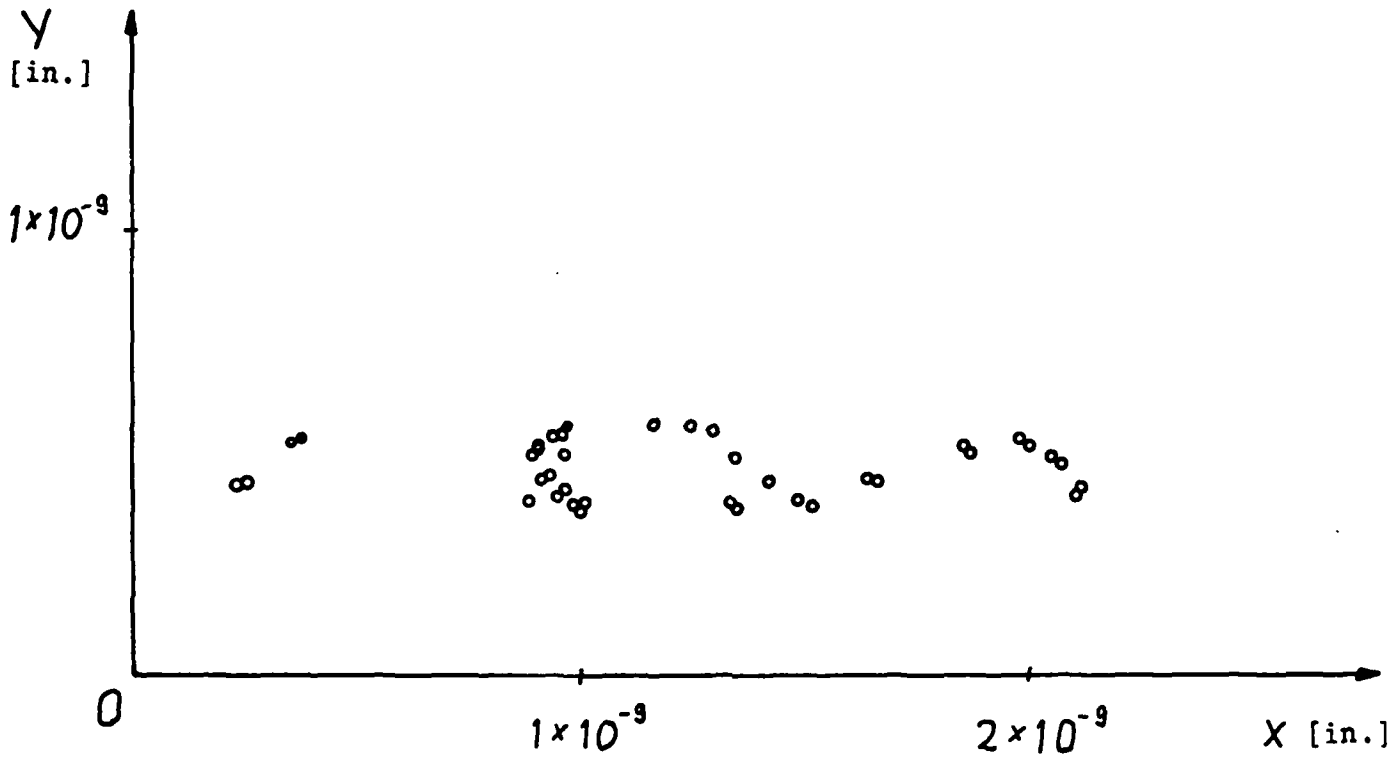

Figure 24: Location of the Crack-Tip Nodes After Applied Shearing Stresses ($\frac{a}{w}$ = 0.6)

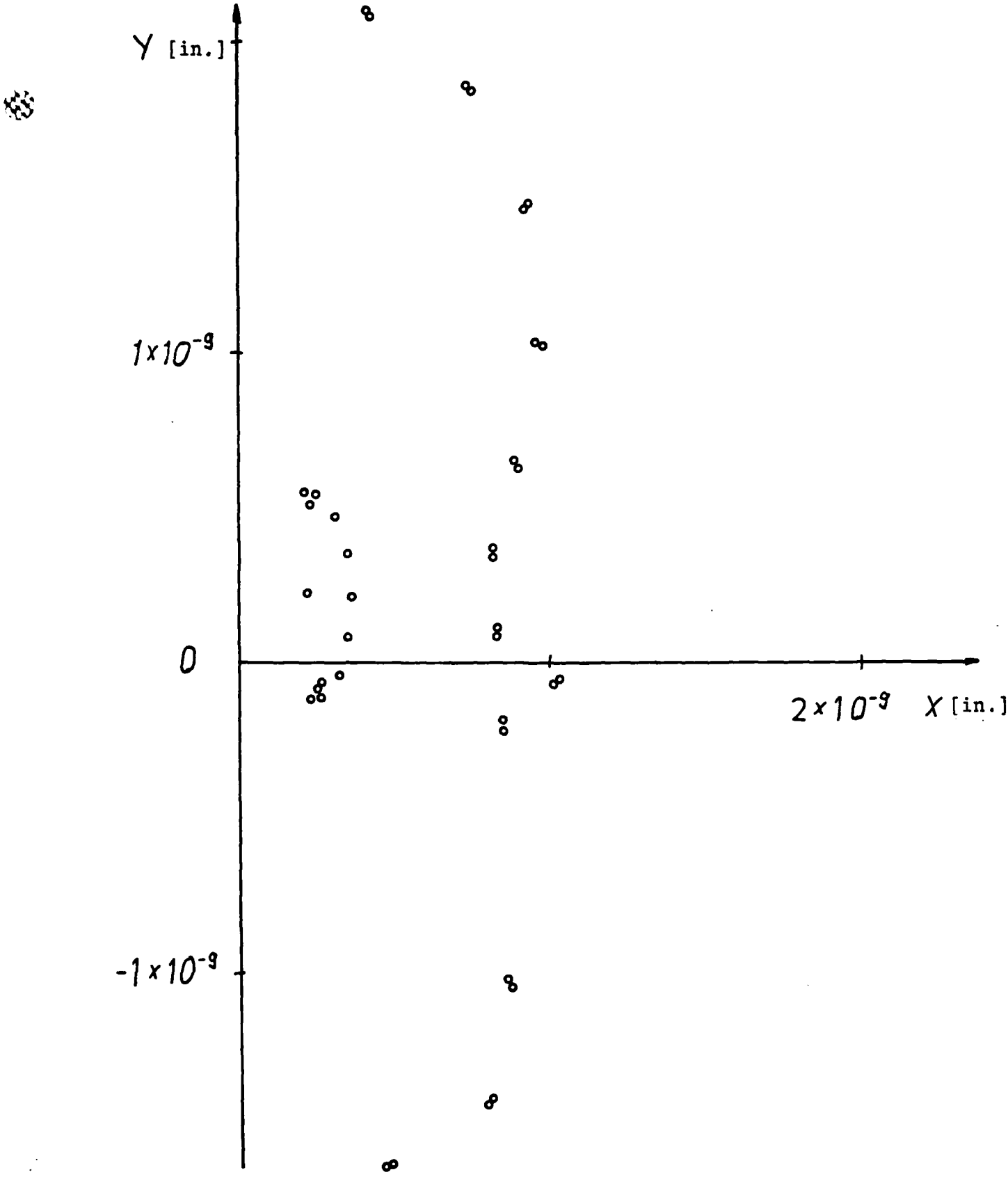

Figure 25: Location of the Crack-Tip Nodes After Applied Tensile Stresses ($\frac{a}{w}$ = 0.6)

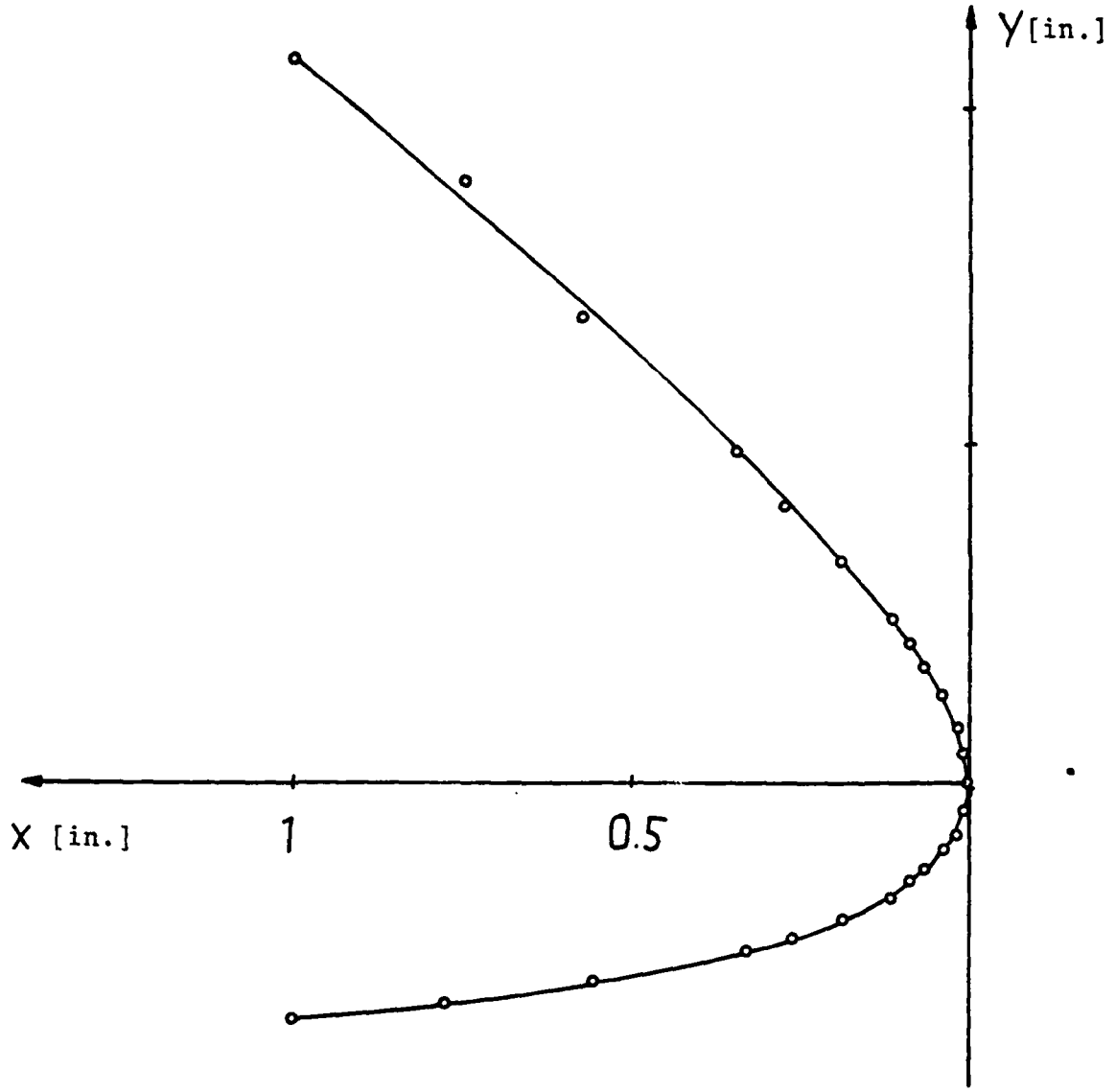

Magnification Factor for Displacements: 1 x 10^7

σ = 1 psi
a = 3 in.
w = 5 in.
t = 2.5 in.

Figure 26: Crack Near Crack Tip After Applied Tensile Force

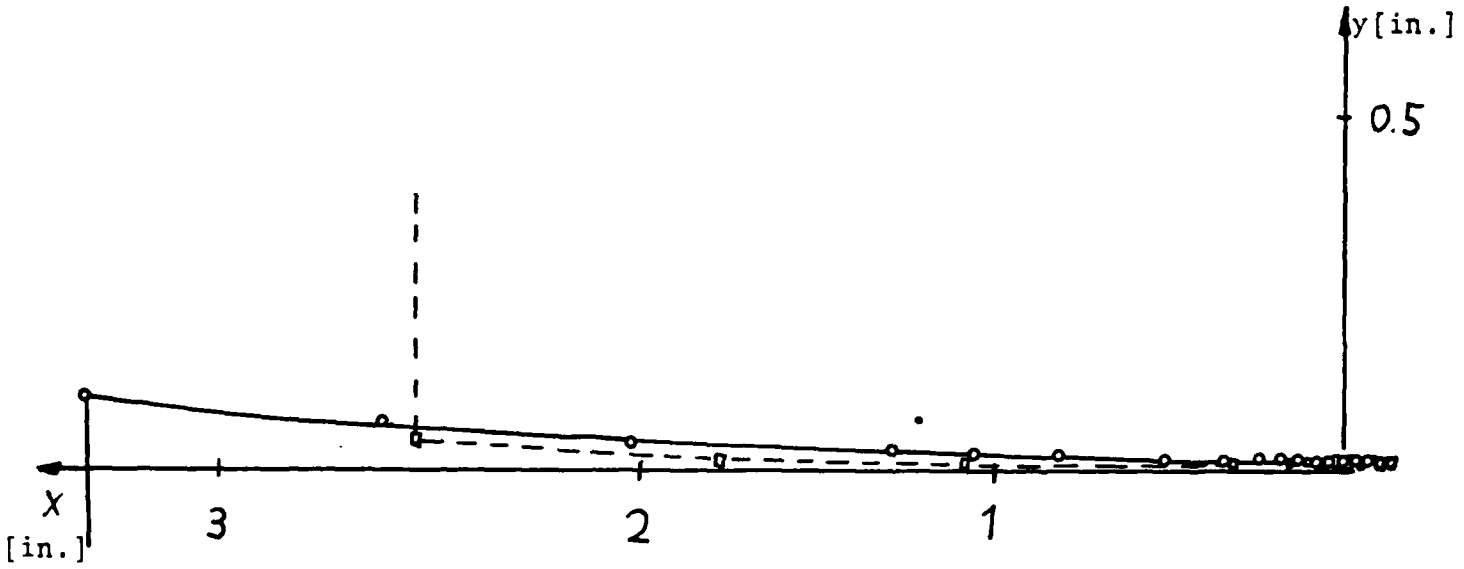

– – – – – – – Upper Crack Surface

——————— Lower Crack Surface

Magnification Factor for Displacements: 2×10^7

τ_o = 1 psi
a = 3 in.
w = 5 in.
t = 2.5 in.

Figure 27: Crack After Applied Shearing Stress ($\frac{a}{w}$ = 0.6)

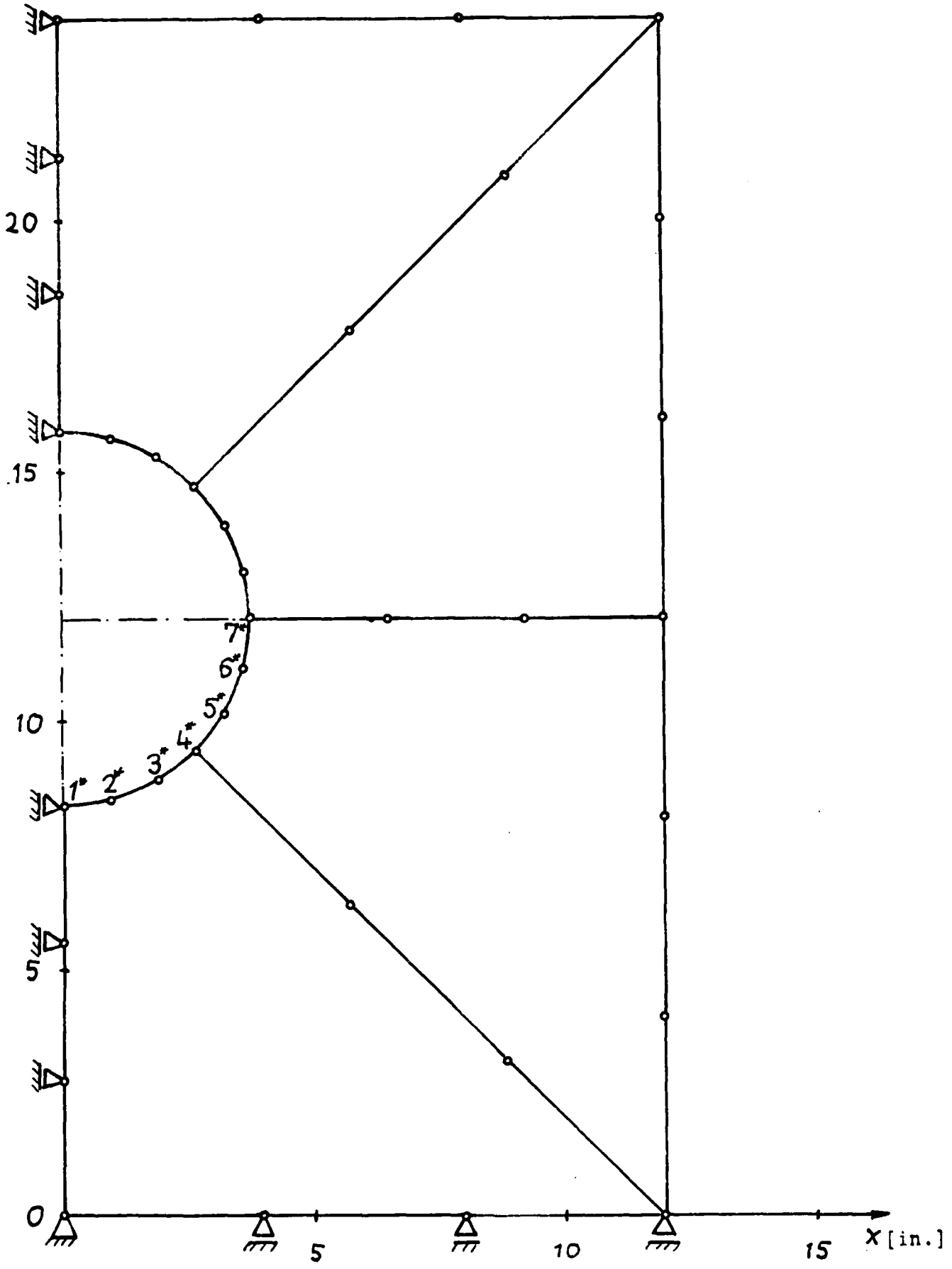

Figure 28: Finite Element Grid of the Plate with One Hole

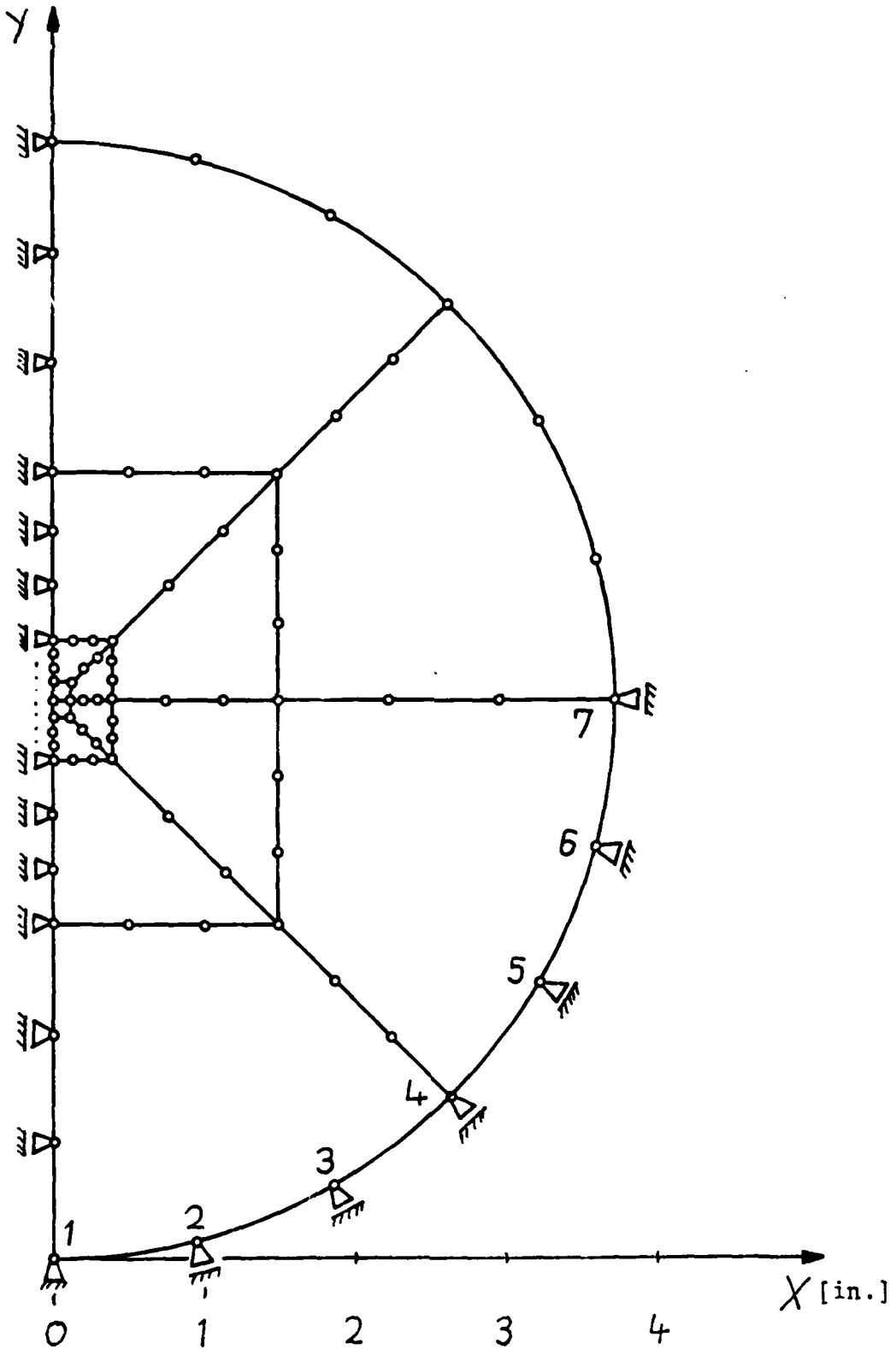

Figure 29: Finite Element Grid of the Bolt

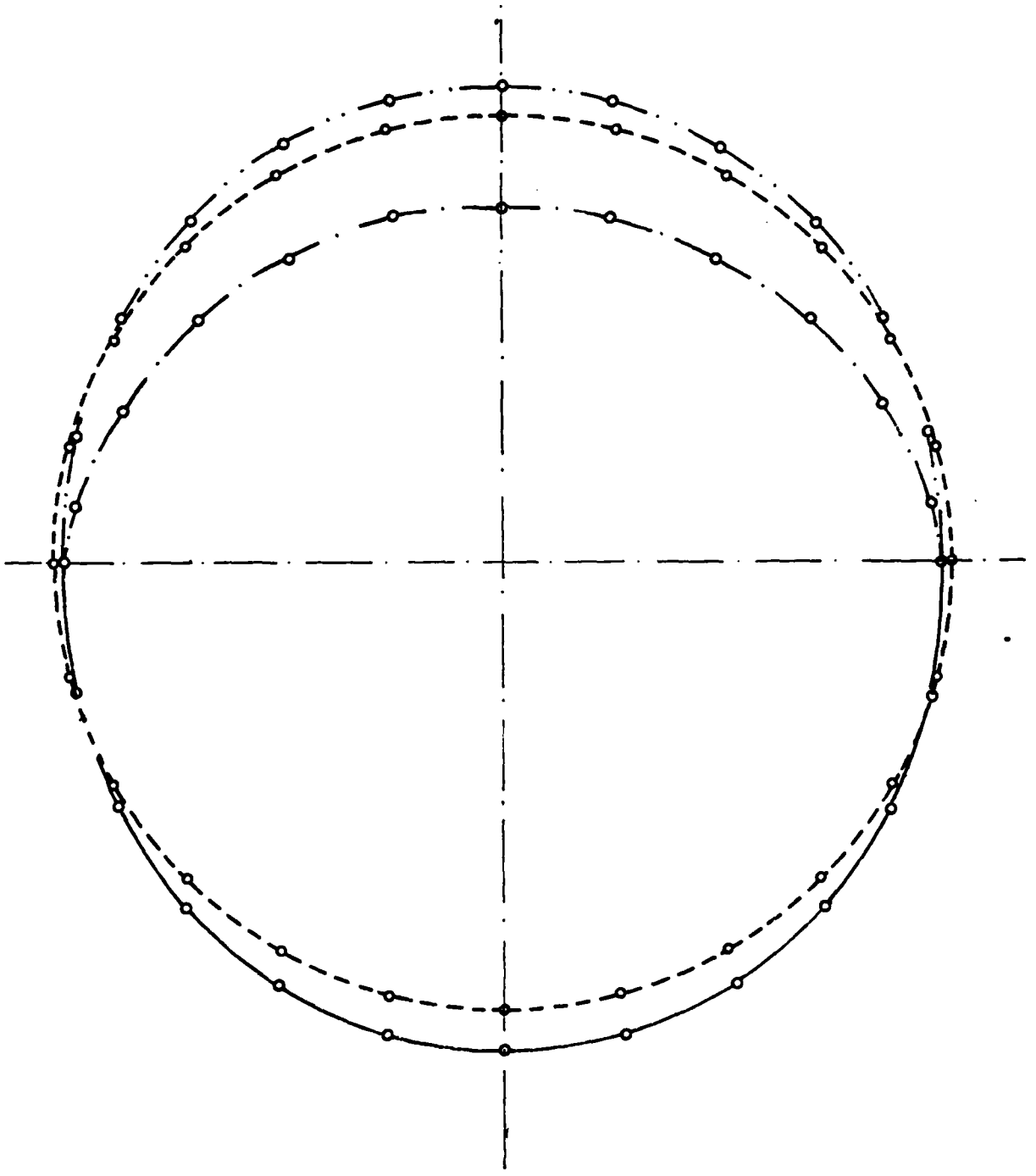

Figure 30: Deformation of the Bolt and of the Plate After Applied Forces

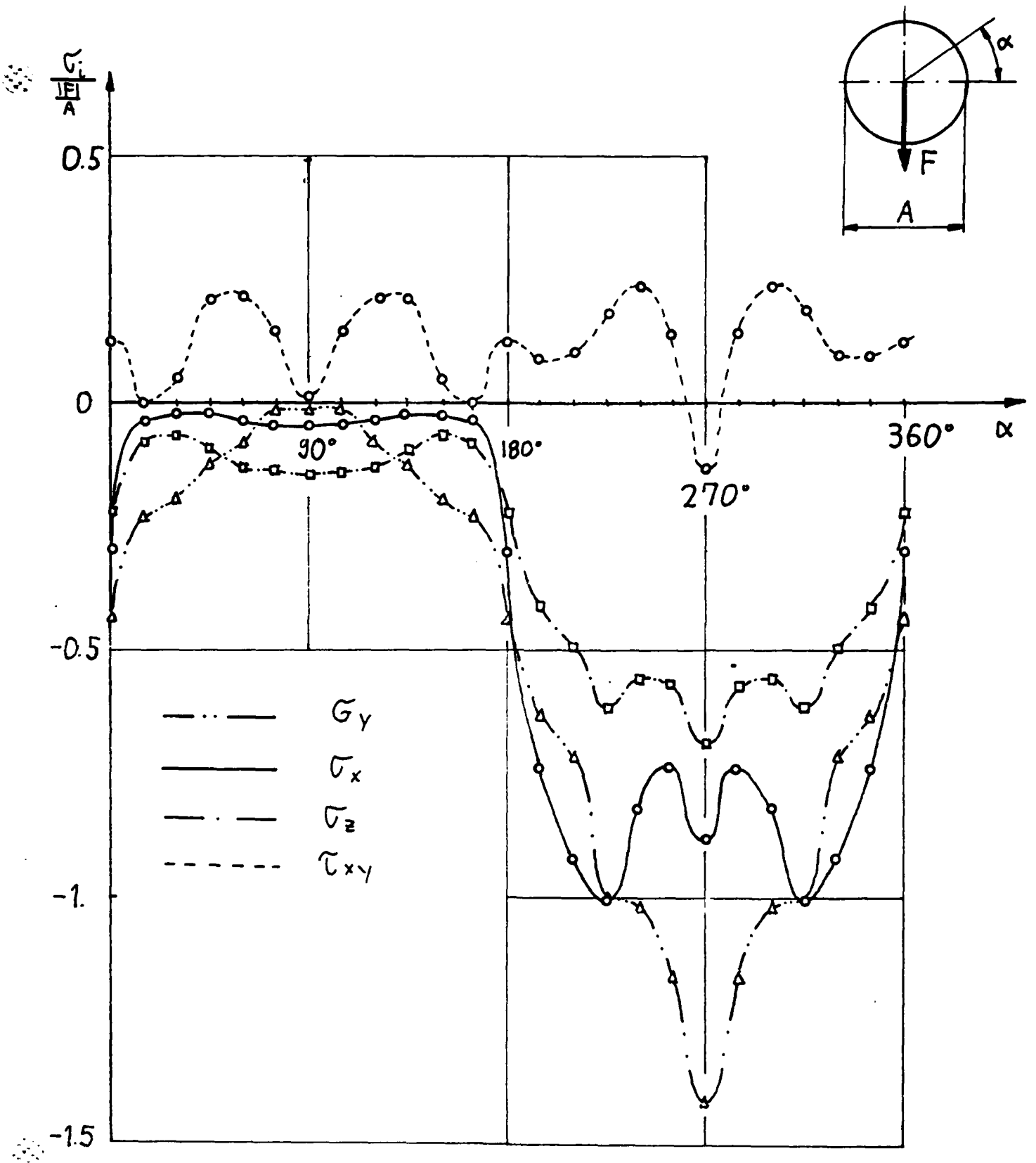

Figure 31: Dimensionless Stresses at the Surface of the Bolt

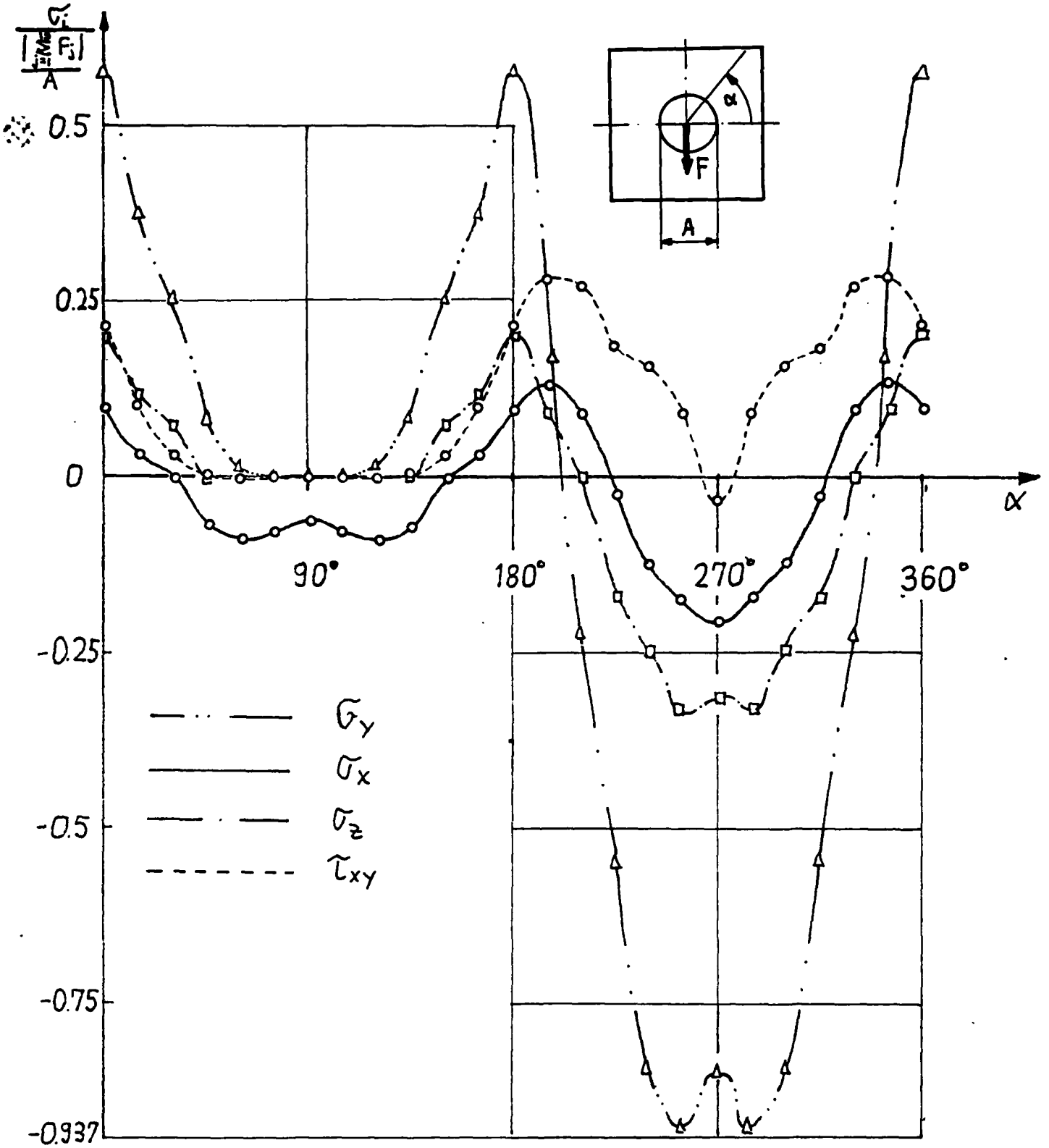

Figure 32: Dimensionless Stress Distribution at the Hole of the Plate

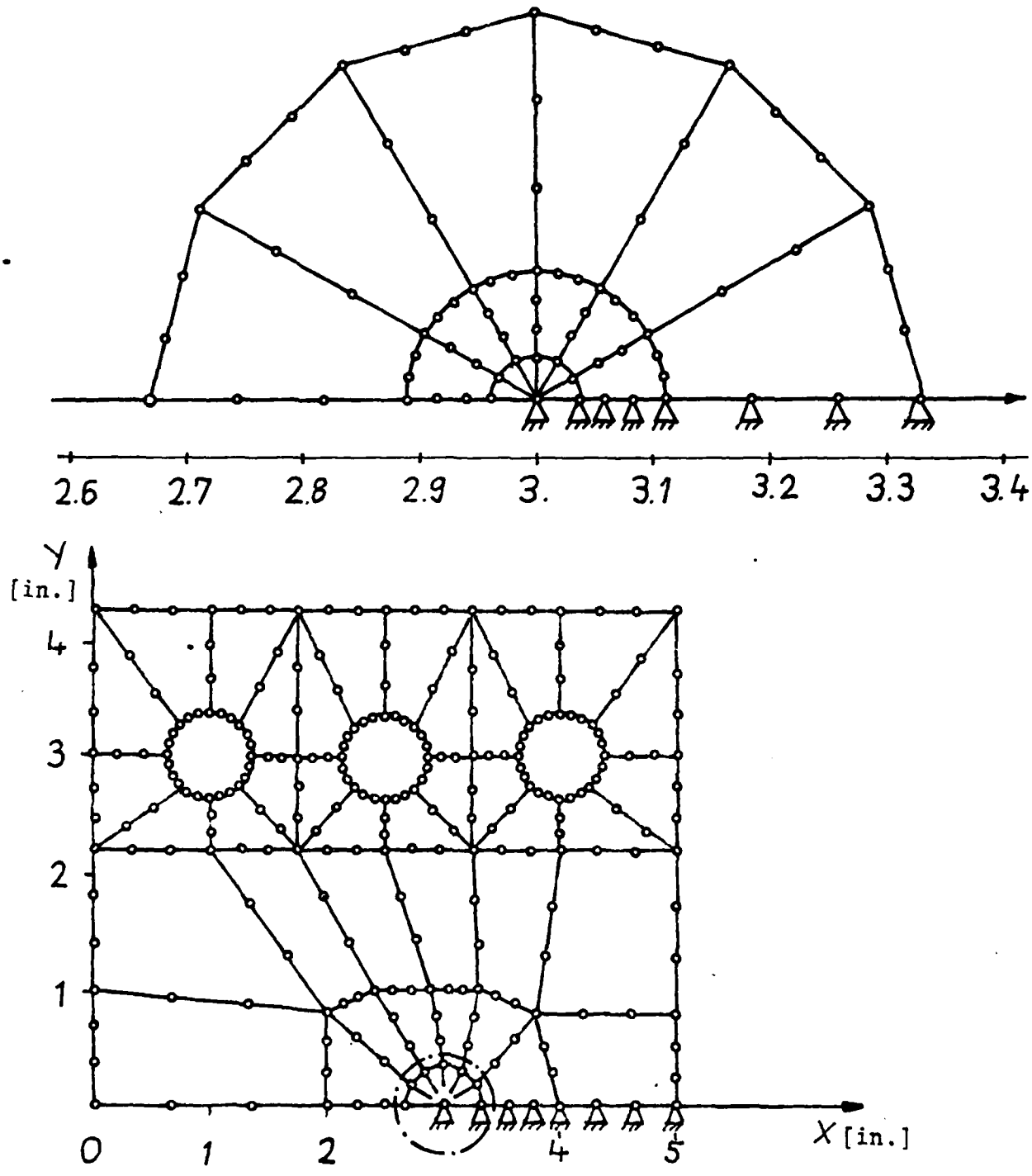

Figure 33: Simplified CTS Specimen with Holes
(56 Elements, 6 $\frac{1}{9}$ & $\frac{4}{9}$ Point Elements)

Figure 34: K Factors for Pure Shear Using Simplified CTS Specimen with Holes ($\frac{a}{w}$ = 0.6, 6 $\frac{1}{9}$ & $\frac{4}{9}$ Point Elements)

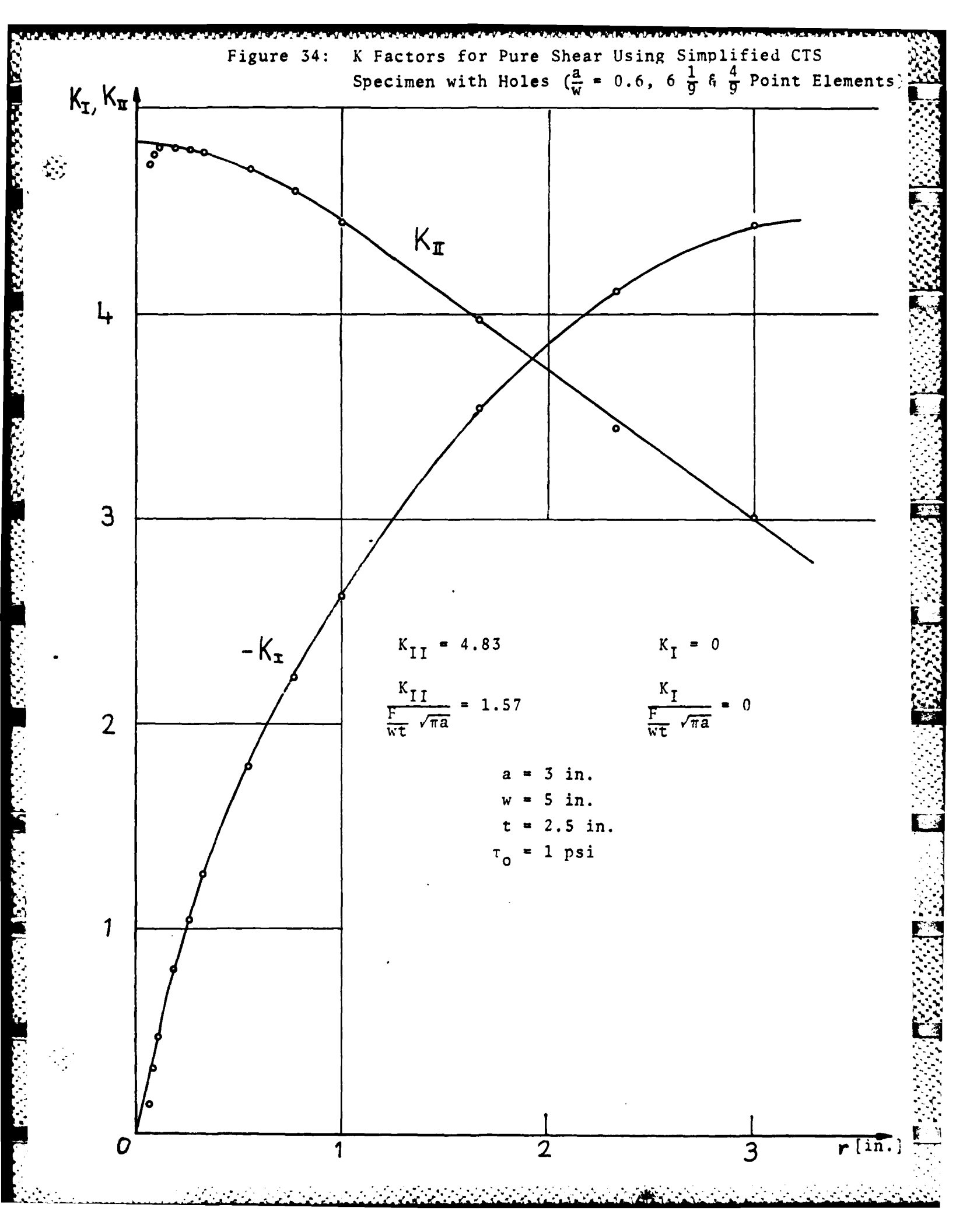

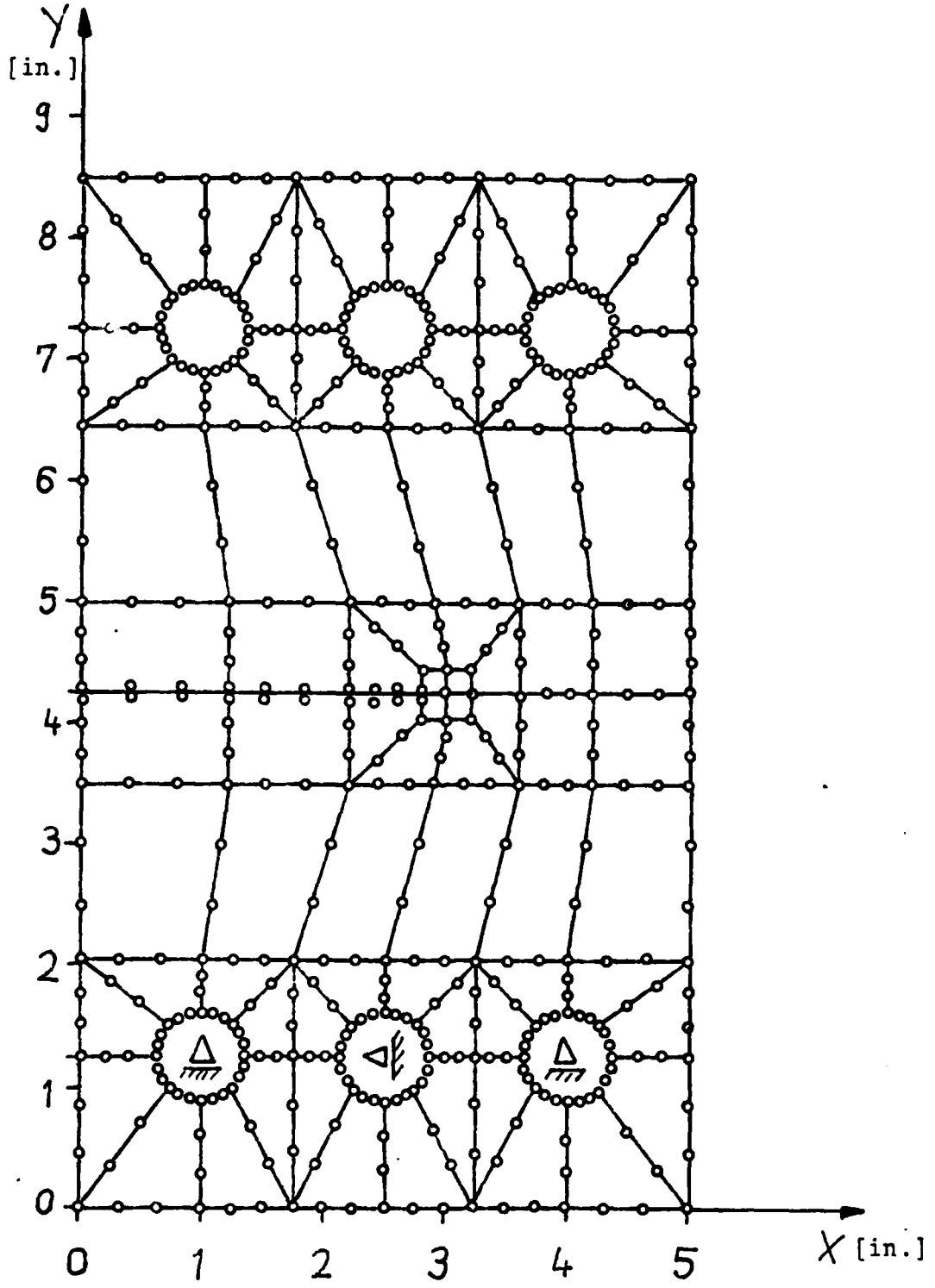

Figure 35: CTS Specimen with Holes
(4 Enriched Elements, $\frac{a}{w} = 0.6$)

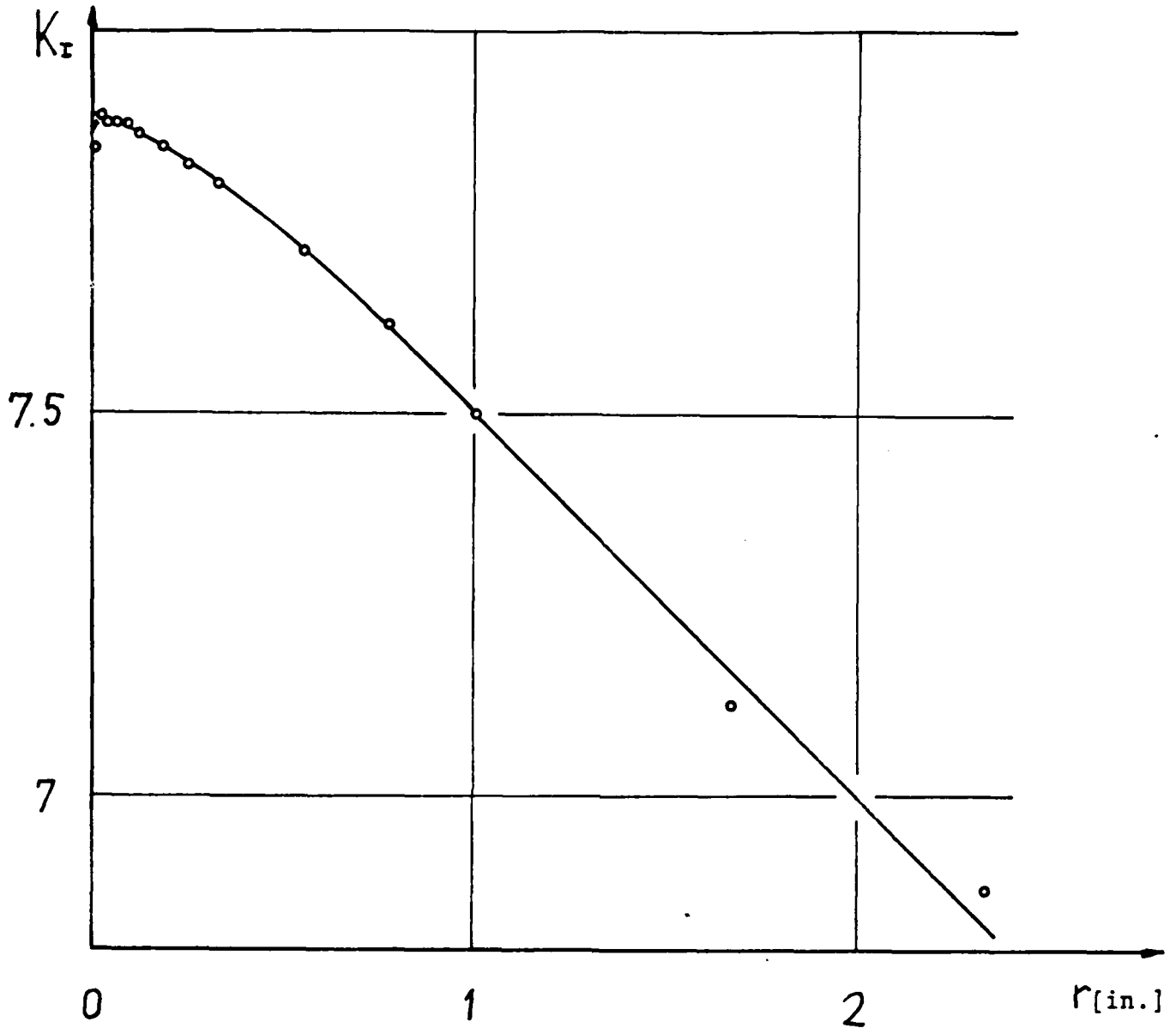

$K_I = 7.88$

$$\frac{K_I}{\frac{F}{wt}\sqrt{\pi a}} = 2.81$$

a = 2.5 in.
w = 5 in.
t = 2.5 in.
σ = 1 psi

Figure 36a: K_I Factor for Pure Tension and $\frac{a}{w} = 0.5$

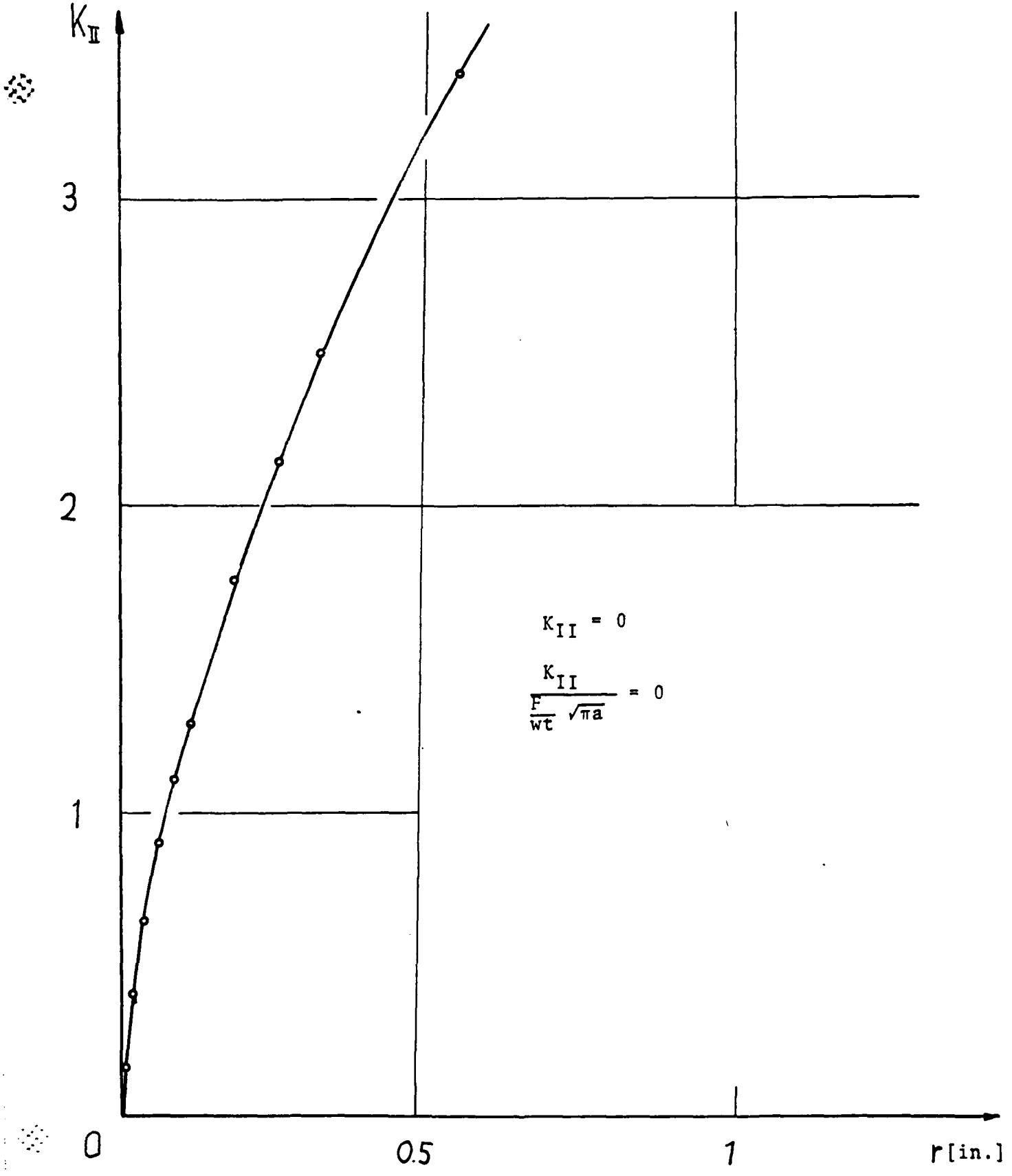

Figure 36b: K_{II} Factor for Pure Tension and $\frac{a}{w} = 0.5$

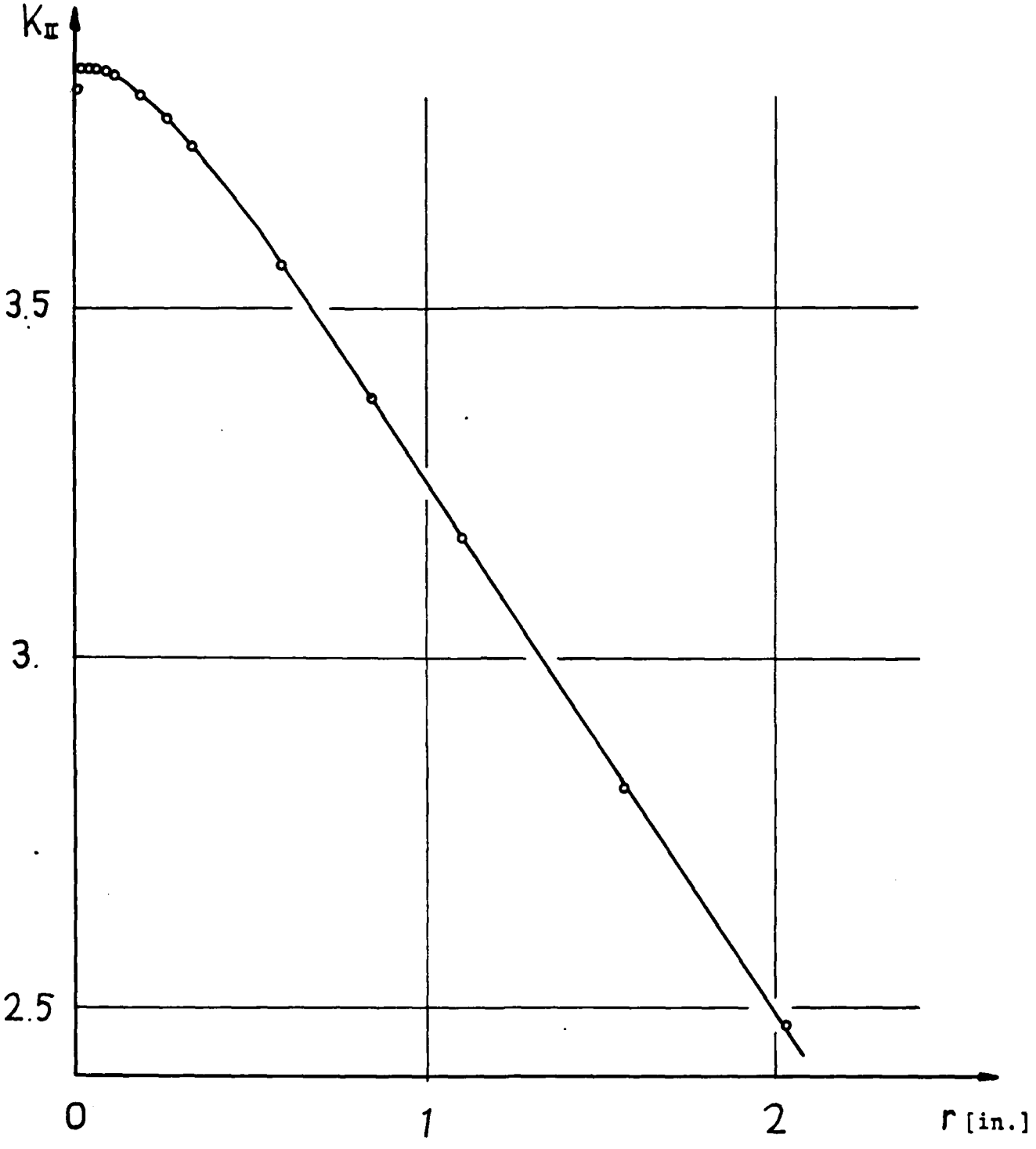

$K_{II} = 3.84$

$\frac{K_{II}}{\frac{F}{wt}\sqrt{\pi a}} = 1.37$

a = 2.5 in.
w = 5 in.
t = 2.5 in.
τ_o = 1 psi

Figure 37a: K_{II} Factor for Pure Tension and $\frac{a}{w} = 0.5$

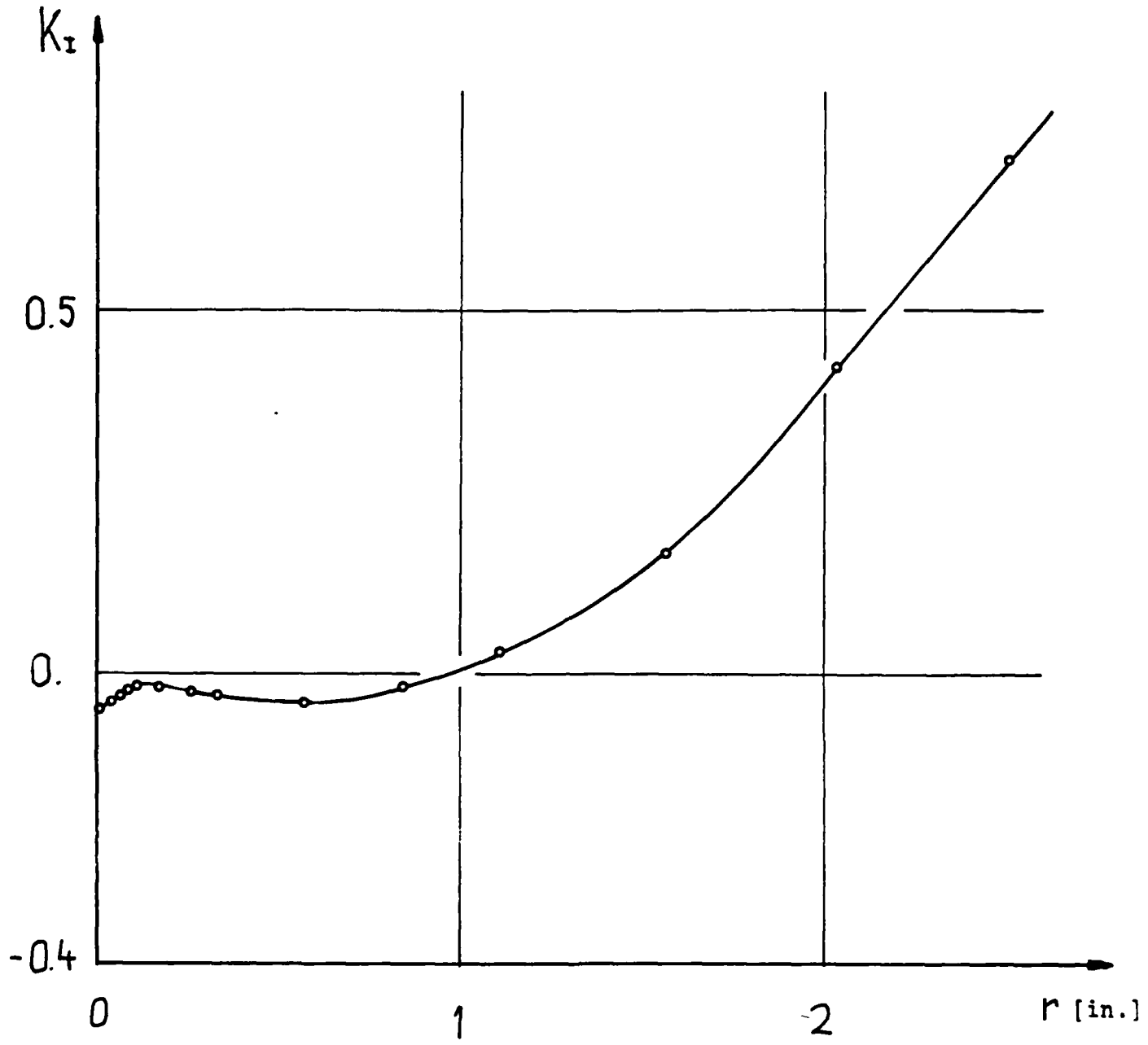

$K_I = - 0.055$

$\frac{K_I}{\frac{F}{wt}\sqrt{\pi a}} = - 0.02$

a = 2.5 in.
w = 5.0 in.
t = 2.5 in.
τ_o = 1 psi

Figure 37b: K_I Factor for Pure Shear and $\frac{a}{w} = 0.5$

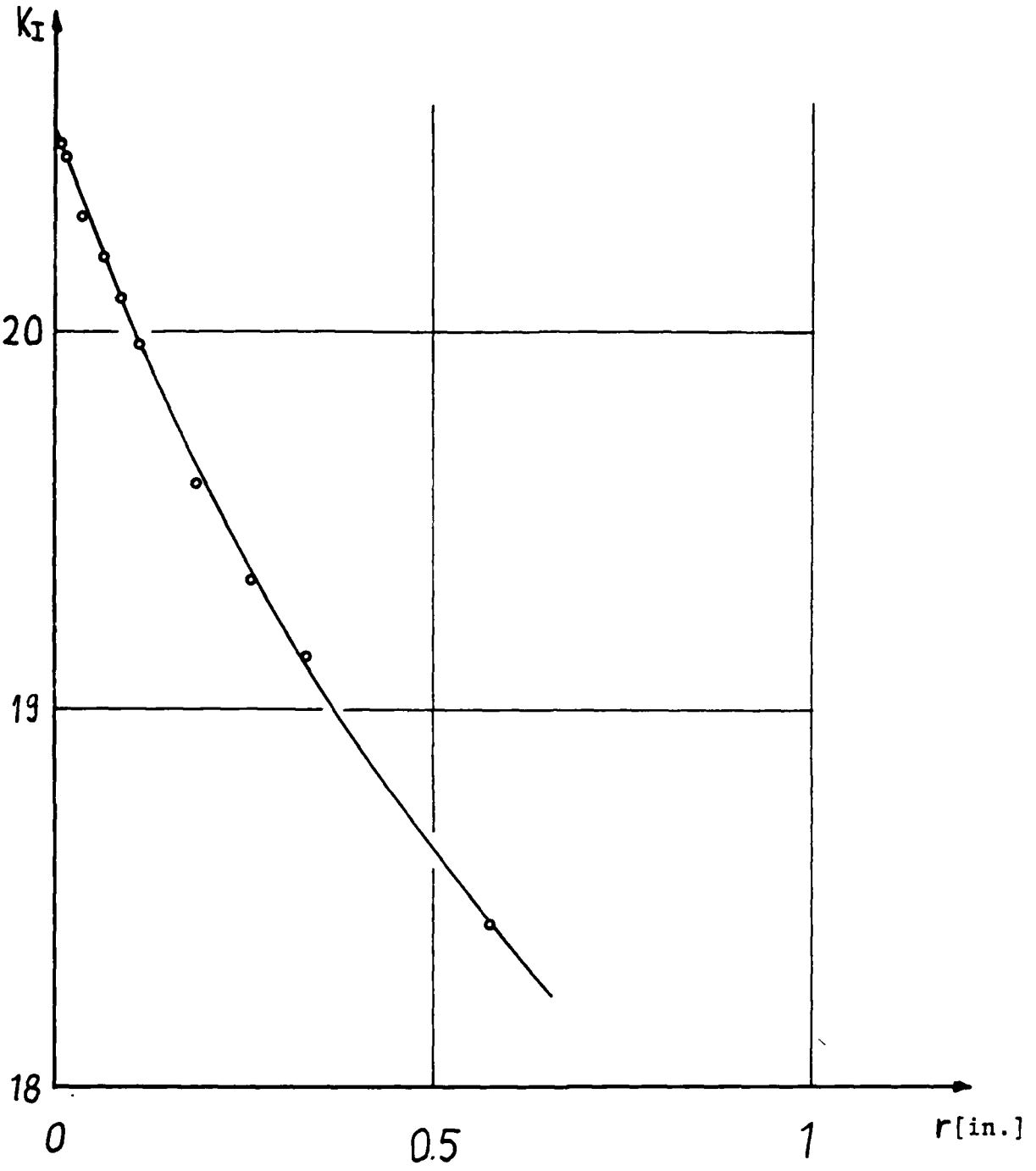

$K_I = 20.52$

$\frac{K_I}{\frac{F}{wt}\sqrt{\pi a}} = 6.19$

a = 3.5 in.
w = 5 in.
t = 2.5 in.
σ = 1 psi

Figure 38a: K_I Factor for Pure Tension and $\frac{a}{w} = 0.7$

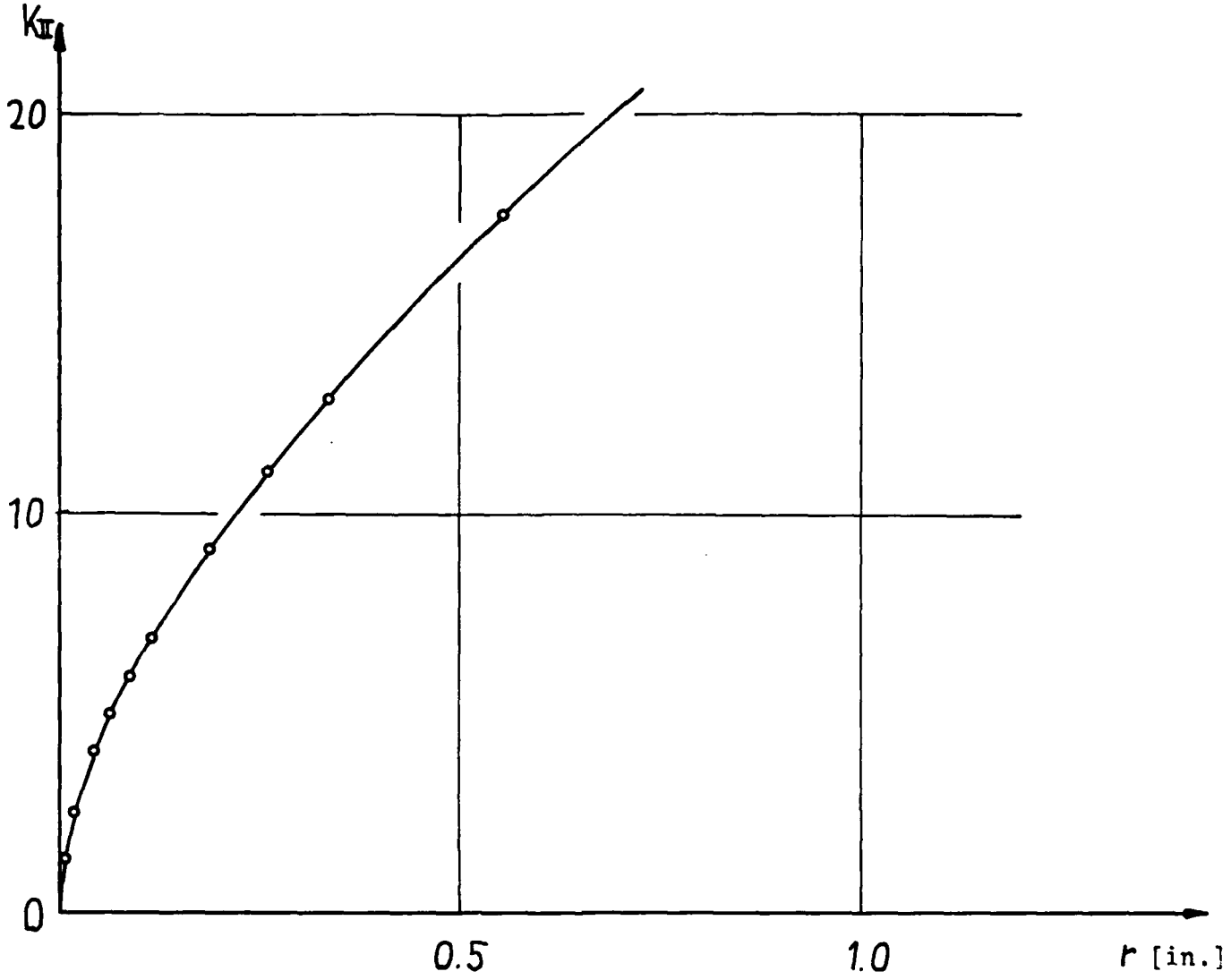

$K_{II} = 0$

$\frac{K_{II}}{\frac{F}{wt}\sqrt{\pi a}} = 0$

a = 3.5 in.
w = 5.0 in.
t = 2.5 in.
σ = 1 psi

Figure 38b: K_{II} Factor for Pure Tension and $\frac{a}{w} = 0.7$

AD-A166 575 CREEP AND FRACTURE CHARACTERISTICS OF MATERIALS AND STRUCTURES AT ELEVATED TEMPERATURES(U) GEORGE WASHINGTON UNIV WASHINGTON DC SCHOOL OF ENGINEERING AN UNCLASSIFIED .. H LIEBOWITZ 14 FEB 86 N00014-84-K-0027 F/G 20/11 2/4 NL

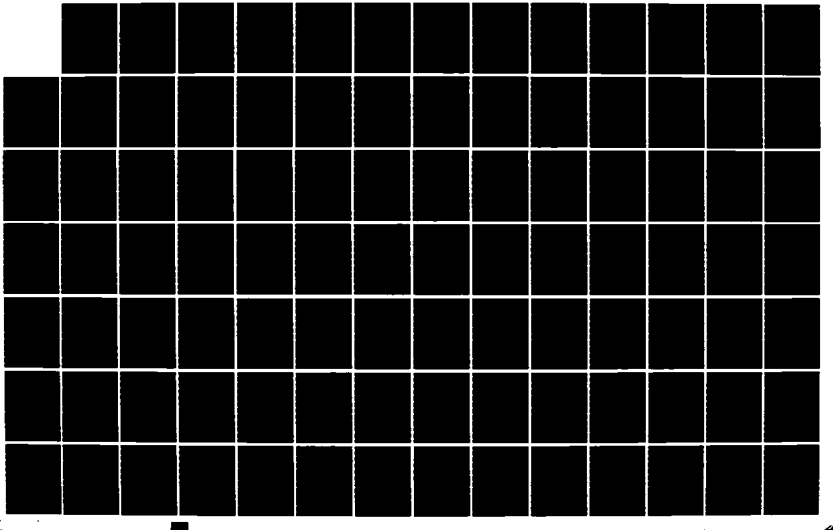

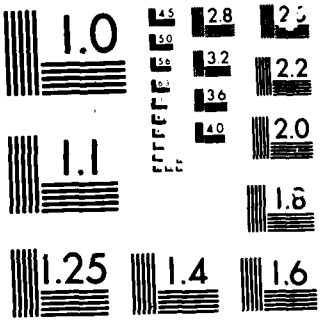

MICROCOPY CHART

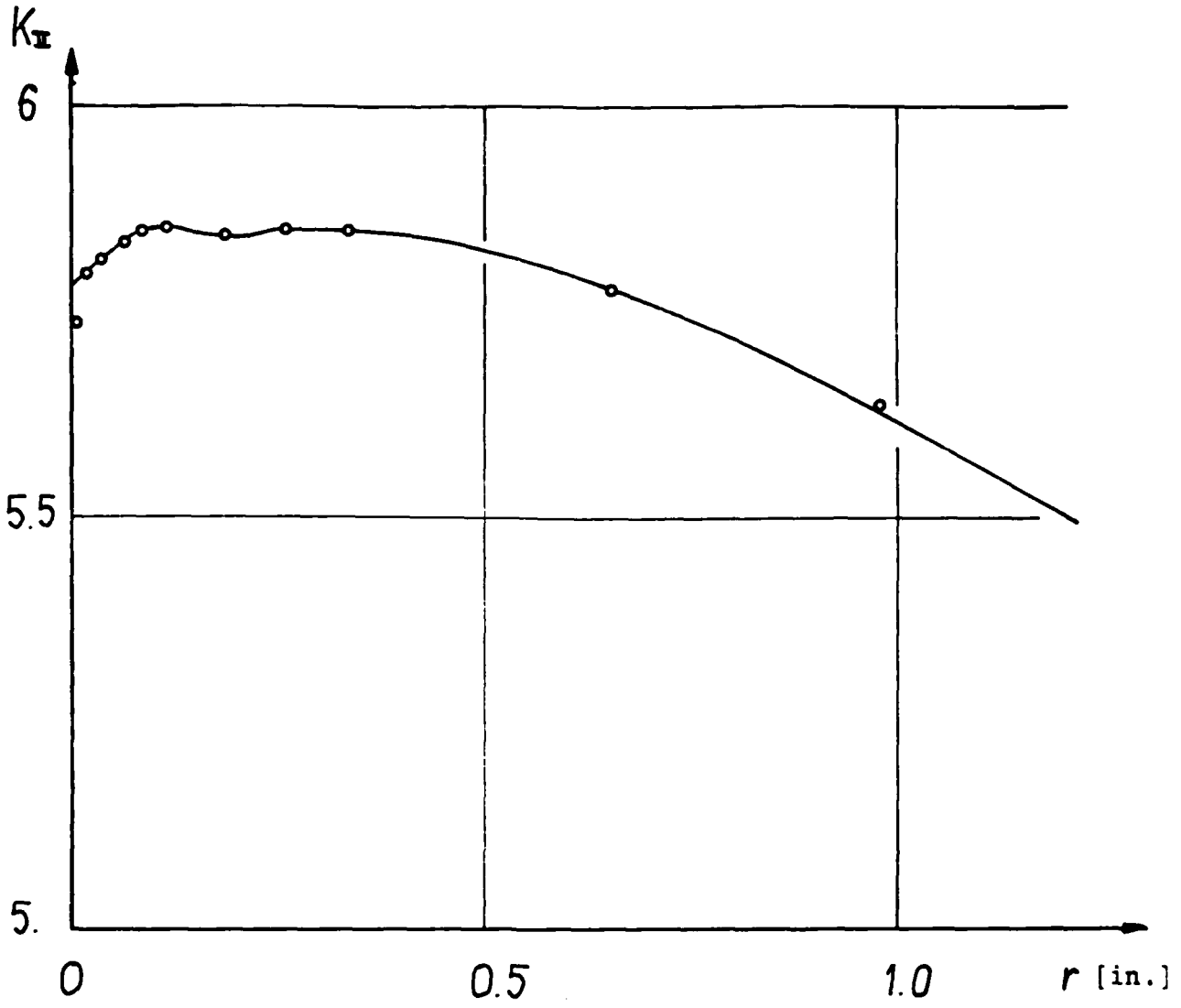

$K_{II} = 5.78$

$\frac{K_{II}}{\frac{F}{wt}\sqrt{\pi a}} = 1.74$

a = 3.5 in.
w = 5.0 in.
t = 2.5 in.
τ_o = 1 psi

Figure 39a: K_{II} Factor for Pure Shear and $\frac{a}{w} = 0.7$

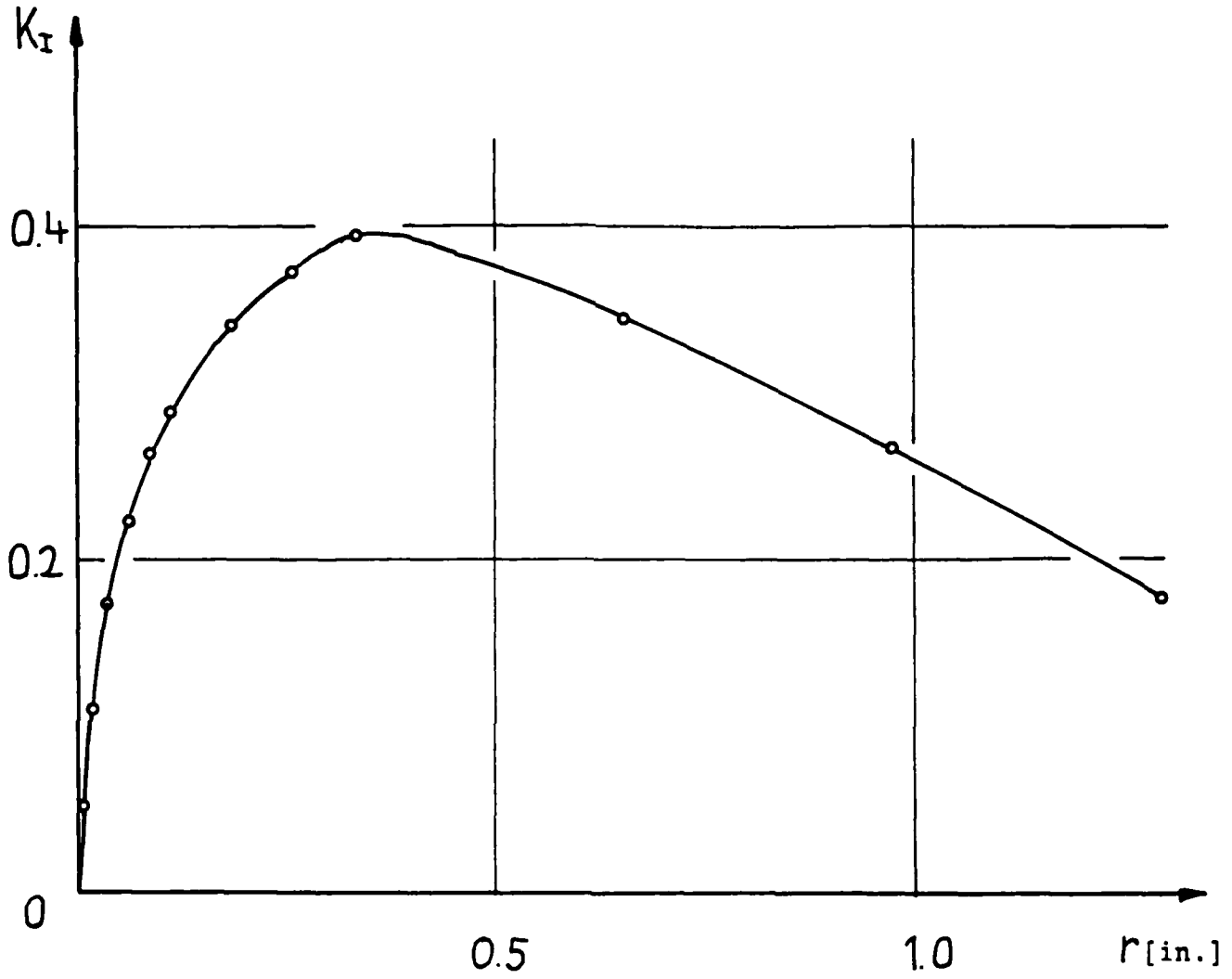

$K_I = 0$

$\frac{K_I}{\frac{F}{wt}\sqrt{\pi a}} = 0$

a = 3.5 in.
w = 5.0 in.
t = 2.5 in.
τ_o = 1 psi

Figure 39b: K_I Factor for Pure Shear and $\frac{a}{w} = 0.7$

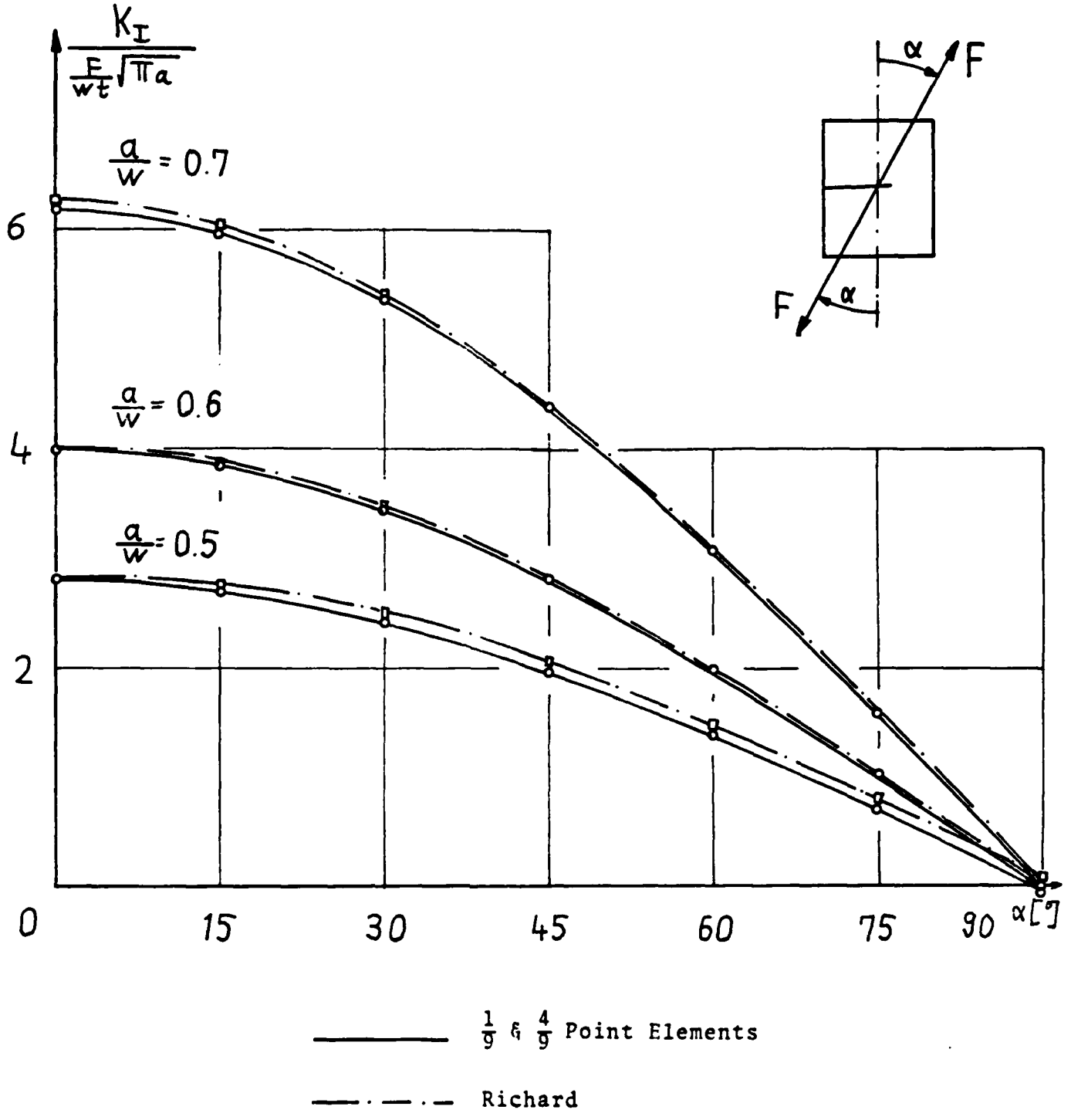

——— $\frac{1}{9}$ & $\frac{4}{9}$ Point Elements

—·—·— Richard

Figure 40: Dimensionless K_I Factors for Different Crack Lengths

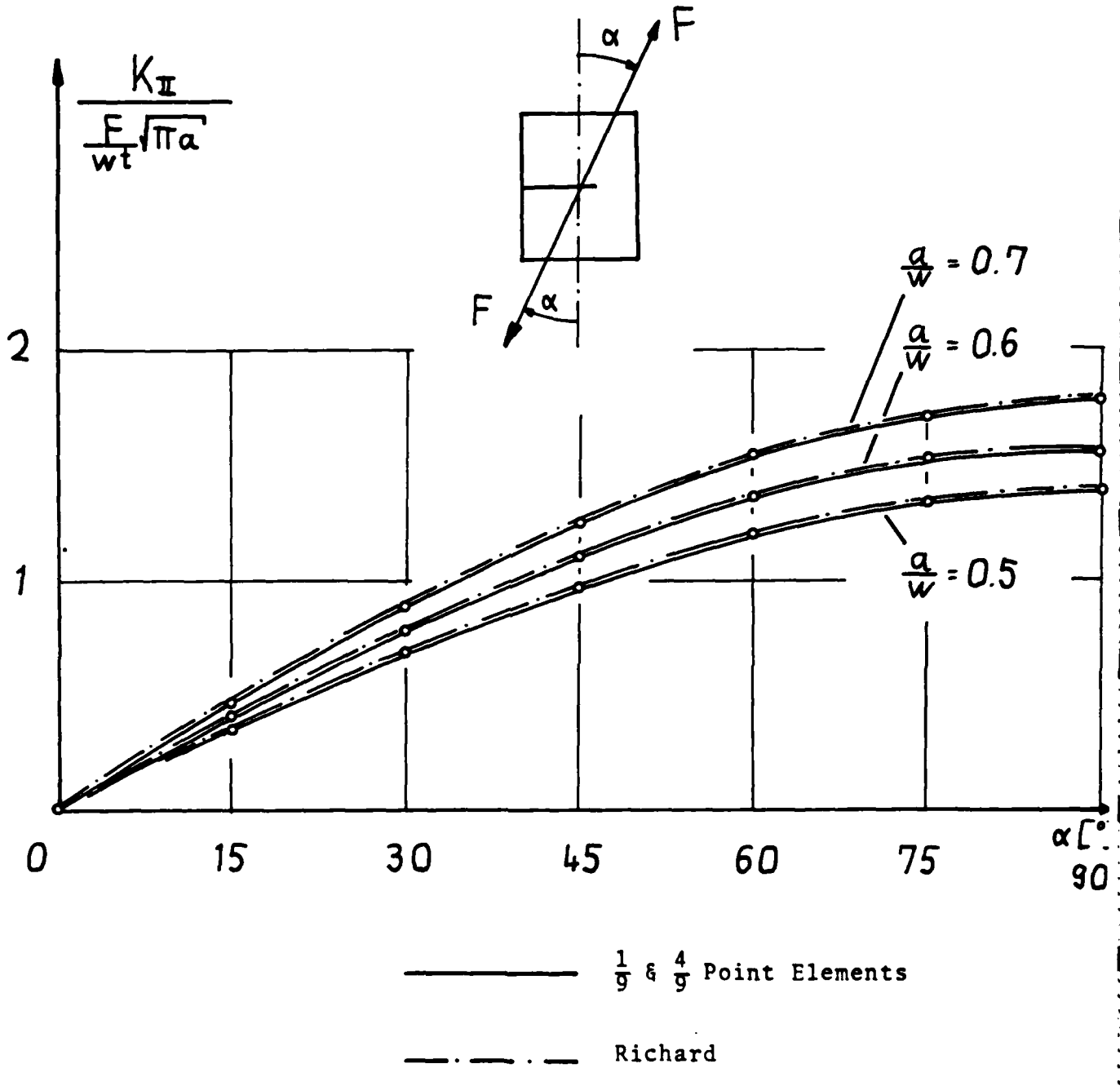

Figure 41: Dimensionless K_{II} Factors for Different Crack Lengths

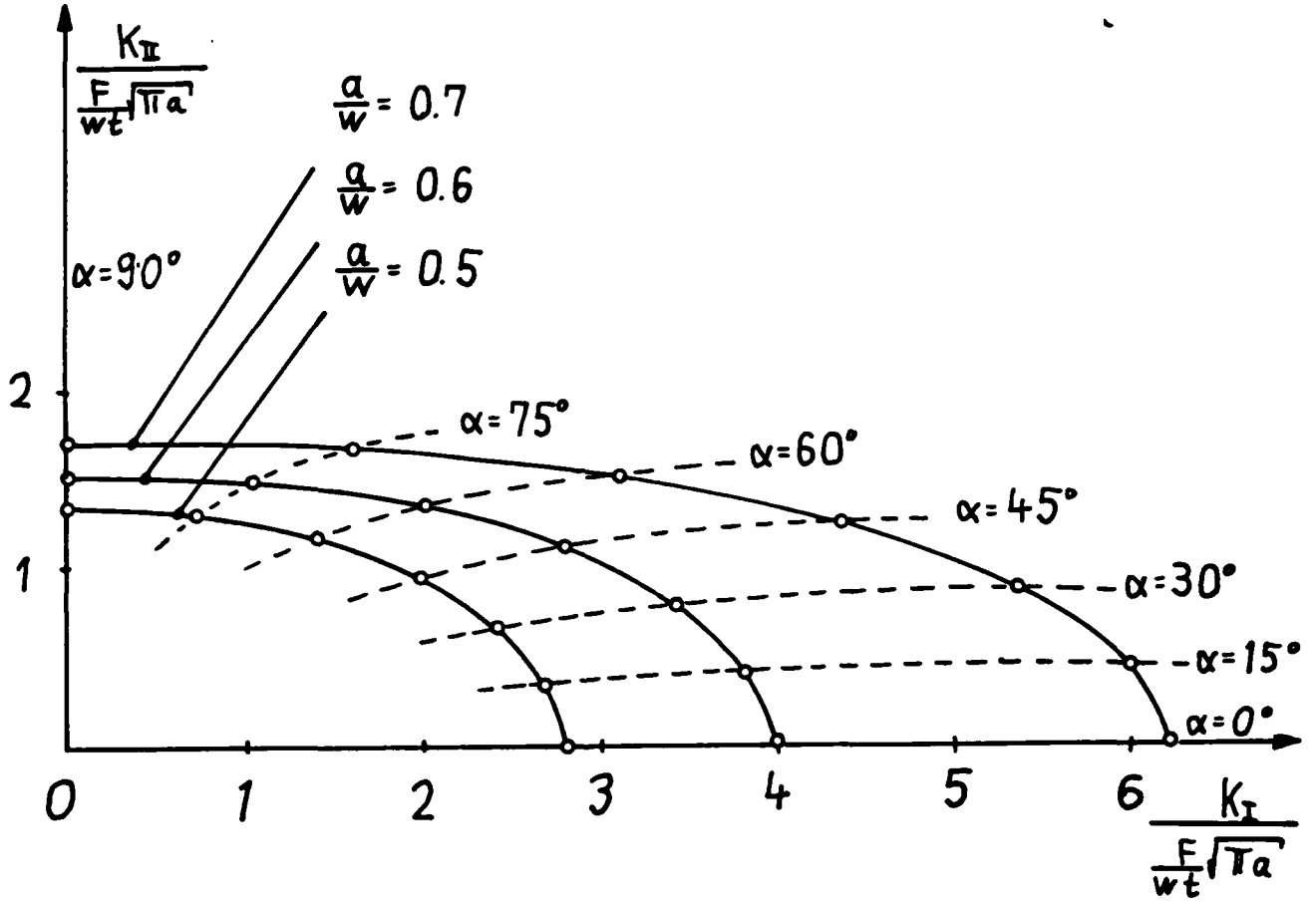

Figure 42: Dimensionless Stress Intensity Factors for Different Crack Lengths ($\frac{1}{9}$ & $\frac{4}{9}$ Point Elements)

APPENDIX B:

"Fracture Under Mixed-Mode Loading,"

By: Roland Gerstner.

Final Report, May, 1985.

FRACTURE UNDER MIXED-MODE LOADING

By Roland Gerstner

Advisor: Professor P. K. Poulose

May 1985

School of Engineering and Applied Science

The George Washington University

Washington, D.C. 20052

Abstract

In a literature survey it was found that the CTS specimen proposed by Richard is the most suitable specimen for mixed mode experiments, which were conducted with PMMA. As it was found in tests with CT specimens that the critical stress intensity K_c of PMMA depends on the stress intensity rate $\dot{K}$, the testing was done at a constant $\dot{K}$. The fracture criterion

$$\frac{K_I}{K_{Ic}} + \left(\frac{K_{II}}{K_{IIc}}\right)^2 = 1$$

gives a reasonable fit to the experimental data. Some problems in mode II testing with the CTS specimen were found that need further consideration. In additional tests the modulus of elasticity and the Poisson ratio were obtained.

CONTENTS

1 Introduction

While mode I fracture mechanics are well established and commonly used, mixed mode fracture mechanics did not reach more than a prelimary stage yet. There is no standardized testing procedure. There are many different failure criteria but none of them can be judged as true or false because of the lack of reliable data.

On the other hand, mixed mode fracture is of great practical intrerest as almost no real structure is so simple that a crack is subjected to pure opening mode. Mixed mode loading occurs at curved and inclined cracks, branched cracks, welded or glued joints, and in many other cases.

This paper starts with a literature review of mixed mode fracture mechanics with three points of interest: mixed mode specimens, fracture criteria, and earlier experimental work. As the values for mechanical properties of plexiglas found in literature differed considerably, testing of these properties was done. A series of tests with CT specimens {1} was conducted to find out the dependancy of the critical stress intensity K_{Ic} on varying stress intensity rates. Finally, mixed mode experiments with the compact tension shear (CTS) specimen proposed by Richard {2-8} were performed.

II Notation

Many researchers used the index $m = K_{II}/K_I$ to characterize mixed mode problems. But for pure mode II ($K_I = 0$) this index is infinity and therefore no diagram over the complete mixed mode range from pure mode I to pure mode II can be drawn.

Another index often used is $\beta = \arctan(K_I/K_{II})$ where $\beta = 90°$ for mode I and $\beta = 0°$ for mode II. This index is highly functional for a large panel specimen with an angled crack (see next chapter) as β is equal to the inclination angle of the crack, but it has no physical meaning in other specimens.

Shih {9} introduced the index $M = (2/\pi)\arctan(K_I/K_{II})$ in his paper. This index never got attention by other researchers.

Hence in this paper the index $n = K_{II}/(K_I + K_{II})$ is used which also is used by Richard {8}. This index goes from 0 for mode I to 1 for mode II and is therefore easy to use. The indices β and m can easily be converted into n by the formulas

$$n = \frac{m}{1 + m} \qquad (1)$$

$$n = \frac{\cos\beta}{\cos\beta + \sin\beta} \qquad (2)$$

Table 1 gives the calculated relations.

III Literature Review

The following literature review consists of the three parts mixed mode specimens, fracture criteria, and earlier experimental work. From this review a plan of investigation is concluded.

1. Mixed Mode Specimens

To date, there is no standadized specimen for mixed mode experiments. During the literature review, 10 different specimens of general use were found which will be discussed briefly. These specimens are (see figure 1)

S1 Panel with an angled center crack under tension (ACCT), sometimes with notch (ACNT).

S2 Panel with a single angled edge crack under tension (SAECT)

S3 Panel with a curvilinear center crack under tension (CCCT)

S4 Panel with a center crack under biaxial tension (CCBT)

S5 Single edge cracked specimen under 3-point bending (SEC3B)

S6 Single edge cracked specimen under 4-point bending (SEC4B)

S7 Tube under torsion with an oblique crack

S8 Brazilian disk (BD)

S9 Specimen proposed by Banks-Sills

S10 Compact tension shear specimen (CTS)

Beside these, spherical shells under pressure {10,11} and X-, H-, and T-shaped specimens were used {12}. The abbreviations in parentheses are used in the following.

As with the most often used ACCT specimen no pure mode II condition can be acieved, the following specimens were employed for mode II testing

S11 Compact shear specimen (CS)

S12 Inplane shear specimen (IPS)

These specimens will be discussed briefly as well.

The panel with an angled crack under uniaxial tenstion (figure 1a) is the most often used specimen {13-23}, but there are some variations: Erdogan and Sih {13} used a large plate (a/b = 0.2) subjected to "uniform tension at infitnity" and gave for that the stress-intensity factors

$$K_I = \sigma\sqrt{\pi a}\sin^2\beta, \quad K_{II} = \sigma\sqrt{\pi a}\sin\beta\cos\beta \qquad (3)$$

which are used by other resesarchers as well.

Shah {18} and Wilson {23} used a narrow panel (a/b = 0.5) with only one loading hole on each end. The stress intensity factors for this configuration are not explicitly given, but it is obvious that they are different from those of the large panel. Wu et al. {34,35} used a large panel (a/b = 0.17) with an angled elliptic notch loaded by three pins on each side. Many researcher do not state at all which kind of ACCT specimen they used.

The obvious problem is that the results cannot be compared simply by the crack angle as the mixed mode ratio n

is different. Equation (2) is strictly valid only for an infinite panel loaded at infinity.

The biggest limitation of this specimen is that no pure mode II condition can be achieved. Therefore researcher could not perform experiments over the complete mixed mode range or they had to use another specimen for mode II experiments. The loads increase considerably for decreasing angle and in some cases the specimens broke in the loading holes for small angles {21}.

Another problem is the fatigue precracking as the application of the load in testing direction would result in curved cracks which are of no use. Several researchers prevented the problem by using only thin machined slits {21,25,33} or by introducing the crack with a razor blade {15} which is possible in the case of PMMA. If fatiguing is necessary as in the case of steel or aluminum alloys, the following procedure has to be done {12}: A central not angled notch is machined in a larger plate. Then this plate is precracked in the usual way. The final specimen is cut out of this lager plate afterwards, as shown in figure 2. This procedure wastes a lot of time and material.

The plate with an angled edge crack subjected to uniaxial tension (SAECT) (figure 1b) is used less often {12,36,37}. The problems in production and application of this specimen are similar to those just stated for the ACCT specimen.

Hussain et al. {38} suggested a plate with a curvilinear

central crack subjected to uniaxial tension (figure 1c) for mixed mode and mode II testing and performed some mode II experiments. The specimen did not get much attention as it is quite difficult to produce a curvilinear crack. The mode II conditon is at $\eta = 77.0°$ (not at 79.6° as stated). A pure mode I condition cannot be achieved as K_I gets zero at $\eta = 137.5$ and there is $K_I < 0$.

The cracked plate under biaxial tension (figure 1d) is used by several workers {25,39-41}. There are some variations: Some used a straight crack and just changed the ratio σ_x/σ_y {39,40}, others rotated the crack {25}, and Radon et al. {41} used curved cracks. A testing machine suitable to produce biaxial loading is necessary. Therefore the effort in machinery is higher than for those specimens which can be tested in uniaxial tension.

The tube under torsion with an oblique crack (figure 1e) got some attention {11,13}, but it is not very easy to handle. Also, not every material is available as tube material.

The three- or four-point bend specimens have some advantages: They are easy to produce and fatigue. They can be tested from pure mode I to pure mode II, although a pure mode II condition may only be achieved with a notch, as pointed out by Richard {42}. The bend specimens got some attention in experimental work {37,43,44}.

The Brazilian disk specimen which also can cover the complete range from mode I to mode II was used by several

researchers {45,46}. As the crack is subjected to compression in this specimen, friction between the crack flanks may occur {42}. The fracture mechanism for a crack under compression may be different from that under tension {47}. Hence the results between tension specimens and the BD specimens may not be comparable:

Banks-Sills et al. {50} recently proposed a new specimen for mode II dominant mixed mode experiments. This specimen is not suitable for mode II experiments. No experiments with this specimen have been reported yet.

The CTS specimen proposed by Richard {2-8} is similar to the Banks-Sills specimen. But instead of gluing the specimen to the grips, Richard uses a statically determinant connection by means of pins. This is easier to handle in practical application. The CTS specimen can be used from pure mode I to pure mode II. Richard et al. {42} claim that the CTS specimen is superior to the Banks-Sills specimen and all other specimens in mode II testing. A problem with the CTS specimen is that the influence of geometrical deviations which are inevitable in machining the specimens is not known yet. No other experiments than those performed by Richard himself are reported in literature so that the basis for direct comparison is tiny.

The K_{IIc} values which are necessary to confirm the different mixed mode fracture criteria are evaluated with two different mode II specimens, the compact shear (CS) specimen {49} and the inplane shear (IPS) specimen. Although

Chrisholm and Jones {49} claim to achieve virtually pure mode II condition at the crack tip of the CS specimen, later researchers got different results: Riddle {50,51} found that K_I is much larger than anticipated and that already small variations in the boundary conditions change the ratio K_{II}/K_I extremely. And Richard et al. {42} came to the conclusion that "this specimen is unsuitable for the evaluation of K_{IIc}". The discussion about this specimen is not settled yet. A new FEM calculation by Elenz {52} shows that the state of stress at the crack tip is essentially mode II. The CS specimen was used by {21} in their experimental work.

The inplane shear specimen did not get that much theoretical attention. It was used by {13,21} for mode II testing, but the introduction of the forces imposes some uncertainties.

In general, it is very difficult to achieve pure mode II condition. Paris and Sih {53} found that only internal or very deep external cracks show significant mode II displacements. Several researchers {9,43,54} found in numerical analyses that the plastic zone increases with increasing K_{II}. Beside some other problems this imposes that the thickness requirement for mode II specimens may be greater than that for mode I specimens {54}. A further discussion of the problems and some other mode II specimens are found in {42}.

The question remains what the influence is on the value of K_{IIc} if the state of stress is not pure mode II but

slightly mixed mode. If K_{IIc} is very sensitive to small changes in the loading condition, the error may be high. It seems though that K_{Ic} is not that sensitive, but a final answer cannot be given with the momentary knowledge.

2. Fracture Criteria

The purpose of the mixed mode frature criteria is to relate the onset of crack growth under mixed mode loading to that under mode I loading. Two principally different groups of fracture criteria can be distinguished: Those which are based on some theoretical or physical considerations and those which are evaluated empirically by a best fit to experimental data.

In all the criteria of the first group, the critical stress intensity K_{Ic} for mode I is set as standard value. The most interesting case therefore is what the criteria predict for pure mode II. The predicted ratio K_{IIc}/K_{Ic} and also the predicted angle of fracture initiation in mode II was calculated for different criteria {13,16,17,38,55-65} and is given in table 16. Some of the criteria are sensitive to the Poisson ratio. In this case $\nu = 0.36$ was used which is found for PMMA.

Although Erdogan and Sih {13} and Nuismer {55} used different approaches in developping their criteria, the prediction of both criteria is the same for the fracture initiation as well as for the fracture angle. Another well

established criterion is Sih's strain energy density function {16,17,59}. The predictions of this criterion depend on the Poisson ratio. While the difference to the other two criteria is within 10% for a Poisson ratio around 0.3, the predictions are very different for extreme values of ν. Therefore, experiments with materials with an extreme Poisson ratio are best to prove the validity of this criterion.

Many criteria {13,17,55,59,66} base on the assumption that fracture is a local phenomen and that hence the stress distribution in the vicinity of the crack tip can be described just by the singular terms of the William's stress funtion {67}. For a definition of the stresses around the crack tip see figure 3.

Inspired by a paper of Cotterell {68}, Williams and Ewing {15} pointed out that the stress σ_x parallel to the crack tip (see figure 3) may not be neglegible. Hence they added the first nonsingular term of the William's stress function {67} in their analysis. Later Eftis, Subromanian and Liebowitz {69,70} confirmed this approach. Several authors {15,71-73} based their fracture criteria on this enlarged function. The problem is that all these criteria cannot be described in terms of K_I and K_{II} only, but need an additional parameter. This parameter must be determined experimentally which usually is done in a way that the resulting function gives the best fit to the experimental data. As the calculation of K_{IIc}/K_{Ic} is not possible without knowing this parameter, these

criteria are not listed in table 2.

Most criteria are for brittle fracture. But there are also four criteria that take plastic deformations into account: the criterion by Shih {9}, the crack separation energy rate criterion {43,73}, the T-criterion {31-33,74}, and the J-integral {63-65}. It is especially interesting that the T-citerion predicts for pure mode II an angle of fracture initiation of about -97 degree, while the J-intgral predicts 0 degree which are extreme values.

A second group of fracture criteria are the empirical criteria. They are evaluated as best fit to the experimental data. Normally they require the knowlegde of K_{Ic}. The most general form of them is

$$\left[\frac{K_I}{K_{Ic}}\right]^u + \left[\frac{K_{II}}{K_{IIc}}\right]^v = 1 \qquad (4)$$

Awaji and Sato {46} found $u = v = 1.6$ for graphite and plaster and $u = v = 2$ for marble. Shah {18} got $u = v = 1$ for steel which was confirmed by Chiu and Liu {39} for aluminum and was found by Leicester {75} for wood. Wu {76} got $u = 1$ and $v = 2$ for wood and fiberglass - reinforced plastics which later was found by Richard {4,8} for PMMA. Lee and Advani {77} confirmed these exponents in an analysis based on the Griffith theory {78}.

The mixed mode problem is dealt with in official regulations too {79,80}. The ASME Boiler and Vessel Code {79} suggests to project the inclined crack in the direction of the maximum stress and subject then the projected crack

to mode I loading. The fracture criterion is

$$K_{Ic} = \sigma\sqrt{\pi(a\sin\beta)} \qquad (5)$$

After some algebraic transformations (see appendix 1), this equation becomes

$$\frac{K_I}{K_{Ic}} = \left[\frac{\frac{K_I}{K_{II}}}{\sqrt{1 + \left[\frac{K_I}{K_{II}}\right]^2}}\right]^{1.5} \qquad (6)$$

This criterion is dicussed in several papers {8,57,81}. As can be seen in figures 4 to 6 in {57}, the ASME criterion makes in some cases prediction of higher fracture loads than other criteria, especially in the case of pure shear. But this does not mean that the ASME criterion is unsafe, as this is just a relative difference and the other criteria are not convincingly verified by experiments either.

This short review of the mixed mode fracture criteria is far from being exhaustive. Already in 1977, Gilles {82} reported of 35 different mixed mode fracture criteria. This paper also is mainly restricted to homogeneous materials subjected to tension. For orthotropic materials (wood, composite materials) or for cracks under compression, other criteria can be found in literature. For a further discussion of fracture criteria and also comparison between them, the reader is referred to {8,19,57,58,81,83-85}.

3. Earlier Experimental Work

There is no standardized testing procedure for mixed mode testing. Most researchers took ASTM E399 {1} as a guideline. But as already mentioned, the thickness requirement stated there may not ensure linear elastic conditions as the plastic zone increases in mixed mode loading. Pook {14} introduced the criterion that the net section stress at fracture initiation should be less than 80% of the yield strength of the material to ensure brittle fracture.

Many researchers already conducted mixed mode experiments. Most research was done with PMMA, but steel and aluminum alloys got considerable attention too.

The problems and results with PMMA will be discussed later, now the other materials will be considered. Tables 3 to 5 give the results found in literature for steel {18,19,25,33,43}, aluminum alloys {12,14,19,20,23,28,33,86}, and several other materials {4,27,29,31,33,46}. As can be seen in column 3 of each table, most researcher used the ACCT specimen. Column 5 gives the range of the experiments by the mixed mode index n. Many researchers did not test the complete range from mode I to mode II. Another important information is, how many specimens were tested, which is given in column 6. It is felt that that 3 or 4 specimens are not enough to make any conclusion about the tested material. Columns 7 to 9 finally give K_{Ic}, K_{IIc}, and K_{IIc}/K_{Ic} as far as they are stated in the cited papers. A comparison of the experimentally found K_{IIc}/K_{Ic} with those predicted by the

different fracture criteria (table 2) reveals that only the J-integral {63-65} and the criterion by Irwin {61,62} predict $K_{IIc}^{I} = K_{Ic}^{I}$ and are therefore close to the experimental results. Most researchers who perfomed these experiments therefore used empirical fracture criteria.

The angle of fracture initiation predicted by the various criteria differ considerably. Hence experimental verification is necessary. An interesting experiment to check the validity of Sih's strain energy density criterion {16,17,59} was performed by Finnie and Weiss {49}. They used cross-rolled beryllium ($\nu = 0.0$) and found that the measured fracture angle is much higher than predicted by the strain energy density criterion but is close to the prediction of the Erdogan and Sih criterion {13}. Awaji and Sato {46} measured the fracture angle in mode II for graphite SA (⊥) ($\nu = 0.07$) and graphite 7477 ($\nu = 0.20$) and found it to be around 67 degrees in both cases. All these experiments give evidence that the angle of fracture initiation is essentially independent of the Poisson ratio.

Although the J-integral and the T-criterion predict totally different fracture angles for mode II, both are verified experimentally. Riddle {50} performed experiments with aluminum and found the angle to be around 0 degree, while Theocaris {31} used Polycarbonate of Bisphenol A (PCBA) and found "angles absolutely greater than 90°".

Plexiglas got the largest attention in mixed mode fracture research {4,11,13,15,21,25-27,33,34,37,40,41,44}.

The results are given in table 6. In addition to the information included in the other tables, this table states the way in which the crack was produced (column 4), the displacement rate used for testing (column 5), and whether slow crack growth was reported in the paper (column 6). Most researchers found K_{IIc}/K_{Ic} to be around 0.9 which is close to the values predicted by several fracture criteria (table 2). This is not that surprising as most of the fracture criteria were constructed to explain the behavior of PMMA.

As it was planned to perform the new experiments with PMMA too, this material got further attention in the literature review.

Many mixed mode experiments require the knowledge of the Poisson ratio. In addition, it is usefull to know the modulus of elasiticity and the strength of the material. The values found in literature {4,7,11,33,37,87-94} are given in table 7. The range for the modulus of elasticity is from 2.0 to 5.0 GPa and for the Poisson ratio values between 0.30 and 0.43 were stated. Often it was not very clear whether the stated value was obtained experimentally or whether it was chosen as the best fit to the respective theory.

The modulus of elasticity is dependent on the straining rate {95}, but most sources do not state this rate. Williams {95} gives the equation

$$E = [0.655 + 2.74(\dot{e})^{0.109}]\text{GPa} \qquad (7)$$

where $\dot{e}$ is the straining rate with the unit 1/s. Williams

applied this formula for $\dot{e} = 5x10^{-5}$ 1/s to 10^{2} 1/s. He therefore got values for E from 1.6 to 5.2 GPa.

The fracture toughness testing of PMMA involves some problems. In the following, those found in the literature are stated and discussed:

1. Most testing machines are designed for metals. Therefore, the lowest load range is around 5000 N. Even with a high accurancy of 0.1%, the error because of the small fracture loads for PMMA may be high. This problem is reported by Phadke et al. {21}. They used a load range of 500 kg (4900 N) with a least count of 0.5 kg (4.9 N). For the smallest reported fracture load of 7.5 kg (73.6 N), the error is 6.7%.

It is also not clear whether ASTM E399 {1} is applicable to PMMA or not, as this norm is designed for metallic materials. Despite this uncertainty, that standard was applied in many papers, as no other standard is known.

2. Many researchers consider PMMA as ideal isotropic and brittle, while other scientists proved that socalled crazes establish at the crack tip {89,96-99}. The crack tip is supposed to have atomar dimensions and the fracture process is a molecular process. As PMMA has large molecular chains, the orientation of these chains influences the state of stress in a way that it is inhomogeneous in molecular dimensions. Crazes only develop in an inhomogeneous state of stress which shows that this material is not that ideal isotropic in a microscopic range. Furthermore, crazes are

kind of plastic deformations which may cause some error in applying LEFM theories.

It was suggestd to anneal the the specimens to reduce the crazes {100} which was done by {34}. In addition, Mai {100} suggested to minimize the occurence of crazes "by a coating of silicone oil onto the specimen surfaces". The influence of this coating is not readily understood and no other reference to it was found in literature.

3. The fracture toughness of PMMA depends on the temperature, the relative humidity of the air or the water content of the material respectively, and the presence of chemicals. Therefore, some researchers stored the specimens under specific conditions for 1500 hours {94}, or did the testing in climatized rooms {100}. But most researchers did not have the facilities and did tne testing under whatever conditions there were in their laboratories.

4. As was discussed in several papers {95,101-104}, the fracture toughness of plexiglas depends on the crack propagation speed. A group of researchers {95,102} state that there exists a "unique relationship between critical stress intensity factor and crack speed which is independent of the test piece geometry used" {95}, while Cotterell {101} claims that "although the fracture toughness does increase with velocity of fracture, ... it is not a function of velocity". The results of the first group show a high data scatter for crack speeds greater than 1 mm/s which is probably due to an inaccurate method of determining the

crack velocity at higher speeds.

5. As Marshall et al. {103} put it, "the most common mistake is the evaluation of K_{Ic} at instability by using the length of the original notch when in fact the crack length after the slow growth regime can be considerably greater". For slow crack growth, PMMA shows a rough surface with furrows in direction of the crack growth, sometimes called "river markings" {94}. Fast fracture produces a smooth, featureless, mirror-like fracture surface {94}. The transition is marked by a sharp line {105}.

The problem lies in the relation of the slow crack growth to the load - displacement curve. It is not clear whether the slow crack growth really does occur before reaching the peak load, or whether the crack just starts slow at peak load. Beside that, a correction for slow crack growth is only possible for pure mode I. Under mixed mode and mode II loading, the crack does not propagate selfsimilar, and after initiation the K_I and K_{II} factors are unknown.

There is considerable amount of mixed mode fracture research done in East Europe {66,106}, Japan {107-109}, and China {112,113}. Abstracts of further Chinese papers can be found in {112,113}. All these works could not be considered in this paper because the respective journals were not available.

4. Summary

1. The CTS specimen is the best specimen for mixed mode experiments found in literature. It can be used for the complete mixed mode range from mode I to mode II and is easy to handle.

2. There are innumerable fracture criteria in literature which are partly contradicting.

3. A considerable amount of experimental mixed mode work was found in literature. The problem is not that there are no experimental results available, but that the available results are not reliable.

4. The mechanical properties for plexiglas stated in the literature differ considerably. Especially the influence of the straining rate on the modulus of elasticity is not clearly understood.

5. The critical stress intensity of plexiglas depends on the crack propagation speed.

5. Plan of Investigation

From these findings in the literature review, it was decided to do the following experimental work with PMMA:

1. Tests with tensile specimens at different straining rates. Specific interest lies on the Poisson ratio and the dependence of the modulus of elasticity on the straining rate.

2. Tests with CT specimens at different loading rates. As it takes a high effort to measure the crack propagation speed accurately, it is tried to find a relation between the stress intensity rate $\dot{K}$ and the critical stress intensity K_{Ic}.

3. Tests with CTS specimens in mode I at different loading rates and comparison of these results with those found with the CT specimens.

4. Tests with CTS specimens under mixed mode loading. If the assumed dependency of the fracture toughness on the stress intensity rate $\dot{K}$ is proved in tests 2 and 3, $\dot{K}$ will be kept constant for all mixed mode loading conditions.

IV Experimental Procedure

1. Material

The material used for the tests was Plexiglas G Acrylic Safety Glazing, produced by Rohm and Haas, Philadelphia (PA). All the specimens were cut out of a single half inch thick plate. As the plate was cast, the thickness varied considerably.

2. Testing Procedure

Table 8 gives the dimensions of the tensile specimens. All specimens were instrumented with an extensometer between point 2 and 3 to measure the elongation. Specimens T1 and T3 were additionally instrumented with a slightly modified extensometer to measure the contraction of the specimen for the evaluation of the Poisson ratio. The results were recorded on a X - Y plotter.

For the measurement of the modulus of elasticity and the Poisson ratio, the specimens were stressed to a level of 11 MPa and then unloaded with a specific displacement rate (table 9). The time of the unloading process was measured to calculate the straining rate. Then the specimens were loaded until they ruptured. The location of frature was noted.

The 6 CT specimens were prepared and tested in the following way: A razor blade was forced into the machined

chevron notch. Then the specimens were fatigue precracked at 5 Hz with a controlled stroke amplitude of 0.15 mm and an initial minimum load of about 65 N. The final crack length typically was reached after 12000 cycles. The crack front was straight. The dimensions of the CT specimens are given in table 10. The specimens were instrumented with a clip gage according to ASTM E399 {1} and a load - COD curve was plotted on a X - Y plotter.

The machine (MTS) in use for the experiments had as lowest load range 1000 lbf with a least count of 1 lbf. In previous tests with this machine it was found that the load control in the lowest range does not work properly. Therefore, displacement control had to be used for all tests. Displacement control was used by most other researchers too {15,21,26,34,37}.

The testing was done with speeds between 5.1 and 63.5 mm/min. In displacement control, the displacement recorded on the plot is proportional to the time. The time until fracture initiation found there and the critical stress intensity K_k was used to calculate the stress intensity rate $\dot{K}$. The exact way of the calculation can be found in appendix 2.

As all the machines and gages in use were in US customary units, the CTS specimens and the grips were slightly modified to meet these units. The used dimensions are shown in figures 4 and 5.

Altogether, 16 CTS specimens were produced and tested. A

razor blade was forced into the machined chevron notch to start the crack. Then the specimens were fatigue precracked at 5 Hz with a controlled stroke amplitude of 0.15 mm and an initial minimum load of about 125 N. The specimens were loaded through the holes at the side of the notch and not through the middle holes as suggested by Richard {8}. The crack length a = 1.5 in which equals a/W = 0.5 was typically reached after 10000 cycles. Two specimens were further fatigued to a/W = 0.55 and two others to a/W = 0.65. The crack front was straight, but the crack tip was only by chance exactly on the center line of the specimen. Most samples showed deviations of up to 0.1 mm, some up to 0.2 mm. The worst case was specimen CTS1 with 1.5 mm deviation (3.8%). In addition, the crack of this specimen was slanted in through thickness direction by about 4 degrees.

The testing of these specimens under mixed mode conditions imposes some problems. Richard {8} suggests in accordance with ASTM E399 {1} to use load control and choose $\dot{F}$ such that the stress intensity rate $\dot{K}$ in mode I is between 0.55 and and 2.75 Mpa$\sqrt{m}$ per second. Richard himself used $\dot{K}$ = 3.3 MPa$\sqrt{m}$/s. He further suggests that the loading rate $\dot{F}$ used for mode I should be contained for mode II and mixed mode loading. The problem now is that $\dot{K}$ changes for $\dot{F}$ = constant at different angles. It was shown by earlier works {95,101,102} that the fracture toughness of PMMA is rate sensitive. Therefore it is felt that the suggested procedure gives no clear distinction between the influences

of mixed mode loading and those of the rate sensitivity.

There are three principally different ways of loading the specimens under different mixed mode conditions:

1. displacement rate $\dot{d}$ = constant
2. loading rate $\dot{F}$ = constant
3. stress intensity rate $\dot{K}$ = constant

Naturally, there are arbitrarily many ways of loading without any constant magnitude. But these do not seem logical.

Most researchers did their mixed mode testing at a constant displacement rate {21,25,26,34,37}. As they used many different specimens, the influence of the changing stress intensity rate is unknown. But for a CTS specimen, the use of a constant displacement rate is questionable, as in this case the stress intensity rate under mode II loading is only 29% and 17% of that under mode I loading for a/W = 0.5 and 0.7 respectively. This can be seen in table 11. The way how these figures were calculated is given in appendix 2.

Richard {8} used for his experiments a constant loading rate. This is already better, but the stress intensity rate under mode II loading is still only 28% of that under mode I loading for a/W = 0.7, as can be seen in table 12.

Hence in the new experiments it was tried to keep the stress intensity rate $\dot{K}$ constant. The problem is that the stress intensity rate is no property of the testing machine as it is in the cases of the displacement or loading rate.

To relate the mixed mode and mode II stress intensity rate to that of mode I, a fracture criterion is necessary. Because of its simplicity and its good agreement to previous results, the fracture criterion {8,76,77}

$$\frac{K_I}{K_{Ic}} + \left[\frac{K_{II}}{K_{IIc}}\right]^2 = 1$$

was used where it was supposed that $K_{IIc} = K_{Ic}$. Then the necessary displacement rate was calculated as stated in appendix 2. The results are shown in table 13.

The constant stress intensity rate condition is equal to the condition of constant time of loading which was used by {11}.

The tests were done with displacement control. A load - LLD curve was plotted. This is sufficient in the case of plexiglas which has such a low modulus of elasticity (3 GPa versus 210 GPa) that all deformations of the machine and the grips can be neglected.

After the testing, pictures of the crack tip with magnification 50x were taken to measure the angle of crack initiation. In addition, the fracture surface was examined.

The calculation of the stress intensities K_I and K_{II} was done using the calibration factors given by Richard {8}, as stated in appendix 3.

V Results and Discussion

1. Mechanical Properties

The plots for the Poisson ratio and the modulus of elasticity were straight. For the calculation of the modulus of elasticity, the average of the cross - section area at point 2 and 3 was used. In addition to the specific tests of the modulus of elasticity, this property was evaluated out of the plots of the rupture tests. The results agree with a deviation of 3% or less.

The specimens broke at different locations and this may be because of stress concentrations due to machining. It was not possible to get consistent values for the ultimate stress σ_{ult}. Hence the yield strength $\sigma_{0.2}$ was evaluated which shows little data scatter. The results are shown in table 14. The average of the Poisson ratio was calculated to be 0.36.

A comparison with table 7 shows that the new results agree well to those stated in the literature. The new results show slightly increasing values for the properties with increasing straining rate. The growth is about 11% in E and $\sigma_{0.2}$ for an eight times higher strain rate, as shown in figure 6. In many cases, this might not be neglegible. Hence the reported increase of E with increasing strain rate could be confirmed.

Equation (7) given by Williams {95} yields much lower values for E than found in the new experiments, but this is

due to the definition. Williams defined the modulus of elasticity as the secant between the origin and the point of 3.5% strain, while usually the initial slope of the straining curve is used. Equation (7) predicts a 15% increase in E for the range covered by the new experiments.

2. Fracture Toughness at Varying Stress Intensity Rates

The load - COD plots for the CT specimens were almost linear and all did fulfill the requirements of ASTM E399. Preinstability crack growth was not observed, but up to the stress intensity rate $\dot{K}$ = 2.15 MPa$\sqrt{m}$/s, the crack propagation speed was low (range of millimeters per second). The fracture surface therefore showed the river markings which are typical for low crack speeds {94}. Only specimen CT6 ($\dot{K}$ = 3.78 MPa$\sqrt{m}$/s) showed the smooth fast-fracture surface.

Table 15 shows the results for the CT specimens. The results are consistent with Marshall et al. {103} who gave a K_{ic} of about 1.2 MPa$\sqrt{m}$ for crack speeds in the range of millimeter per second.

Then 4 CTS specimens were tested under mode I loading at different stress intensity rates. Again, the load - displacement curves were almost linear and met the requirements of ASTM E399. Only specimen CTS7 ($\dot{K}$ = 0.23 MPa$\sqrt{m}$/s) showed the rough slow - fracture surface, the other specimens had a smooth fracture surface.

The results are shown in table 16. All K_{Ic} values from tests with CTS specimens are significantly greater than those from CT specimens at the same stress intensity rate $\dot{K}$. This can be seen in figure 7. Also the change from the rough to the smooth fracture surface happened at a much lower $\dot{K}$ for the CTS specimens than for the CT specimens. The reason for that behavior is not clearly understood. It might be that the fracture process happens faster in a CTS specimen as this specimen is stiffer and more elastic energy is stored at the onset of fracture. The crack separation rate for the two specimens might be different. Chiang and Miller {43} calculated the crack separation energy rate for ACCT and SENB specimens and found it to be different. They attributed the difference to the effect of hydrostatic pressure which influences the plastic zone around the crack tip. Whatever the reason may be, it can be concluded that there is no unique relationship between the stress intensity rate and the critical stress intensity.

As the crack speed was not measured in the new experiments, the statement that the relation between the crack speed and the critical stress intensity is unique and independent of the specimen geometry {95} could not be confirmed. But an analysis of the slope of the test plot after crack initiation showed that a higher K_{Ic} was correlated to a steeper falling curve which means a faster crack speed.

Although the values for the critical stress intensity

obtained with CTS specimens are generally higher than those found with CT specimens, they are still within the range found in literature. The question remains why Richard {4,8} got a 30% higher value with the same specimen for the same material.

The first reason for this difference is that he used a much higher stress intensity rate. A second reason may be that Richard had curved crack fronts, as can be seen in figures 86 and 87 in {8}. The curved crack front is due to the higher frequency used for fatigue precracking and was found in earlier tests by Poulose too. The higher frequency causes a heating of the specimen which is probably responsible for the effect. As was found by Towers and Smith {114} in a numerical analysis of the CT specimen, a curved crack front which still meets ASTM E399 requirements can have an up to 28% higher fracture load than an equivalent straight crack front.

In summary it can be said that the critcal stress intensity of PMMA increases slightly with increasing stress intensity rate. For small variations of the stress intensity rate, the variation of the critical stress intensity is not outstanding of natural data scatter, but a change of $\dot{K}$ by a factor 2 or more is not neglegible.

3. Fracture Toughness under Mixed Mode Loading

Beside two specimens in mode I which were already

mentioned in the previous chapter, all specimens were loaded at a stress intensity rate of 1.0 MPa$\sqrt{m}$/s with a maximum deviation of 15%, as can be seen in table 17. The deviations are due to inaccurancy in the calculation of the displacement rate and scatter of the stiffness in different specimens.

Out of the 16 tested specimens, three (CTS1, CTS12, CTS13) had to be rejected. All of them showed the same effect: The crack growth started slowly at one side of the crack and moved up to 3 mm before the instability condition was reaohed. The fracture surface was slanted in thickness direction. In all cases, some geometrical deviations could be found. As two of the rejected specimens were tested under mode II loading, it seems that this condition is especially sensitive to deviations of the specimen geomety.

The fracture surface of all other specimens was smooth (mirror surface) and showed none or very little (< 0.5 mm) slow crack growth which then was neglected. The results of the mixed mode experiments are given in table 18.

K_{Ic} was calculated as the average of the results of specimens CTS2, CTS9, and CTS11 and had the value 1.26 MPa$\sqrt{m}$. The evaluation of K_{IIc} is a little vague. First of all, out of the 5 tested specimens 2 had to be rejected. The result of the remaining 3 is not that consistent either. The mean value of the two specimens with a/W = 0.5 is 1.39 MPa$\sqrt{m}$ which yields K_{IIc}/K_{Ic} = 1.10. Taking the specimen with a/W = 0.65 in account, the average of the three specimens is K_{IIc} =

1.35 MPa$\sqrt{m}$ which gives K_{IIc}/K_{Ic} =1.07. In any case, $K_{IIc}/K_{Ic} > 1$. This is much more than the values found in literature for PMMA. As already mentioned, most researchers found K_{IIc}/K_{Ic} to be around 0.9 (table 6). Only Phadke et al. {21} found K_{IIc}/K_{Ic} to be up to 1.0, depending on which mode II specimen they used for the evaluation of K_{IIc}. But the new results correlate well to results found for steels (table 3), aluminum alloys (table 4) and different other materials (table 5). For many materials K_{IIc}/K_{Ic} around 1.1 was found.

The reason for this discrepancy between the results for PMMA and other materials might be that most researchers neglected the influence of the stress intensity rate on the critical stress intensity of PMMA. Richard {4,8} found K_{IIc}/K_{Ic} = 0.93, but as pointed out ealier, his stress intensity rate for mode II was just about 30% of that for mode I. Assuming that the dependancy of the critical stress intensity on the stress intensity rate is the same for mode II as it is for mode I and also assuming that the dependancy can be described by a line in the semilog - plot figure 7, the stated value for K_{IIc} is about 7% too low. A correction for this would result in K_{IIc}/K_{Ic} of about 1.

A problem that could have influenced the new results is crack closure. Especially for a/W < 0.55, there is some negative stress intensity K_I for $\alpha = 90°$ (see figure 5 in {2} or figure 78 in {8}). This might have had an influence on the results with a/W = 0.5.

For a/W = 0.65 and $\alpha = 90°$, K_I is virtually zero. But as

the tested specimens had an extremely long fatigue crack (16.5 mm), even a very small negative K_I may influence the results. This is confirmed by Bäuerle {115} who made a new FEM analysis of the CTS specimen. Although he found for $\alpha = 90°$ K_I to be almost zero at the crack tip, K_I got increasingly negative along the crack flanks. As the surfaces of the fatigue crack are in touch with each other, they get pressed together due to the negative K_I, causing an unknown error in the results. The crack closure problem may be increased by the inevitable out of middle location of the crack tip. It is therefore felt that a mode II specimen should have a small amount of positive K_I to reduce crack closure and friction problems. This requirement is met by the modified CTS specimen {42,116} (see figure 8).

As can be seen in figure 9, the mixed mode fracture criterion

$$\frac{K_I}{K_{Ic}} + \left[\frac{K_{II}}{K_{IIc}}\right]^2 = 1$$

suggested by several authors {8,76,77} gives a good fit to the experimental results. This criterion can be transformed into {8}

$$K_v = \frac{1}{2}\left[K_I + \sqrt{K_I^2 + 4(\alpha_i K_{II})^2} \right]$$

where K_v is the comparative stress intensity factor and $\alpha_i = (K_{Ic}/K_{IIc})$. The safe - design condition is then

$$K_v \leq K_{Ic}$$

A look at table 2 reveals that just the criterion by

Irwin {61,62} and the J-integral {63-65} predict $f_c = 1$ and therefore promise to give a reasonable fit to the data. But as can be seen in figure 10, neither one provides a very good fit to the experimental data.

Another criterion of interest is the ASME Boiler and Vessel Code {79} because of its simplicity. As can be seen in figure 10, it gives a reasonable fit to the experimental data up to n = 0.5 ($\beta = 45°$). Beyond that, the predictions are not accurate, but at least they are on the safe side.

In a K_I/K_{Ic} - K_{II}/K_{Ic} plot, a vector

$$V = \frac{\sqrt{K_I^2 + K_{II}^2}}{K_{Ic}} = f(n)$$

is defined as the distance of a certain point to the origin of the coordinate system. This vector also can be used to describe the behavior of a material over the mixed mode ratio n. A fracture criterion $K_z = K_{Ic} f(n)$ with the safety condition $K_z < K_{Ic}$ can be evaluated. For the new experimental data, the function

$$f(n) = 1 + 2.934n - 15.70n^2 + 24.81n^3 - 11.97n^4$$

was found to give a reasonable fit , as can be seen in figure 11. Although this kind of plot seems very unusual, it has some advantages, especially that the fracture angle can be drawn in the same plot or at least with the same x - axis so that the relation between the critical stress intensity and the frature angle is better visible.

The angle of fracture initiation in mode II was found to be - 70°. This confirms the criteria by Erdogan and Sih {13}

and Nuismer {55}, while the other criteria make more or less different predictions. The measured fracture angle with the Erdogan and Sih criterion and the empirical criterion by Richard {8} are shown in figure 12. The measured fracture angles of beryllium ($\nu = 0.0$) {47} are given in the same figure. It is remarkable that they are very close to the new results despite the big difference in the Poisson ratio. It seems that the angle of fracture initiation is independent of the Poisson ratio.

VI Conclusions

1. The thickness of the CTS specimen should be symbolized by B and not by t, because t can easily be held for a symbol for the time. B is used to describe the thickness of the CT specimen {1}, the CS specimen {49-51}, and the new compact shear (NCS) specimen {117}, and there is no reason why this should be changed.

2. The testing of the specimens should be done in a way that the comparative stress intensity rate $\dot{K}_v$ is constant for all mixed mode conditions and not with a constant loading rate. To calculate $\dot{K}_v$, the criterion

$$\dot{K}_v = \frac{1}{2}\left[\dot{K}_I + \sqrt{\dot{K}_I^2 + 4\dot{K}_{II}^2}\right]$$

as a first approximation is sufficient. Even if it turns out that the implied assumption $K_{IIc} = K_{Ic}$ is not accurate, the difference in the stress intensity rate over the mixed mode range will be much less than with just taking a constant loading rate.

3. As there are some crack closure problems in pure mode II, the crack should be as short as possible. There should be set not only a lower limit for the crack length {8} but also an upper. In order to cut the length of the touching surfaces, it has to be considered whether a straight through notch should be used instead of a chevron notch. Maybe the original CTS specimen should be replaced at all by the modified CTS specimen {42} for mode II testing. The modified CTS specimen has a slightly positive K_I for $\alpha = 90°$ {116}.

4. More research is needed to find out the influences of deviations of the specimen geometry. It is not enough just to keep the machining tolerances, as the fatigue crack tends to grow away from the center line. Relatively small deviations already showed a significant effect.

5. Both the mechanical properties and the fracture toughness of PMMA are slightly sensitive to the loading rate. For changes of more than factor 2 in the loading rate, the deviations are not neglegible.

6. The fracture criterion

$$\frac{K_I}{K_{Ic}} + \left[\frac{K_{II}}{K_{IIc}}\right]^2 = 1$$

gives a good fit to the experimental found mixed mode fracture initiation.

7. The ASME Boiler and Vessel Code gives a reasonable fit to the experimental data up to a crack inclination of 45°. The predictions for steeper inclinations are not accurate but they are on the safe side.

8. The criterion of maximum tangential stress proposed by Erdogan and Sih gives the best fit to the experimentally found angle of fracture initiation. It seems that this angle is independent of the Poisson ratio.

Acknowledgement

This work was done at the George Washington University, Washington D.C., as part of a student exchange program between this school and the Staatliche Materialprufanstalt Stttgart, Federal Republic of Germany.

I want to thank

Dr. P.K. Poulose who was a very helpful advisor,

Dr.H. Liebowitz and Dr. C.M. Gilmore from the George Washington University as well as Dr. K. Kussmaul and Dr. H. Dietmann from the MPA Stuttgart who arranged the exchange program,

and finally the Deutscher Akademischer Austauschdienst that supported the program financially.

Washington D.C., May 1985

Roland Gesthes

References

1 ASTM E399-83, Plane - strain fracture toughness of metallic materials. The American Society for Testing and Materials (1983)

2 K. Benitz and H.A. Richard, Eine Bruchmechanikprobe und Belastungsvorrichtung zur Bestimmung von Risszähigkeiten bei überlagerter Normal- und Schubbeanspruchung. Z.Werkstofftechnik 12, 297-300 (1981)

3 H.A. Richard, Einleitung von überlagerter Normal- und Scherbeanspruchung in Bruchmechanikproben, 13. Sitzung des DVM Arbeitskreis "Bruchvorgänge", Hannover (1981)

4 H.A. Richard et al., Ein Beitrag zur experimentellen Überprüfung der Sprödbruchkriterien für überlagerte Normal- und Schubbeanspruchung von Rissen, 15. Sitzung des DVM Arbeitskreis "Bruchvorgänge", Darmstadt (1983)

5 H.A. Richard, Bruchvorgänge bei Mixed - Mode - Beanspruchung von Rissen. VDI - Berichte Nr. 480, 69-72 (1983)

6 H.A. Richard, Examination of brittle fracture criteria for overlapping mode I and mode II loading applied to cracks. AFMMS - Conference, Freiburg (1983)

7 H.A. Richard, Some theoretical and experimental aspects of mixed mode fractures. In: Advances in Fracture Research, Proc. ICF6, eds. S.R. Valluri et al., vol.5, 3337-3344, Pergamon Press (1984)

8 H.A. Richard, Bruchvorhersagen bei überlagerter Normal- und Schubbeanspruchung sowie reiner Schubbeanspruchung

von Rissen. Habilitationsschrift, Kaiserslautern (1984)

9 C.T. Shih, Small - scale yielding analysis of mixed mode plane - strain crack problems. ASTM STP 560, 187-210 (1974)

10 E.S. Folias, A finite line crack in a pressurized spherical shell. Int. J. Fract. Mech. 1, 1-8 (1965)

11 P.D. Ewing and J.G. Williams, The fracture of spherical shells under pressure and circular tubes with angled cracks in torsion. Int. J. Fracture 10, 537-544 (1974)

12 P. Jodin et al., Experimental and theoretical study of cracks in mixed mode conditions. Fracture and Fatigue, Proc. 3rd Colloquium on Fracture, ed. J.C. Radon, 349-358 (1980)

13 F. Erdogan and G.C. Sih, On the crack extension in plates under plane loading and transverse shear. J. Basic Engineering 85, 519-525 (1963)

14 L.P. Pook, The effect of crack angle on fracture toughness. Engng Fracture Mech. 3, 205-218 (1971)

15 J.G. Williams and P.D. Ewing, Fracture under complex stress - the angled crack problem. Int. J. Fract. Mech. 8, 441-446 (1972)

16 G.C. Sih, Some basic problems in fracture mechanics and new concepts. Engng Fracture Mech. 5, 365-377 (1973)

17 G.C. Sih, Strain - energy - density factor applied to mixed mode crack problems. Int. J. Fracture 10, 305-321 (1974)

18 R.C. Shah, Fracture under combined modes in 4340 steel.

ASTM STP 560, 29-52 (1974)

19 P. Jodin and G. Pluvinage, Validation expérimentale des critères de rupture en condition polymodale (mode I+II). Mécanique, Matériaux, Electricité 338, 101-112 (1978)

20 A.F.-C. Liu, Crack growth and failure of aluminum under in-plane shear. AIAA Journal 12, 180-185 (1975)

21 V.K. Phadke et al., Verification of Sih's hteory in a CS specimen. In: Fracture Mechanics and Technology, vol.2, 983-993, Sijthoff and Noordhoff, Aalphen aan den Rijn (1977)

22 K. Paleniswamy and W.G. Knauss, On the problem of crack extension in brittle solids under general loading. In: Mechanics Today, ed. S. Nemat-Nasser, Vol.4, 87-148, Pergamon Press, Oxford (1976)

23 W.K. Wilson, On combined mode fracture mechanics. Research Report 69-1E7-FMECH-R1, Westinghouse Research Lab. (1969)

24 Fracture 1977, Advances in Research on Strength and Fracture of Materials, ICF4, ed. D.M. Taplin, Pergamon Press, Oxford (1977)

25 Y. Ueda et al., Brittle fracture characteristics under biaxial loading. In: {24}, vol.2A, 173-182 (1977)

26 U. Seidelmann, U. Solesz and H. Kordisch, Determination of critical stress intensity factors under mixed mode loading conditions by shadow - optics. In: {24}, vol.3B, 621-626

27 H. Kordisch, Untersuchungen zum Verhalten von Rissen

unter überlagerter Normal- und Scherbeanspruchung. Dissertation Uni. Karlsruhe (1982); Abstract of this paper in: Schweissen Schneiden 36, 83-84 (1984)

28 P.G. Tracy et al., On the stastistical nature of fracture. Int. J. Fracture 18, 253-277 (1982)

29 F. Lemant and A. Pineau, Mixed mode fracture of a brittle orthotropic material - example of strongly textured zinc sheets. Engng Fracture Mech. 14, 91-105 (1981)

31 P.S. Theocaris et al., Experimental study of the T - criterion in ductile fractures. Engng Fracture Mech. 17, 439-447 (1983)

32 P.S. Theocaris, The fracure load and the initial angle of fracture in ductile materials. Materialprüf. 25, 185-190 (1983)

33 P.S. Theocaris. A higher - order approximation for the T - criterion of fracture in biaxial fields. Engng Fracture Mech. 19, 975-991 (1984)

34 H.C. Wu et al., Experimental investigation of the angled elliptic notch problem in tension. ASME J. Appl. Mech. 44, 455-461 (1977)

35 H.C. Wu and K.J. Chang, Angled elliptic notch problem in compression and tension. ASME J. Appl. Mech. 45, 258-262 (1978)

36 D.G. Smith and C.W. Smith, Photoelastic determination of mixed mode stress intensity factors. Engng Fracture Mech. 4, 357-366 (1972)

37 P.D. Ewing et al., Further results on the angled crack

problem. Int. J. Fracture 12, 85-93 (1976)

38 M.A. Hussain et al., Strain energy release rate for a crack under combined mode I and mode II. ASTM STP 560, 1-28 (1974)

39 Chiu and A.F. Liu, Mixed mode fracture of shear panels - a finite element analysis. ASTM STP 590, 263-280 (1976)

40 J.C. Radon et al., Fracture toughness of PMMA under biaxial stress, In {24}, vol. 3B, 1113-1118 (1977)

41 P.S. Leevers et al., Crack growth in plastic panels under biaxial stress. Polymer 17, 627-632 (1976)

42 H.A. Richard et al., Kritische Bewertung von Proben zur Bestimmung der Risszähigkeit K_{Ic}. 16. Sitzung des DVM - Arbeitskreis "Bruchvorgänge", Karlsruhe (1984)

43 W.T. Chiang and K.J. Miller, Fracture behavior and stress fields of cracked bend specimens subjected to mixed mode loading. Engng Fracture Mech. 18, 621-632 (1984)

44 K.R. Raju, On the sliding mode stress intensity factors for a three - point bend K2 specimen and mode II fracture toughness. Int. J. Fracture 17, R193-R197 (1981)

45 C. Atkinson et al., Combined mode fracture via the cracked Brazilian disk test. Int. J. Fracture 18, 279-291 (1982)

46 H. Awaji and S. Sato, Combined mode fracture toughness by the disk test. J. Engng Materials and Technology 100, 175-182 (1978)

47 I. Finnie and H.D. Weiss, Some observations on Sih's strain energy density approach for fracture prediction.

Int. J. Fracture 10, 136-137 (1974)

48 L. Banks-Sills et al., A mixed mode fracture specimen for mode II dominant deformation. Engng Fracture Mech. 20, 145-157 (1984)

49 D.B. Chrisholm and D.L. Jones, An analytical and experimental stress analysis of a practical mode II fracture test specimen. Experimental Mech. 17, 7-13 (1977)

50 R.A. Riddle, The application of the J - integral to fracture under mixed mode loading. Ph.D. Thesis, University of California, Berkeley (1981)

51 R.A. Riddle et al., An evaluation of the compact shear specimen for mixed mode fracture studies. J. Engng Materials and Technology 105, 268-272 (1983)

52 T.W. Elenz, Master's Thesis, George Washington University, Washinton D.C. (1985)

53 P.C: Paris and G.C. Sih, Stress analysis of cracks. ASTM STP 381, p.30 (1965)

54 L. Banks-Sills and M. Arcan, An edge - cracked mode II fracture specimen. Experimental Mech. 23, 257-261 (1983)

55 R.J. Nuismer, An energy release rate criterion for mixed mode fracture. Int. J. Fracture 11, 245-250 (1975)

56 M. Amestoy et al., Analytic asymptotic solution of the kinked crack problem. In: Advances in Fracture Research, ed. D. Francois, vol.1, 107-113, Pergamon Press, Oxford (1981)

57 D. Radaj and M. Heib, Numerische Untersuchungen zum

Rissbruchkriterium bei überlagerter Zug-, Druck- und Schubbeanspruchung. Schweissen Schneiden 29, 135-139 (1977)

58 D. Radaj and M. Heib, Energy density fracture criteria for cracks under mixed mode loading. Materialprüf. 20, 256-282 (1978)

59 G.C. Sih, A special theory of crack propagation. Mechanics of Fracture, vol.1, pp XXI-XLV, Leyde (1973)

60 G. Di Leonardo, Fracture toughness characterization of materials under multiaxial loading. Int. J. Fracture 15, 537-552 (1979)

61 G.R. Irwin, Analysis of stresses and strains near the end of a crack transversing a plate. ASME J. Appl. Mech. 24, 361-364 (1957)

62 G.R. Irwin, Fracture. In: Handbuch der Physik, ed. S. Flügge, vol.6, 551-590, Berlin (1958)

63 B.-Y. Yu, A discussion on mixed mode J - integral fracture criterion. Engng Fracture Mech. 16, 156 (1982)

64 H. Ishikawa et al., J - integral of a mixed mode crack and its application. 3rd Int. Conf. on Materials, vol.3, 447-455, Lambridge, England (1979)

65 H.D. Bui, Associated path independent J - integrals for seperating mixed modes. J. Mech. Phys. Solids 31, 439-448 (1983)

66 N.B. Romalis, Local fracture criterion in the case of nonsymmetric external loading. Soviet Applied Mechanics 15, 1227-1230 (1979)

67 M.L. Williams, On the stress distribution at the base of a stationary crack. ASME J. Appl. Mech. 24, 109-114 (1957)

68 B. Cotterell, Notes on the paths and stability of cracks. Int. J. Fract. Mech. 2, 526-533 (1966)

69 J. Eftis, N. Subromanian, and H. Liebowitz, Crack border stress and displacement equations revisited. Engng Fracture Mech. 9, 189-210 (1977)

70 J. Eftis and N. Subromanian, Biaxial load effects on the crack border elastic strain energy and strain energy rate. Engng Fracture Mech. 9, 753-764 (1977)

71 G.H. Lindsey, Some observations on the fracture under combined loading. ASTM STP 536, 22-31 (1973)

72 J.L. Swedlow, Criteria for growth af t.e angled crack. ASTM STP 601, 506-521 (1976)

73 A.P. Kfouri and K.J. Miller, Crack seperation energy rates for inclined cracks in an elastic - plastic material. In: Three Dimensional Relations and Ductile Fracture, ed. S. Nemat-Nasser, pp 83-109, North Holland, Amsterdam (1981)

74 P.S. Theocaris, Mises elastic - plastic boundary as the core region in fracture criteria. Engng Fracture Mech. 16, 425-432 (1982)

75 R.H. Leicester, Proceedings, Conference Australian Fracture Group 23, pp 156-164, Melbourne, Australia (1974)

76 E.M. Wu, Application of fracture mechanics to anisotropic

plates. ASME J. Appl. Mech. 34, 967-974 (1967)

77 K.Y. Lee and S.H. Advani, Fracture criteria and stress intensity factors including the effect of crack closure. Engng Fracture Mech. 16, 257-264 (1982)

78 A.A. Griffith, Theory of rupture. Proc. 1st Int. Congress Appl. Mech., pp 53-63 (1924)

79 ASME Boiler and Vessel Code, Section XI (1980)

80 DVS - Merkblatt: Bruchmechanische Bewertung von Fehlern in Schweissverbindungen. DVS 2401 (1981)

81 H.P. Rossmanith and M. Tiefenböck, Über Sicherheitsabschätzungen bei der bruchmechanischen Fehlerbewertung für biaxiale Beanspruchung. Materialprüf. 25,181-186 (1983)

82 P. Gilles, ONERA communication (Dec. 1977)

83 S.K. Maiti and R.A. Smith, Comparison of the criteria for mixed mode brittle fracture based on the preinstability stress - strain field. Part I: Slit and elliptical cracks under uniaxial tensile loading. Int. J. Fracture 23, 281-295 (1983)

84 S.K. Maiti and R.A. Smith, ...Part II: Pure shear and uniaxial compressive loading. Int. J. Fracture 24, 5-22 (1984)

85 S.K. Maiti and R.A. Smith, Criteria for brittle fracture in biaxial tension. Engng Fracture Mech. 19, 793-804 (1984)

86 Boeing Aerospace Co., Seattle Wash., Data according to [18]

87 H. Dubbel, Taschenbuch des Maschinenbaus, 14. Auflage, Springer, Berlin (1981)

88 Modern Plastics Encyclopedia 1981-82, McGraw Hill, New York (1981)

89 L. Mascia, Engineering interpretation of mechanical failures. In: Thremoplastics: Materials Engineering, 181-269, Applied Science Publishers LTD, London (1982)

90 M. Buhelt, Sources of error by strain gage measurement of models made of plexiglas. Statens Byggeforskningsinstitut, København (1971)

91 B.W. Preece and J.D. Daries, Models for structural concrete. London (1964)

92 C. Zimmermann et al., Dynamic energy release rate and fracture heat in PMMA and a high - stregth steel. Engng Fracture Mech. 20, 777-782 (1984)

93 H.H. Kausch, Bruchverhalten, Bauteilgestaltung und Zuverlässigkeit von Kunststoffwerkstoffen. Materialprüf. 20, 22-26 (1978)

94 P.S. Leevers et al., Fatigue crack growth in PMMA and rigid PVC under biaxial stress. Engng Fracture Mech. 11, 487-498 (1979)

95 J.G. Williams, Visco - elastic and thermal effects on crack growth in PMMA. Int J. Fract. Mech. 8, 393-401 (1972)

96 R.P. Kambour, Mechanism of fracture in glassy polymers II: Survey of crazing response during crack propagation in several polymers. J. Polymer Sci., Part A-2, 4, 17-24

(1966)

97 R.P. Kambour, Mechanism af fracture in glassy polymers III: Direct observation of the craze ahead of the propagating crack in PMMA and Polystyrene. J. Polymer Sci., Part A-4, 4, 349-358 (1966)

98 R.P. Kambour, Stress - strain behavior of the craze. Polymer Engng Sci. 8, 281-289 (1968)

99 A.S. Argon et al., Initiation and growth of crazes in glassy polymers. In: {24}, vol.1, 445-470 (1977)

100 Y.W. Mai, Quasi - static cracking of PMMA in hostile environments. Int. J. Fracture 10, 288-291 (1974)

101 B. Cotterell, Fracture propagation in organic glasses. Int. J. Fract. Mech. 4, 209-218 (1968)

102 G.P. Marshall et al., Crack and craze propagation in polymers: A fracture mechanics approach. Plastics and Polymers, pp 75-81 (1969)

103 G.P. Marshall and J.G. Williams, Correlation of fracture data for PMMA. J. Mat. Sci.8, 138-140 (1973)

104 F.A. Johnson and C.G. Radon, Fracture process and molecular kinetics of PMMA. J. Polymer Sci. 11, 1995-2020 (1973)

105 W. Döll, Wissenschaftlicher Bericht 4/74, Institut für Festkörpermechanik, Freiburg (1974)

106 V.V. Panasyuk et al., Propagation of an arbitrarily oriented rectilinear crack during extension of a plate. NASA Technical Translation TTF-402 from Prikladnaya Mekhanika 1, no.2 (1965)

107 Y. Matsuo, Probalistic analysis of the brittle fracture loci under biaxial stress state. Bull JSME 24, 290-294 (1981)

108 Y. Matsuo, On the relative coefficients of the multiaxial probabitility distribution function for fracture. Bull JSME 24, 495-500 (1981)

109 K. Watanabe and H. Shiomi, Extension of crack energy density concept of arbitrary direction and energy release rate to non - self - similar crack growth. Bull JSME 27, 1077-1084 (1984)

110 H. Gao et al., An investigation on the brittle fracture of $K_I - K_{II}$ combined mode cracks. Acta Metallurgica Sinica 15, 380-391 (1979)

111 K.-C. Hwang and S.-W. Yu, On the maximum energy release rate fracture criterion for combined mode I-II-III cracks. Acta Mechanica Solida Sinica, pp 313-321 (1983)

112 Li Hao, ed., A selection of Chinese articles and abstracts. Engng Fracture Mech. 16, 1-156 (1982)

113 McHenry and I. Harry, Report on the ICF International Symposium on Fracture Mechanics: Beijing, Peoples Republic of China. Int. J. Fracture 26, R3-R9 (1984)

114 O.L. Towers and A.P. Smith, Stress intensity factors for curved crack fronts in compact tension specimens. Int. J. Fracture 25, R43-R48 (1984)

115 P. Bäuerle, Thesis, George Washington University, Washington D.C. (1985)

116 H.A. Richard, private communication (Feb 1985)

117 H.A. Richard, New compact shear specimen. Int. J. Fracture 17, R105-R107 (1981)

β	$m=\frac{K_{II}}{K_I}$	$n=\frac{K_{II}}{K_I+K_{II}}$	
90°	0.0	0.0	mode I
75°	0.268	0.211	
60°	0.577	0.366	
45°	1.0	0.500	mixed mode
30°	1.732	0.634	
15°	3.732	0.789	
0°	∞	1.0	mode II

Table 1 Relation between β, m, and n

	Poisson ratio	$\frac{K_{IIc}}{K_{Ic}}$	mode II - θ
Erdogan and Sih [13]	i	0.87	70.5°
Nuismer [55]	i	0.87	70.5°
Hussain et al. [38]	i	0.63	75.2°
Ametoy et al. [56]	i	0.81	77°
Radaj and Heib [57,58]	i	1.32	99°
Sih [16,17,59]	0.36	0.85	84.6°
Di Leonardo [60]	0.36	0.85	-
Irwin [61,62]	i	1.00	-
J - integral [63-65]	i	1.00	0°

legend: i = independent

\- = no prediction

Table 2 Prediction of different fracture criteria for mode II

1	2 Material	3 Spec	4 T[°C]	5 n_{min}	5 n_{max}	6 A	7 K_{Ic}	8 K_{IIc}	9 $\frac{K_{IIc}}{K_{Ic}}$
Ueda [25]	M SM41	ACNT	RT	0	0.5	12*	-	-	-
	M SM41	CNBT	RT	0	0.5	8*	-	-	-
Shah [18]	H 4340	CCT	RT	0		2	80.4	-	1.1[1]
	H 4340	Tube	RT	1		2	-	88.3	
	H 4340	ACCT	-140	0	0.79	8	45.7	49.7	1.1[1]
Pluvinage [19]	H 18MnMoV	ACCT	RT	0.46	0.63	3	-	-	-
Chiang [43]	H GC-4	SECB	RT	0	0.66	8	49.6	-	-
Theocaris [33]	S -	ACNT	RT	0	0.92	110	-	-	-

1) doubtful method of determining K_{IIc}

Table 3 Mixed mode results for several steels

Legend to tables 3 to 5

column 2 M = mild steel

H = high strength steel

S = spring steel

column 3 specimens, see chapter III 1.

column 4 RT = room temperature

column 6 A = number of the tested specimens

column 7 + 8 values in $MPa\sqrt{m}$

* = value found in a figure

- = not stated in the paper

1	2	3	4	5		6	7	8	9
	Material	Spec	T[°C]	n_{min}	n_{max}	A	K_{Ic}	K_{IIc}	$\frac{K_{IIc}}{K_{Ic}}$
Tracy [28]	7075T6	ACCT	RT	0	0.63	122	-	-	-
Boeing [86]	7075T651	ACCT	-	0	0.6	4	70.0	70.0	1.0
Liu [20]	7075T7651	1)	RT	0	1	4	75.5	89.2	1.2[2]
	2024T3	1)	RT	0	1	3	74.2	74.7	1.0[3]
Jodin [12]	2024		-	-	-	5	-	-	-
Wilson [23]	7178T651	ACCT	-	0	0.8*	14*	-	-	-
Pook [14]	DTD5050	ACNT	-	0	0.63	11	31.5	-	-
Pluvinage [19]	AU4G	ACCT	RT	0	0.85	10	-	-	-
Theocaris [33]	57S	ACNT	RT	0	0.92	110	-	-	-

1) shear panel
2) with a CCT specimen, $K_{Ic} = 89.2$ and $K_{IIc}/K_{Ic} = 1.0$
3) with a CCT specimen, $K_{Ic} = 99.4$ and $K_{IIc}/K_{Ic} = 0.75$

legend see table 3

Table 4 Mixed mode results for several aluminum alloys

1	2	3	4	5		6	7	8	9
	Material	Spec	T[°C]	n_{min}	n_{max}	A	K_{Ic}	K_{IIc}	$\frac{K_{IIc}}{K_{Ic}}$
Kordisch [27]	Glass	ACCT	-	0	0.92[1]	13[1]	-	-	-
	PU	ACCT	-	0	0.85[1]	28[1]	-	-	-
Richard [4]	Araldit B	CTS	RT	0	1	20	0.59	1.46	2.48
Theocaris [31]	PCBA	ACNT	RT	0	0.92	110	7.0[1]	-	-
Theocaris [33]	Bronze[2]	ACNT	RT	0	0.92	300	-	-	-
Lemant [29]	Zinc	ACCT	-196	0	0.63	8	-	-	-
Awaji and Sato [46]	G[3] SA24 //	BD	RT	0	1	13	0.72	0.83	1.15
	G SA24	BD	RT	0	1	9	0.69	0.76	1.11
	G 7477	BD	RT	0	1	19	0.94	1.09	1.16
	G SM1-24	BD	RT	0	1	7	0.81	0.89	1.09
	Plaster	BD	RT	0	1	7	0.13	0.15	1.14
	Marble	BD	RT	0	1	10	0.93	1.05	1.13

1) calculated from given data
2) three different types of bronze
3) G = graphite

legend see table 3

Table 5 Mixed mode results for various materials

1 Reference	2 Spec	3 B	4	5 d	6	7 n_{min}	7 n_{max}	8 A	9 K_{Ic}	10 K_{IIc}	11 $\frac{K_{Ic}}{K_{IIc}}$
Richard [4]	CTS	20 30	F	[1]	N	0	1	44	1.64	1.52	0.93
Ewing [11]	[2]	-	R	[3]	-	-	-	50	1.80	-	-
	Tube	6.3	-	[4]	N	0	1	38*	1.12	1.0*	0.89
Erdogan	ACCT	3.0	-	-	P	0	0.73	45*	0.92	-	0.89
& Sih [13]	IPS	3.0	-	[5]	-	1		9	-	0.82	
Williams [15]	ACCT	3.2	R	5.0	Y	0	0.98*	150[6]	1.37	-	-
Phadke [21]	CT	5.0 2.8[7]	N	0.2	N	0		15	0.99	-	0.90
	CS	5.0 2.8	N	0.2	N	1		13	-	0.90	
	CS[8]	5.0	N	0.2	N	1		4	-	0.67[9]	
	IPS	2.8	N	0.2	N	1		4	-	0.99	1.0
	ACNT	2.5 3.5	N	0.4	N	0	0.54	9	0.98	-	
Ueda [25]	ACNT	4	N	-	-	0	0.85	24	-	-	-
	CNBT	4	N	-	-	0	0.85	18	-	-	-
Seidelmann [26]	ACCT	3.0	F	0.1	[3]	0	0.73	45*	1.46	-	-
Kordisch [27]	ACCT	-	-	-	-	0	0.98*	117*	-	-	0.9*
Theocaris [33]	ACNT	1.5	N	-	-	0	0.92	110	-	-	-
Wu [34]	ACNT	3.2	N	1.3	N	0	0.98*	60	-	-	-
Ewing [37]	SAECT	3.0	R	5	-	-	-	10	-	-	-
	SEC4B	6.0	R	5	-	-	-	10	-	-	-
Radon [40]	CCBT	4.0	R	[10]	Y	0		23[11]	1.51	-	-
Leevers [41]	CCBT	-	-	-	Y	0		4	1.87	-	-
Raju [44]	DEC3B	-	-	-	-	1		2	-	1.36	-

Table 6 Mixed mode fracture data for PMMA stated in literature

Footnotes to table 6

1) load control $\dot{F} = 4$kN/s
2) spherical shells ⌀ 178 - 270 mm under water pressure
3) constant time of loading 15 s
4) constant time of loading 75 s
5) loaded by running water
6) only 47 specimens evaluated for K_I, K_{II} because of preinstability crack growth
7) in table 1 of that paper, B = 3mm is stated
8) the ligament in front of the crack tip was reduced to 2.5 mm. The results are probably not valid because of the uncertain state of stress at the crack tip and possible residual stresses due to grinding.
9) slow crack growth only in mode I .
10) constant stress intensity rate $\dot{K} = 0.2$ MPa$\sqrt{m}$/s
11) 6 specimens at $p_x/p_y = 0$, 17 at $p_x/p_y > 0$

Legend to table 6

column 3 B = thickness of the specimen in [mm]

column 4 introducing of the crack
F = fatigue precracking
R = razor blade forced into the notch
N = machined notch

column 5 $\dot{d}$ = displacement rate in $\left[\frac{mm}{min}\right]$

column 6 did preinstability crack growtth occur?
N = no, Y = yes, P = in some specimens

column 8 A = number of the tested specimens
* = value found in a figure
- = not stated in the paper

Reference	E [GPa]	ν	σ_{ult} [MPa]	$\sigma_{0.2}$ [MPa]	t [s]	$\dot{e}$
Dubbel [87]	2.7 - 3.7	-	50 - 77	-	-	-
Encyclopedia [88]	2.6 - 3.1	0.35	48 - 76	-	-	-
Mascia [89]	3.12	0.33	-	-	100	-
Ewing [11]	-	0.35	-	-	-	-
Richard [4]	-	0.30	-	-	-	-
Richard [7]	-	0.36	-	-	-	-
Ewing [37]	2.0	0.43	-	-	-	-
Buhelt [90]	3.41	0.33	-	-	180	-
Preece [91]	-	0.35-0.37	-	-	-	-
Zimmermann [92]	5.0	0.35	-	-	-	high
Kausch [93]	3.3	-	65	-	-	-
Leevers [94]	2.9	-	80	-	-	-
Rohm & Haas	2.90	0.35	72	-	-	-
Theocaris [33]	3.4	0.34	72.9	64.3	-	-

Table 7 Mechanical properties of PMMA stated in literature

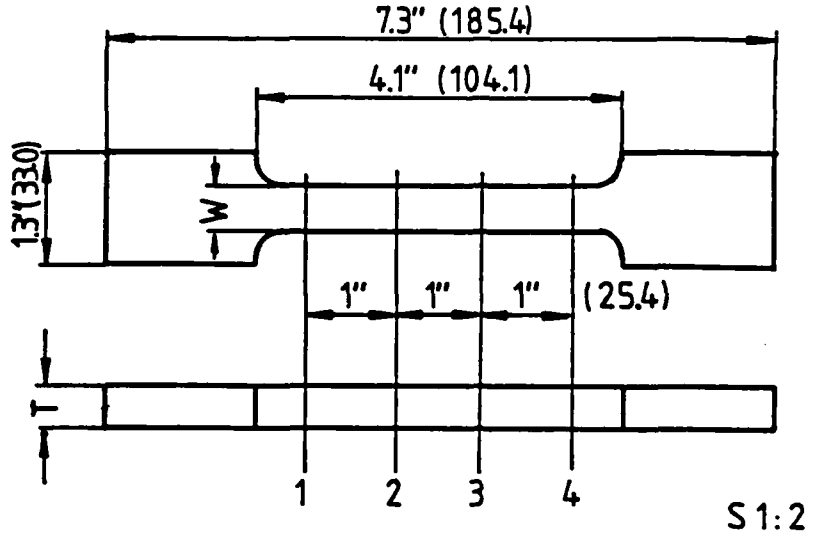

Spec	width [mm]				thickness [mm]			
	1	2	3	4	1	2	3	4
T1	12.5	12.6	12.6	12.7	12.0	12.0	12.1	12.2
T2	12.5	12.6	12.5	12.7	12.1	12.1	12.0	11.9
T3	12.7	12.8	12.9	13.0	12.1	12.1	12.0	11.9
T4	12.4	12.4	12.5	12.5	12.2	12.1	12.1	12.0

Table 8 Dimensions of the tensile specimens

Spec	$\dot{d}$ $\left[\frac{mm}{min}\right]$	$\dot{e}$ $\left[\frac{\%}{min}\right]$	location of fracture
T1	0.38	0.3	at 4
T2	0.76	0.6	at 4
T3	3.0	2.4	between 2 and 3
T4	1.5	1.2	between 3 and 4

Table 9 Testing conditions for the tensile specimens

Spec	W [mm]	a [mm]	a/W	B [mm]
CT1	50.8 (2.0")	28.2	0.555	12.0
CT2		25.1	0.495	11.7
CT3		24.9	0.490	11.7
CT4		25.4	0.500	11.7
CT5		25.1	0.495	11.7
CT6		31.0	0.610	11.7

Table 10 Dimensions of the CT specimens

α	$\frac{\dot{d}}{\dot{d}_0}$	$\frac{\dot{P}}{\dot{P}_0}$	a/W = 0.5 $\frac{\dot{K}}{\dot{K}_0}$	a/W = 0.7 $\frac{\dot{K}}{\dot{K}_0}$
0°	1.0	1.0	1.0	1.0
15°	1.0	0.96	0.94	0.93
30°	1.0	0.78	0.71	0.69
45°	1.0	0.67	0.56	0.51
60°	1.0	0.56	0.40	0.34
75°	1.0	0.56	0.33	0.24
90°	1.0	0.59	0.29	0.17

Table 11 Relation between $\dot{d}$, $\dot{P}$, and $\dot{K}$ for a constant displacement rate $\dot{d}$

α	$\frac{\dot{d}}{\dot{d}_0}$	$\frac{\dot{F}}{\dot{F}_0}$	a/W = 0.5	a/W = 0.7
			$\frac{\dot{K}}{\dot{K}_0}$	$\frac{\dot{K}}{\dot{K}_0}$
0°	1.0	1.0	1.0	1.0
15°	1.04	1.0	0.98	0.97
30°	1.30	1.0	0.92	0.89
45°	1.49	1.0	0.83	0.76
60°	1.79	1.0	0.72	0.60
75°	1.79	1.0	0.60	0.43
90°	1.68	1.0	0.49	0.28

Table 12 Relation between $\dot{d}$, $\dot{F}$, and $\dot{K}$ for a constant loading rate $\dot{F}$

α	$\frac{\dot{K}}{\dot{K}_0}$	a/W = 0.5		a/W = 0.7	
		$\frac{\dot{F}}{\dot{F}_0}$	$\frac{\dot{d}}{\dot{d}_0}$	$\frac{\dot{F}}{\dot{F}_0}$	$\frac{\dot{d}}{\dot{d}_0}$
0°	1.0	1.0	1.0	1.0	1.0
15°	1.0	1.02	1.06	1.03	1.07
30°	1.0	1.09	1.41	1.12	1.46
45°	1.0	1.20	1.78	1.32	1.96
60°	1.0	1.39	2.50	1.67	2.94
75°	1.0	1.67	2.99	2.33	4.18
90°	1.0	2.04	3.45	3.57	5.88

Table 13 Relation between $\dot{d}$, $\dot{F}$, and $\dot{K}$ for a constant stress intensity rate $\dot{K}$

E [GPa]	ν	σ_{ult} [MPa]	$\sigma_{0.2}$ [MPa]	time [s]	$\dot{e}$ $\left[\frac{\%}{min}\right]$
3.27	0.37	75	57	18	2.4
3.15	-	69	55	35	1.2
3.03	-	69	56	70	0.6
2.94	0.36	58	51	140	0.3

Table 14 Mechanical properties of PMMA

Spec.	$\dot{d}$ $\left[\frac{mm}{min}\right]$	$\dot{K}$ $\left[\frac{MPa\sqrt{m}}{s}\right]$	F_c [N]	K_{Ic} [$MPa\sqrt{m}$]
CT1	5.1	0.32	244	1.04
CT2	5.1	0.33	290	1.05
CT3	10.2	0.71	315	1.13
CT4	15.3	1.09	316	1.16
CT5	30.5	2.15	317	1.15
CT6	63.5	3.78	232	1.25

Table 15 Testing conditions and results for the CT specimens (mode I)

Spec.	$\dot{d}$ $\left[\frac{mm}{min}\right]$	$\dot{K}$ $\left[\frac{MPa\sqrt{m}}{s}\right]$	F_c [kN]	K_{Ic} [$MPa\sqrt{m}$]
CTS7	2.5	0.23	1.01	1.12
CTS9	10.9	0.96	1.12	1.23
CTS2	10.9	1.00	1.19	1.29
CTS11	12.7	1.25	1.17	1.27

Table 16 Testing conditions and results for the CTS specimens (mode I)

α	Spec.	$\frac{a}{W}$	B [mm]	$\dot{d}$ $\left[\frac{mm}{min}\right]$	$\dot{K}_V$ $\left[\frac{MPa\sqrt{m}}{s}\right]$
0°	CTS9	0.5	11.8	10.9	0.96
	CTS2	0.5	11.9	10.9	1.00
	CTS11	0.5	12.0	12.7	1.25
15°	CTS12	0.5	11.6	11.9	1.01
30°	CTS14	0.5	12.0	15.2	1.10
	CTS5	0.55	12.2	15.2	1.16
45°	CTS10	0.5	11.7	19.5	1.03
60°	CTS4	0.5	11.7	25.4	0.97
75°	CTS8	0.5	12.4	29.3	0.92
	CTS6	0.5	12.6	29.3	0.88
90°	CTS15	0.5	12.2	38.1	1.09
	CTS3	0.5	11.6	38.1	1.09
	CTS1	0.55	11.7	38.1	1.09
	CTS16	0.65	12.3	34.6	0.99
	CTS13	0.65	11.8	34.6	1.04

Table 17 Testing conditions for the CTS specimens

(mixed mode)

α	Spec.	F_c [kN]	K_I [MPa$\sqrt{m}$]	K_{II} [MPa$\sqrt{m}$]	$-\theta$
0°	CTS9	1.12	1.23	0	0°
	CTS2	1.19	1.29	0	0°
	CTS11	1.17	1.27	0	0°
15°	CTS12	invalid			
30°	CTS14	1.52	1.38	0.39	30°
	CTS5	1.22	1.37	0.34	32°
45°	CTS10	1.52	1.14	0.57	34°
60°	CTS4	1.60	0.85	0.76	49°
75°	CTS8	2.20	0.53	1.10	56°
	CTS6	2.28	0.53	1.09	65°
90°	CTS15	2.67	(-0.06)	1.37	71°
	CTS3	2.60	(-0.08)	1.42	69°
	CTS1	invalid			
	CTS16	1.76	0	1.25	70°
	CTS13	invalid			

Table 18 Results for the CTS specimens (mixed mode)

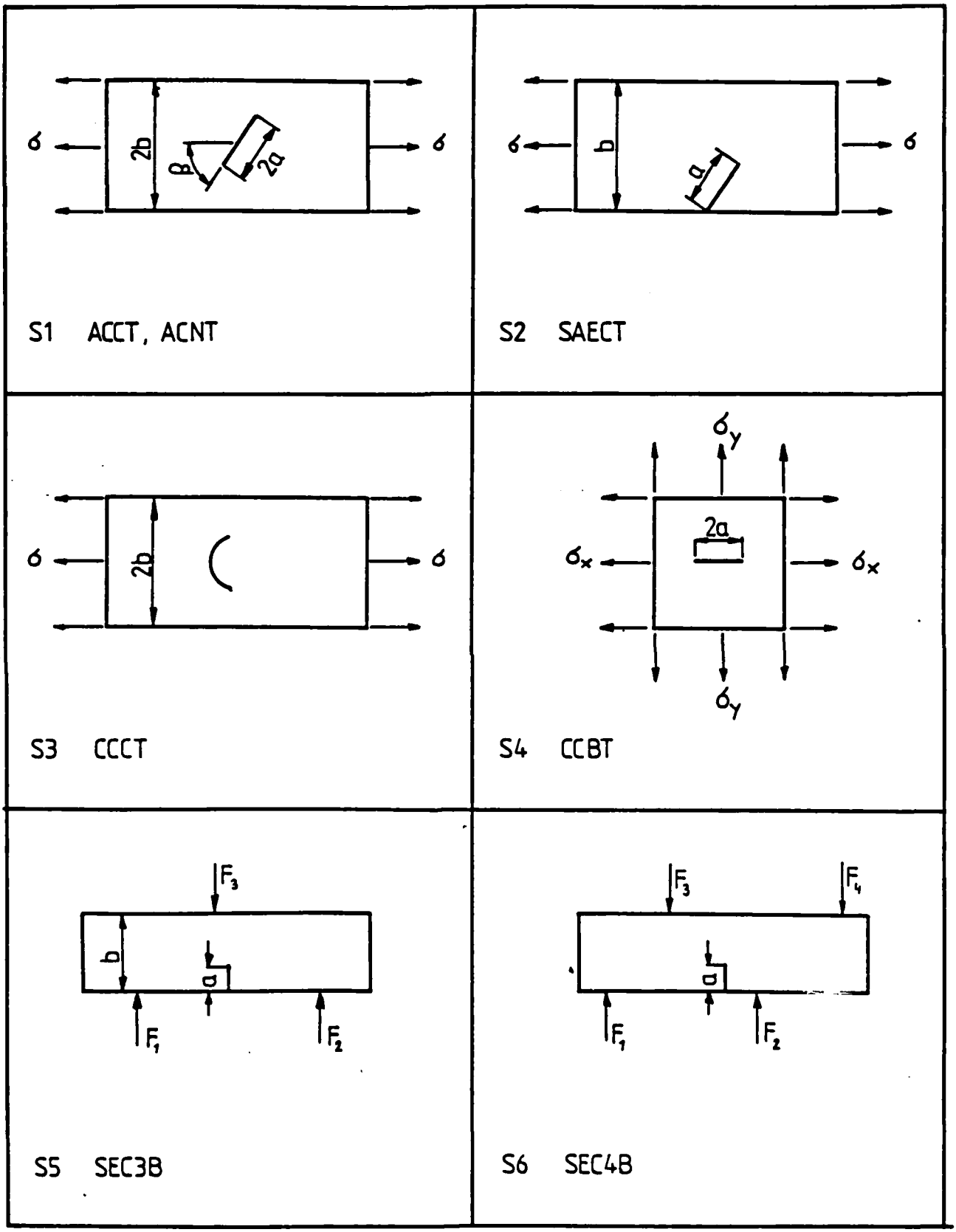

Figure 1 Mixed mode specimens

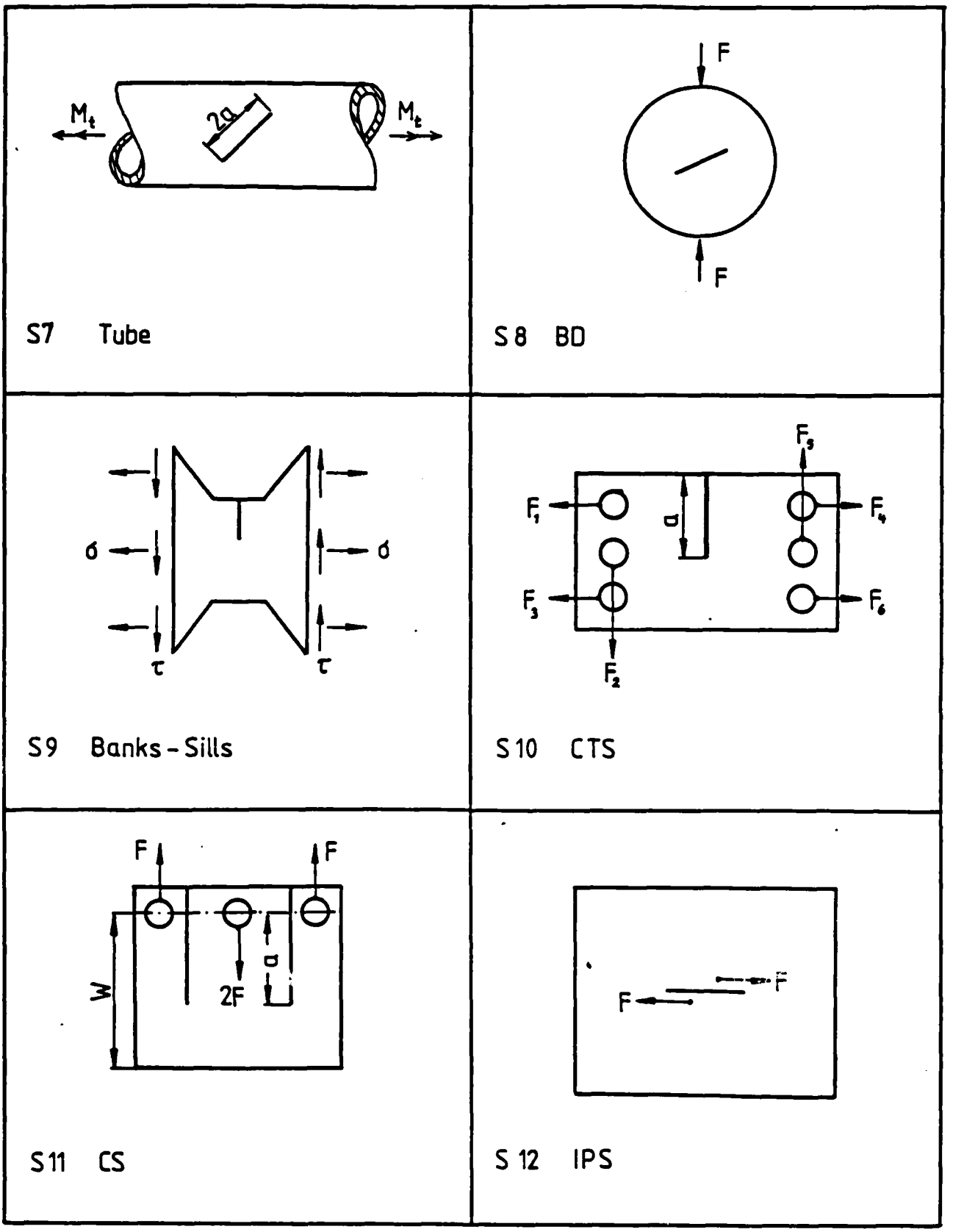

Figure 1 continued Mixed mode specimens

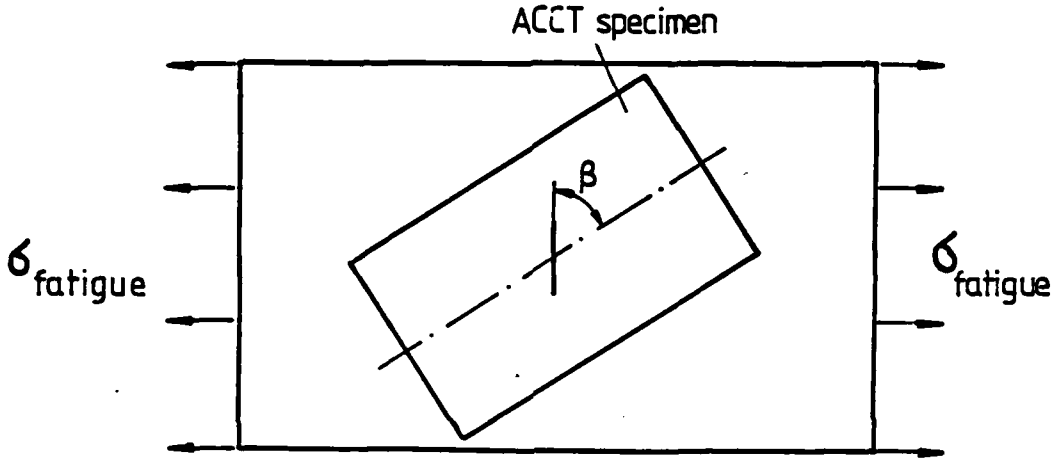

Figure 2 Production of a ACCT specimen

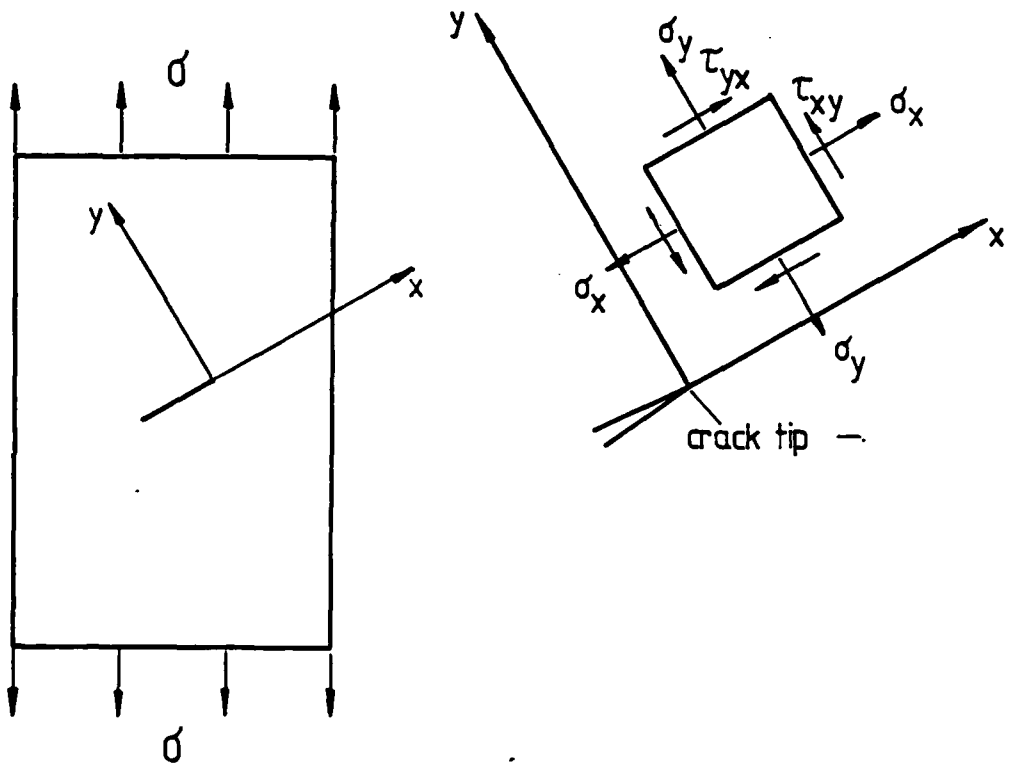

Figure 3 Stresses around the crack tip

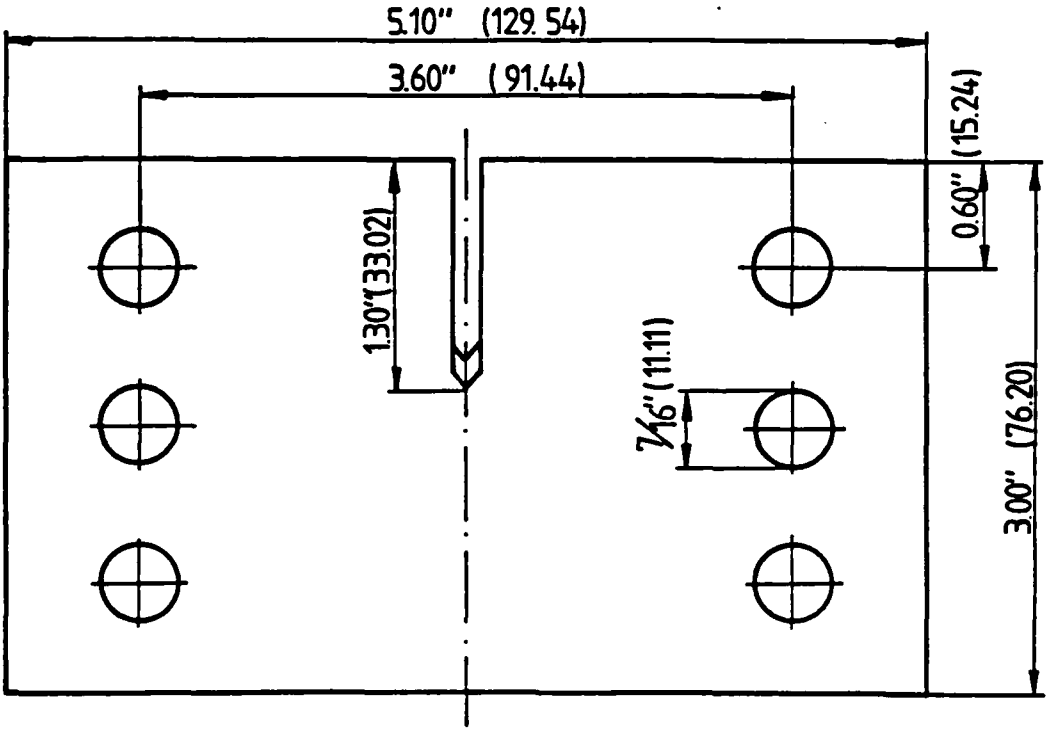

S 1:1

all values in parentheses are in millimeter

Figure 4 CTS specimen with W = 3.0" (76.2mm)

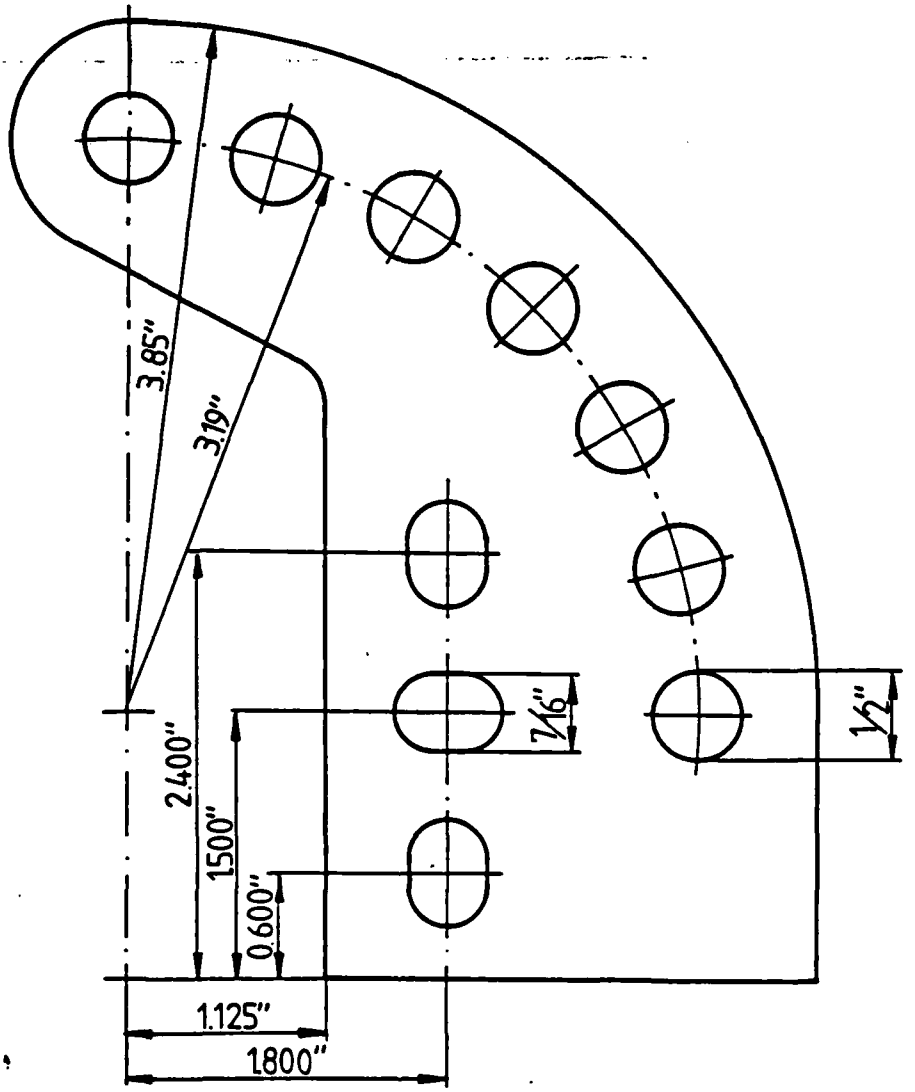

W = 3.00" S 1:1

Figure 5 Grip for the CTS specimen, modified for US customary units

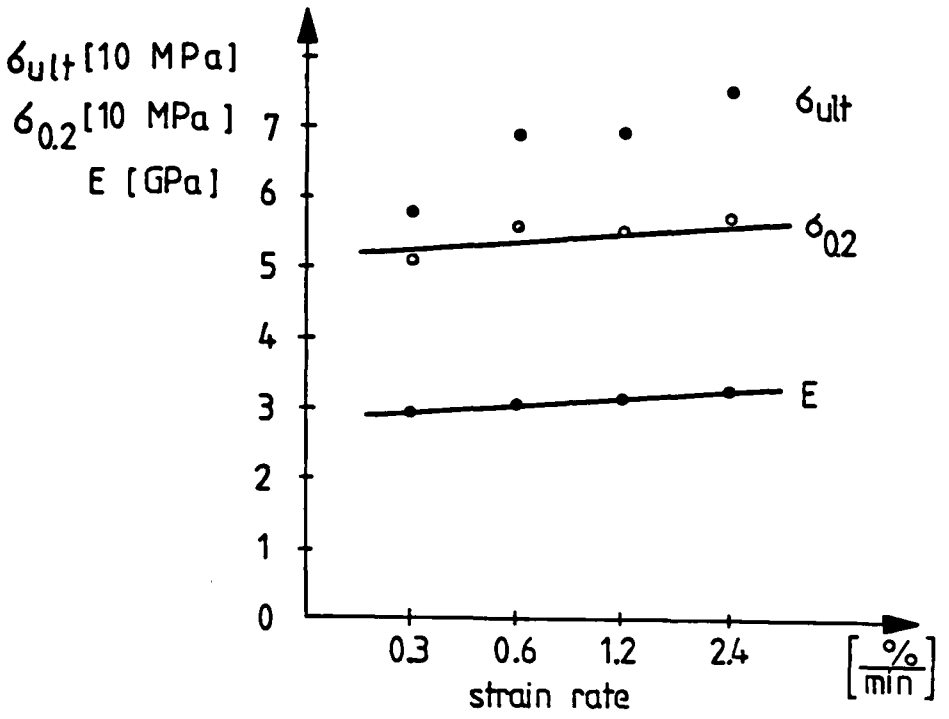

Figure 6 Behavior of σ_{ult}, $\sigma_{0.2}$, and E for increasing strain rate

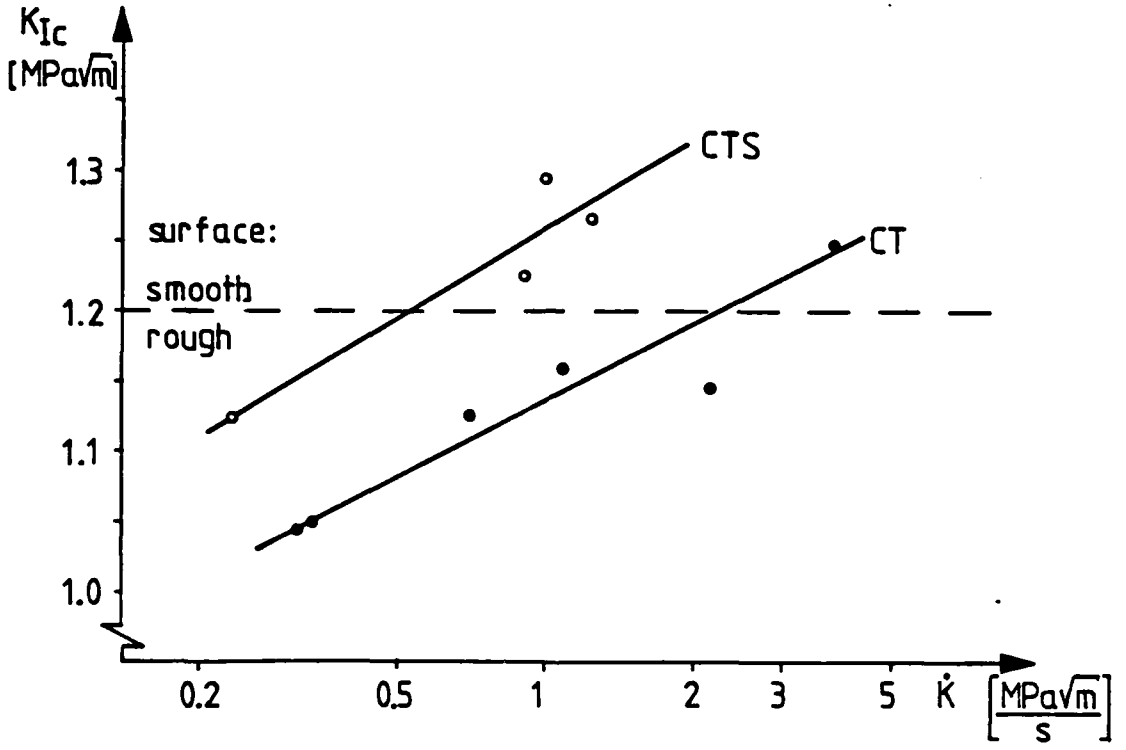

Figure 7 Behavior of K_{Ic} for increasing stress intensity rates $\dot{K}$

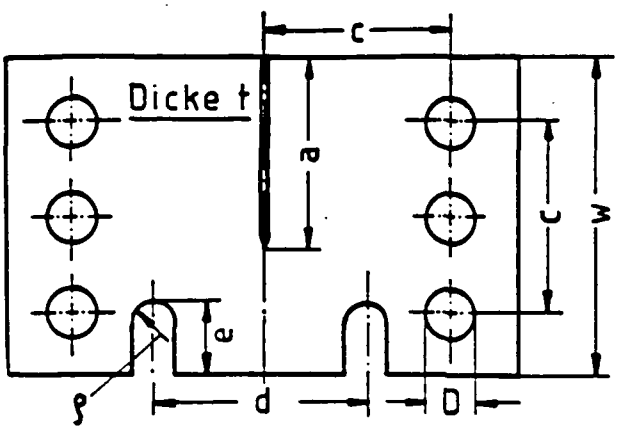

a/w = 0,55....0,65
c/w = 0,6
D/w = 0,167
d/w = 0,667
e/w = 0,278
ρ/w = 0,056

Figure 8 Modified CTS specimen [42]

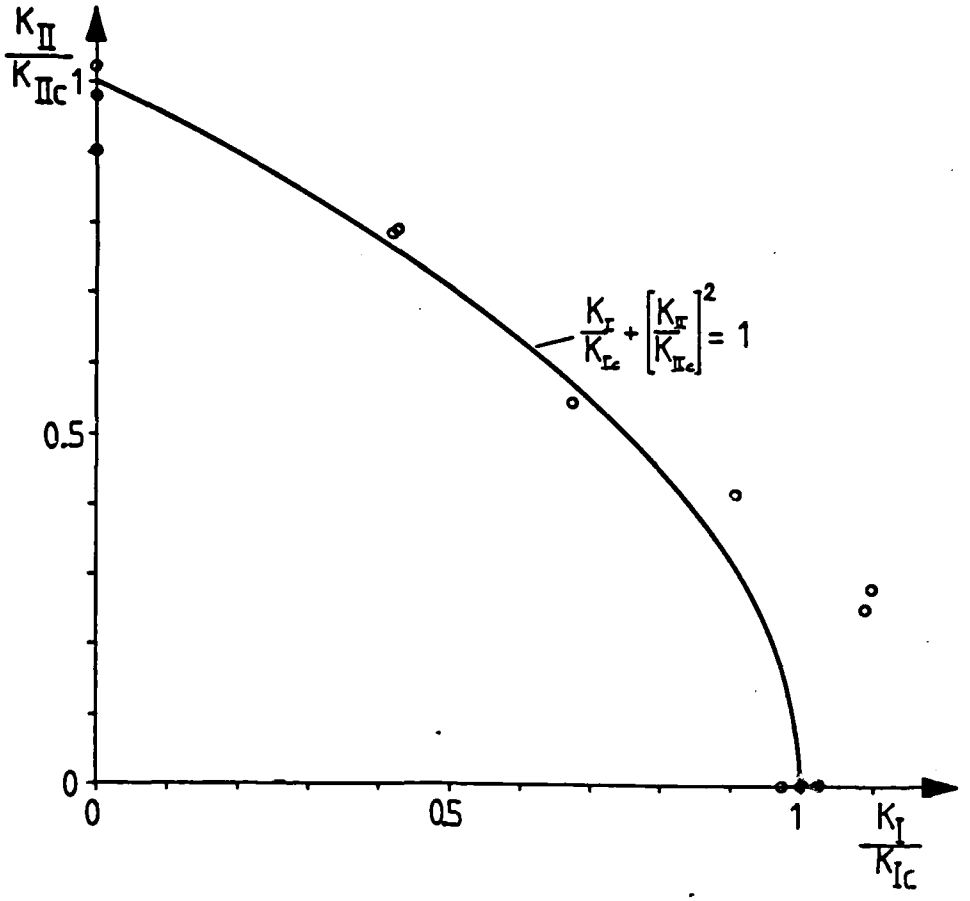

Figure 9 Fracture toughness of PMMA under mixed mode loading

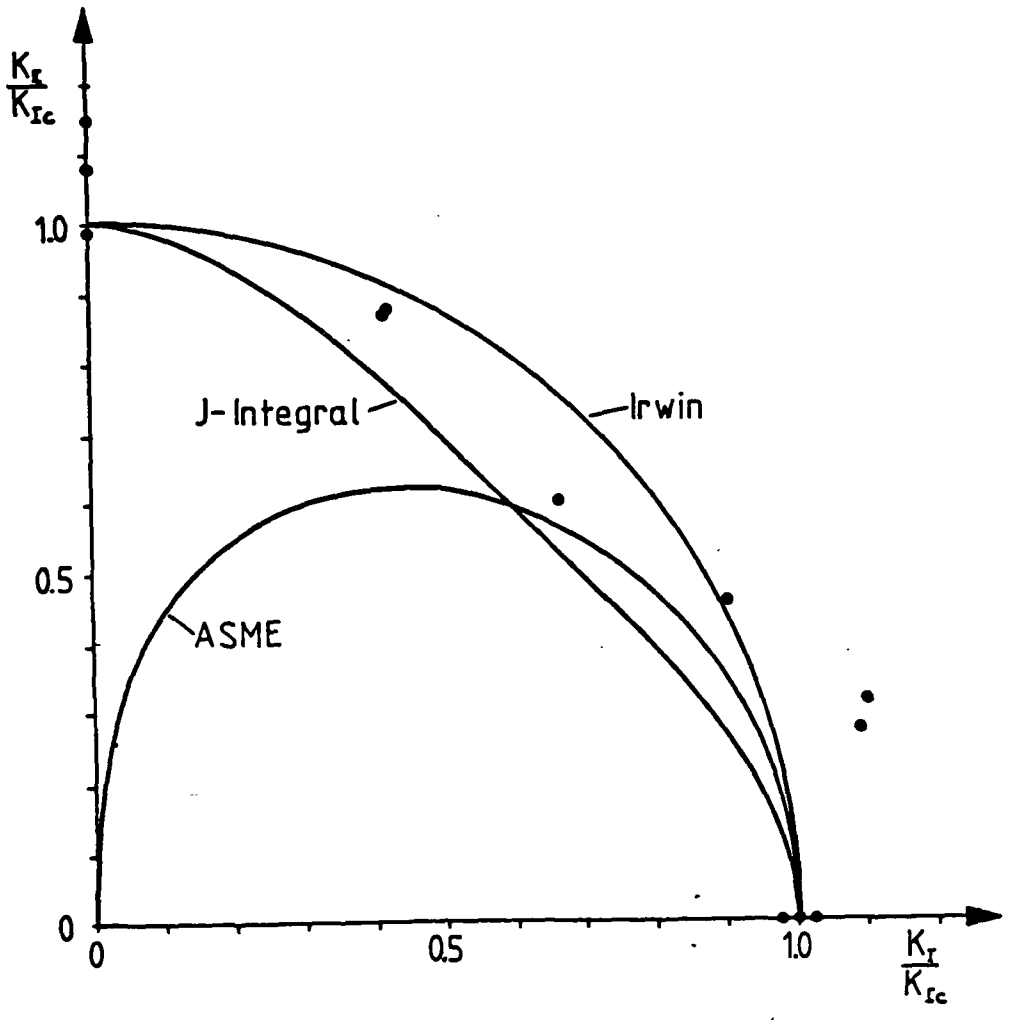

Figure 10 Fracture toughness of PMMA under mixed mode loading

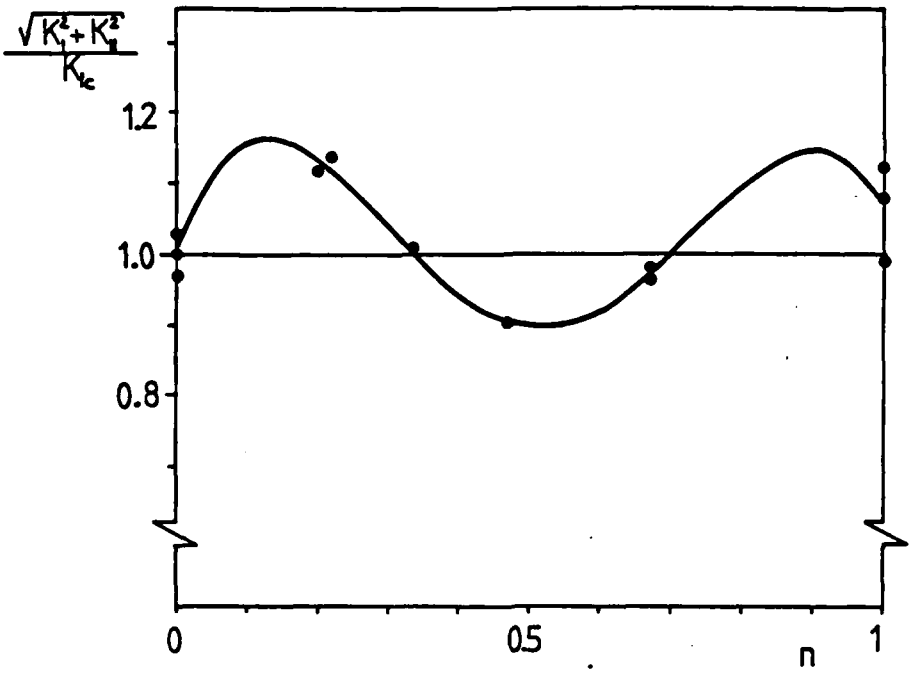

Figure 11 Fracture toughness of PMMA under mixed mode loading

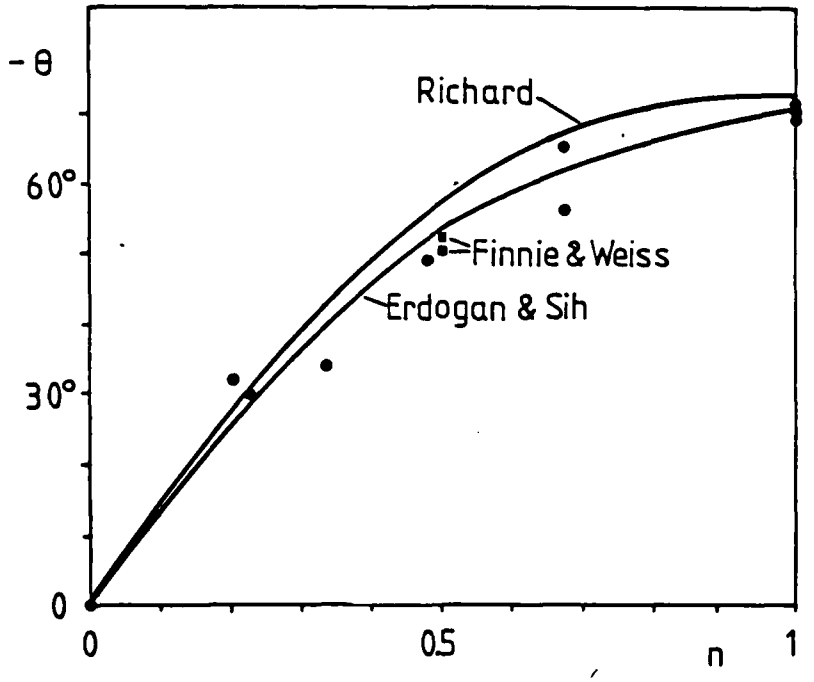

Figure 12 Angle of fracture initiation under mixed mode loading

Appendix 1

The citerion {8,76,77)

$$\frac{K_I}{K_{Ic}} + \left[\frac{K_{II}}{K_{IIc}}\right]^2 = 1$$

can be transformed in the following way: Multiplying both sides by K_{Ic}^2 and adding $(1/4)K_I^2$ one obtains

$$K_I K_{Ic} + \left[\frac{K_{Ic}}{K_{IIc}}\right]^2 K_{II}^2 + \frac{1}{4}K_I^2 = K_{Ic}^2 + \frac{1}{4}K_I^2$$

$$(K_{Ic} - \frac{1}{2}K_I)^2 = \frac{1}{4}K_I^2 + \left[\frac{K_{Ic}}{K_{IIc}}\right]^2 K_{II}^2$$

Introducing $\alpha_1 = K_{Ic}/K_{IIc}$ and extracting the root, this finally yields

$$K_{Ic} = \frac{1}{2}(K_I + \sqrt{K_I + 4(\alpha_1 K_{II})^2})$$

The ASME Boiler and Vessel Code {79} gives the criterion

$$K_{Ic} = \sigma\sqrt{\pi a \sin\beta}$$

With $K_I = \sigma\sqrt{\pi a}\,\sin^2\beta$ for an infinite plate, one obtains

$$K_{Ic} = K_I(\sin\beta)^{-1.5}$$

With $\beta = \arctan(K_I/K_{II})$ and applying the respective trigonometrical formula, this yields

$$\frac{K_I}{K_{Ic}} = \left[\frac{\frac{K_I}{K_{II}}}{\sqrt{1 + \left[\frac{K_I}{K_{II}}\right]^2}}\right]^{1.5}$$

Appendix 2: Calculation of the Stress Intensity Rate $\dot{K}$

The calculation is done for specimen CT4 as an example. This specimen broke at the critical stress intensity K_{Ic} = 1.16 MPa$\sqrt{m}$ and showed there a COD of 0.439 mm. Neglecting the deformations of the crack flanks, the point of measuring the COD has the distance L_1 = 1.625" to the crack tip, while the load line has L_2 = 1.00". LLD and COD are related by the simple geometrical relation

$$\frac{LLD}{COD} = \frac{L_2}{L_1}$$

which yields LLD = 0.270 mm at the initiation of fracture.

In displacement control, the LLD is related to the displacement rate d by

$$LLD = \dot{d}t$$

with which the time until fracture can be calculated:

$$t_c = \frac{LLD}{\dot{d}} = 1.07s$$

The average stress intensity rate $\dot{K}$ then is calculated by

$$\dot{K} = \frac{K_{Ic}}{t_c} = 1.09 \text{ MPa}\sqrt{m}/s$$

The calculation for the other CT specimens is done in the same way.

For the CTS specimens, the LLD was recorded and therefore the conversion from COD to LLD is not necessary.

It is intented to keep $\dot{K}$ constant for the mixed mode loading. The problem is that a relation between the machine parameter $\dot{d}$ and $\dot{K}$ has to be found. The loading rate $\dot{F}$ is related to $\dot{d}$ by

$$\dot{F} = \dot{d}i$$

where i is the slope of the load - LLD plot. The relation between $\dot{K}$ and $\dot{F}$ is given by

$$\dot{K} = \dot{F}\frac{\sqrt{\pi a}}{WB} Y_v$$

where W is the width of the specimen, B is the thickness, and Y_v the comparative calibration factor. Richard {8} made the FEM calculation and got the calibration factors Y_I and Y_{II} for the mode I and mode II component respectively (see appendix 3). These factors have to be related by a fracture criterion. The criterion

$$\frac{K_I}{K_{Ic}} + \left[\frac{K_{II}}{K_{IIc}}\right]^2 = 1$$

was chosen and the assumption $K_{IIc} = K_{Ic}$ was made. With this criterion, Y_v can be calculated by

$$Y_v = \frac{1}{2}(Y_I + \sqrt{Y_I^2 + 4Y_{II}^2})$$

This has been done for a/W = 0.5 and a/W = 0.7.

The last remaining unknown is the slope i which has to be determined experimentally. For this reason, one specimen was loaded to about 450 N and then unloaded, both at a

displacement rate of 2.5 mm/min. After the final testing, the slope found there was compared with first results. The results agreed reasonably, only for pure mode II a larger deviation was found. The average values for the slope, which depends on the specimen geometry, together with the calculated comparative calibration factor are given in table 19. Tables 11 through 13 are calculated with these data.

	Y_v		i
α	a/W = 0.5	a/W = 0.7	[N/m]
0°	2.84	6.26	5.2
15°	2.77	6.08	5.0
30°	2.60	5.56	4.0
45°	2.36	4.74	3.5
60°	2.05	3.75	2.9
75°	1.70	2.70	2.9
90°	1.39	1.77	3.1

Table 19 Slope i and comparative calibration factor Y_v for the CTS specimen

Appendix 3

To calculate K_I and K_{II}, Richard {8} gives the formulas

$$K_I = F\frac{\sqrt{\pi a}}{WB} Y_I$$

$$K_{II} = F\frac{\sqrt{\pi a}}{WB} Y_{II}$$

where Y_I and Y_{II} are the calibration factors for the CTS specimens evluated by a FEM calculation. Y_I and Y_{II} have the following values {8}

α	$a/W = 0.50$		$a/W = 0.55$		$a/W = 0.60$		$a/W = 0.65$		$a/W = 0.70$	
	Y_I	Y_{II}	Y_I	Y_{II}	Y_I	Y_{II}	Y_I	Y_{II}	Y_I	Y_{II}
0°	2.84	0.00	3.34	0.00	4.02	0.00	4.94	0.00	6.26	0.00
15°	2.72	0.36	3.22	0.38	3.87	0.40	4.76	0.42	6.05	0.45
30°	2.42	0.69	2.87	0.73	3.46	0.78	4.27	0.82	5.42	0.87
45°	1.95	0.98	2.33	1.04	2.82	1.11	3.48	1.17	4.42	1.24
60°	1.35	1.20	1.63	1.28	1.99	1.36	2.46	1.44	3.13	1.53
75°	0.65	1.34	0.81	1.43	1.02	1.52	1.27	1.61	1.62	1.71
90°	0.08	1.39	0.05	1.49	0.02	1.58	0.00	1.67	0.00	1.77

Table 20 Calibration factors for the CTS specimen

APPENDIX C:

"Prediction of Plasticity Characteristics for Three-Dimensional Fracture Specimens Comparison With Experiment"

By: E. T. Moyer, Jr., P. K. Poulose and H. Liebowitz.

Accepted for publication in the International Journal of Engineering Fracture Mechanics, October 1985.

PREDICTION OF PLASTICITY CHARACTERISTICS FOR THREE-DIMENSIONAL FRACTURE SPECIMENS COMPARISON WITH EXPERIMENT

By

E. T. Moyer, Jr.
P. K. Poulose
H. Liebowitz

The School of Engineering and Applied Science

The George Washington University

Washington, D.C. 20052

ABSTRACT

A center-cracked panel of 7075-Aluminum alloy which has overaged from the T651 condition was loaded in tension and subsequently unloaded to zero applied load. The permanent surface deformation was measured close to the intersections of the crack front with the free surfaces. The permanent deformation (being a good indicator of the extent of plastic deformation) was used to measure the accuracy of finite element analyses. cont'd

The same specimen was modeled using 20-node three-dimensional isoparametric elements. A fully incremental elastic-plastic formulation was employed in the stress analysis. The residual surface deformations after unloading were compared to the experimental results.

The average experimental results compare quite favorably with the finite element predictions. The average results were employed to minimize the influence of material inhomogeneity, load misalignment, and lack of symmetry in the fatigue crack. The scatter in the results from measuring the different sides is discussed.

INTRODUCTION

Over the past 35 years, the field of fracture mechanics has evolved and developed into an important and useful tool for the design of engineering components and structures. Several major problems dealing with the criticality of cracks in engineering components and structures can now be answered with great accuracy. Specifically, problems involving straight cracks in brittle materials undergoing Mode I deformation only can be accurately predicted. Most problems which occur in practice, however, involve materials which are ductile in the loading applications for which they are employed. Many cracks are also initiated in sites which involve complicated loading which involve more than a single fracture mode. Finally, most problems arising in application involve geometries which can not be accurately approximated two-dimensionally. The major research in fracture mechanics today, therefore, is geared toward addressing the issues of ductility, mixed-mode loading and three-dimensionality.

The issue of plasticity and ductility in fracture specimens has long been a concern of researchers. Many attempts have been made to propose fracture criteria which account for ductility and to develop numerical tools to perform stress analyses. The development and refinement of the finite element method has

greatly aided the progress in this area. Many two-dimensional studies have been performed using elastic-plastic finite element modeling. While much of the early work has been demonstrated erroneously, several accurate computational procedures are now available. The area of failure prediction has not been as successful as the area of stress analysis. No viable ductile fracture criteria have been proposed which pass the tests of specimen and geometry independence, consistent and theoretically sound formulation, and reproducibility. The best that can be said for the existing criteria is that for limited realms of applicability (usually vary within 10-15% of the range of brittle criteria), the proposed methods offer conservative estimates for failure loads which are not as strict as the brittle predictions. It is important to recognize at the outset that elastic-plastic fracture parameters (e.g., J-integral, CTOD, CMOD, etc.) can either be shown to be theoretically invalid for true plasticity problems, or, are simply experimental observations which not do pass the test of specimen and geometry independence.

During the past three years, the authors have focused their research on addressing the three-dimensional aspects of ductile fracture. A major first step has been the development of an accurate and theoretically consistent computational approach to the stress analysis of three-dimensional fracture specimens. In

a series of recent papers [1,2,3], the effect of specimen thickness, material hardening characteristics and mesh characteristics have been investigated. These results give much insight into the necessary properties for ductile fracture criteria. While no new criteria have emerged to date (either from the authors or others), the groundwork for analyzing and assessing criteria has been established.

A major problem with ductile fracture problems in three-dimensions is the establishment of the accuracy of the analysis. Convergence studies are extremely costly and only show the consistency of the approach. They in no way guarantee agreement with the behavior of real materials. To address this problem, the study presented in this paper compares the deformation predicted from a full three-dimensional incremental plasticity finite element analysis to the deformations measured in the laboratory. A center-cracked panel was chosen for the study for two reasons: first, the authors' previous studies have been performed on center-cracked panels and second, the specimen is easier to model with finite elements as the effects of the loading holes are easier to account for (by using an accurate gauge length). While a successful comparison does not guarantee the accuracy of any given study other than the present, it is the most rigorous way of establishing the validity of the approach and demonstrating the qualitative agreement of the predictions made previously with the behavior of real fracture specimens.

AD-A166 575 CREEP AND FRACTURE CHARACTERISTICS OF MATERIALS AND STRUCTURES AT ELEVATED TEMPERATURES(U) GEORGE WASHINGTON UNIV WASHINGTON DC SCHOOL OF ENGINEERING AN UNCLASSIFIED .. H LIEBOWITZ 14 FEB 86 N00014-84-K-0027 F/G 20/11 NL

3/4

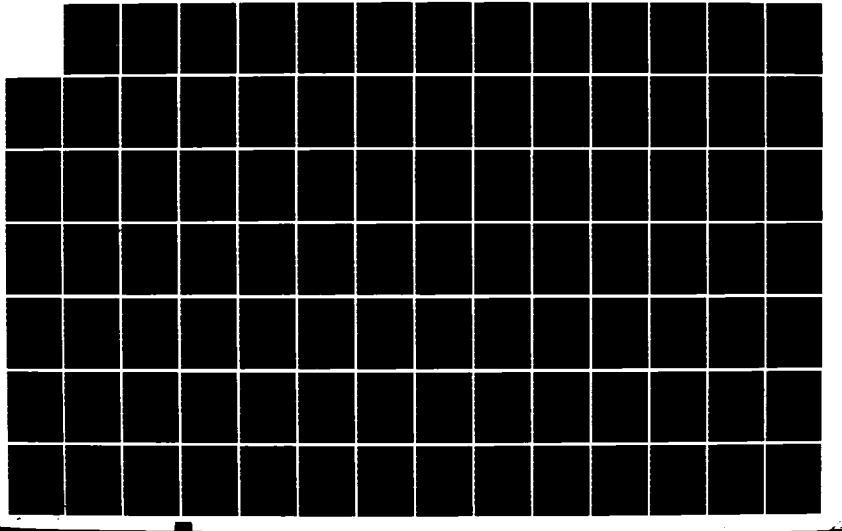

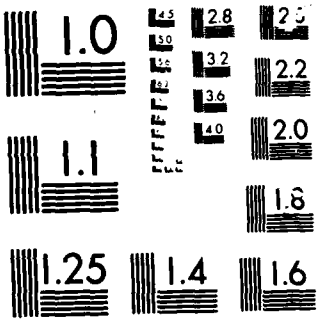

MICROCOPY CHART

ELASTIC-PLASTIC FINITE ELEMENT FORMULATION

The stress analysis in this study is performed utilizing the finite element method to solve the basic elastic-plastic governing equations for the deformation of continuum solids. J_2 flow theory plasticity is employed with the standard associative flow law. The Newton-Raphson, or Tangent-Stiffness approach is employed in the finite element formulation to handle nonlinearities. The Updated Lagrangian coordinate system is employed to handle finite strains. The formulation of all equations is outlined in this section.

The J_2 flow theory of plasticity assumes that the material in question yield, or starts deforming plastically when the "effective stress" (or von-Mises stress) reaches a critical value (called the yield stress). Prior to the onset of plasticity, the material is assumed to behave linear elastically. Subsequently, the deviatoric stress components are related to the deviatoric strain rate through the tensor relation

$$\dot{e}_{ij} = \begin{cases} \dfrac{1+\nu}{E}\dot{S}_{ij} + \dfrac{3}{Z} f(\sigma_e)\, S'_{ij}\, \dot{\sigma}_e & \left[\begin{array}{l}\sigma'_e = R_{yd} \\ \dot{\sigma}_e > 0 .\end{array}\right] \\ \dfrac{1+\nu}{E}\dot{S}_{ij} \quad \text{(otherwise)} & \end{cases} \tag{1}$$

where $\dot{e}_{ij}$ are the deviatoric strain rates given by

$$\dot{e}_{ij} = \dot{\epsilon}_{ij} - \frac{1}{3} \dot{\epsilon}_{pp} \delta_{ij} \tag{2}$$

S_{ij} are the current deviatoric stress components given by

$$S_{ij} = \sigma_{ij} - \frac{1}{3} \sigma_{pp} \delta_{ij} \tag{3}$$

S'_{ij} are the deviatoric stress components measured relative to the current yield surface center given by

$$S'_{ij} = S_{ij} - a_{ij} \tag{4}$$

a_{ij} are the coordinates in stress space of the current yield surface center, σ_{ij} are the Cauchy stress components, ϵ_{ij} are the "true" strain components (discussed in a subsequent section), σ_e is the effective stress given by

$$\sigma_e = \sqrt{\frac{3}{2} S_{ij} S_{ij}} \tag{5}$$

and σ'_e is the effective stress measured relative to the current yield surface center

$$\sigma'_e = \sqrt{\frac{3}{2} S'_{ij} S'_{ij}} \quad . \tag{6}$$

The function $f(\sigma_e)$ is derived from the uniaxial stress-strain curve and is consistent with the Associated Plasticity Theory (a complete discussion is given in Reference [4]). Derivation of $f(\sigma_e)$ for a multilinear representation of the stress-strain curve will be discussed subsequently.

For plastic strains which are incompressible, the hydrostatic plastic strain rate is zero. The total hydrostatic strain rate, therefore, is related to the related to the hydrostatic stress rate by

$$\dot{\varepsilon}_{pp} = \frac{1 - 2\nu}{E} \dot{\sigma}_{pp} \tag{7}$$

Engineering materials exhibit different types of uniaxial hardening behavior when subsequently unloaded after being plastically deformed. Generally, the behavior falls between two extremes called kinematic and isotropic hardening. The uniaxial representation of these behaviors for a bilinear material are shown in Figure 1. To allow for various hardening behaviors in the multiaxial formulation, the yield surface is permitted to move and expand under certain constraints. These motions are controlled by a single parameter, β, which can be varied from 0 to 1. A value of zero represents isotropic behavior and a value of 1 represents kinematic behavior. The resulting yield surfaces in a three-dimensional principle stress space are shown in Figure 2. The yield surface center moves at a rate governed by

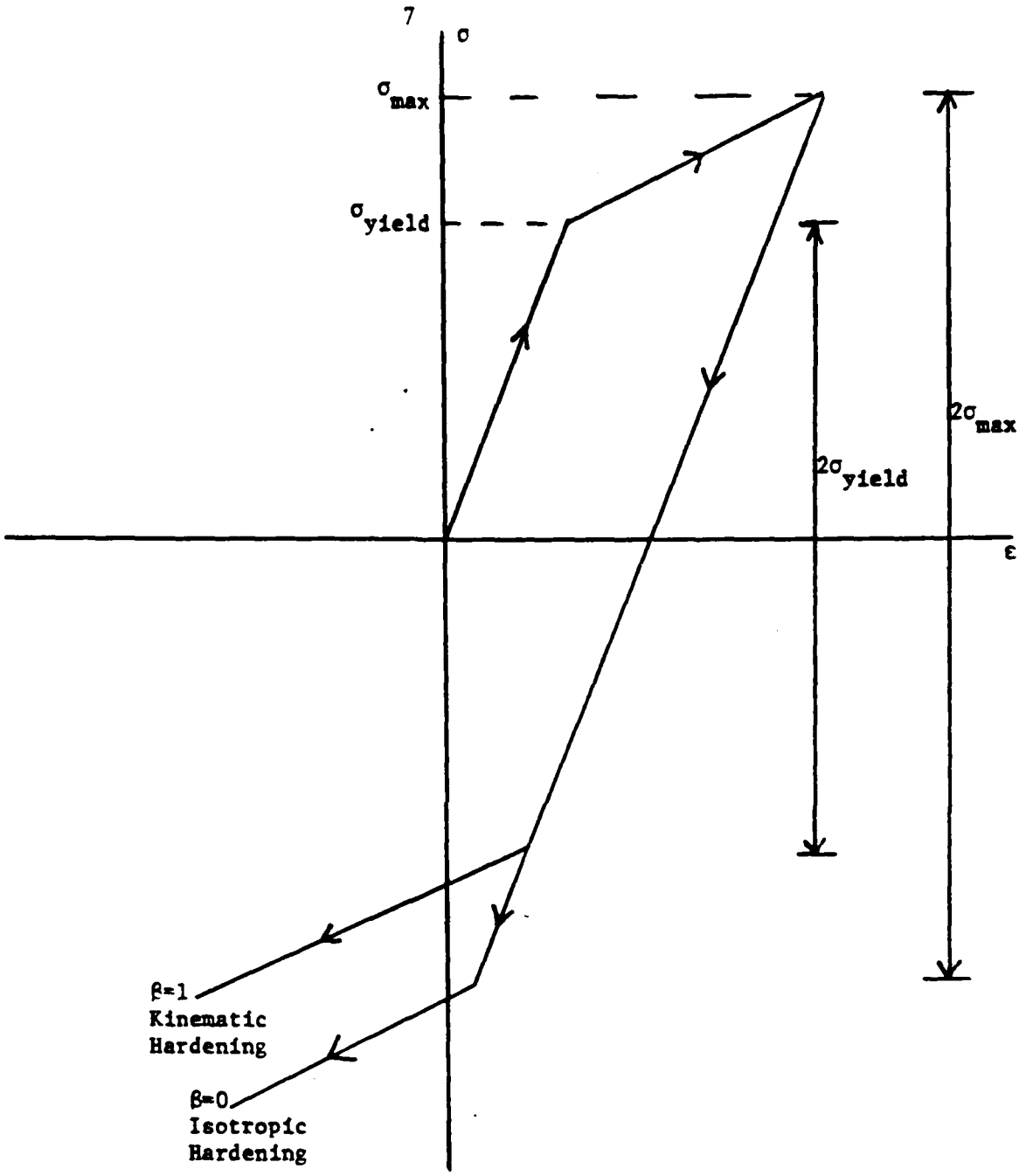

Figure 1: Uniaxial Bilinear Representation of Kinematic and Isotropic Hardening.

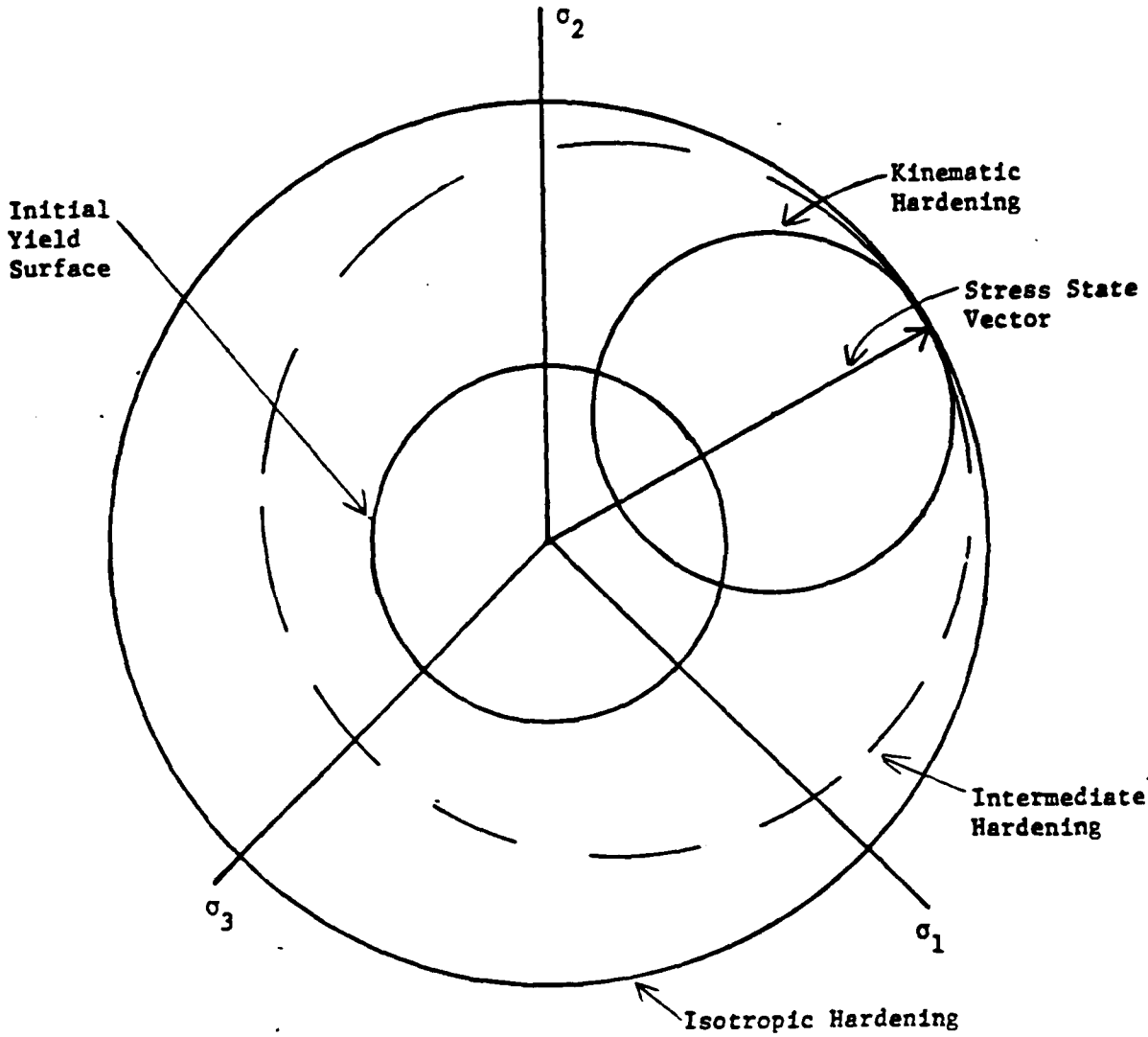

Figure 2: Hardening Models in Principle Stress Space.

$$\dot{a}_{ij} = \left\{ \begin{array}{ll} \frac{3}{2} \beta S'_{kl} \dot{S}_{kl} S'_{ij} / (\sigma'_e)^2 & \left[\begin{array}{l} \sigma'_e = \sigma_{yd} \\ \dot{\sigma}_e > 0 \end{array} \right] \\ 0 \text{ (otherwise)} & \\ 0 \leq \beta \leq 1 & \end{array} \right\} \tag{8}$$

$\beta = 0 \rightarrow$ Isotropic Hardening

$\beta = 1 \rightarrow$ Kinematic Hardening

$$\sigma'_y = 2 \sigma_y + 2 \beta(\sigma_{max} - \sigma_y) \tag{9}$$

To allow for finite strains and rotations, Updated Lagrangian approach is adopted [5]. The coordinate system is convected with the deformation. In this coordinate system, the "true strain" rate is related to the determination rate (or velocity) through

$$\dot{\sigma}_{ij} = C_{ijkl} \dot{\epsilon}_{kl} \tag{10}$$

In the absence of rotation the stress tensor is related to the strain rate tensor in the classical manner, i.e.,

$$\dot{W}_{ij} = \frac{1}{2}\left(\frac{\partial \dot{U}_i}{\partial X_j} - \frac{\partial \dot{U}_j}{\partial X_i}\right) \tag{11}$$

This stress measure is the Cauchy stress. Under finite rotations, the stress tensor is not invariant. At zero strain rate, the stress rate is given by where W are the rotation rates

$$\dot{\sigma}_{ij} = \dot{W}_{ip}\,\sigma_{pj} - \dot{W}_{pj}\,\sigma_{ip} \tag{12}$$

The total stress-deformation relation is, therefore,

$$\dot{\sigma}_{ij} = C_{ijkl}\,\dot{\epsilon}_{kl} + \dot{W}_{ik}\,\sigma_{kj} - \dot{W}_{kj}\,\sigma_{ik} \tag{13}$$

Equations (1) - (13) form a complete incremental representation of finite plastic deformation. It only remains, therefore, to quantify the uniaxial behavior through the function $f(\sigma_e)$. There are many functional ways to represent uniaxial loading behavior. From a computation standpoint, a multilinear representation is easily implemented and, by allowing for enough segments, can be arbitrarily accurate. Consider the multilinear representation of a true stress-true

strain curve shown in Figure 3. The functional relationship between the stress and strain are given by

$$\varepsilon = \frac{\sigma}{E} + \frac{\alpha_1}{E}(\sigma_2 - \sigma_1) + \frac{\alpha_2}{E}(\sigma_3 - \sigma_2) + \ldots \frac{\alpha_m}{E}(\sigma - \sigma_m) \tag{14}$$

$$\sigma_m < \sigma \leq \sigma_{m+1}$$

The plastic strain rate, therefore, is given by

$$\dot{\varepsilon}_p = \alpha_m \dot{\sigma}_e / E \tag{15}$$

Using equation (1) and recognizing that for uniaxial deformation, effective quantities are proportional to the uniaxial components, the function $f(\sigma_e)$ can be reduced to

$$f(\sigma_e) = \alpha_m / E\sigma_e \tag{16}$$

The function is only linearly dependent on the current slope of the uniaxial curve. By specifying enough segments, virtually any hardening behavior can be accurately described.

Equations (1), (8) and (9) provide the fundamental relationships between stress and strain rates. The equilibrium conditions (governing equations) for a continuum body in the absence of body forces and inertia effects can be written as

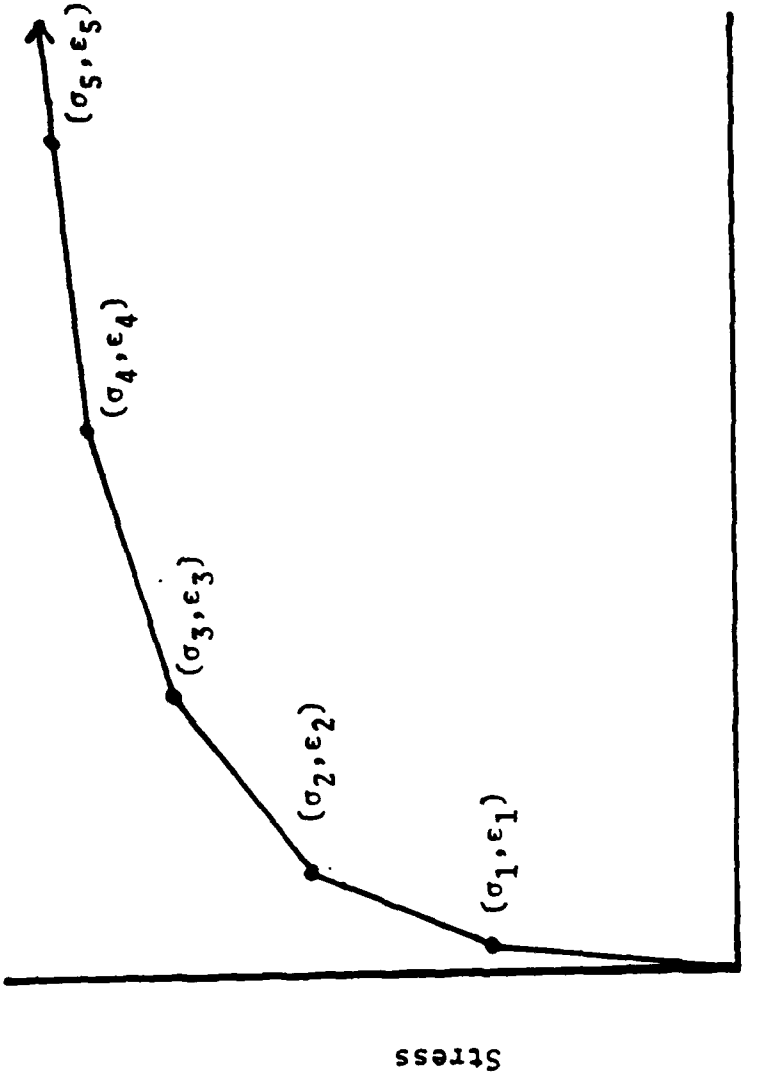

Figure 3: Multilinear Approximation For A Uniaxial Stress-Strain Curve With Hardening.

$$\partial \dot{\sigma}_{ij} / \partial x_j = 0 \tag{17}$$

with the boundary conditions

$$\dot{\sigma}_{ij} n_j = \dot{T}_i \text{ on } S_T$$

and (18)

$$\dot{u}_i = \dot{u}_i \text{ on } S_u$$

where $\dot{T}_i$ are the specified loading rates on the boundary experiencing applied tractions (S_T) and $\dot{u}_i$ are the velocities specified on the remainder of the boundary (S_u).

Equation (13) provides the fundamental relation between the stress state and the deformation gradients. For many problems in application the assumption of "small strain" introduces minimal error (mathematically, this means assuming infinitesimal displacements and strains). If this assumption is made, the strain rates are related to the velocity gradients by

$$\dot{\epsilon}_{ij} = \frac{1}{2}(\partial \dot{u}_i / \partial x_j + \partial \dot{u}_j / \partial x_i) \tag{19}$$

This simplification also means that the reference coordinate system and the material coordinate system are coincidental throughout the deformation. In the computer code described, the option of finite or infinitesimal strain theory is left to the user. The use finite strains slows convergence considerably for problems where the deformations are small. As the strains grow, however, the solutions assuming infinitesimal theory diverge from the finite strain results. Eventually infinitesimal solutions will fail to converge regardless of how small the load increments are taken.

By either employing the Principle of Virtual Work for increments of displacement or by performing the standard Galerkin technique on the governing equations, (17) and (18), the finite element equations governing the nodal velocities, $\dot{\underset{\sim}{U}}$, can be written in terms of the loading rate vector, R, in the form

$$\underset{\sim}{K}(\underset{\sim}{U}) \cdot \dot{\underset{\sim}{U}} - \dot{\underset{\sim}{R}} = 0 \tag{20}$$

The standard finite element assumptions made are given by

$$\underset{\sim}{u} = \underset{\sim}{N} \cdot \underset{\sim}{U}$$

$$\dot{\underset{\sim}{\varepsilon}} = \underset{\sim}{B} \cdot \dot{\underset{\sim}{U}}$$

$$\dot{\underset{\sim}{\sigma}} = \underset{\sim}{D}(\underset{\sim}{U}) \cdot \dot{\underset{\sim}{\varepsilon}} \tag{21}$$

$$K(U) = \sum_{\text{elements}} \int_{\text{element volume}} \underset{\sim}{B}^{T} \underset{\sim}{D}(\underset{\sim}{U}) \underset{\sim}{B} \, dV$$

where $\underset{\sim}{N}$ are the shape functions. The set of rate equations (20) will be integrated one load increment ($\Delta\underset{\sim}{R}$) at a given time to determine the corresponding new displacement increment, $\Delta\underset{\sim}{U}$. The Newton-Raphson or tangent stiffness solution procedure is employed. At load increment $L + 1$, the initial solution $\Delta\underset{\sim}{U}^{i}_{L+1}$ is found from

$$\underset{\sim}{K}(\underset{\sim}{U}_{L}) \cdot \Delta\underset{\sim}{U}^{i}_{L+1} = \Delta\underset{\sim}{R}_{L+1} \tag{22}$$

The "new" displacement is then used in the stiffness matrix,

$K(U_{L} + \sum_{i=1}^{m} \Delta U^{i}_{L+1})$, and a new correction is obtained from

$$\underset{\sim}{K}\left[\underset{\sim}{U}_L + \sum_{i=1}^{m} \Delta\underset{\sim}{U}_{L+1}^{i}\right] \cdot \Delta\underset{\sim}{U}_{L+1}^{m+1} + \Delta\underset{\sim}{R}_{L+1} -$$

$$\underset{\sim}{U}_L + \sum_{i=1}^{m} \Delta\underset{\sim}{U}_{L+1}^{i} \qquad (23)$$

$$\int_{\underset{\sim}{U}_L} \underset{\sim}{K}(\underset{\sim}{U})\, d\underset{\sim}{U} = \underset{\sim}{F}_{L+1}^{i+1}$$

where the integral is approximated using Simpson's rule. The procedure is repeated until two convergence criteria are met:

$$\left|\underset{\sim}{F}_{L+1}^{i+1}\right|^2 / \left|\Delta\underset{\sim}{R}_{L+1}\right|^2 \leq C_1$$

and (24)

$$\left|\underset{\sim}{F}_{L+1}^{i+1}\right|^2 / \left|\underset{\sim}{R}_{L+1}\right|^2 \leq C_2$$

where $\underset{\sim}{R}_{L+1}$ is the total load at step L + 1.

In this study, 20-node quadratic isoparametric elements were employed exclusively. All integration was carried out utilizing 3 x 3 x 3 Gauss-Legendre quadrature formulae. Strains were calculated at the Gauss integration points in each element from the strain-displacement relations of (19). Stresses were cumulatively calculated at the Gauss points from the stress-strain relations.

Directly calculating strains and stresses from the finite element relations (21) at points on element boundaries inherently yields poor results. This is especially true when C^0 shape functions are employed. A superior approach is to calculate the stresses and strains at the Legendre quadrature points and to extrapolate or smooth them to the boundaries. This approach has been shown to yield very accurate results for a wide variety of geometric mappings. In this study the smoothing technique as developed in [6] is employed for all stress and strain evaluations.

For elastic-plastic studies, the authors prefer to model the crack front region with a convergent mesh of conventional elements rather than to employ a "singular" element. Experience with both elastic and elastic-plastic studies [3,7] demonstrates this approach to be accurate (although, for elastic problems, more costly). Since the nature of the singularity is unknown in the elastic-plastic problem, it is presumptuous to employ a singular element and may lead to erroneous results.

PROBLEM DESCRIPTION

Consider a panel of overaged 7075 (T7651) aluminum with a central through the thickness crack. A typical panel is shown in Figure 4. The panel used in this study had a width of 8.89cm and a crack length to width ratio of .0.5. The specimen thickness was 0.984mm and the specimen length was 17.78cm. The uniaxial stress-strain curve for the material is shown in Figure 5. The metallurgical aspects of this material and its ductility are discussed in a subsequent section.

Since the panel was loaded normal to the crack only, symmetry allowed the modeling of one octant. The finite element grid used in this study is shown in Figures 6a, 6b and 6c. The smallest elements near the crack front had planer dimensions of a/20 (where a is the half length of the crack). The convergence of this grid is discussed in [3,7].

The grid shown consists of 96 20-node isoparametric elements with 624 total nodes. The total grid has 1872 degrees of freedom. The system was solved by the frontal method. The total storage required for the entire program was 2.2 Megabytes (for double precision computations). Total runtime for the problem discussed was 48CPU Hours on a VAX 11/780.

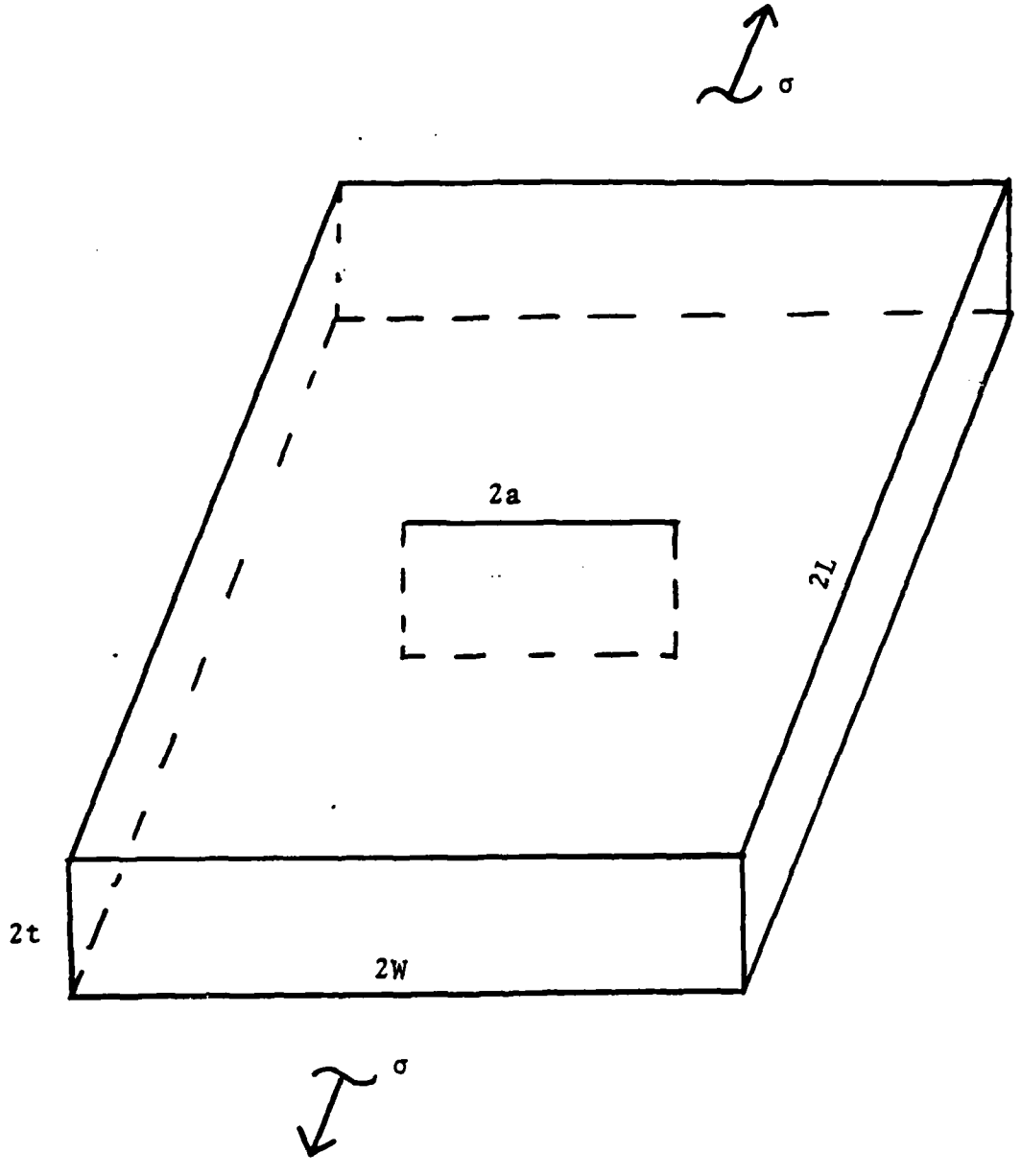

Figure 4: Typical Center Cracked Panel.

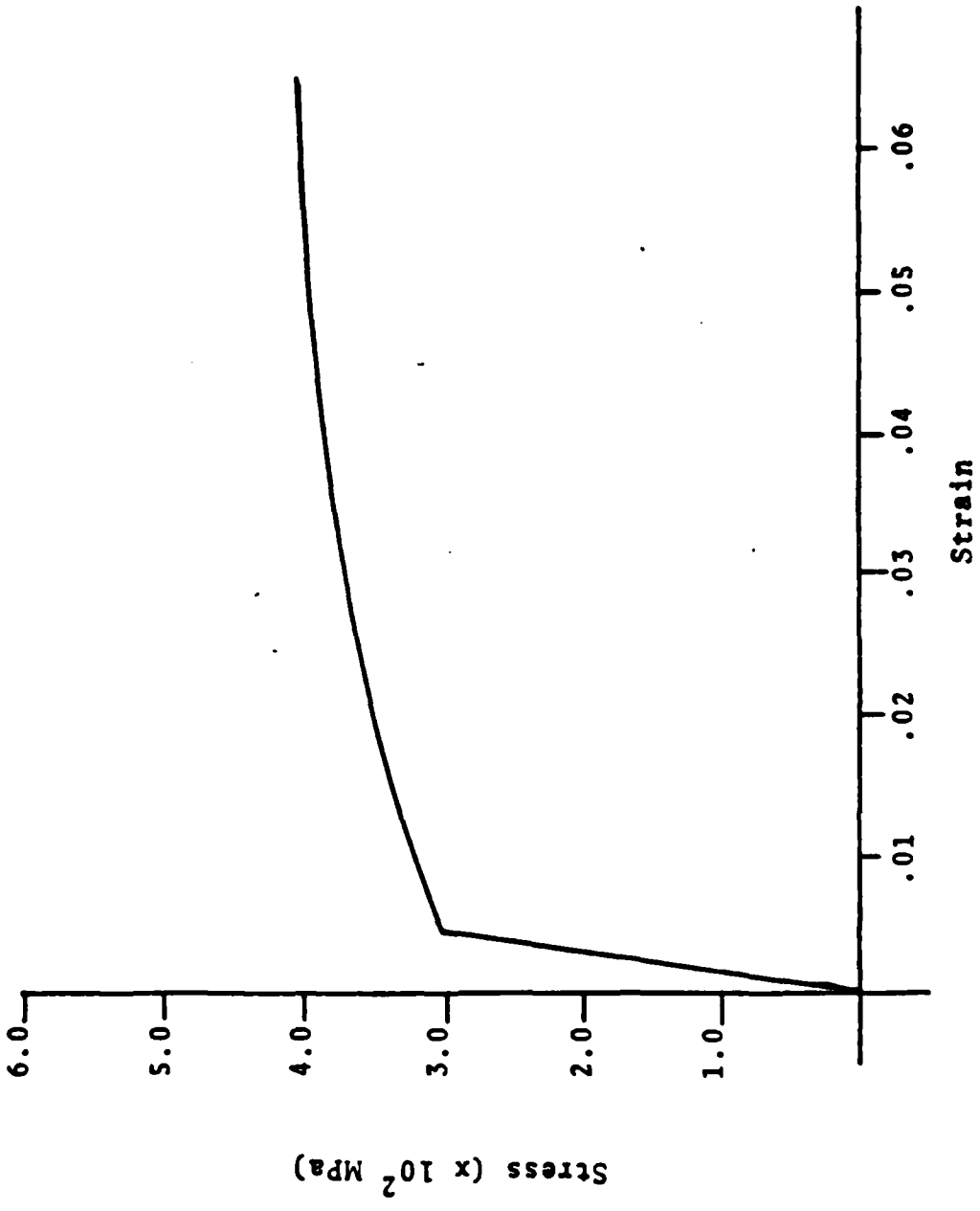

Figure 5: Uniaxial Stress-Strain Curve.

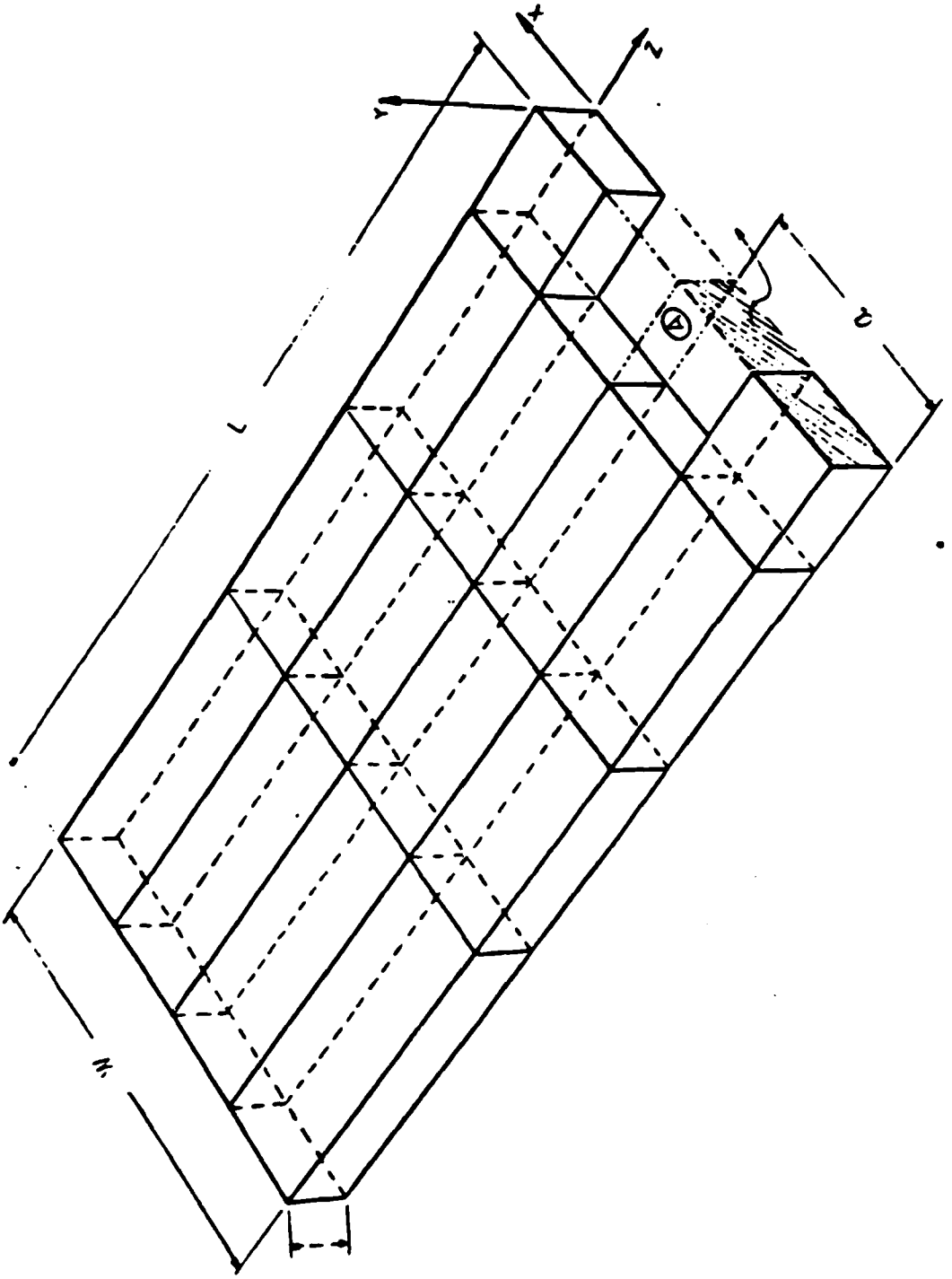

Figure 6a: Finite Element Grid - Coarse Outer Region.

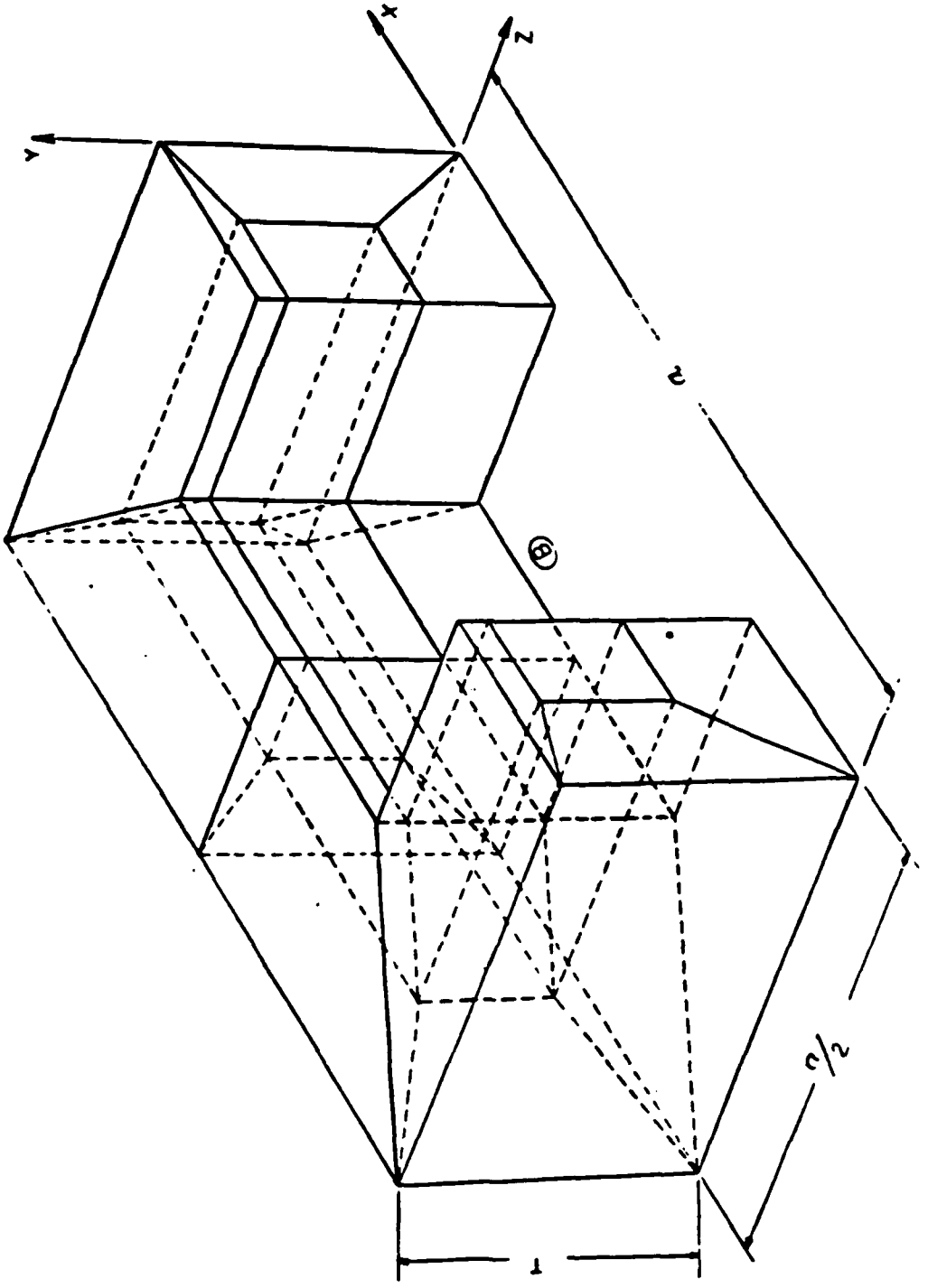

Figure 6b: Finite Element Grid - Blowup Of Region A.

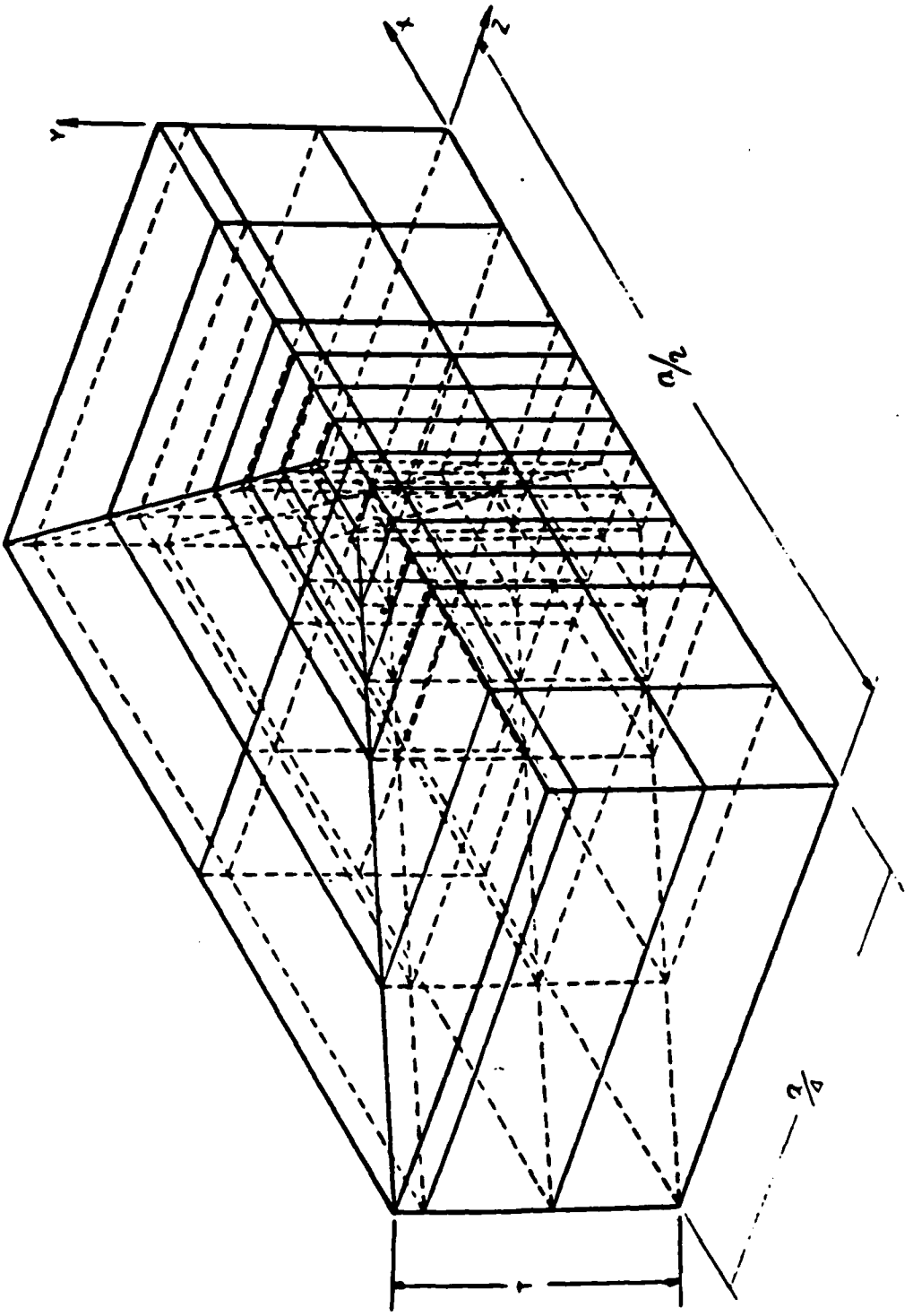

Figure 6c: Finite Element Grid - Near Tip Region B.

EXPERIMENTAL PROCEDURE

The ease and accuracy of measurement of the crack tip plastic zone shape will be high if the plastic zone is very large. This would require a material in a very ductile condition. However, such high ductility would create a large curvature in the crack front during fatigue precracking and difficulties in obtaining convergence in finite element analysis. Hence, an alloy in a moderately ductile condition was found to be desirable. These conditions were obtained in 7075 aluminum alloy by overaging from the T651 condition for 72 hours at 178°C (352°F). In this T7651 condition the alloy had a yield strength of 307MPa and ultimate tensile strength of 407MPa.

The specimen geometry used for this study was the center-cracked type with width, w = 89mm and crack length, 2a = 44.5mm. Fatigue cracks were initiated and extended from machined notches to obtain sharp crack tips. The fatigue precracking was performed at a load at least 50% lower than the load applied for plastic zone formation. After the fatigue crack was grown, the specimen was loaded to a desired load value to produce plastic zones at crack tips. The maximum load was limited by the load needed for crack growth initiation, as the experimental results were to be compared with the results of finite element analysis without crack

extension. Attempts were made to obtain as large a plastic zone as possible without crack growth; hence, the selected load was very close to that needed for stable crack growth initiation. Although initiation of stable crack growth is generally accompanied by a sudden drop in the load, in ductile materials, this drop is not easily detectable. Hence, to assure that no crack growth took place during loading, the specimen was fatigue cracked again after plastic zone size measurement to extend the crack approximately 2.5 to 5mm. The specimen was then loaded to fracture. If crack growth occurred during initial loading for formation of the plastic zone, the crack growth region would be marked by a dull appearance, distinguishing it from the fatigue crack growth region on either side. The results from such specimens were rejected.

The plastic zone size was determined by measuring the permanent reduction in thickness after the specimen was initially loaded and unloaded. The contours of the plastic zones were measured using a surface profile measuring device. The sensor of the device consisted of a pointer with a small tip radius attached to one end of a thin hardened titanium alloy sheet that was 51mm long, 19mm wide and 1.3mm thick. The other end of the sheet was rigidly mounted by sandwiching between two aluminum pieces. Two strain gauges of resistance 120ohms were mounted on each face of the titanium alloy

sheet. These strain gauges formed four arms of a Wheatstone bridge circuit. The circuit was similar to those used in load cells, extensometers and clip gauges. The output from the circuit was proportional to the movement of the pointer. The signal was amplified using a D.C. conditioner. The use of the thin titanium alloy sheet reduced the pressure on the specimen by the pointer, and scratching of the surface was minimized.

The specimen was mounted horizontally on a table with two micrometer screw feeds at right angles to each other. The specimen was mounted in such a way that the direction of crack (x-direction) was parallel to the direction of traverse of one micrometer screw. When the sensor was mounted the pointer was pressing against the specimen vertically. The specimen was moved underneath the sensor using the micrometer screw-feeds. The output from the sensor was used to drive the x-axis of an x-y recorder. The y-direction displacement of the table was measured using an extensometer attached to the system, and the output from the extensometer was used to drive the y-axis of the x-y recorder. Several traverses in the y-direction were made for each face of the specimen at regular intervals of distance from the crack tip in the x-direction. The curves obtained from these traverses were used to establish points around the crack tip corresponding to a given thickness reduction. From these, contour lines for different thicknesses were established. This process was repeated for all the four faces of the specimen.

EXPERIMENTAL RESULTS

The contour lines delineate the size and shape of the plastic zone. The thickness of the specimen falls between those required for plane stress and plane strain conditions. The plastic zones obtained had a shape representative of this thickness range.

A set of contour lines obtained from one face of the specimen are shown in Fig. 7. The scatter in the data for the outer contour lines is higher than the inner ones. This is because the rate of thickness variation decreases with increasing distance from the cracked tip, as can be seen from the differences in the spacings between adjacent contour lines. Although the resolution of the sensor is very high and is limited only by the extent of the amplification of the signal, errors can be introduced due to any nonplanarity of the initial specimen surface and slight variations in the pressure applied on the micrometer screws while advancing manually. The planarity of the surface was checked initially before deforming the specimen. The variations in pressure can cause an error of approximately 0.0025mm. The depth of 0.0051mm and 0.0102mm represented by the outer contour lines are very sensitive to these variations. The scatter in the data, also is produced by the nonhomogeneity of the material, caused by coring and inclusions during casting and orientation effects during subsequent mechanical processing.

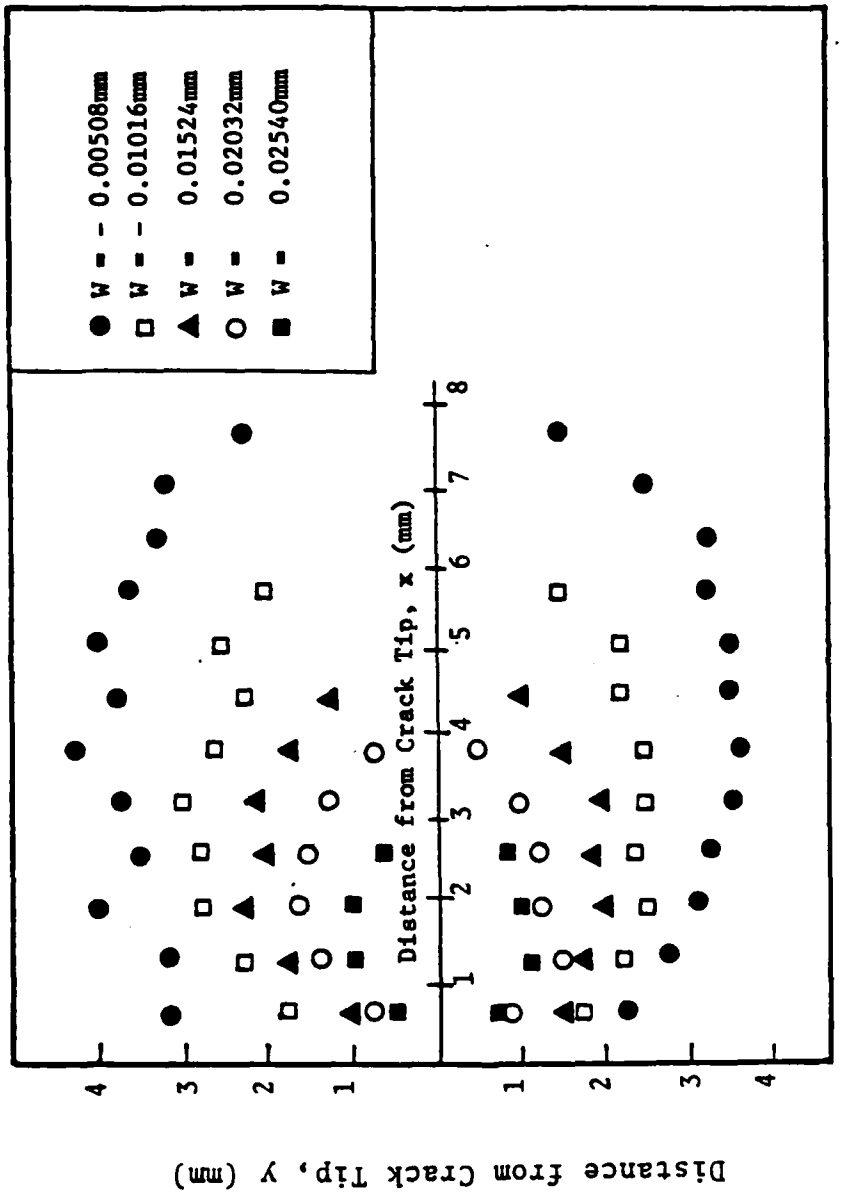

Figure 7: Surface Displacements Near a Crack Tip.

It is also seen that the plastic zone is not exactly symmetrical to the initial notch direction, which also can be attributed to inhomogeneity. Plastic deformation occurs more extensively in the softer regions. Material inhomogeneity also may cause change in the orientation of the fatigue crack, which tilts the zone ahead of it. Nonsymmetry can also be produced by misalignment of the specimen and the testing machine, but the misalignment in the set up used was negligible.

In the finite element analysis inhomogeneity is not taken into consideration and hence, the zone is assumed to be symmetrical. A comparison with the finite element results can be made by averaging the distance of each set of contour lines from the initial notch direction. Such contour lines determined from the four faces are shown in Figs. 8-11. The zone sizes are slightly different for the four faces. This also results from the uneven crack growth during fatigue cracking due to inhomogeneity. Since the excess deformation in one region is compensated by the lack of it in another, averaging the results minimizes the error involved.

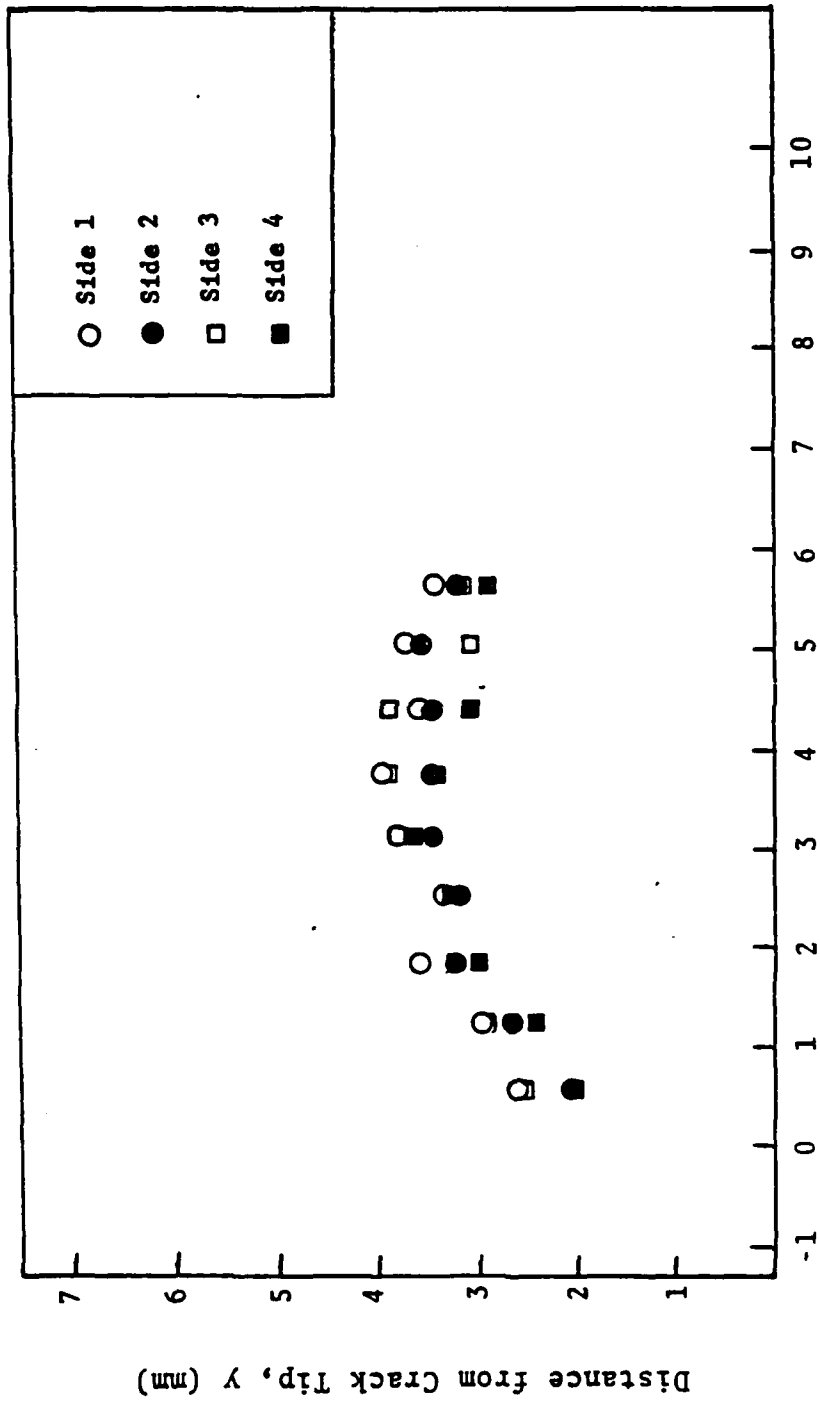

Figure 8: Contour Lines of Depth, 0.00508mm.

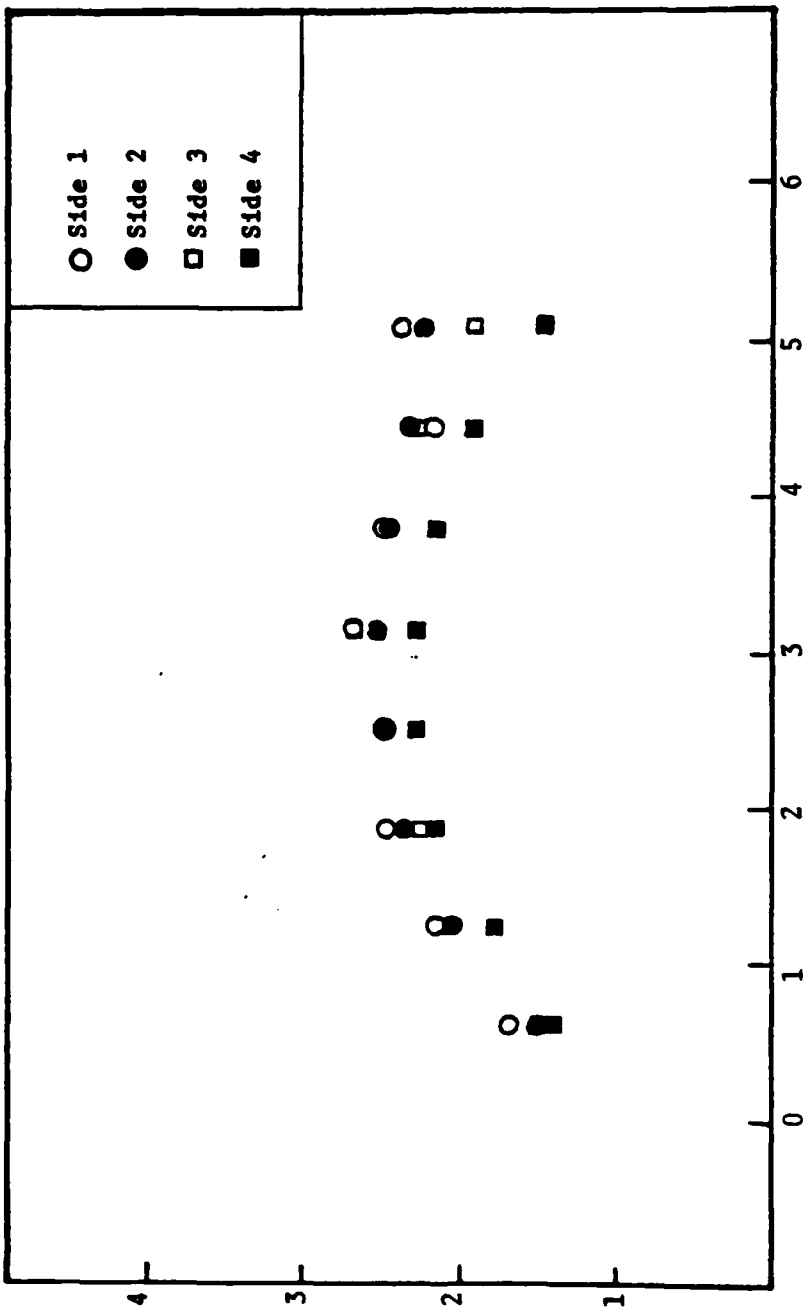

Figure 9: Contour Lines of Depth, 0.01016mm.

Figure 10: Contour Lines of Depth 0.01524mm.

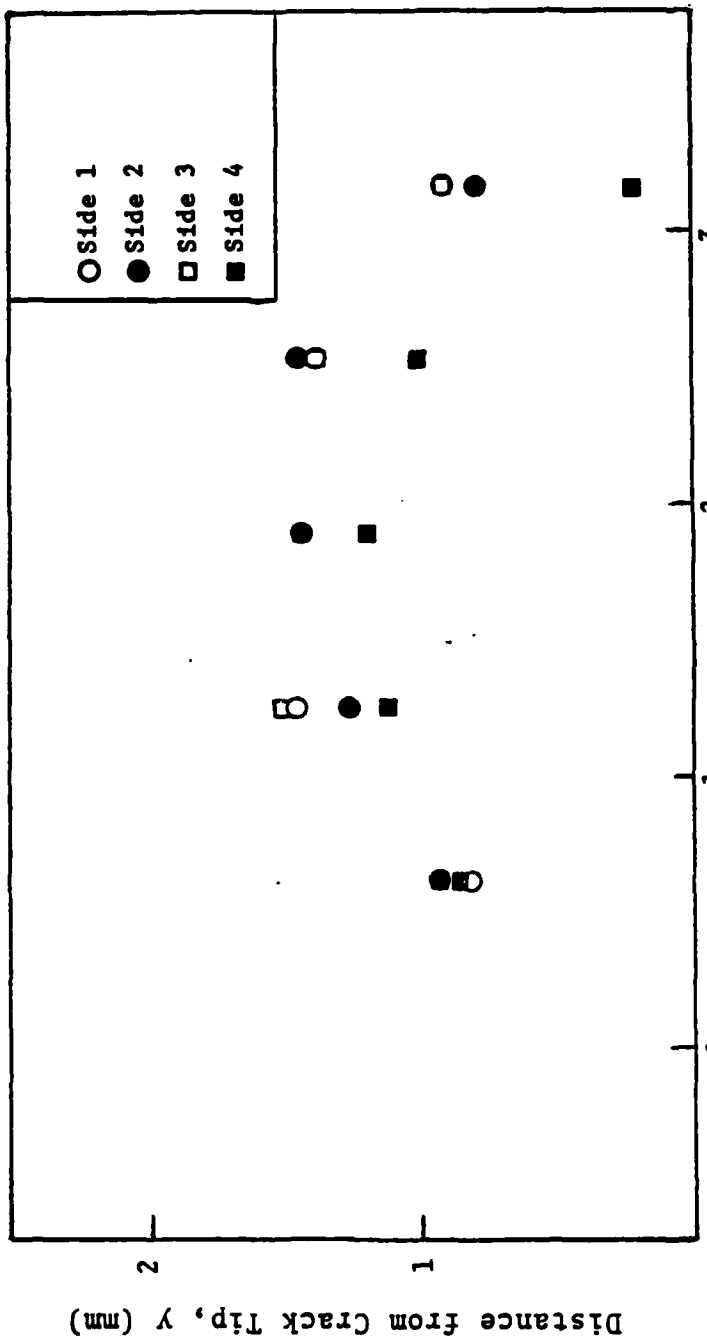

Figure 11: Contour Lines of Depth 0.02032mm.

COMPARISON EXPERIMENTAL AND FINITE ELEMENT RESULTS

The finite element analysis discussed previously was performed and the residual deformation after unloading the specimen was calculated. These results were plotted as contraction contours and are shown in Fig. 12. The average results (the average of all four sides as previously discussed) are also plotted from the experiment. The results from the finite element analysis are in good agreement with those obtained from the experiment.

The finite element predicts slightly more plasticity than the experiment predicts. This is expected since the finite element formulation assumes all nonlinearity is due to plastic (or permanent) deformation. In real materials, however, there is some recoverable nonlinear deformation (i.e., nonlinear elastic deformation). The averaging, material inhomogeneity and error in the two methods more than account for the deviations (less than 4%, maximum).

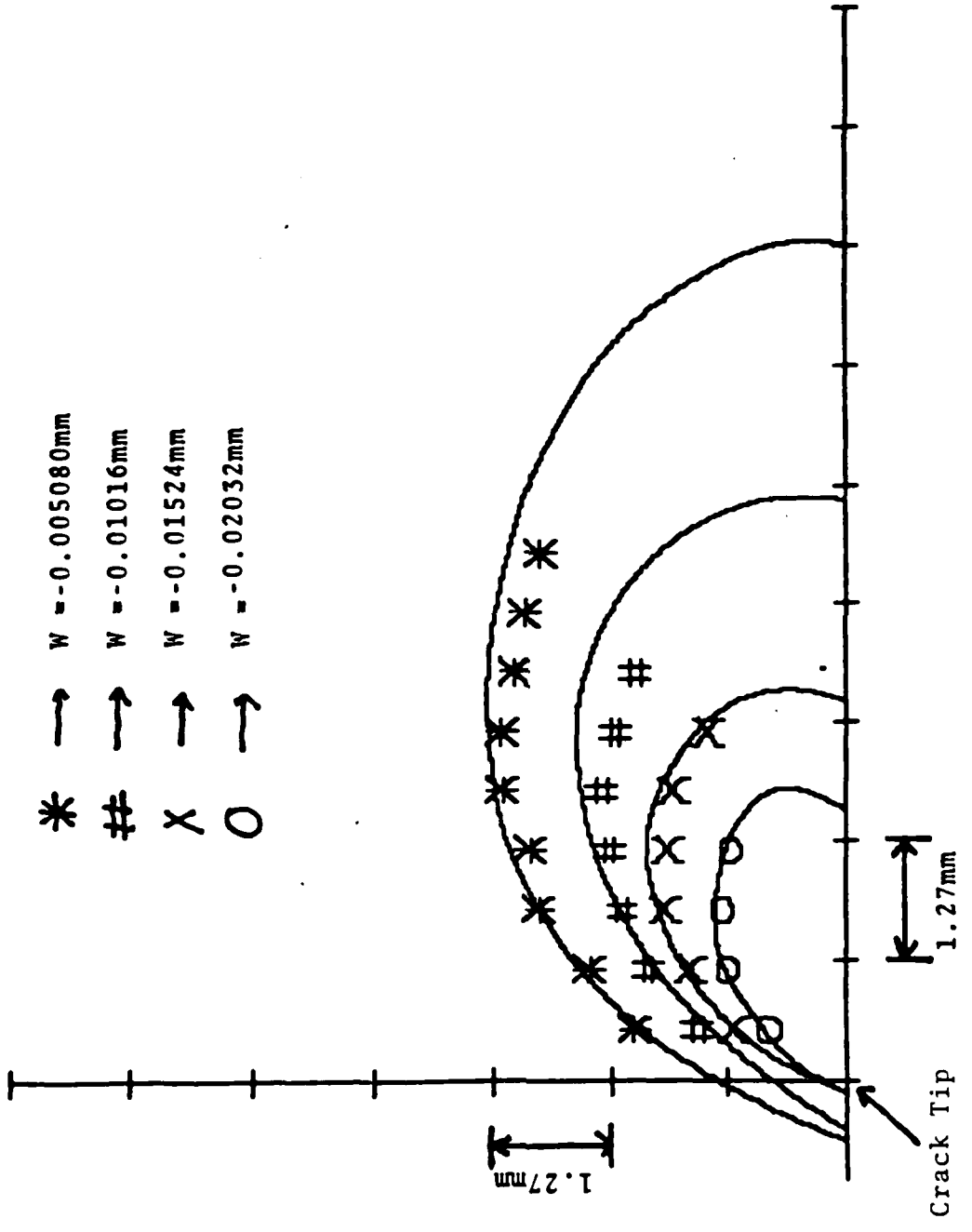

Figure 12: Comparison of Surface Displacements.

CONCLUDING REMARKS

Comparison was made between the experimental and finite element surface contractions for a center-cracked panel. The results compare favorably indicating the accuracy and realistic modeling of this finite element formulation and modeling. The deviations between the results which were observed are less than can be accounted for due to inherent error in the measurements. In fact, the results are more accurate than one would expect.

It is important to highlight several factors when discussing three dimensional finite element analyses in general, and in particular for nonlinear problems. The results are highly dependent on the grid characteristics and on the convergence algorithm employed. Additional degrees of freedom do not guarantee a more accurate solution [1,2,3]. When employing three dimensional finite element models, convergence studies alone are not sufficient. Comparison between predictions and true material behavior is essential. With regard to fracture problems, it is essential to compare predictions from analysis with local parameters as erroneous local models can be forced to produce results which agree globally (i.e., on remote quantities, e.g., nonlinear compliance).

The unique aspect of the study presented in this paper is the direct comparison with experimentally measured local quantities demonstrates the accuracy of the modeling employed. This approach can now confidently be applied to fracture problems for the testing of fracture criteria and the prediction of crack growth and instability. Without such a demonstration, numerical solutions and verification of failure criteria are always suspect. Due to the complicated nature of the problem, each component of the analysis must be verified independently to guarantee accurate solutions and meaningful predictions. This component is lacking in three-dimensional studies reported to date.

ACKNOWLEDGEMENT

This work was sponsored by the Office of Naval Research under Contract Number: N00014-84-K-0027.

REFERENCES

1] E. Thomas Moyer, Jr. and H. Liebowitz, "Plastic Deformation and Hardening Characteristics in Three-Dimensional Fracture Specimens. Presented at the ICF International Symposium on Fracture Mechanics (Proceedings published in China Science Press), Beijing, China, November 22-25, 1983.

2] E. Thomas Moyer, Jr. and Harold Liebowitz, "Effect of Specimen Thickness on Crack Front Plasticity Characteristics in Three-Dimensions." Presented at the Sixth International Conference on Fracture, New Delhi, India, December 4-10, 1984.

3] E. T. Moyer, Jr. and H. Liebowitz, "Finite Element Methodology for Elastic-Plastic Fracture Problems in 3-Dimensions." To appear in the commemorative issue of the Journal of Numerical Methods in Engineering in memory of Bruce Irons, 1985.

4] R. Hill, The Mathematical Theory of Plasticity, Oxford University Press, London, 1956.

5] S. W. Key, "A Finite Element Procedure for the Large Deformation Dynamic Response of Axisymmetric Solids." Computer Methods in Applied Mechanics and Engineering, Vol. 4, pp. 195-218, 1974.

APPENDIX D:

"Accurate Modeling of Ductile and Creep Fracture Specimens and Processes,"

By: E. Thomas Moyer, Jr.

Presented at the ASM Conference on Fatigue, Corrosion Cracking, Fracture Mechanics and Failure Analysis, 2-6 December 1985, Hotel Utah, Salt Lake City, Utah.

ACCURATE MODELING OF DUCTILE AND CREEP FRACTURE SPECIMENS AND PROCESSES

By

E. Thomas Moyer, Jr.
Senior Research Engineer

This study was sponsored under
ONR Contract #N00014-84-K-0027

School of Engineering and Applied Science
The George Washington University
Washington, D.C. 20052

ABSTRACT

The modeling of fracture specimens and the application to growth problems is discussed for elasto-plastic materials. Emphasis is placed on modeling three-dimensional effects and slow crack growth. Extensions to creep modeling is discussed through reference. Directions of on-going and needed future research is included.

The modeling of fracture phenomena in materials which exhibit nonlinearities has been a topic of interest for many years. As early as the 1940's, researchers have recognized that real materials used in engineering practice exhibit both material and geometric nonlinearities. Since that time, much effort has been made to address and quantify the effect of nonlinearities on fracture and ultimate failure of materials. The purpose of this paper is to summarize many aspects of the modeling of nonlinear fracture mechanics. Specifically, the paper will address the elasto-plastic and elasto-visco-plastic behavior of metallic materials and the applicability of modeling phenomena to fracture problems in these regimes. The emphasis will be on numerical modeling schemes which can be experimentally verified and computationally implemented. Failure criterion and fracture modeling is the topic of a separate study.

The problem of modeling fracture problems in nonlinear materials can be subdivided into three major numerical (or

theoretical) problems: the constitutive modeling of the fundamental nonlinearities (both geometrical and material), the prediction of stable crack growth and fracture instability, and the numerical modeling of stable crack growth. This paper will address the computational approach to fracture modeling and the three-dimensional nature of ductile crack specimens. Discussion will also be presented on the modeling of stable crack growth from a computational viewpoint. Failure and fracture prediction can only be intelligently addressed through studies employing accurate modeling of the nonlinear problem and are in the realm of ongoing and incomplete research. The methodology for time dependent visco-plastic behavior will be discussed as extensions and modifications of these problems.

COMPUTATIONAL APPROACH TO ELASTIC-PLASTIC FRACTURE PROBLEMS

Many authors have demonstrated the three-dimensional nature of ductile fracture phenomena (for a review of the literature, see [1]). To address the accuracy of the Finite Element Method and standard plasticity analyses for analyzing fracture specimens it is necessary to examine the local deformation near the crack. Several authors have demonstrated that quantitative agreement with gross specimen quantities such as compliance, global energy (including "Energy Integrals"), gauge displacements, etc. do not guarantee accurate local predictions (see, for example, [2,3,4]). To

address this problem, a local deformation prediction is compared with experiment.

A panel of overaged 7075 (T7651) aluminum was tested experimentally. The specimen was a center-cracked panel with width 8.89cm and crack length to width ratio of 0.5. The specimen was loaded to the highest applied load precluding crack growth and subsequently unloaded. The residual surface deformations were measured using a special LVDT probe and measuring technique described in [5].

The same panel was analyzed using the Finite Element Method. J-flow theory plasticity was employed with a multilinear uniaxial hardening curve. A mixed kinematic and isotropic hardening law with balanced weights was employed together with an adaptive load incrementation scheme [6]. Geometric nonlinearity was modeled using the Updated-Lagrangian approach [6,1]. The converged idealization and complete formulation of the problem can be found in [1]. The panel was loaded incrementally and unloaded to zero applied load. As expected, much residual stress and deformation remained. The residual displacements on the specimen surface were compared with experiment. The comparative results are summarized in Figure 1. The solid lines are the numerically predicted surface constrictions and the discrete points are from the experimental data.

The average of the four sides was compared as the local inhomogeneity and lack of symmetry is virtually eliminated in

the experimental average. The results demonstrate the accuracy of the finite element modeling and solution procedure being employed. The experimental data and predicted contours differ by less than 3%. This is more accurate than was expected comparing with claims made for the finite element solution of crack problems in two dimensions.

The comparison presented above and described fully in [5] demonstrates the accuracy of the current numerical approach and modeling. The results predicted subsequently would model fairly well the true deformation in engineering fracture specimens. The remainder of the problems to be discussed will qualitatively examine some of the more important aspects of fracture specimens and modeling.

To investigate the effect of material hardening model, a center-cracked panel 8.89cm wide was studied. The crack length to width ratio is 0.5 and the specimen length to width ratio is 2.0. The idealization is the same as discussed previously [1]. The loading is normal to the crack direction and reaches a maximum load equal to 1/3 for the material yield stress. The material is modeled as either exhibiting kinematic hardening behavior, isotropic hardening behavior or a mixed hardening behavior (as described previously). Since the global applied loading is monotonic, the three hardening models would predict identical response if the local deformation were truly proportional in nature (assuming no crack growth).

Figures 2, 3 and 4 show the yield zones on the surface of the specimen at maximum load for each of the hardening models. The local response is definitely nonproportional. The isotropic model predicts more yielding on the crack extent line than either of the other two models. This would suggest a more ductile response ahead of the crack (implying a greater tendency toward stable crack growth prior to final failure). The results with mixed hardening have proven to be the closest to what is observed experimentally. The others, therefore, should be viewed with that fact in mind.

The largest affect of hardening model is the yield characteristics on the crack extent line. The maximum yield radius and the "skewing" of the yield zones is fairly independent of the hardening model. It is important to emphasize, however, that the differences between the predictions are significant and the local response is highly nonproportional.

Figures 5, 6 and 7 show the yield zones on the midplane of the specimen. These zones demonstrate the same hardening effects as do the surface zones. The greatest influence of hardening model is seen on the line of crack extent. On the midplane of the specimen, a plane-strain type of zone would be expected (i.e., similar to zones predicted with a 2-dimensional plane-strain analysis). The mixed hardening model demonstrates the most realistic results (which is consistent with the surface observations).

The results demonstrate that the local response near a crack is not of the proportional type. This has significant implications with respect to valid failure criteria and analysis models. The results presented also demonstrate that a mixed hardening rule is the most realistic for modeling the aluminum alloys investigated so far and is probably best for most engineering metals. A complete discussion of the hardening modeling effects and the implications of these findings can be found in [7].

To study thickness effects, the specimen thickness is varied and the different zone sizes and shapes are reported (the same center-cracked panel is used with mixed hardening assumptions). Figures 8a, 8b, 8c and 8d show the surface yield zones as a function of thickness. The thickness is varied from 1.5 times the ASTM plane strain requirement to a very thin panel dimension (total thickness of about 3mm). Even for the thinnest specimens, the classical "plane stress" zones are not recovered demonstrating that the assumptions of 2-D plane stress are not valid for this specimen. Also, even for very thick specimens, the predicted zone does not conform to classical plane strain zones (the surface deformation will never conform to 2-D assumptions since not only is the surface normal stress zero but the strains required to produce plastic incompressibility require a nonuniform normal strain through the thickness which is incompatible with 2-D plane strain). It is important to remember that a state of stress with zero

normal and antiplane shear does not need to reduce to 2-D plane stress.

Figures 9a, 9b, 9c and 9d show the midplane zones for the four thicknesses. As the thickness increases, it is obvious that the zones approach plane strain zones (which they should). Even at the largest thickness, however, they show some skewing due to the finite geometry. From these results, the ASTM criterion may not be good enough for ductile materials.

The yield radii and extent of yielding ahead of the crack tip are summarized in the tables. It is important to note that the yield radius changes by about 10% with thickness, however, the yielding ahead of the tip changes drastically and, thus, the plastic area changes. Since more energy is being dissipated with larger areas, the ductility and fracture properties are obviously dependent.

This study demonstrates the thickness effects on local yield characteristics and also mandates 3-D analysis for accurate quantitative predictions. A complete discussion on the effects of specimen thickness can be found in [6].

MODELING STABLE CRACK GROWTH

The modeling of stable crack growth is important for the prediction of ductile fracture phenomena. The processes of stable crack growth and plasticity are almost always present in application and, indeed, are

Table 1a - Yield radii as a function of thickness for surface yield zones

Thickness	r_{max}/a	r_o/a
T = 2.54cm	0.307	0.045
T = 1.27cm	0.327	0.075
T = 6.35mm	0.331	0.205
T = 3.175mm	0.343	0.296

r_{max} → maximum yield radius
r_o → yield radius along crack line

Table 1b - Yield radii as a function of thickness for midplane yield zones

Thickness	r_{max}/a	r_o/a
T = 2.54cm	0.260	0.039
T = 1.27cm	0.280	0.071
T = 6.35mm	0.283	0.193
T = 3.175mm	0.299	0.288

extremely interrelated. The modeling of this process, however, must be numerically accurate independent of any particular failure criterion.

Ductile fracture is inherently a three-dimensional problem as has been demonstrated both in this paper and elsewhere ([1] provides a review of the topic). No studies to date, however, have successfully modeled a slow growth process in three-dimensions. A major reason for this is the extreme number of degrees of freedom needed to model such a process if standard crack growth (fixed grid) modeling is employed. A

better approach is to employ the "Mesh Adaptive" technique introduced in [8].

The standard method used to simulate crack growth consists of employing a grid with extremely small elements along the line of crack extent. Nodal forces (or displacements through a spring release method [9]) are relaxed at certain load levels to create new free surface. If a criterion independent study is done, this method will yield very good agreement with experiment (see, for example, [10], for a typical example). Convergence studies have demonstrated, however, that a typical Mode I center-cracked panel which exhibits 15% total crack growth can require upwards of 1500 DOF to achieve good accuracy. The extension of this method to three-dimensions, therefore, is not realistic.

In the "Mesh Adaptive" approach, a standard stress analysis is performed until the onset of stable growth is predicted (either directly from experiment or from a theory). The load is then incremented a small amount (the amount is influenced only by numerical convergence, however, an amount correspondent to 2 percent crack growth or less is accurate for most aluminum alloys) and the amount of crack growth is predicted (or calculated from experiment). The near crack mesh is convected to the new location of the crack tip. The stress along the new free surface is relaxed to zero and the new resultant plastic state is calculated in the entire specimen. The new stress state is then extrapolated to the new geometry and the process is repeated for each increment of crack growth.

Comparison with this experiment has demonstrated this approach to yield accurate predictions for several 2024 aluminum specimens. Convergence studies on a previously studied problem [8] have demonstrated a DOF reduction of about 200% and a computation time reduction of about 100%. For three-dimensional problems, the "Mesh Adaptive" method should yield even greater improvements. Computation time, however, will still be extreme if accurate predictions are desired.

MODELING VISCO-PLASTIC BEHAVIOR

To model visco-plastic or creep behavior the rate equations of stress and strain are formulated to satisfy equilibrium and geometric compatibility. The formulation (an outline of which can be found in [11] in addition to many other standard texts) then requires only the constitutive behavior and flow rule. From the standpoint of fracture mechanics, the material modeling is the only unsolved problem. The fracture modeling is done exactly as in elastic-plastic problems. Fracture prediction, however, is still an open question.

The constitutive modeling of visco-plastic behavior is still an open issue. Generally the models can be divided into two categories: those that depend on internal variables and those which utilize only stress and strain measures for their flow rules. A good (although somewhat biased review can be

found in [11]). From a computational standpoint, a visco-plastic flow rule should be only implicitly dependent on time and contain parameters which are true material constants. The last requirement is the most difficult to achieve.

An additional problem involved is the material variability or "scatter" in the visco-plastic regime. Many of the materials involved show uniaxial scatter of 100% or greater in their primary creep behavior [12]. A theory, however, will not predict this scatter if it is deterministic. Two approaches are open: choose a statistical theory or attempt to qualitatively model applications by quantification of a single material sample. If the latter approach is chosen, consistent results can be obtained. This approach is the one currently employed by most authors and reasonable results are obtained (for a review, see [13]).

Studies are underway to address these problems, however, visco-plastic modeling of engineering fracture problems is still an unsolved and open question. The problem, however, is one of constitutive modeling. Fracture modeling is identical to that for elasto-plastic problems.

SUMMARY

The emphasis of this paper has been on the three-dimensional nature of ductile fracture specimens, a short review of the state-of-the-art modeling and an emphasis on the importance of careful modeling and the importance of convergence studies for nonlinear problems. The three-dimensional nature of fracture must be addressed before meaningful prediction can be made on the failure of real engineering materials in application. Two-dimensional studies are a necessary first step in the research process, however, great caution needs to be exercised in the interpretation of results as the criteria which appear to predict reasonable answers to a few, idealized example problems may not have any application to real situations (e.g., [14]).

ACKNOWLEDGMENT

This work was sponsored under the Office of Naval Research Contract #N00014-84-K-0027 to The George Washington University.

REFERENCES

1. Moyer, E. T., Jr. and Liebowitz, H., Finite Element Methodology for Elastic-Plastic Fracture Problems in 3-Dimensions. To appear in the Commemorative Issue of J. Numerical Methods in Engineering in Memory of Bruce Irons (1985).

2. Jolles, M., Schroedl, M. and Watson, T. J., On the Geometry Dependence of R-Curves, 21st Annual Mtg. of SES, Virginia Polytechnic Institute and State University, Blacksburg, Virginia, October 15-17 (1984).

3. Kakreti, A. R., Khan, A. S. and Iranmanesh, A., "Fracture Prediction in Elastic-Plastic Problems Using Finite Element Method" in Applications of Fracture Mechanics to Materials and Structures (eds. G. C. Sih, E. Sommer and W. Dahl, Nijhoff, Hague) (1983).

4. Bakker, A., "On the Numerical Evaluation of J in 3-Dimensions" in Applications of Fracture Mechanics to Materials and Structures (eds. G. C. Sih, E. Sommer and W. Dahl, Nijhoff, Hague)(1983).

5. Moyer, E. T., Jr., Poulose, P. K. and Liebowitz, H., Prediction of Plasticity Characteristics for Three-Dimensional Fracture Specimens Comparison with Experiment. Accepted for publication in International J. Engineering Fracture Mechanics, October (1985).

6. Moyer, E. Thomas, Jr. and Liebowitz, Harold, Effect of Specimen Thickness on Crack Front Plasticity Characteristics in Three-Dimensions. Proceedings of the 6th International Conference on Fracture, New Delhi, India, Dec. 4-10 (1984).

7. Moyer, E. Thomas, Jr. and Liebowitz, H., Plastic Deformation and Hardening Characteristics in Three-Dimensional Fracture Specimens. Presented at ICF International Symposium on Fracture Mechanics (Proceedings published in China Science Press), Beijing, China, Nov. 22-25 (1983).

8. Moyer, E. Thomas, Jr. and Liebowitz, Harold, A Mesh Adaptive Method for Modeling Slow Crack Growth. Presented at 21st Annual Mtg. of SES, Virginia Polytechnic Institute and State University, Blacksburg, Virginia, October 15-17 (1984)

9. Lee, James D. and Liebowitz, Harold, Considerations of Crack Growth and Plasticity in Finite Element Analysis, J. of Computers and Structures, 8, No. 3/4, pp. 401-403 (1978).

10. Gifford, L. N. and Hilton, P. D., Preliminary Documentation of PAPST - Nonlinear Fracture and Stress Analysis by Finite Elements, NDW-DTNSRDC 3960/43b, Feb. (1981).

11. Chaboche, J. L. and Rousselier, G., On the Plastic and Viscoplastic Constitutive Equations, J. Pressure Vessel Tech., 105, p. 153 (1983).

12. Garwood, S. J., "Effect of Temperature of Orientation and Constraint on the Toughness of A533B Class I Steel" in Applications of Fracture Mechanics to Materials and Structures (eds. G. C. Sih, E. Sommer and W. Dahl, Nijhoff, Hague)(1983).

13. Wilson, R. E. and Palazotto, A. N., Viscoplasticity in a Superalloy at Elevated Temperatures Considering Tension and Compression Loading, International J. Engineering Fracture Mechanics, 22, p. 927 (1985).

14. Jolles, M. I., Schroedl, M. A. and Watson, T. J., Three-Dimensional Aspects of Fracture Mechanics. Presented at 22nd Annual Mtg. of SES, Pennsylvania State University, University Park, Pennsylvania, October 6-9 (1985).

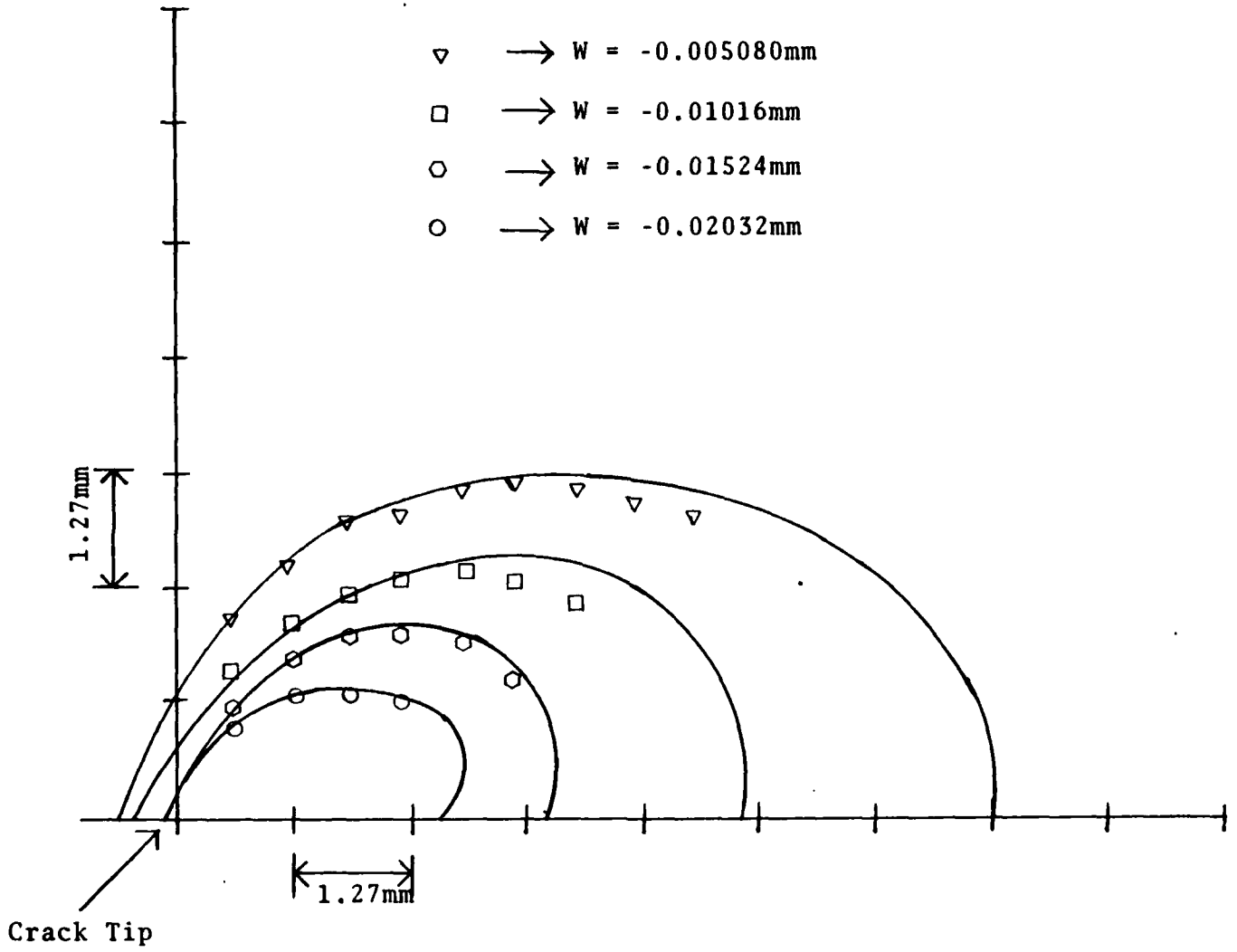

Fig. 1 - Comparison of surface displacements

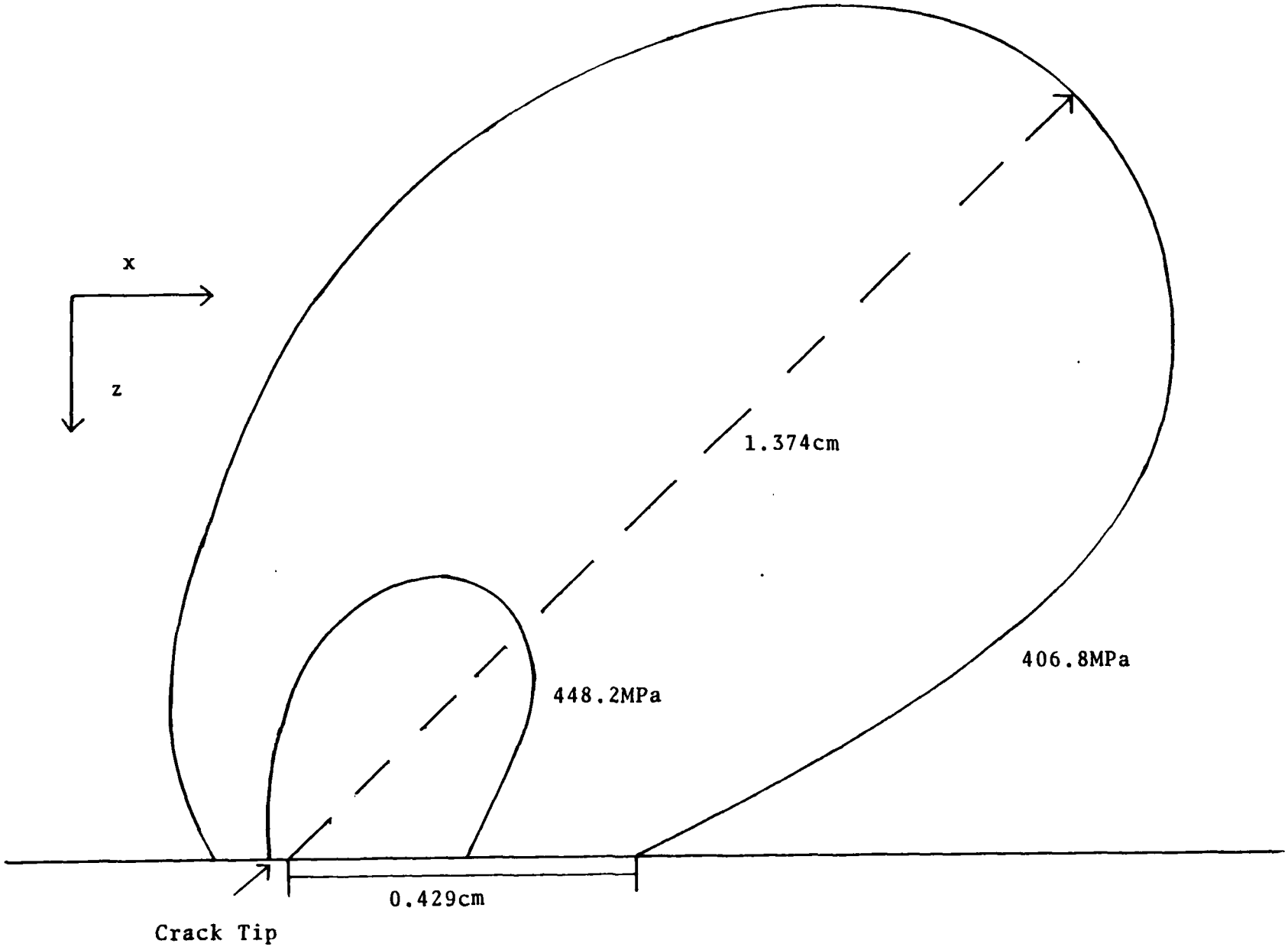

Fig. 2 - von Mises stress contours near the crack tip on specimen surface at maximum load - isotropic hardening

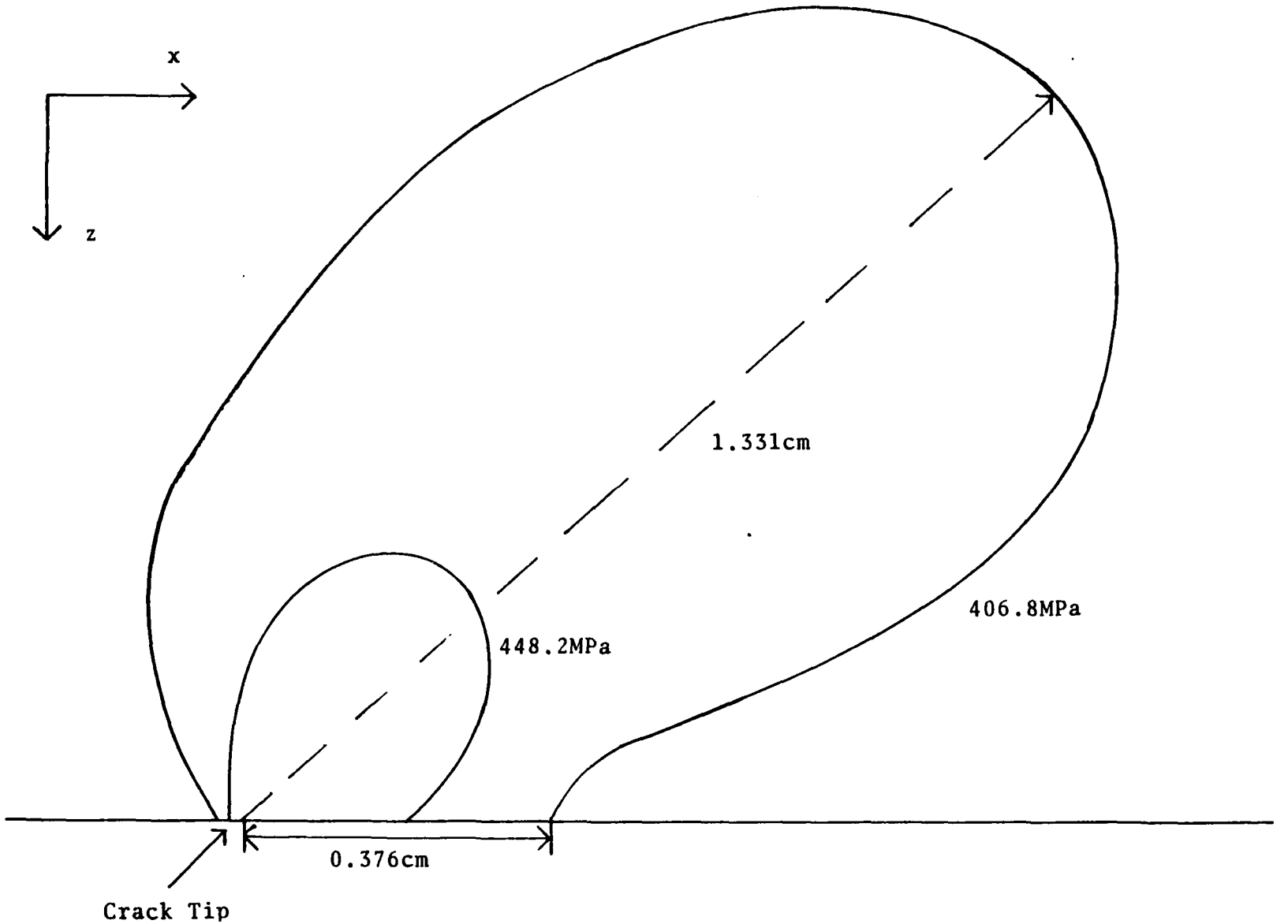

Fig. 3 - von Mises stress contours near the crack tip on specimen surface at maximum load - kinematic hardening

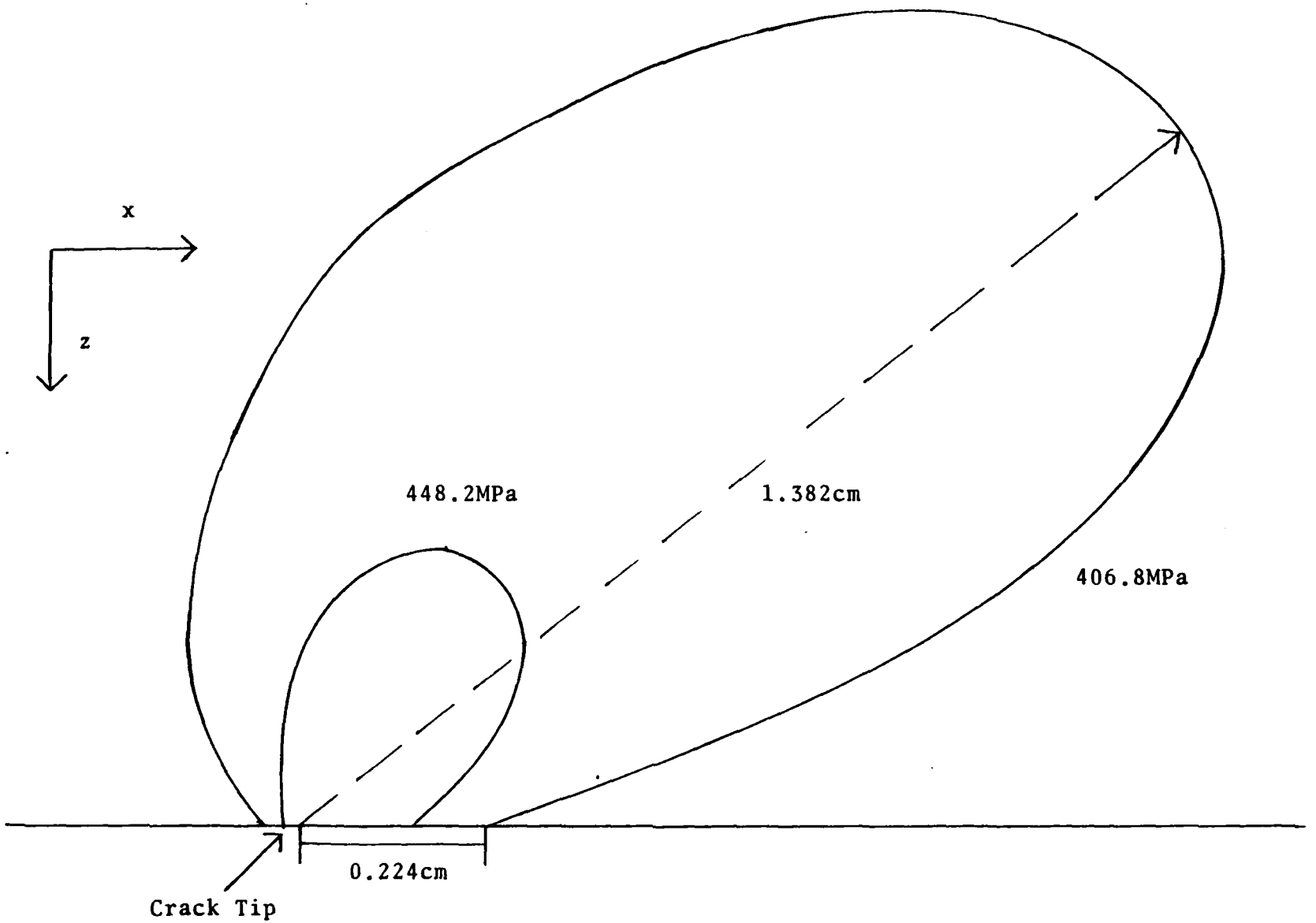

Fig. 4 - von Mises stress contours near the crack tip on specimen surface at maximum load - mixed hardening

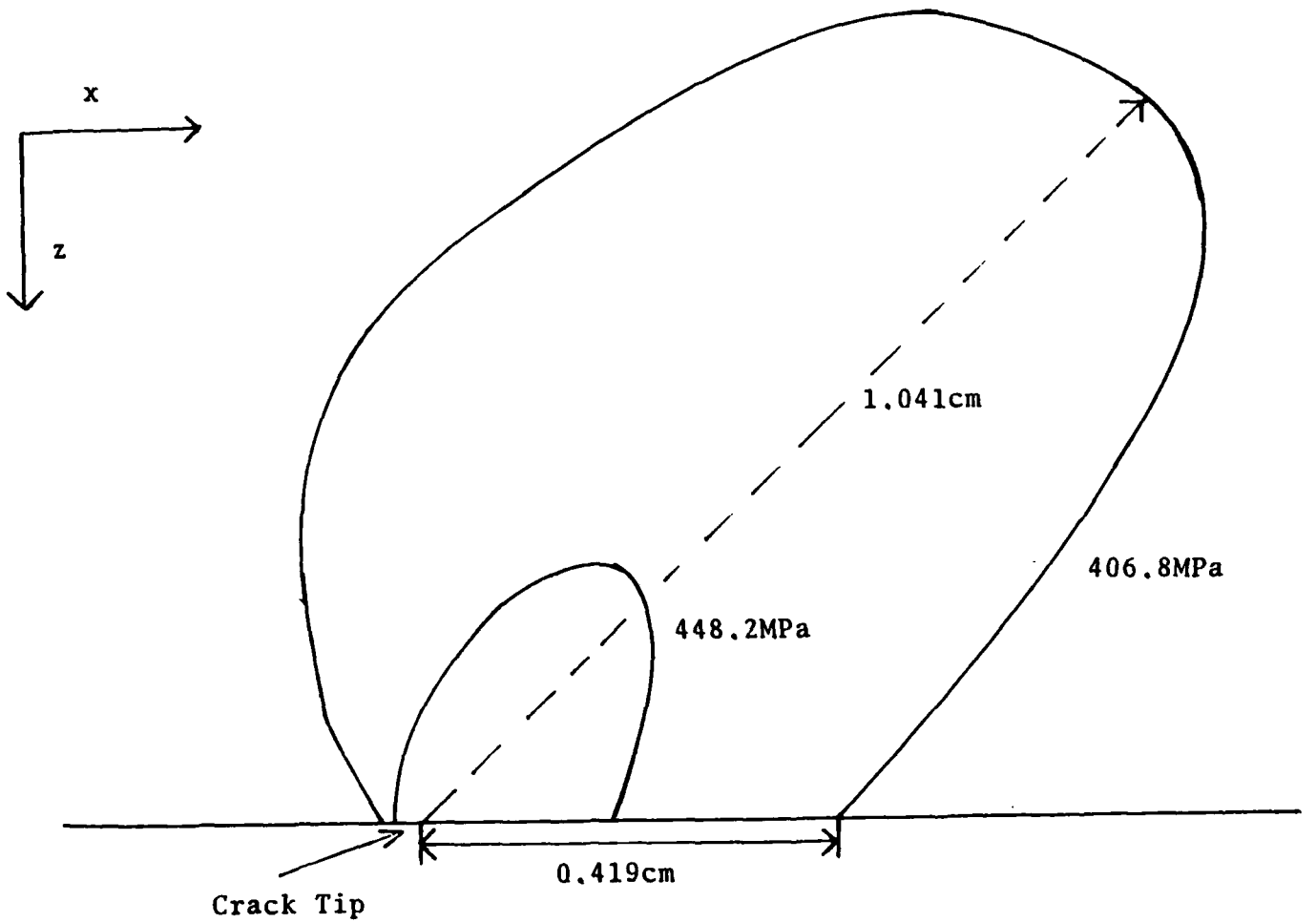

Fig. 5 - von Mises stress contours near the crack tip on specimen midplane maximum load - isotropic hardening

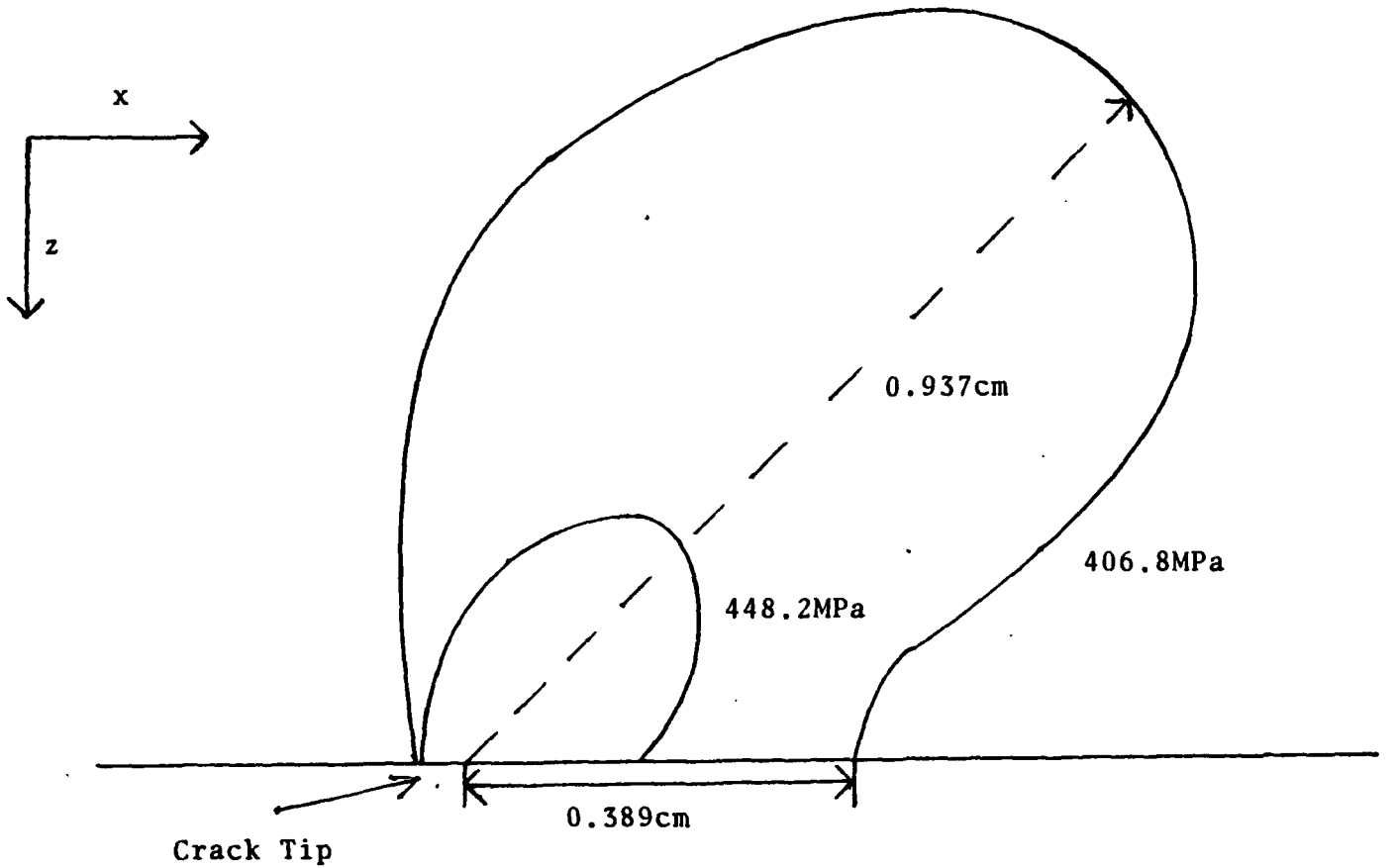

Fig. 6 - von Mises stress contours near the crack tip on specimen midplane at maximum load - kinematic hardening

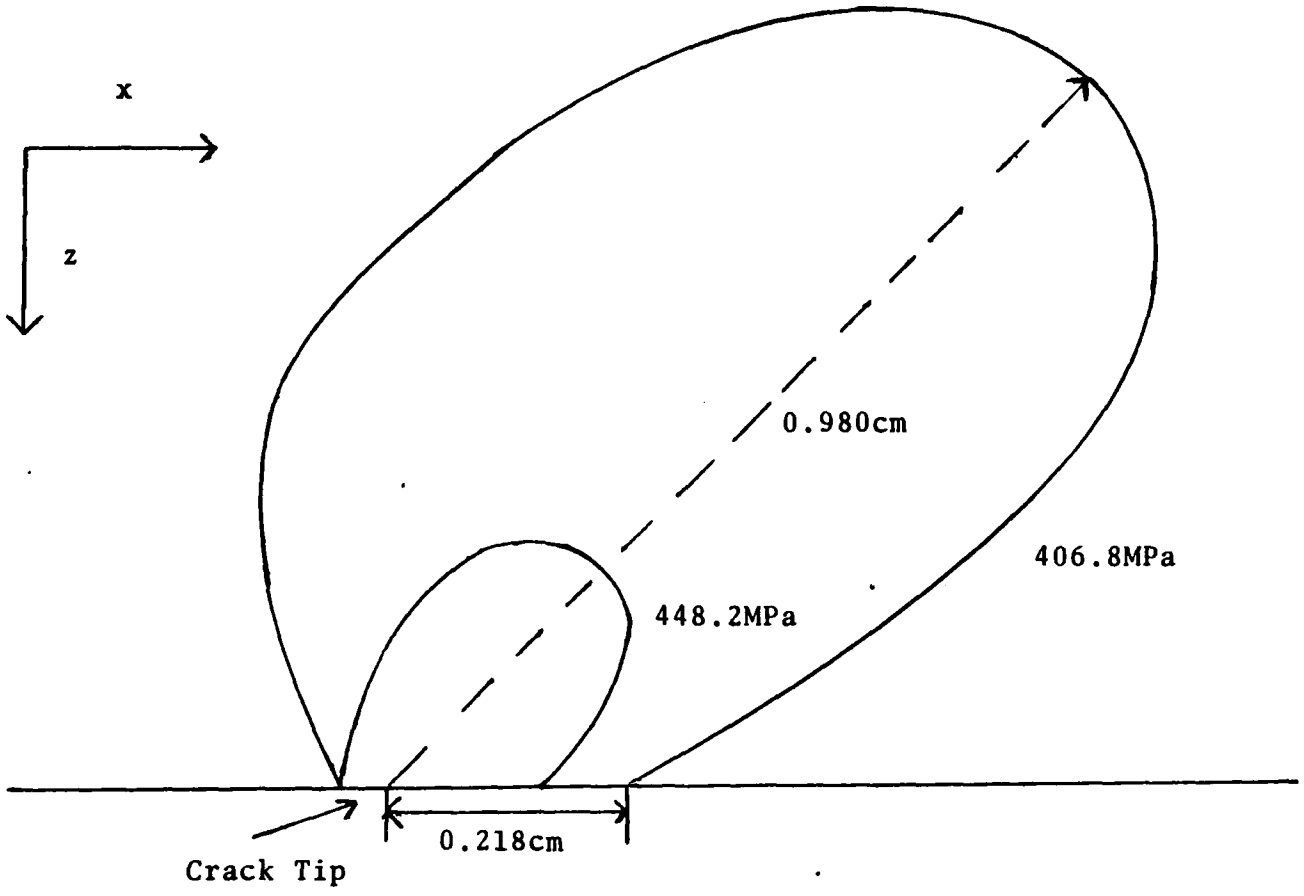

Fig. 7 - von Mises stress contours near the crack tip on specimen midplane at maximum load - mixed hardening

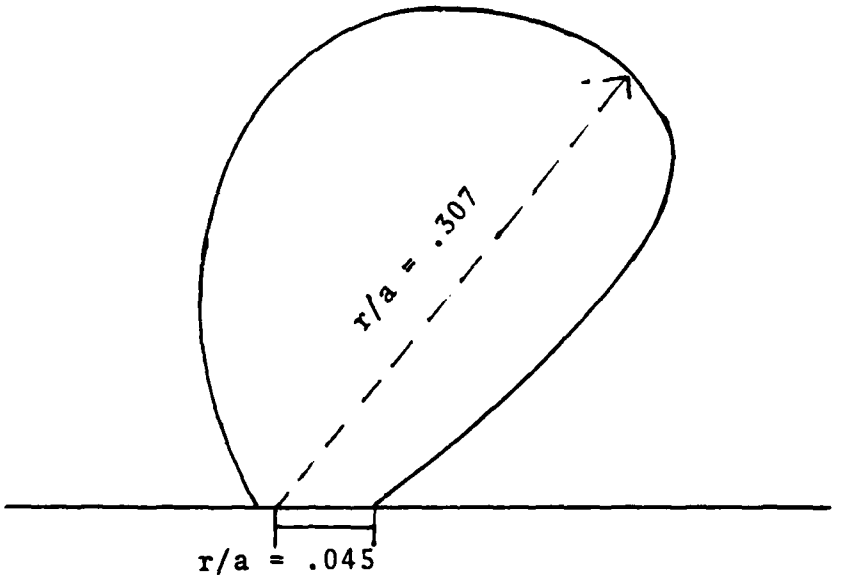

Fig. 8a - Surface yield zones for specimen with 2T = 2.54cm

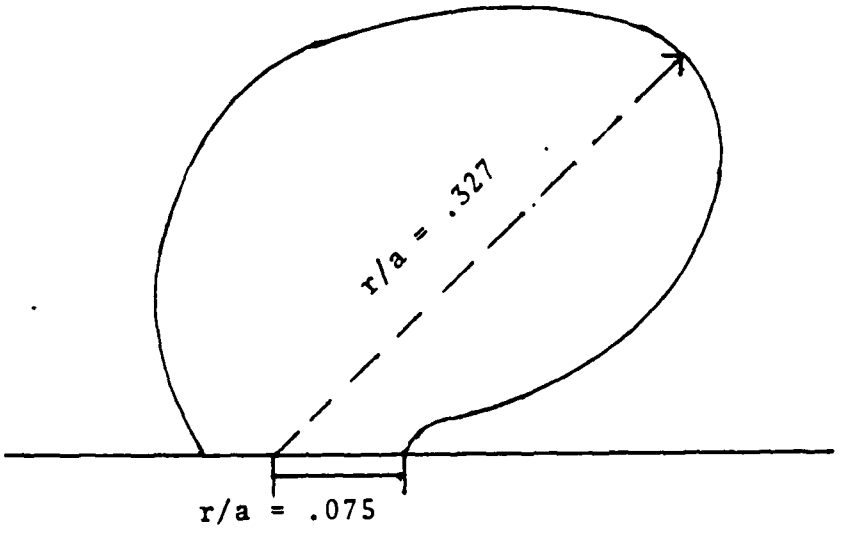

Fig. 8b - Surface yield zones for specimen with 2T = 1.27cm

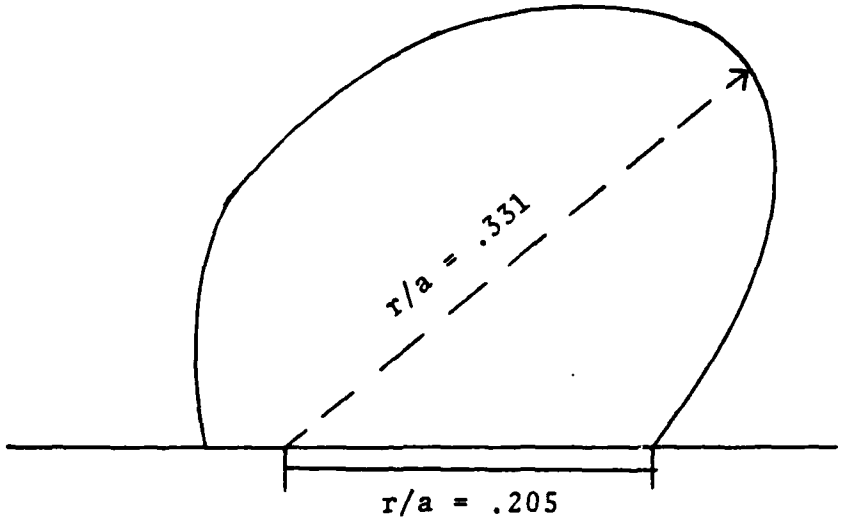

Fig. 8c - Surface yield zones for specimen with 2T = 6.35mm

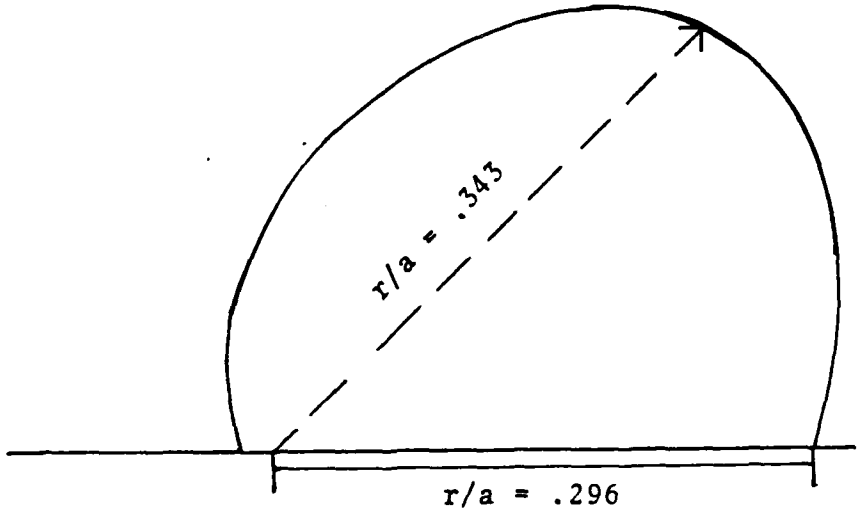

Fig. 8d - Surface yield zones for specimen with 2T = 3.175mm

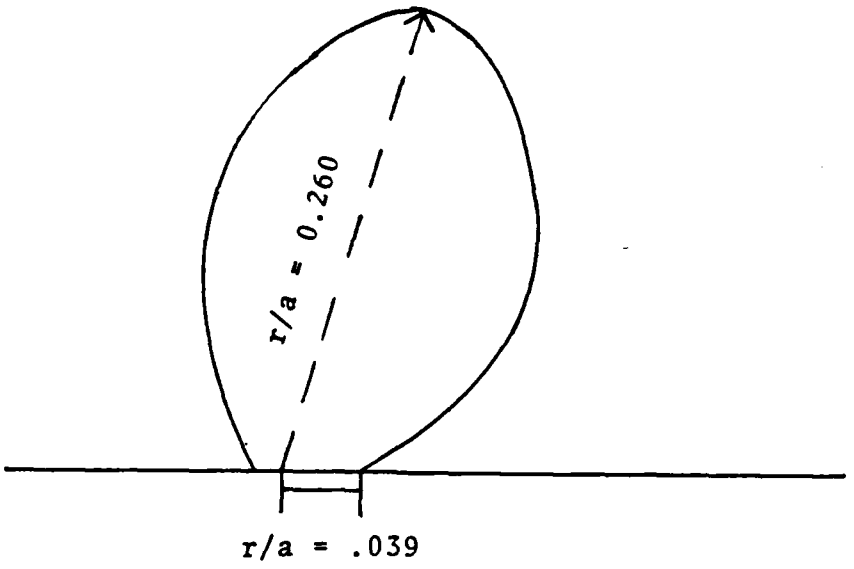

Fig. 9a - Midplane yield zones for specimen with 2T = 2.54cm

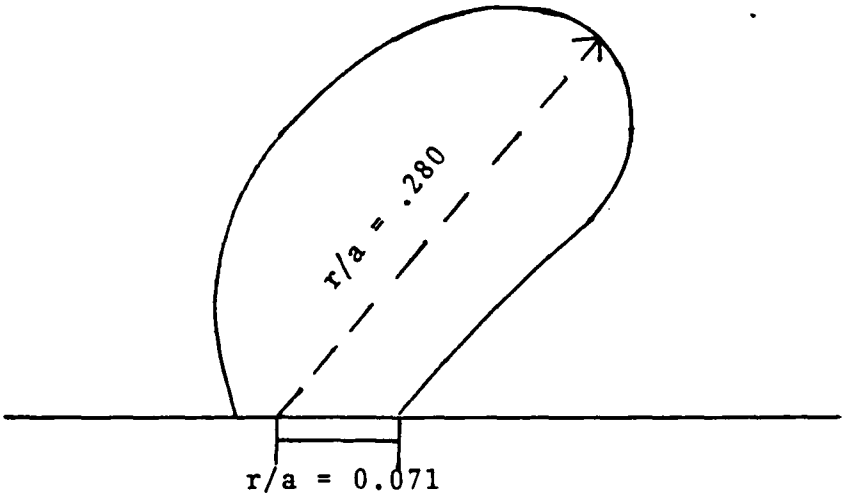

Fig. 9b - Midplane yield zones for specimen with 2T = 1.27cm

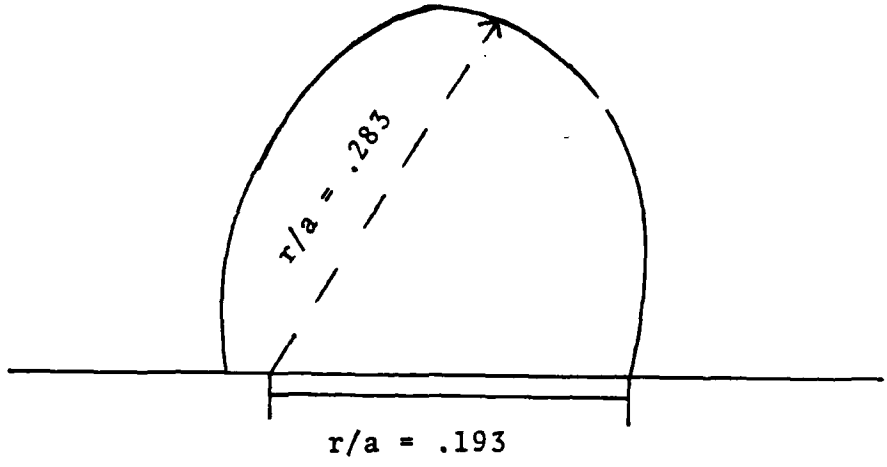

Fig. 9c - Midplane yield zones for specimen with 2T = 6.35mm

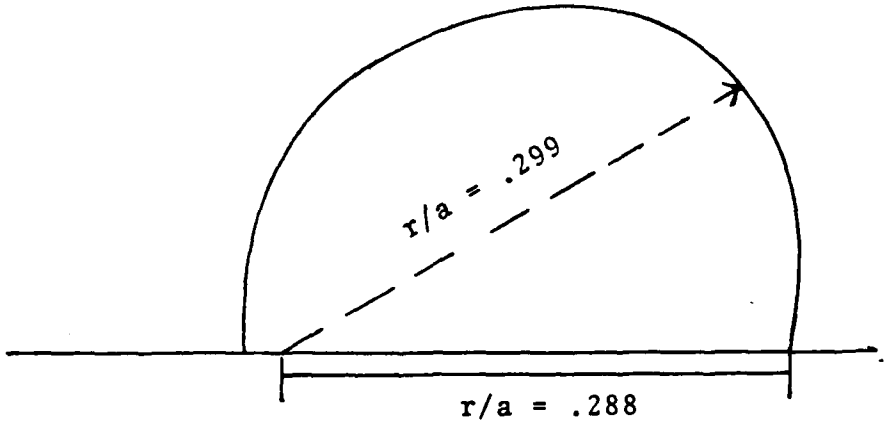

Fig. 9d - Midplane yield zones for specimen with 2T = 3.175mm

APPENDIX E:

Creep Testing and Constitutive Modeling

By: E. Thomas Moyer, Jr. and P. K. Poulose.

The first step in characterizing creep crack growth is the establishment of valid constitutive parameters for modeling the deformation process. To this end, several uniaxial tests were conducted. These results are then processed and correlated with postulated constitutive models.

Testing Apparatus

An "ATS" Lever Arm Tester Series 2410 was used for the creep testing. The test stand is designed to apply static stress to a test specimen for an extended period of time at a constant elevated temperature. The apparatus consists of a balance beam that connects the test specimen to a weight pan. Ratios of 3 to 1 and 20 to 1 are designated between the weight pan and the specimen. The lower ratio is used to provide optimum accuracy at lower loads. The weight pan is part of the overall weights and is suspended with a chain to prevent bending movements to the load trains.

On the specimen side of the machine, a balance beam leveling motor compensates for the elongation of the test specimen. If this is not available, the balance beam may become unlevel, thus changing the calibration of the weight system. This is important in maintaining the load accuracy within the ASTM requirements.

A tabular furnace with an electrical-resistance winding heats the test specimen through radiation in an air atmosphere. The furnace has three heating zones. The tube is

located in a vertical position, with pull rods connected to the specimen. The temperature is controlled by means of a thermocouple, located in the vicinity of the test specimen, within ±1°C.

When creep data are required, the specimen strain must be measured as a function of time. This is difficult because use of strain-measuring transducers is not practical at the test temperature. A mechanical linkage must be attached to the specimen to transmit the strain to the strain-measuring equipment outside the high-temperature environment. A linear variable differential transformer was used to measure the strain. It consists of a movable metal core that changes the electrical characteristics with small motion associated with strain measurements. The linkage is made of an alloy that can withstand the test temperature encountered.

Specimen Preparation

The test specimens were cut from a 1/2" thick sheet of Alloy 718 with composition listed in Table 1. The tensile axis of the specimen were perpendicular to the rolling direction. The specimens were heat treated and machined to the ASTM specifications. The heat treatment procedure is shown in Table 2. The specimens were then surface treated in order to eliminate any scratches and other stress raisers that may have remained from the machining.

Specimen Loading

Attention was paid to avoid straining the specimens when mounting them in the adapters and load train. With the specimen in place, the load train was examined carefully for any misalignment that may have caused bending of the specimen under load.

The upper load train was suspended from the lever arm, and the compensating weight adjusted so that the lever arm balanced. Strain-measuring clamps and the extensometer were attached to the specimen, and the load train was inserted into the furnace with the specimen centered. The specimen was stabilized at the temperature before loading at least for one hour.

Loading the weight pan was done smoothly and without excessive shock. This was done by lowering the supporting jack under the load pan. In the case of step loading, the weight was placed on the weight pan in measured increments, and the strain corresponding to each step of loading was recorded.

Temperature Control

The specimen should not be overheated while brought to temperature. To do this, the specimen was brought to 10°C below the desired temperature in about 1-1/2 hours. Then, over a longer period, the specimen was brought to the desired temperature.

Table 1. Chemical Composition of Alloy 718.

Composition, Weight Percent		
0.04 C	Bal. Fe	1.00 Ti
0.19 Mn	51.14 Ni	0.52 Al
0.05 Si	17.96 Cr	0.43 Co
0.005 P	3.12 Mo	0.02 Cu
0.005 S	5.19 Cb and Ta	0.003 B

Table 2. Heat Treatment of Alloy 718.

Anneal at 955°C for 1 hour - air cool
Age at 720°C for 8 hours, furnace cool to 620°C
Hold at 620°C for total aging time of 18 hours

Results

Two series of uniaxial tests were conducted: one at 550°C and one at 650°C. The results are summarized in Tables 3 and 4. The strain vs time curves are shown in Figures 1-9. Evident from these tests is that the specimen exhibits moderate primary creep at 550°C and virtually none at 650°C. This is evident at all the load levels tested. For the 550°C data, at time explicit model was fit to the data. The results are given in Table 5. These results can either be used directly as a

constitutive law, or, can be correlated with a time-implicit differential model allowing for more general hardening. Many candidate models exist and are currently being investigated. The 650°C data exhibits virtually no primary creep. Unfortunately (from a modeling standpoint), much tertiary behavior is evident prior to failure. Since tertiary creep involves many deformation and failure modes simultaneously, modeling is difficult. The approach to be used in fracture studies is to assume tertiary behavior does not occur and that the fracture mechanics models the damage which is not accounted for by the hardening laws of primary and secondary creep.

Fracture tests are currently underway. Compact tension specimens will be loaded at constant load and temperature. Crack growth, crack opening, gauge displacement, mouth displacement, etc., will be measured. Finite element studies are also underway to model the growth. The results will be presented when they are completed.

Table 3. Tensile Properties of Alloy 718 at 550°C.

Yield Strength = 144.08 KSI

Ultimate Strength = 176.78 KSI

Elongation = 20.72%

Specimen Number	Stress (KSI)	Time to Failure
5	152.9	210 hours
4	153.4	87 hours
9	155.1	189 hours
6	155.2	212 hours
7	157.2	190 hours

Table 4. Tensile Properties of Alloy 718 at 650°C.

Yield Strength = 133.89 KSI

Ultimate Strength = 163.67 KSI

Elongation = 25.7%

Specimen Number	Stress (KSI)	Time to Failure
13	143.2	90 minutes
14	132.9	240 minutes
15	110.1	41 hours, 30 minutes
16	99.9	227 hours, 30 minutes

Table 5. 550°C Data Fit to Model.

$$\varepsilon = \varepsilon_0 + \dot{\varepsilon}_0 t + \varepsilon_A (1-e^{-rt})$$

Specimen Number	ε_0	$\dot{\varepsilon}_0$	ε_A	r	Max Error
4	0.0252	2.265×10^{-6}	4.758×10^{-3}	1.612×10^{-3}	1.89%
5	0.0336	2.389×10^{-6}	5.442×10^{-3}	2.353×10^{-3}	1.95%
6	0.0264	2.082×10^{-6}	4.783×10^{-3}	1.806×10^{-3}	1.99%
7	0.0398	4.488×10^{-6}	5.162×10^{-3}	2.983×10^{-3}	1.35%
8	0.0403	3.304×10^{-6}	6.199×10^{-3}	3.339×10^{-3}	1.51%

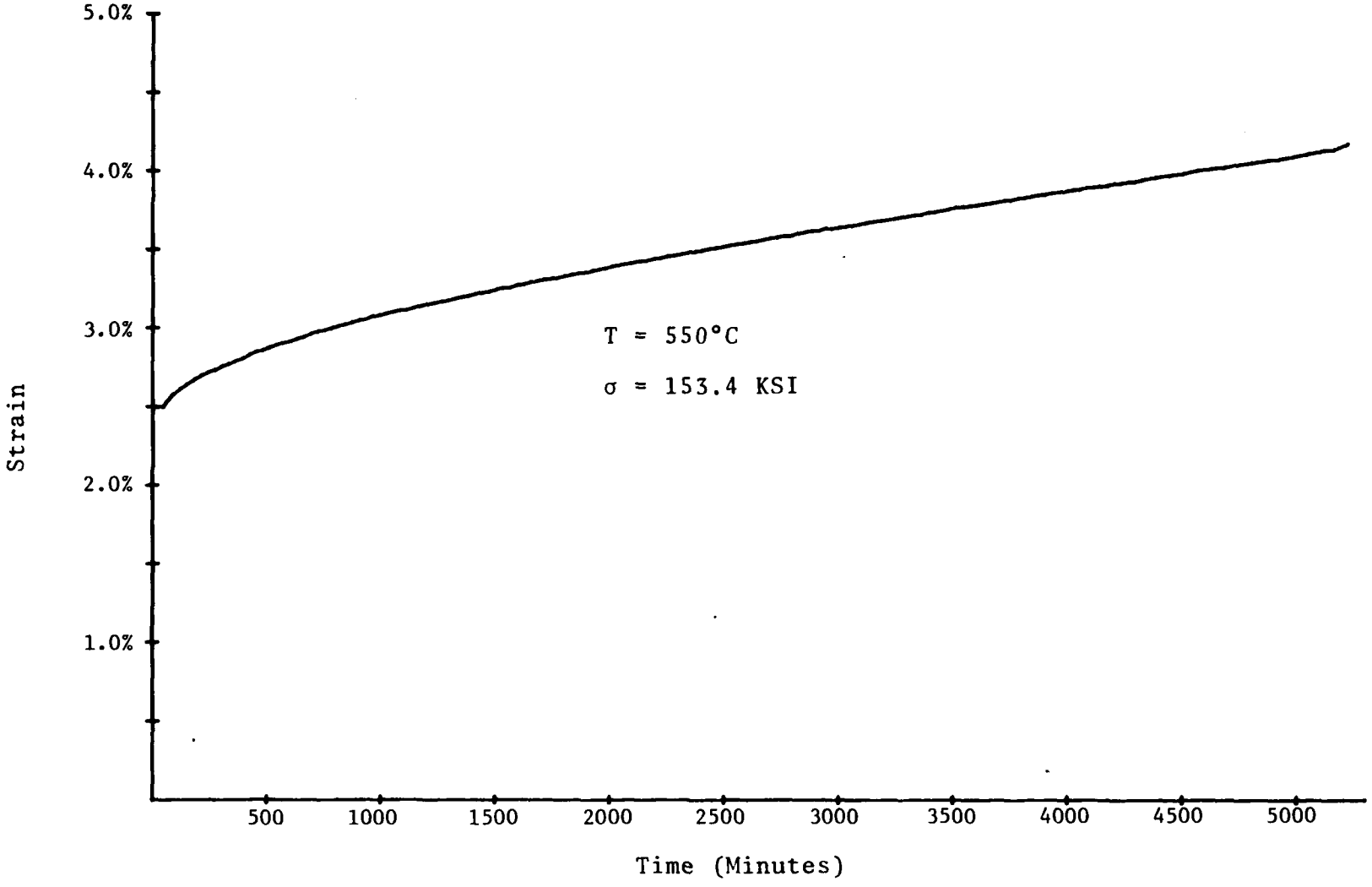

Figure 1: Strain vs Time for Specimen #4.

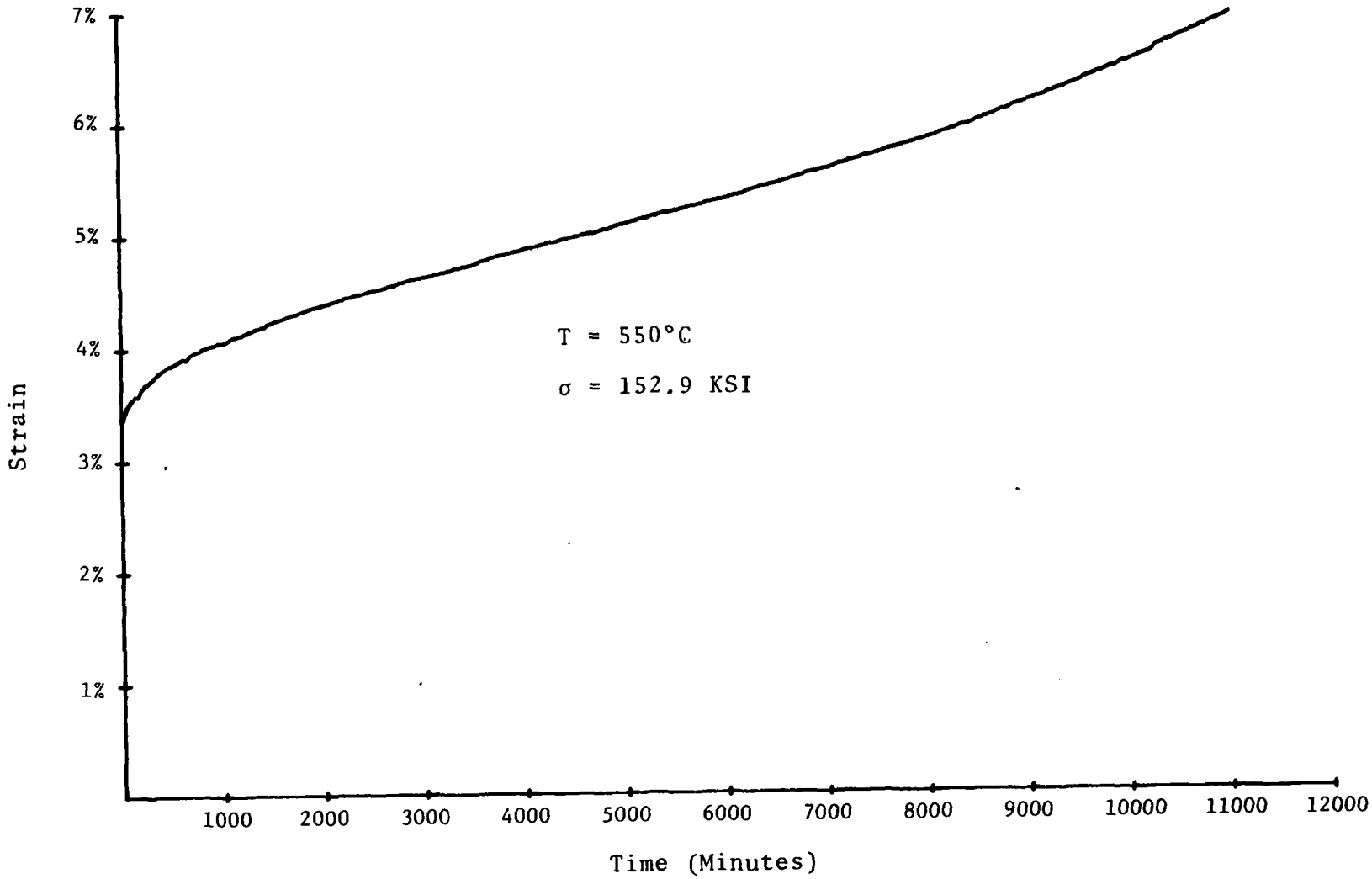

Figure 2: Strain vs Time for Specimen #5.

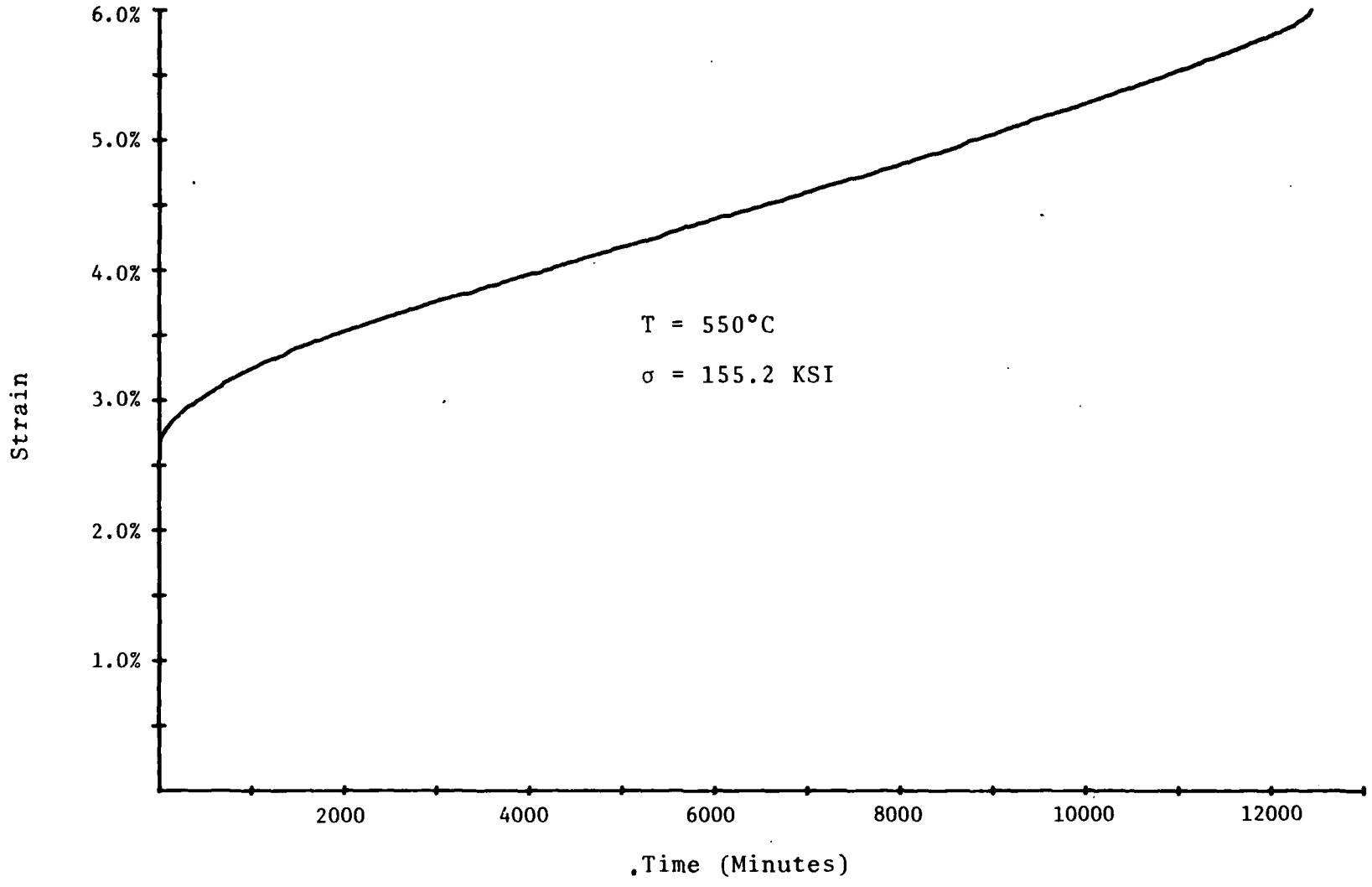

Figure 3: Strain vs Time for Specimen #6.

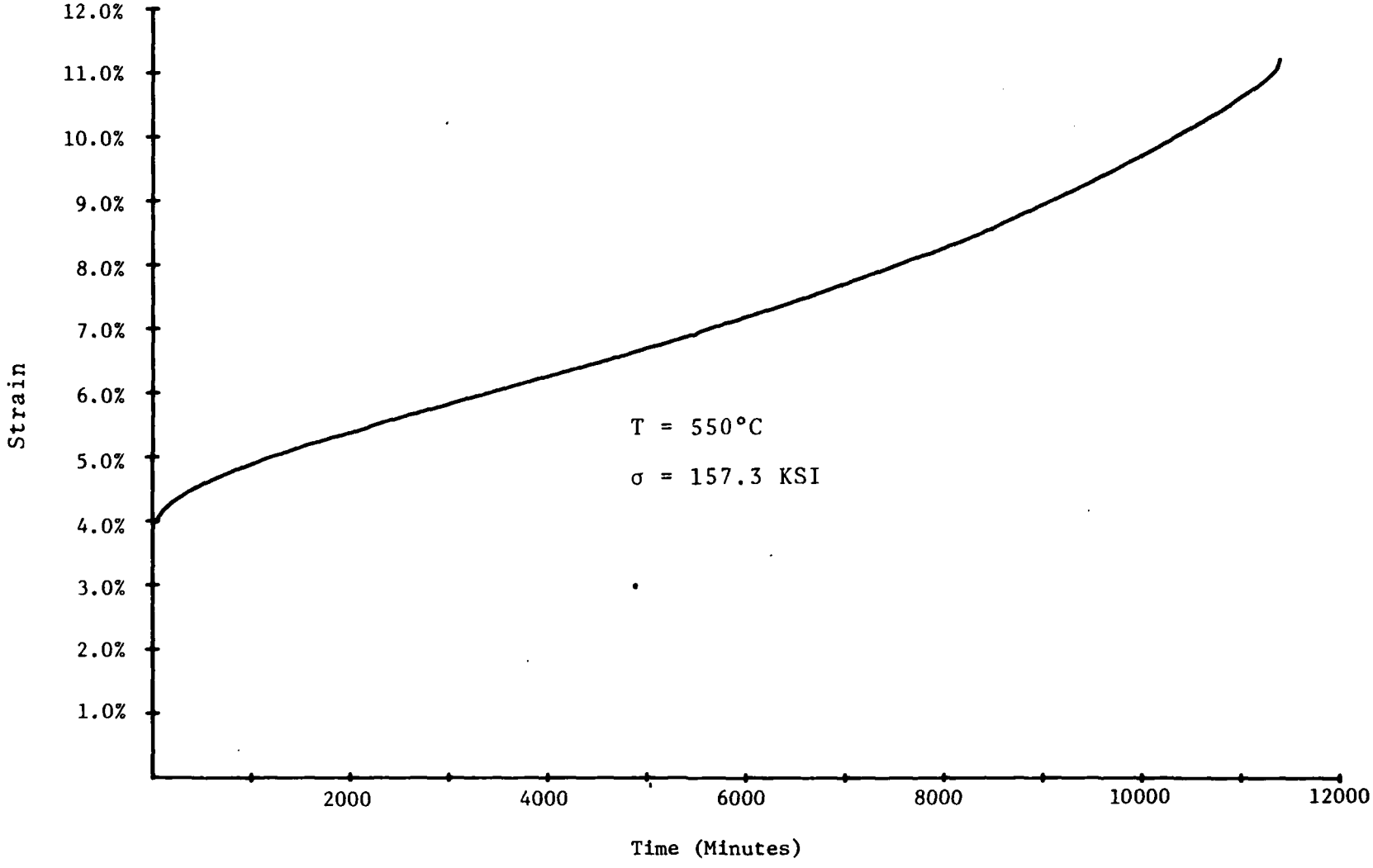

Figure 4: Strain vs Time for Specimen #7.

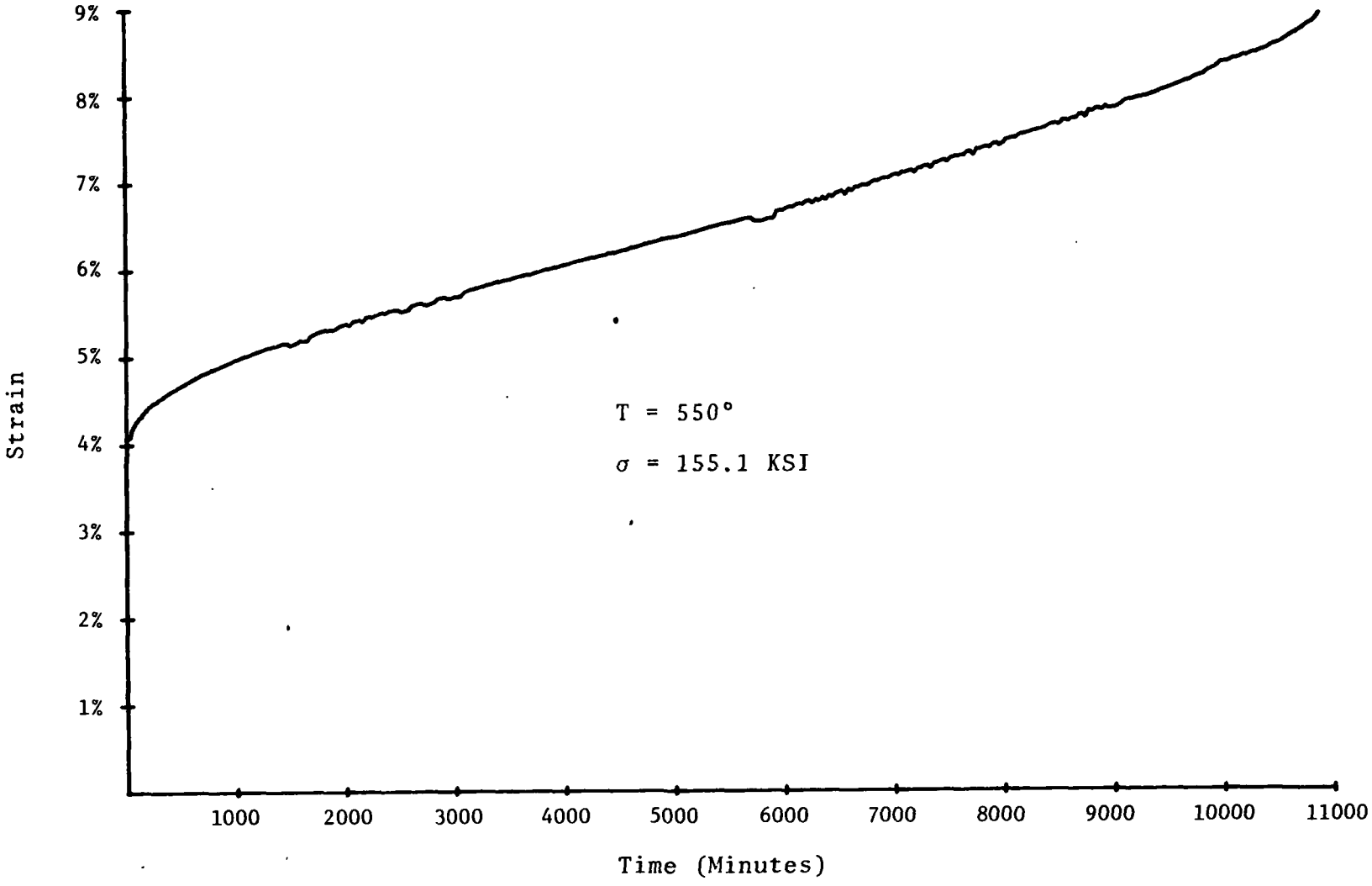

Figure 5: Strain vs Time for Specimen #9.

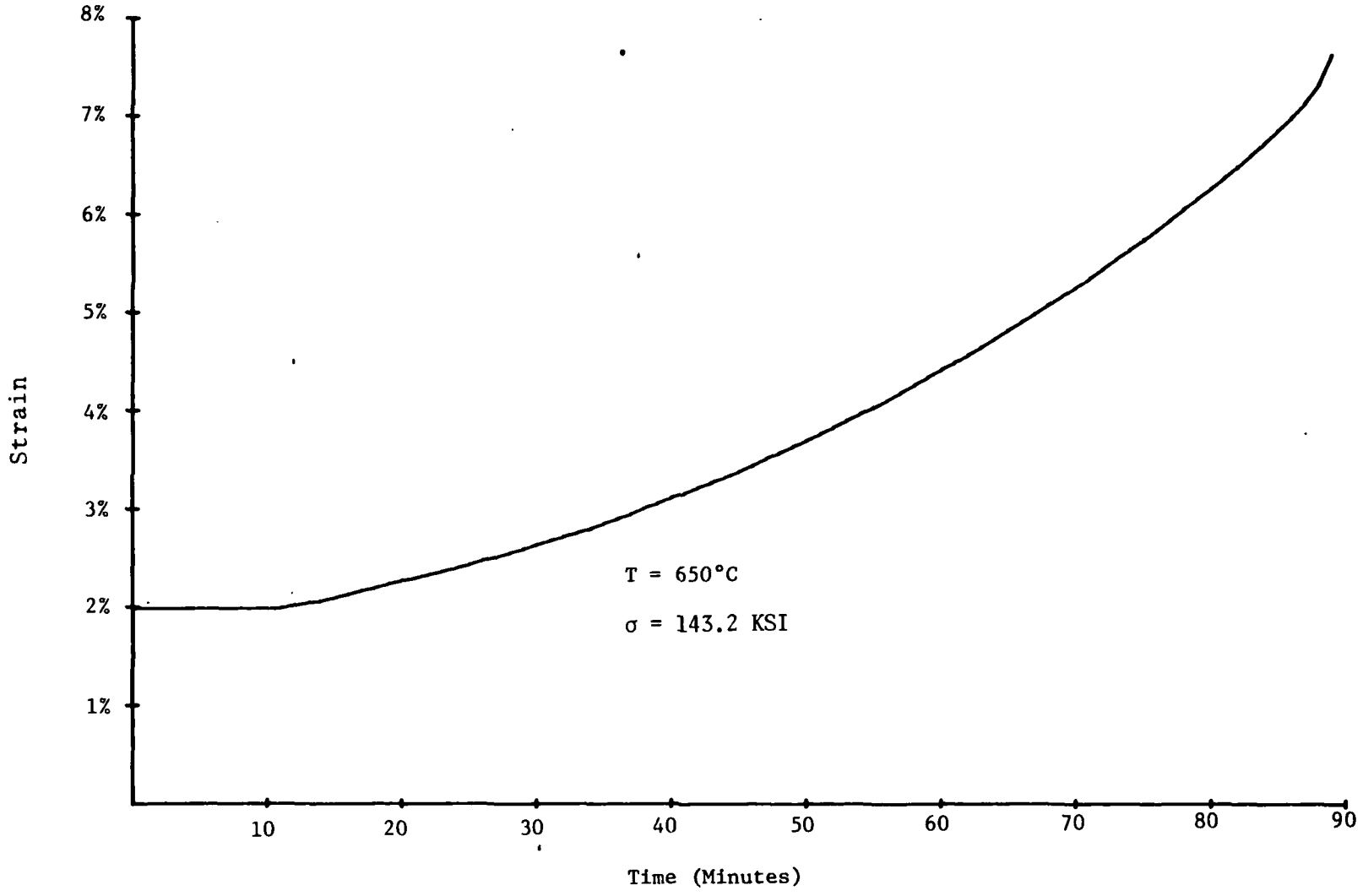

Figure 6: Strain vs Time for Specimen #13.

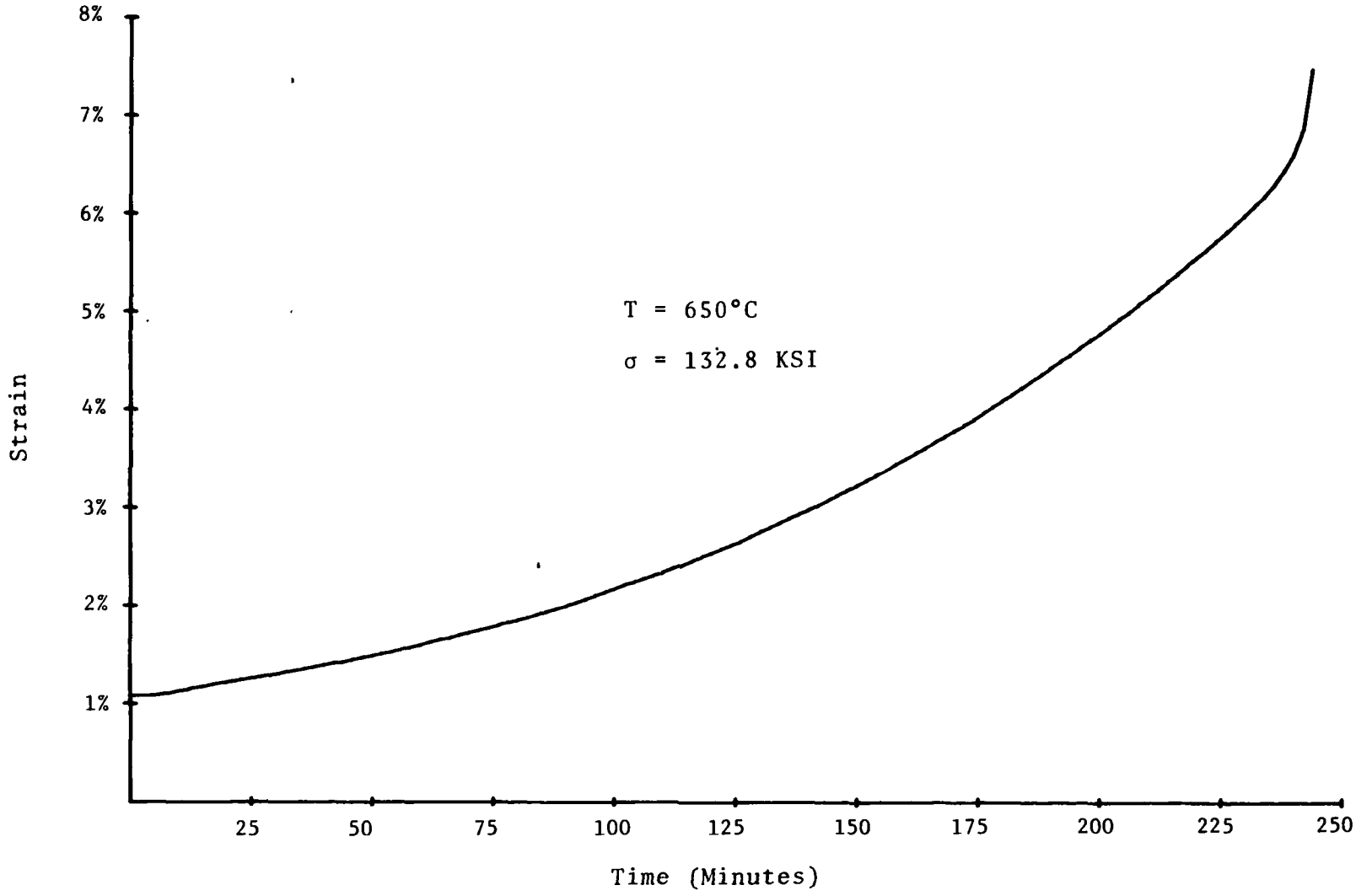

Figure 7: Strain vs Time for Specimen #14.

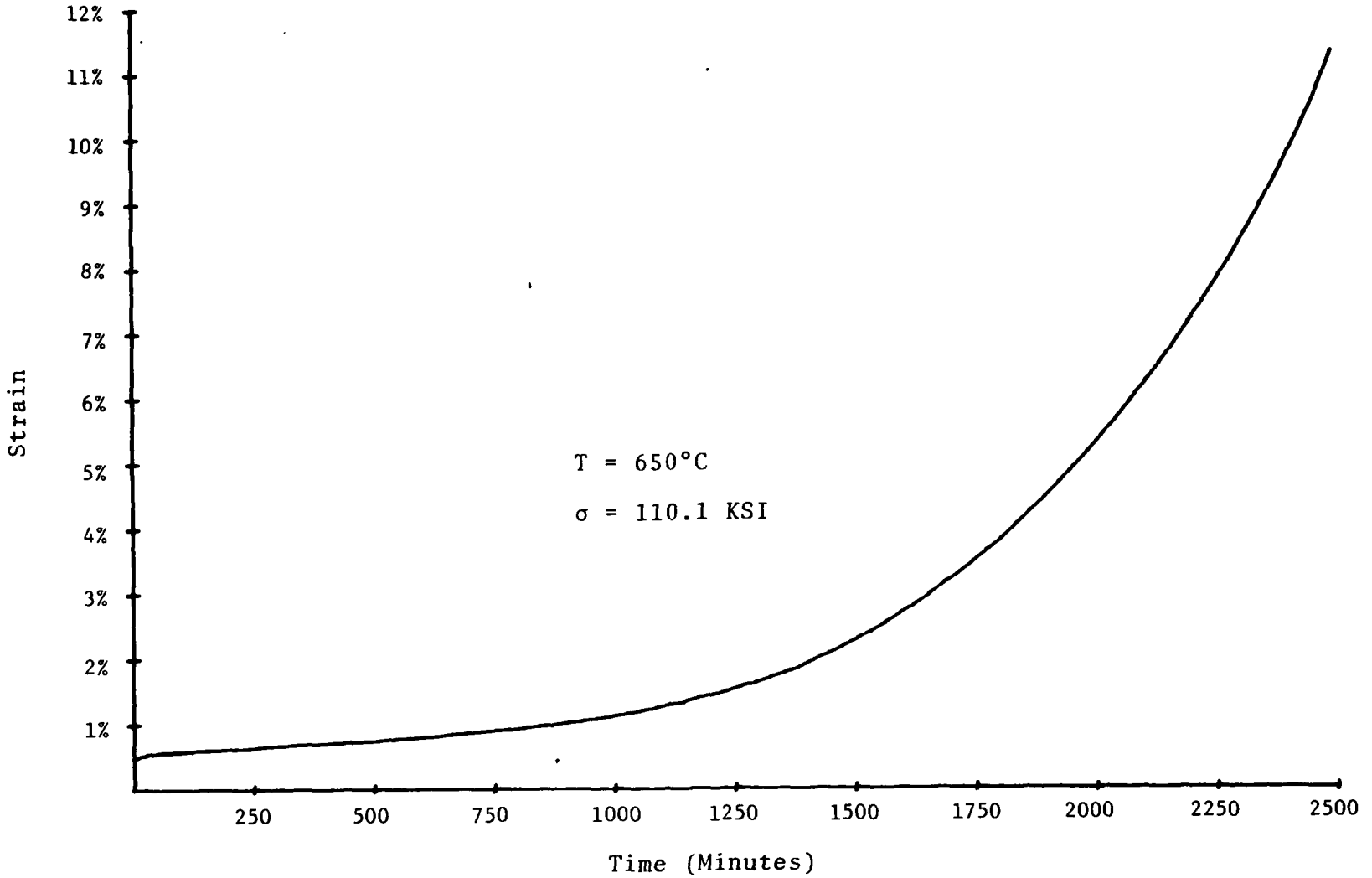

Figure 8: Strain vs Time for Specimen #15.

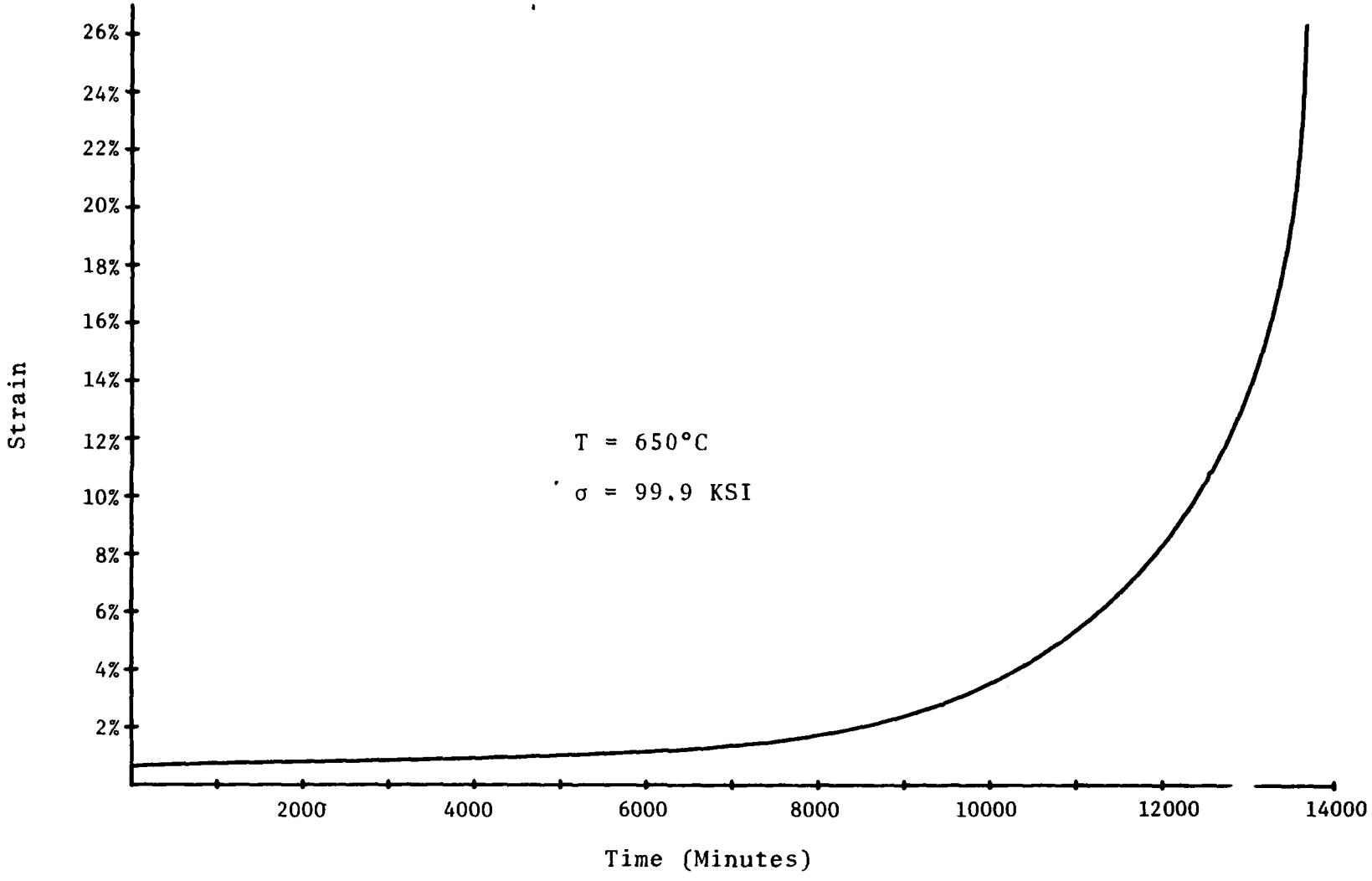

Figure 9: Strain vs Time for Specimen #16.

APPENDIX F:

"Finite Element Formulation for Creep Problems"

By: E. Thomas Moyer, Jr.

This section outlines the formulation being employed in the creep-fracture studies. The total strain rate is decomposed into an elastic and visco-plastic portion in the form (uniaxially).

$$\dot{\varepsilon} = \dot{\varepsilon}_e + \dot{\varepsilon}_{vp} \tag{1}$$

where the subscript e will refer to elastic quantities and the subscript vp will refer to plastic quantities. The total stress rate is related to the elastic strain rate in the form

$$\dot{\sigma} = D\,\dot{\varepsilon}_e \tag{2}$$

All deformation is assumed to be elastic except when the flow function, F, first reaches the condition

$$F(\sigma, \varepsilon_{vp}) - F_0 = 0 \tag{3}$$

where F_0 is the initial flow stress. The total uniaxial stress can be written as

$$\sigma = \sigma_y + H' \varepsilon_{vp} \tag{4}$$

where σ_y is the uniaxial yield stress. The elastic (or initial strain) is related to the zero time stress as

$$\varepsilon_0 = \varepsilon_e = \frac{\sigma}{E} \tag{5}$$

This relation also holds at other times relating the total stress to the elastic strain. Integrating the above, the visco-plastic strain is given in the form

$$\varepsilon_{vp} = \dot{\varepsilon}_0 \, t + \varepsilon_A \, (1-e^{-rt}) \tag{6}$$

$$\dot{\varepsilon}_{vp} = \dot{\varepsilon}_0 + \varepsilon_A \, re^{-rt} \tag{7}$$

where $\dot{\varepsilon}_0$, ε_A, r are material parameters.

For multi-dimensional problems, the visco-plastic strain rate generalizes to the form

$$\dot{\underset{\sim}{\varepsilon}}_{vp} = \gamma \, \langle \Phi(F) \rangle \, \frac{\partial F}{\partial \underset{\sim}{\sigma}} \tag{8}$$

where γ is the fluidity parameter and Φ is the yield function. The total strain can be represented as

$$\underset{\sim}{\varepsilon} = \underset{\sim}{\varepsilon}_e + \underset{\sim}{\varepsilon}_{vp} \tag{9}$$

and the visco-plastic strain can be simplified to

$$\dot{\underset{\sim}{\varepsilon}}_{vp} = \gamma \, \langle \Phi \rangle \, \underset{\sim}{a} \tag{10}$$

$$\underset{\sim}{a}^T = \frac{\partial F}{\partial \underset{\sim}{\sigma}} \tag{11}$$

For many practical applications, the choice of a flow function in the form

$$\Phi(F) = \left(\frac{F - F_0}{F_0}\right)^N \qquad F > F_0 \qquad (12)$$

$$= 0 \qquad \text{otherwise}$$

is appropriate (especially for metallic materials).

The equations formulated above are solved incrementally using an explicit time integrator. The increments of visco-plastic strain are given by (at time t_n)

$$\Delta \underset{\sim}{\varepsilon}_{vp}^{n} = \Delta t_n \, \dot{\underset{\sim}{\varepsilon}}_{vp}^{n} \qquad (13)$$

The strain rates are incremented by the relation

$$\dot{\underset{\sim}{\varepsilon}}_{vp}^{n+1} = \dot{\underset{\sim}{\varepsilon}}_{vp}^{n} + \underset{\sim}{H}^{n} \, \Delta \underset{\sim}{\sigma}^{n} \qquad (14)$$

where

$$\underset{\sim}{H}^{n} = \left(\frac{\partial \dot{\underset{\sim}{\varepsilon}}_{vp}}{\partial \underset{\sim}{\sigma}} \right)^{n} = \underset{\sim}{H}^{n} (\underset{\sim}{\sigma}^{n}) \qquad (15)$$

$$\Delta \underset{\sim}{\sigma}^{n} = \underset{\sim}{D} \, \Delta \underset{\sim}{\varepsilon}_{e}^{n} = \underset{\sim}{D}(\Delta \underset{\sim}{\varepsilon}^{n} - \Delta \underset{\sim}{\varepsilon}_{vp}^{n}) \qquad (16)$$

The strain increments can be written as (in terms of the incremental displacement additions)

$$\Delta \underset{\sim}{\varepsilon}^{n} = \underset{\sim}{B}^{n} \, \Delta \underset{\sim}{d}^{n} \qquad (17)$$

yielding

$$\Delta \underset{\sim}{\sigma}^{n} = \underset{\sim}{D} \left[\underset{\sim}{B}^{n} \Delta \underset{\sim}{d}^{n} - \dot{\underset{\sim}{\varepsilon}}_{vp}^{n} \Delta t\right] \tag{18}$$

relation for the stress increment.

The $\underset{\sim}{B}$ matrix relating the strain to the displacements can be decomposed into a linear and nonlinear portion as

$$\underset{\sim}{B}^{n} = \underset{\sim 0}{B} + \underset{\sim NL}{B}^{n} \tag{19}$$

The special case of linear deformations renders $\underset{\sim NL}{B} = 0$.

The equilibrium conditions for a given time increment can be written as

$$\int_{V} [\underset{\sim}{B}^{n}]^{T} \Delta \underset{\sim}{\sigma}^{n} \, d V + \Delta \underset{\sim}{f}^{n} = 0 \tag{20}$$

where Δf^{n} are the incremental forces applied during the previous time increment. The solution is

$$\Delta \underset{\sim}{d}^{n} = [\underset{\sim T}{K}^{n}]^{-1} \underline{\Delta} \underset{\sim}{V}^{n} \tag{21}$$

where

$$\Delta \underset{\sim}{V}^{n} = \int_{V} [\underset{\sim}{B}^{n}]^{T} \underset{\sim}{D} \dot{\underset{\sim}{\varepsilon}}_{vp}^{n} \Delta t \, d V + \Delta \underset{\sim}{f}^{n} \tag{22}$$

and the stiffness matrix is

$$\underset{\sim T}{K}^{n} = \int_{V} (\underset{\sim}{B}^{n})^{T} \underset{\sim}{D} \underset{\sim}{B}^{n} \tag{23}$$

The stresses, displacements, strain increments and strains are then updated as

$$\underset{\sim}{\sigma}^{n+1} = \underset{\sim}{\sigma}^{n} + \Delta \underset{\sim}{\sigma}^{n} \tag{24}$$

$$\underset{\sim}{d}^{n+1} = \underset{\sim}{d}^{n} + \Delta \underset{\sim}{d}^{n}$$

$$\Delta \underset{\sim vp}{\varepsilon}^{n} = \underset{\sim}{B}^{n} \Delta \underset{\sim}{d}^{n} - \underset{\sim}{D}^{-1} \Delta \underset{\sim}{\sigma}^{n} \tag{25}$$

$$\underset{\sim vp}{\varepsilon}^{n+1} = \underset{\sim vp}{\varepsilon}^{n} + \Delta \underset{\sim vp}{\varepsilon}^{n} \tag{26}$$

For most problems of interest, large strains can occur. A Total Lagrangian formulation is adopted here. The $\underset{\sim}{B}$ matrix is decomposed as

$$\underset{\sim}{B} = \underset{\sim 0}{B} + \underset{\sim NL}{B} \tag{27}$$

The stiffness matrix can then be written as

$$\underset{\sim}{K} = \underset{\sim 0}{K} + \underset{\sim NL}{K} \tag{28}$$

where the linear and nonlinear portions are given as

$$\underset{\sim 0}{K} = \int_V \underset{\sim 0}{B}^{T} \underset{\sim}{D} \underset{\sim 0}{B} \, d\, V \tag{29}$$

$$\underset{\sim NL}{K} = \int_V (\underset{\sim 0}{B}^{T} \underset{\sim}{D} \underset{\sim NL}{B} + \underset{\sim NL}{B}^{T} \underset{\sim}{D} \underset{\sim NL}{B} + \underset{\sim NL}{B}^{T} \underset{\sim}{D} \underset{\sim 0}{B}) d\, V \tag{30}$$

The displacement increments can then be written as

$$\Delta \underset{\sim}{d}^{n} = [\underset{\sim T}{K}^{n}]^{-1} \Delta \underset{\sim}{V}^{n} \tag{31}$$

$$\Delta \underset{\sim}{d}^{n} = \underset{\sim 0}{K}^{-1} \Delta \underset{\sim}{V}^{n} + \underset{\sim NL}{K}^{-1} \Delta \underset{\sim}{V}^{n} \tag{32}$$

where

$$\Delta \underset{\sim}{V}^{n} = \Delta \underset{\sim 0}{V}^{n} + \Delta \underset{\sim NL}{V}^{n} + \Delta \underset{\sim}{f}^{n} \tag{33}$$

$$\Delta \underset{\sim 0}{V}^{n} = \int_{V} \underset{\sim 0}{B}^{T} \underset{\sim}{D} \underset{\sim vp}{\varepsilon}^{n} \Delta t \, d V \tag{34}$$

$$\Delta V_{NL}^{n} = \int_{V} B_{NL}^{T} D \dot{\varepsilon}_{vp}^{n} \Delta t_{n} \, d V \tag{35}$$

The total stress increment becomes

$$\Delta \underset{\sim}{\sigma}^{n} = \underset{\sim}{D}(\underset{\sim 0}{B} \Delta \underset{\sim}{d}^{n} - \dot{\underset{\sim vp}{\varepsilon}}^{n} \Delta t) + \underset{\sim}{D} \underset{\sim NL}{B} \Delta \underset{\sim}{d}^{n} \tag{36}$$

In this formulation, the strain is decomposed into a linear and nonlinear component. For the special case of plane problems, the specific forms are

$$\underset{\sim}{\varepsilon} = \underset{\sim L}{\varepsilon} + \underset{\sim NL}{\varepsilon} \tag{37}$$

The $\underset{\sim}{B}$ matrices are

$$\underset{\sim 0}{B} = \begin{bmatrix} \frac{\partial N_i}{\partial x} & 0 \\ 0 & \frac{\partial N_i}{\partial y} \\ \frac{\partial N_i}{\partial y} & \frac{\partial N_i}{\partial x} \end{bmatrix} \tag{38}$$

$$B_{NL} = \begin{bmatrix} \frac{\partial u}{\partial x}\frac{\partial N_i}{\partial x} & \frac{\partial v}{\partial x}\frac{\partial N_i}{\partial x} \\ \frac{\partial u}{\partial y}\frac{\partial N_i}{\partial y} & \frac{\partial v}{\partial y}\frac{\partial N_i}{\partial y} \\ \frac{\partial u}{\partial y}\frac{\partial N_i}{\partial x} + \frac{\partial u}{\partial x}\frac{\partial N_i}{\partial y} & \frac{\partial v}{\partial y}\frac{\partial N_i}{\partial x} + \frac{\partial v}{\partial x}\frac{\partial N_i}{\partial y} \end{bmatrix} \quad (39)$$

The strain components can then be written as

$$\underset{\sim}{\varepsilon}_L = \begin{bmatrix} \frac{\partial u}{\partial x} \\ \frac{\partial v}{\partial y} \\ \frac{\partial u}{\partial y} + \frac{\partial v}{\partial x} \end{bmatrix} \quad (40)$$

$$\varepsilon_{NL} = \begin{bmatrix} \frac{1}{2}\left(\frac{\partial u}{\partial x}\right)^2 + \frac{1}{2}\left(\frac{\partial v}{\partial x}\right)^2 \\ \frac{1}{2}\left(\frac{\partial u}{\partial y}\right)^2 + \frac{1}{2}\left(\frac{\partial v}{\partial y}\right)^2 \\ \left(\frac{\partial u}{\partial x}\right)\left(\frac{\partial u}{\partial y}\right) + \left(\frac{\partial v}{\partial x}\right)\left(\frac{\partial v}{\partial y}\right) \end{bmatrix} \quad (41)$$

The formulation summarized above has been implemented in a computer code and rigorously tested. The next stage of the research is centering on modeling slow crack growth and alternative constitutive formulations.

APPENDIX G:

Finite Element Methodology for Elastic-Plastic Fracture Problems in 3-Dimensions.

By: E. T. Moyer, Jr. and H. Liebowitz.

To appear in the Commemorative Issue of the Journal of Numerical Methods in Engineering in Memory of Bruce Irons, 1985.

FINITE ELEMENT METHODOLOGY FOR ELASTIC-PLASTIC FRACTURE PROBLEMS IN 3-DIMENSIONS

By

E. T. Moyer, Jr.

and

H. Liebowitz

School of Engineering and Applied Science

The George Washington University

Washington, D.C. 20052

ABSTRACT

The governing finite element system for elastic-plastic analysis of fracture specimens in three-dimensions is formulated. The formulation accounts for mixed material hardening, finite strains, finite rotations and plastic incompressibility. The implementation of these aspects into a computational formula is presented and alternative formulations are compared. Small strain theory is recovered as a special case to the present formulation.

Analysis is performed on a finite thickness center cracked specimen. The grid characteristics required for converged solutions are discussed. The effect of material hardening model and specimen thickness are studied. The local yield state is examined as a gauge of the local deformation processes. The implications on the fracture behavior of the specimen is discussed.

Local surface displacements are compared to experimentally measured yield surfaces. The formulation is shown to predict extremely accurate local deformation in the neighborhood of the crack front. Contrary to the few three-dimensional fracture studies carried out to date, this analysis concentrates on the local deformation behavior which ultimately controls fracture. Accurate resolution of this behavior is essential before meaningful fracture criteria in three-dimensions can be developed.

INTRODUCTION

The field of fracture mechanics has developed, primarily over the past 35 years, as an important and useful tool for the design of engineering components and structures. Much of the success of fracture analysis is due to the advancement of the finite element method as an accurate approach to numerical stress analysis for problems which involve geometric discontinuities and singularities. Originally, fracture studies were aimed at predicting brittle failure of materials. While a necessary first step, this approach did not give meaningful results to many problems of practical importance. Much of the later work in fracture mechanics, therefore, is geared toward addressing the problem of ductile fracture.

Ductile fracture problems involve much local nonlinear deformation. Analytical approaches to the concerned boundary value problem have proven largely futile. To obtain analytical solutions, far too many unrealistic and inappropriate assumptions are required. Numerical solutions are, therefore, imperative. Much work has been done in the area of elastic-plastic stress analysis of fracture specimens. Very little, however, has been carried out in three-dimensions. In application, most components are not thick enough to be considered in plane strain. Indeed, most true plane strain fractures are brittle in nature. Plane stress analysis on fracture specimens is rarely

applicable. The assumption of plane stress violates the compatibility equations which are essential to the formulation of the full boundary value problem. While this is unimportant far from the crack tip, elastic solutions demonstrate the breakdown of the assumption near the crack tip [1]. In plastic analysis, the assumption is further compounded by the fact that four general deformation regions can be identified near the crack front: a) the near tip, elastic, plane strain region; b) a near tip region governed by an asymptotic "plane stress like" region (which, in fact shows contributions from both elastic plane strain, plastic plane stress and possibly boundary influence); c) a transition region in which the deformation is nonlinear, not dominated but influenced by the singular stress field (also a fully three-dimensional region); d) the exterior region which is either plane stress dominated, plane strain dominated or fully three-dimensional depending on specimen geometry and thickness [2,3].

While two-dimensional elastic-plastic studies may provide some insight into the qualitative aspects of ductile fracture, they cannot be expected to yield quantitatively useful results for problems which are not dominantly brittle. This is not to imply that two-dimensional studies are not important. They must be done to provide qualitative and preliminary information which would be far too costly to obtain with three-dimensional analysis. For the

quantitative prediction of ductile fracture phenomena, however, two-dimensional studies cannot be relied upon. The success reported for problems with reasonable ductility in the literature can more than be accounted for by the use of global fracture criterion which are theoretically (as well as computationally) unsound. This will be expounded upon in a later section.

The work discussed in this paper has evolved over the past three years in an effort to systematically, consistently and accurately address the problem of ductile fracture. The work is by no means complete. The full, incremental elastic-plastic finite element formulation is presented. Much debate exists in the literature with regard to valid formulations and yield criterion for ductile fracture specimens. Specific choices were made in the formulation based on experience with two-dimensional studies. It is believed that the current approach will be adequate for most engineering metals at room temperature.

Results are presented for three different aspects of ductile fracture specimens. An important aspect of any numerical study is the validation of the accuracy of the numerical method being employed. With regard to finite element modeling of ductile fracture, this is extremely important (not only is it necessary to theoretically formulate a valid approach, it is critical to demonstrate the accuracy of the discretization employed). Verification of the finite element approach is demonstrated in this work.

A comparison is made with experimentally measured local deformations. This approach eliminates the problem of criteria bias evident in most ductile fracture studies. Results are also presented demonstrating the effect of hardening modeling and specimen thickness on local plasticity characteristics.

PLASTICITY FORMULATION

Several approaches to continuum plasticity have been proposed over the past several decades. Most are based on either stress or strain yield criterion and various hardening assumptions. No clearly "BEST" approach has emerged to date. For most engineering metals, however, the J_2 flow theory of plasticity is widely accepted for practical applications. This approach is reviewed and employed in the current investigations [4].

The J_2 flow theory of plasticity assumes that the material in question yield, or starts deforming plastically when the "effective stress" (or von-Mises stress) reaches a critical value (called the yield stress). Prior to the onset of plasticity, the material is assumed to behave linear elastically. Subsequently, the deviatoric stress components are related to the deviatoric strain rate through the tensor relation

$$\dot{e}_{ij} = \begin{cases} \dfrac{1+\nu}{E}\,\dot{S}_{ij} + \dfrac{3}{2}\,f\,(\sigma_e)\,S'_{ij}\,\dot{\sigma}_e & \left[\begin{array}{l}\sigma'_e = R_{yd} \\ \dot{\sigma}_e > 0\end{array}\right] \\ \dfrac{1+\nu}{E}\,\dot{S}_{ij} \quad \text{(otherwise)} & \end{cases} \tag{1}$$

where $\dot{e}_{ij}$ are the deviatoric strain rates given by

$$\dot{e}_{ij} = \dot{\varepsilon}_{ij} - \frac{1}{3}\,\dot{\varepsilon}_{pp}\,\delta_{ij} \tag{2}$$

S_{ij} are the current deviatoric stress components given by

$$S_{ij} = \sigma_{ij} - \frac{1}{3} \sigma_{pp} \delta_{ij} \tag{3}$$

S'_{ij} are the deviatoric stress components measured relative to the current yield surface center given by

$$S'_{ij} = S_{ij} - a_{ij} \tag{4}$$

a_{ij} are the coordinates in stress space of the current yield surface center, σ_{ij} are the Cauchy stress components, ε_{ij} are the "true" strain components (discussed in a subsequent section), σ_e is the effective stress given by

$$\sigma_e = \sqrt{\frac{3}{2} S_{ij} S_{ij}} \tag{5}$$

and σ'_e is the effective stress measured relative to the current yield surface center

$$\sigma'_e = \sqrt{\frac{3}{2} S'_{ij} S'_{ij}} \quad . \tag{6}$$

The function $f(\sigma_e)$ is derived from the uniaxial stress-strain curve and is consistent with the Associated Plasticity theory (a complete discussion is given in Reference [5]. Derivation of $f(\sigma_e)$ for a multilinear representation of the stress-strain curve will be discussed subsequently.

AD-A166 575 CREEP AND FRACTURE CHARACTERISTICS OF MATERIALS AND STRUCTURES AT ELEVATED TEMPERATURES(U) GEORGE WASHINGTON UNIV WASHINGTON DC SCHOOL OF ENGINEERING AN .. H LIEBOWITZ 14 FEB 86 N00014-84-K-0027 F/G 20/11 4/4

UNCLASSIFIED NL

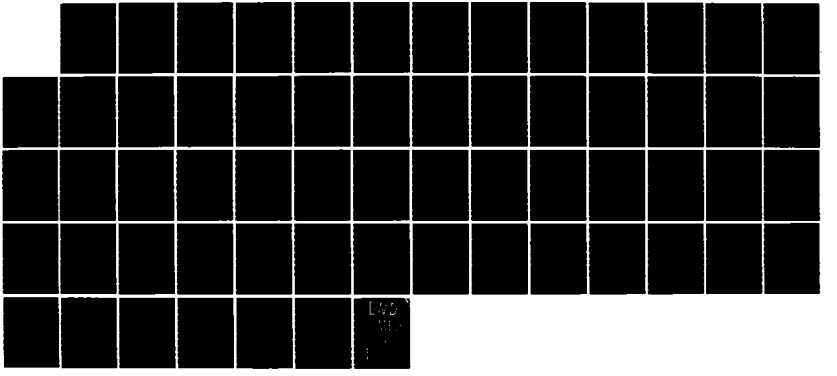

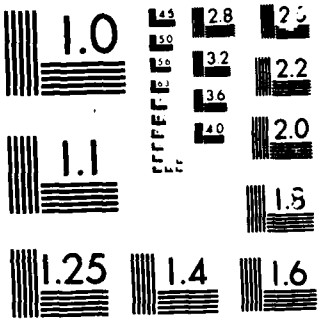

MICROCOPY CHART

For plastic strains which are incompressible, the hydrostatic plastic strain rate is zero. The total hydrostatic strain rate, therefore, is related to the hydrostatic stress rate by

$$\dot{\varepsilon}_{pp} = \frac{1 - 2\nu}{E} \dot{\sigma}_{pp} \tag{7}$$

Engineering materials exhibit different types of uniaxial hardening behavior when subsequently unloaded after being plastically deformed. Generally, the behavior falls between two extremes called kinematic and isotropic hardening. The uniaxial representation of these behaviors for a bilinear material are shown in Figure 1. To allow for various hardening behaviors in the multiaxial formulation, the yield surface is permitted to move and expand under certain constraints. These motions are controlled by a single parameter, β , which can be varied from 0 to 1. A value of zero represents isotropic behavior and a value of 1 represents kinematic behavior. The resulting yield surfaces in a three-dimensional principle stress space are shown in Figure 2. The yield surface center moves at a rate governed by

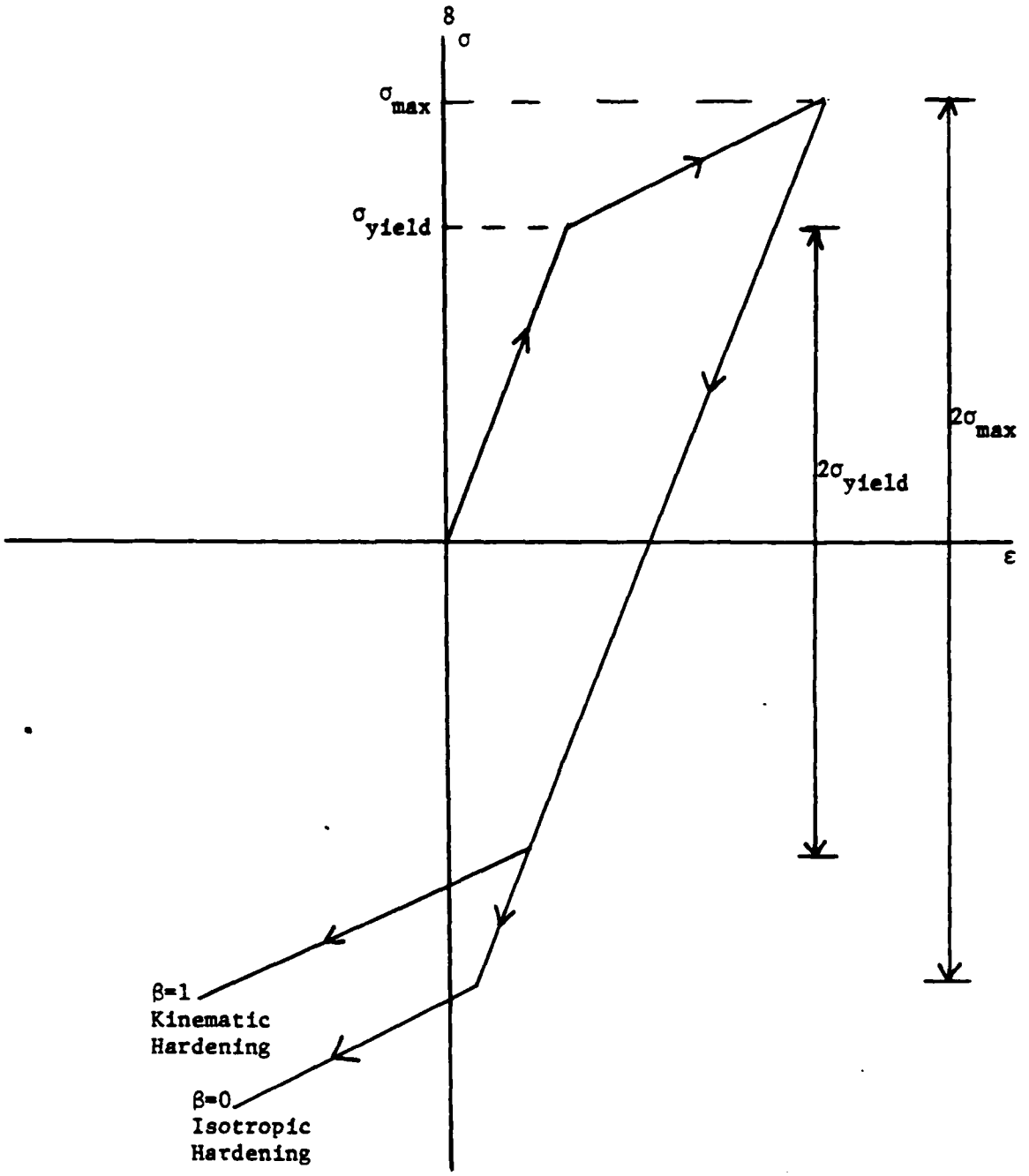

Figure 1: Uniaxial Bilinear Representation of Kinematic and Isotropic Hardening.

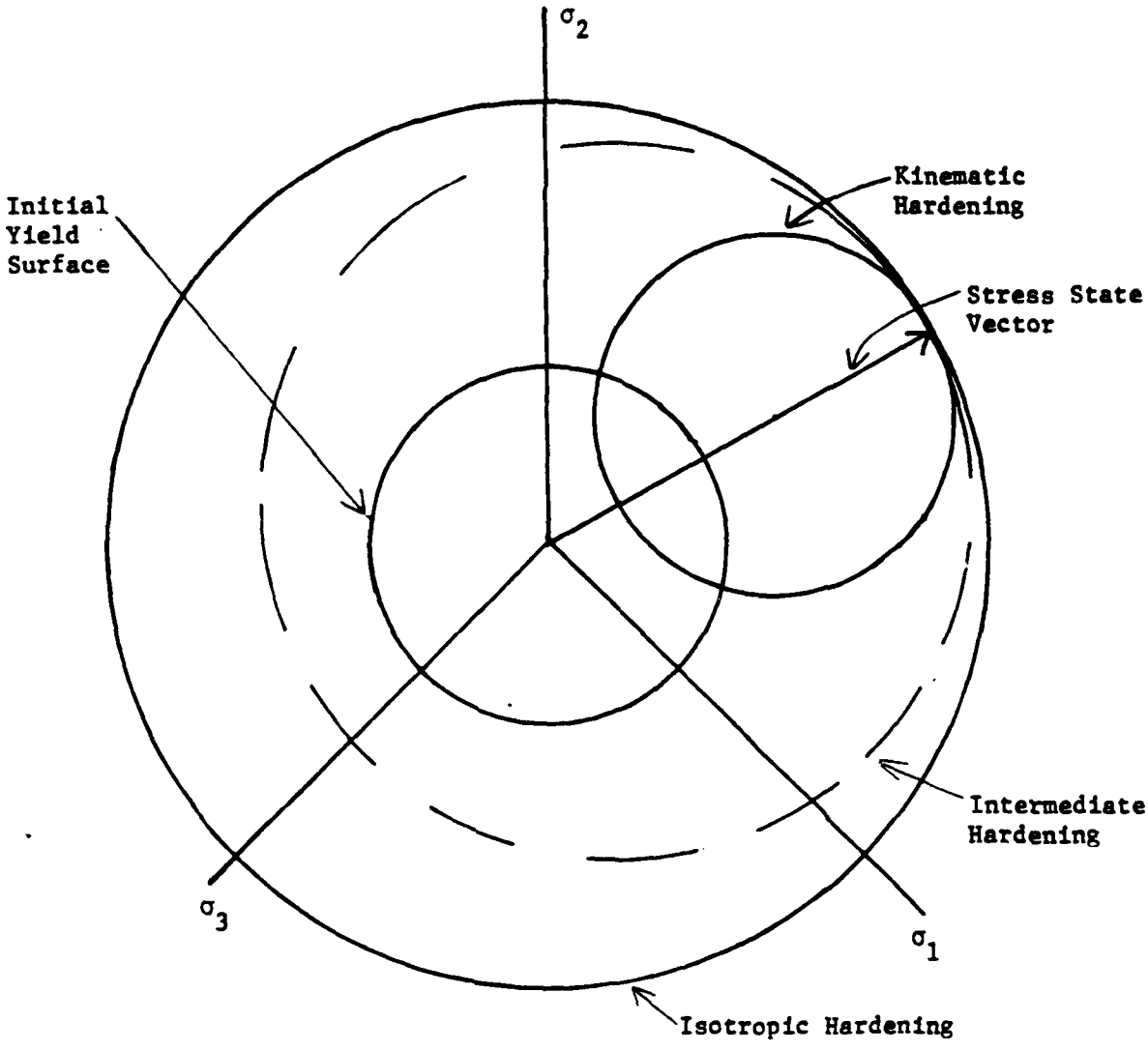

Figure 2: Hardening Models in Principle Stress Space.

$$\dot{a}_{ij} = \left\{ \begin{array}{ll} \frac{3}{2} \beta S'_{kl} \dot{S}_{kl} S'_{ij} / (\sigma'_e)^2 & \left[\begin{array}{l} \sigma'_e = \sigma_{yd} \\ \dot{\sigma}_e > 0 \end{array} \right] \\ 0 \text{ (otherwise)} & \\ 0 \leq \beta \leq 1 & \end{array} \right\} \tag{8}$$

$\beta = 0 \rightarrow$ Isotropic Hardening

$\beta = 1 \rightarrow$ Kinematic Hardening

The radius expands according to the relation

$$\sigma'_y = 2 \sigma_y + 2 \beta(\sigma_{max} - \sigma_y) \tag{9}$$

To allow for finite strains and rotations, Updated Lagrangian approach is adopted [6]. The coordinate system is convected with the deformation. In this coordinate system, the "true strain" rate is related to the deformation rate (or velocity) through

$$\dot{\sigma}_{ij} = C_{ijkl} \dot{\epsilon}_{kl} \tag{10}$$

In the absence of rotation the stress tensor is related to the strain rate tensor in the classical manner, i.e.,

$$\dot{w}_{ij} = \frac{1}{2} \left(\frac{\partial \dot{U}_i}{\partial X_j} - \frac{\partial \dot{U}_j}{\partial X_i} \right) \tag{11}$$

This stress measure is the Cauchy stress. Under finite rotations, the stress tensor is not invariant. At zero

strain rate, the stress rate is given by where W are the rotation rates

$$\dot{\sigma}_{ij} = \dot{W}_{ip}\,\sigma_{pj} - \dot{W}_{pj}\,\sigma_{ip} \tag{12}$$

The total stress-deformation relation is, therefore,

$$\dot{\sigma}_{ij} = C_{ijkl}\,\dot{\varepsilon}_{kl} + \dot{W}_{ik}\,\sigma_{kj} - \dot{W}_{kj}\,\sigma_{ik} \tag{13}$$

Equations (1) - (13) form a complete incremental representation of finite plastic deformation. It only remains, therefore, to quantify the uniaxial behavior through the function $f(\sigma_e)$. There are many functional ways to represent uniaxial loading behavior. From a computation standpoint, a multilinear representation is easily implemented and, by allowing for enough segments, can be arbitrarily accurate. Consider the multilinear representation of a true stress-true strain curve shown in Figure 3. The functional relationship between the stress and strain are given by

$$\varepsilon = \frac{\sigma}{E} + \frac{\alpha_1}{E}(\sigma_2 - \sigma_1) + \frac{\alpha_2}{E}(\sigma_3 - \sigma_2) + \ldots \frac{\alpha_m}{E}(\sigma - \sigma_m) \qquad \sigma_m < \sigma \leq \sigma_{m+1} \tag{14}$$

The plastic strain rate, therefore, is given by

$$\dot{\varepsilon}_p = \alpha_m\,\dot{\sigma}_e/E \tag{15}$$

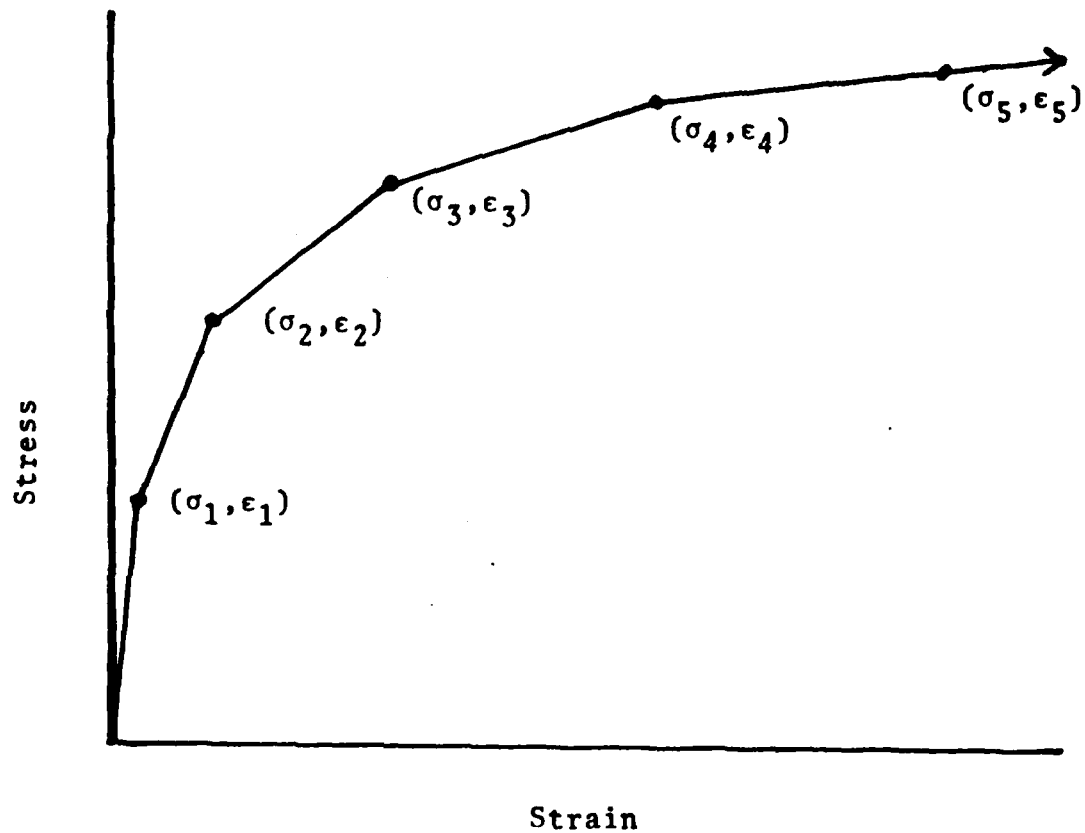

Figure 3: Multilinear Approximation For A Uniaxial Stress-Strain Curve With Hardening.

Using equation (1) and recognizing that for uniaxial deformation, effective quantities are proportional to the uniaxial components, the function $f(\sigma_e)$ can be reduced to

$$f(\sigma_e) = \alpha_m/E\sigma_e \tag{16}$$

The function is only linearly dependent on the current slope of the uniaxial curve. By specifying enough segments, virtually any hardening behavior can be accurately described.

The above formulation is chosen for implementation with the Finite Element Method to be described subsequently. It is important to recognize that the formulation is representative of a wide class of materials and can model many different variations of material hardening. This formulation has been employed with considerable success in many investigation of material deformation and fracture mechanics. Several well known two-dimensional codes were developed and have been widely employed for many years (see, for example, [7] and [8]).

FINITE ELEMENT FORMULATION

Equations (1), (8) and (9) provide the fundamental relationships between stress and strain rates. The equilibrium conditions (governing equations) for a continuum body in the absence of body forces and inertia effects can be written as

$$\partial \dot{\sigma}_{ij}/\partial x_j = 0 \tag{17}$$

with the boundary conditions

$$\dot{\sigma}_{ij} n_j = \dot{T}_i \text{ on } S_T$$

and (18)

$$\dot{u}_i = \mathring{u}_i \text{ on } S_u$$

where $\dot{T}_i$ are the specified loading rates on the boundary experiencing applied tractions (S_T) and $\mathring{u}_i$ are the velocities specified on the remainder of the boundary (S_u).

Equation (13) provides the fundamental relation between the stress state and the deformation gradients. For many problems in application the assumption of "small strain" introduces minimal error (mathematically, this means assuming infinitesimal displacements and strains). If this assumption is made, the strain rates are related to the velocity gradients by

$$\dot{\epsilon}_{ij} = \frac{1}{2}(\partial \dot{u}_i/\partial x_j + \partial \dot{u}_j/\partial x_i) \tag{19}$$

This simplification also means that the reference coordinate system and the material coordinate system are coincidental throughout the deformation. In the computer code described, the option of finite or infinitesimal strain theory is left to the user. The use finite strains slows convergence considerably for problems where the deformations are small. As the strains grow, however, the solutions assuming infinitesimal theory diverge from the finite strain results. Eventually infinitesimal solutions will fail to converge regardless of how small the load increments are taken.

By either employing the Principle of Virtual Work for increments of displacement or by performing the standard Galerkin technique on the governing equations, (17) and (18), the finite element equations governing the nodal velocities, $\dot{\underset{\sim}{U}}$, can be written in terms of the loading rate vector, $\dot{\underset{\sim}{R}}$, in the form

$$\underset{\sim}{K}(\underset{\sim}{U}) \cdot \dot{\underset{\sim}{U}} - \dot{\underset{\sim}{R}} = 0 \tag{20}$$

The standard finite element assumptions made are given by

$$\underset{\sim}{u} = \underset{\sim}{N} \cdot \underset{\sim}{U}$$

$$\dot{\underset{\sim}{\varepsilon}} = \underset{\sim}{B} \cdot \dot{\underset{\sim}{U}}$$

$$\dot{\underset{\sim}{\sigma}} = \underset{\sim}{D}(\underset{\sim}{U}) \cdot \dot{\underset{\sim}{\varepsilon}} \tag{21}$$

$$\underset{\sim}{K}(\underset{\sim}{U}) = \sum_{\text{elements}} \int_{\text{element volume}} \underset{\sim}{B}^T \underset{\sim}{D}(\underset{\sim}{U})\ \underset{\sim}{B}\ dV$$

where $\underset{\sim}{N}$ are the shape functions. The set of rate equations (20) will be integrated one load increment ($\Delta\underset{\sim}{R}$) at a given time to determine the corresponding new displacement increment, $\Delta\underset{\sim}{U}$. The Newton-Raphson or tangent stiffness solution procedure is employed. At load increment L + 1, the initial solution $\Delta\underset{\sim}{U}^i_{L+1}$ is found from

$$\underset{\sim}{K}(\underset{\sim}{U}_L) \cdot \Delta\underset{\sim}{U}^i_{L+1} = \Delta\underset{\sim}{R}_{L+1} \tag{22}$$

The "new" displacement is then used in the stiffness matrix,

$K(U_L + \sum_{i=1}^{m} \Delta U^i_{L+1})$, and a new correction is obtained from

$$\underset{\sim}{K}\left[\underset{\sim}{U}_L + \sum_{i=1}^{m} \Delta\underset{\sim}{U}^i_{L+1}\right] \cdot \Delta\underset{\sim}{U}^{m+1}_{L+1} = \Delta\underset{\sim}{R}_{L+1} -$$

$$\underset{\sim}{U}_L + \sum_{i=1}^{m} \Delta\underset{\sim}{U}^i_{L+1} \tag{23}$$

$$\int_{\underset{\sim}{U}_L} \underset{\sim}{K}(\underset{\sim}{U}) \, d\underset{\sim}{U} = \underset{\sim}{F}^{i+1}_{L+1}$$

where the integral is approximated using Simpson's rule. The procedure is repeated until two convergence criteria are met:

$$\left|\underset{\sim}{F}^{i+1}_{L+1}\right|^2 / \left|\Delta\underset{\sim}{R}_{L+1}\right|^2 \leq C_1$$

and (24)

$$\left|\underset{\sim}{F}^{i+1}_{L+1}\right|^2 / \left|\underset{\sim}{R}_{L+1}\right|^2 \leq C_2$$

where $\underset{\sim}{R}_{L+1}$ is the total load at step L + 1.

In this study, 20-node quadratic isoparametric elements were employed exclusively. All integration was carried out utilizing 3 x 3 x 3 Gauss-Legendre quadrature formulae. Strains were calculated at the Gauss integration points in each element from the strain-displacement relations of (19). Stresses were cumulatively calculated at the Gauss points

from the stress-strain relations.

Directly calculating strains and stresses from the finite element relations (21) at points on element boundaries inherently yields poor results. This is especially true when C^0 shape functions are employed. A superior approach is to calculate the stresses and strains at the Legendre quadrature points and to extrapolate or smooth them to the boundaries. This approach has been shown to yield very accurate results for a wide variety of geometric mappings. In this study the smoothing technique as developed in [9] is employed for all stress and strain evaluations.

Currently, four methods of accounting for the crack tip singularity are widely employed. Each of these methods is based on an established technique in LEFM (Linear Elastic Fracture Mechanics). The first method, the enriched element approach (where the shape functions are modified with the asymptotic crack solution vanishing at the nodes) has been employed both for the multilinear stress-strain models and for power law hardening models [10]. Enriched elements based on the power law hardening model assume that the enriched element is fully yielded. This assumption is physically unrealistic, especially behind the crack tip. The singular solution employed for the power law hardening case also assumes a circular yield zone which is far from realistic. The solutions generated using enriched elements and a multilinear stress-strain assumption are reasonably accurate providing a judicious choice of enriched element size and sur-

rounding grid characteristics is made. The major drawback to the use of enriched elements is the computation time required to obtain convergence due to element incompatibility. The second method, the most basic approach, uses a very fine mesh near the crack tip and employs only conventional elements. This method produces reasonable results far from the crack region but questionable local results. Convergence is usually rapid, therefore, gross specimen behavior can be obtained quickly. With unrealistically fine grids, good local results can be obtained (except in the elements bordering the crack tip) but only at the expense of computer time [11]. The third method is based on the fact that if isoparametric elements are chosen with midside nodes, jucicious choice of the placement of these nodes results in the inducement of a $\sqrt{r}$ term in the displacement shape functions [12, 13]. These elements are essentially equivalent to enriching the shape functions, however, element compatibility is preserved resulting in faster convergence. The fourth technique of modeling crack tip behavior is through the use of hybrid elements where elements bordering a surface with traction boundary conditions are forced to satisfy those conditions exactly and the elements bordering a surface with displacment boundary conditions are also forced exactly. The element boundaries are then matched by using Lagrange multipliers in the variational equations to ensure element equilibrium and continuity in an approximate sense. Little work has been done on comparisons of hybrid methods to

conventional methods in elastic-plastic crack problems, however, the technique was applied with questionable success in [14]. The preferred method in the literature is still to use a very fine mesh and standard elements. Complete discussions of the above methods can be found in [15-17].

FINITE ELEMENT DISCRETIZATIONS

In this paper, three basic aspects of the finite element solution of ductile fracture problems are examined. All three involve a rectangular panel with finite thickness and a center crack through the thickness. Due to the unknown singular nature near a crack front and the problem of the intersection of a crack front with a free surface, only conventional (quadratic) 20-node isoparametric elements are employed in this work. Studies on linear elastic through crack specimens has demonstrated the accuracy of this approach for predicting local deformation and stress responses [18].

For all the problems discussed in this paper, the grid shown in Figures 4a, 4b and 4c is employed. This grid was used to predict stress intensity factors for linear elastic problems. The results (discussed in [18]) demonstrate the accuracy is on the same scale with other approaches. The advantage of this modeling is, since the singularity is not accounted for directly, it should be directly employable in an elastic plastic study. To verify this, results are compared with experimental measurements in a subsequent section.

The grid shown consists of 96 isoparametric elements with 624 total nodes (each element has 20 nodes). The total number of degrees of freedom is 1872. Runtimes for the studies to be presented were rather lengthy on a VAX 11/780.

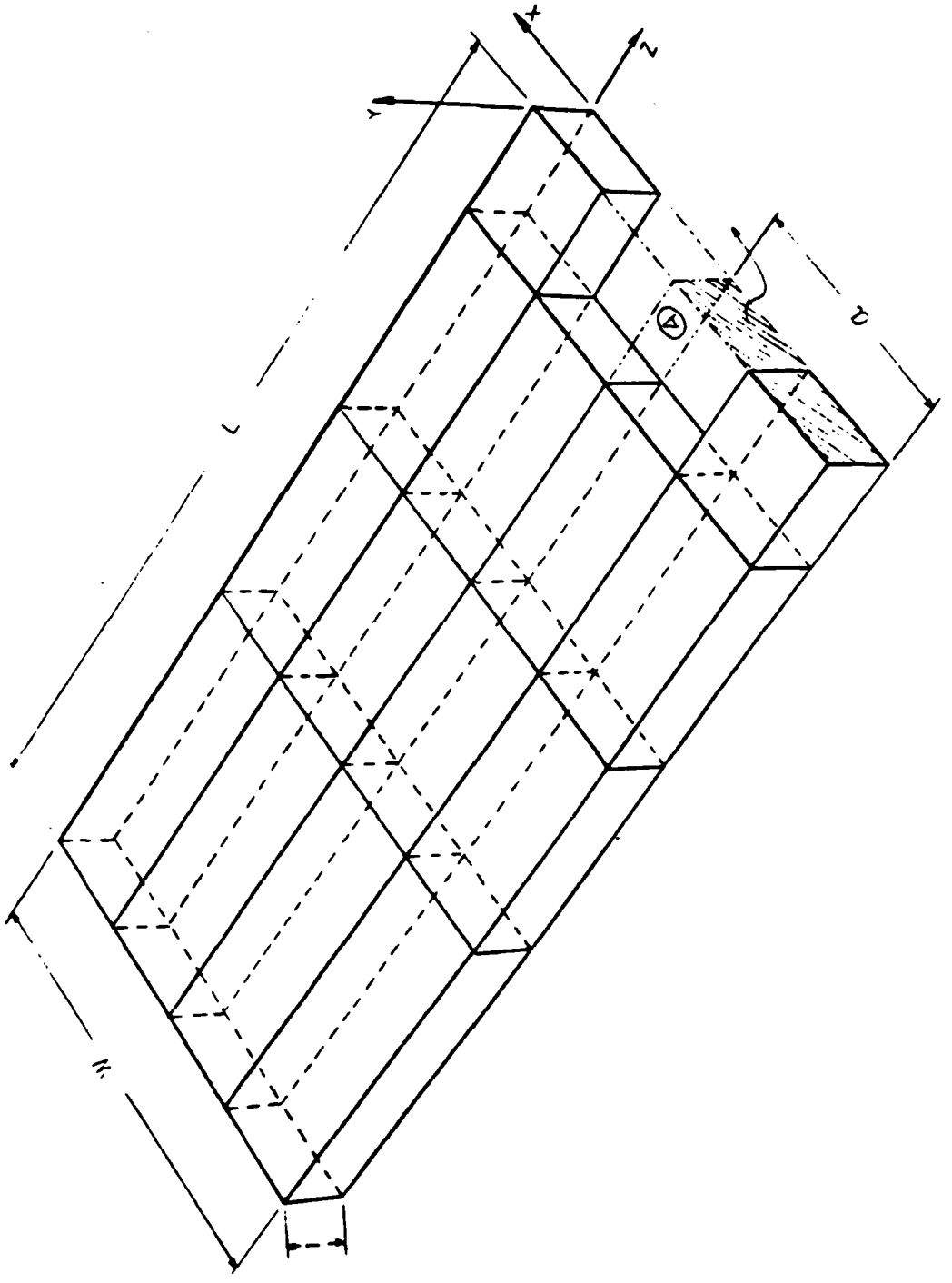

Figure 4a: Finite Element Grid - Coarse Outer Region.

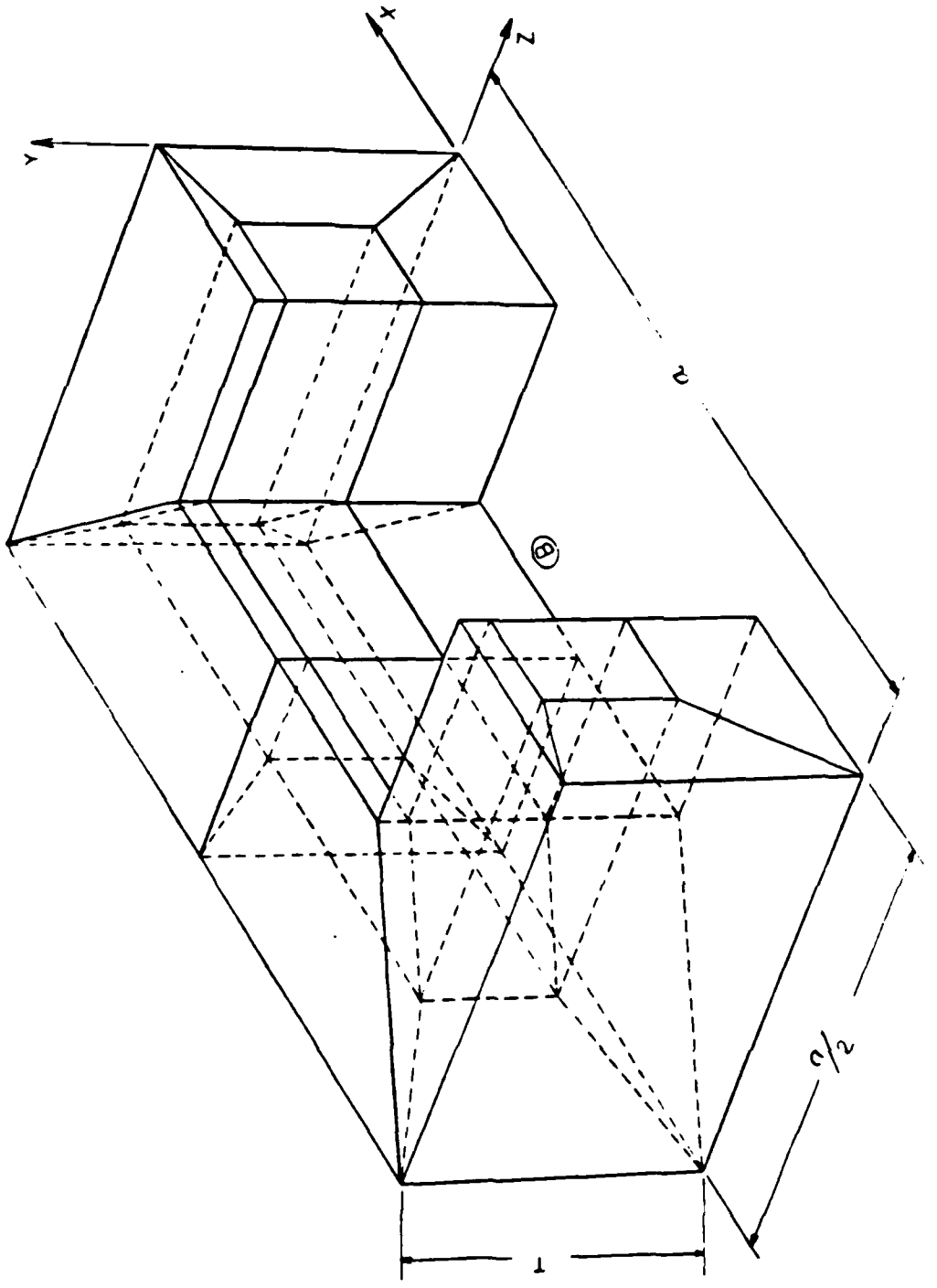

Figure 4b: Finite Element Grid - Blowup Of Region A.

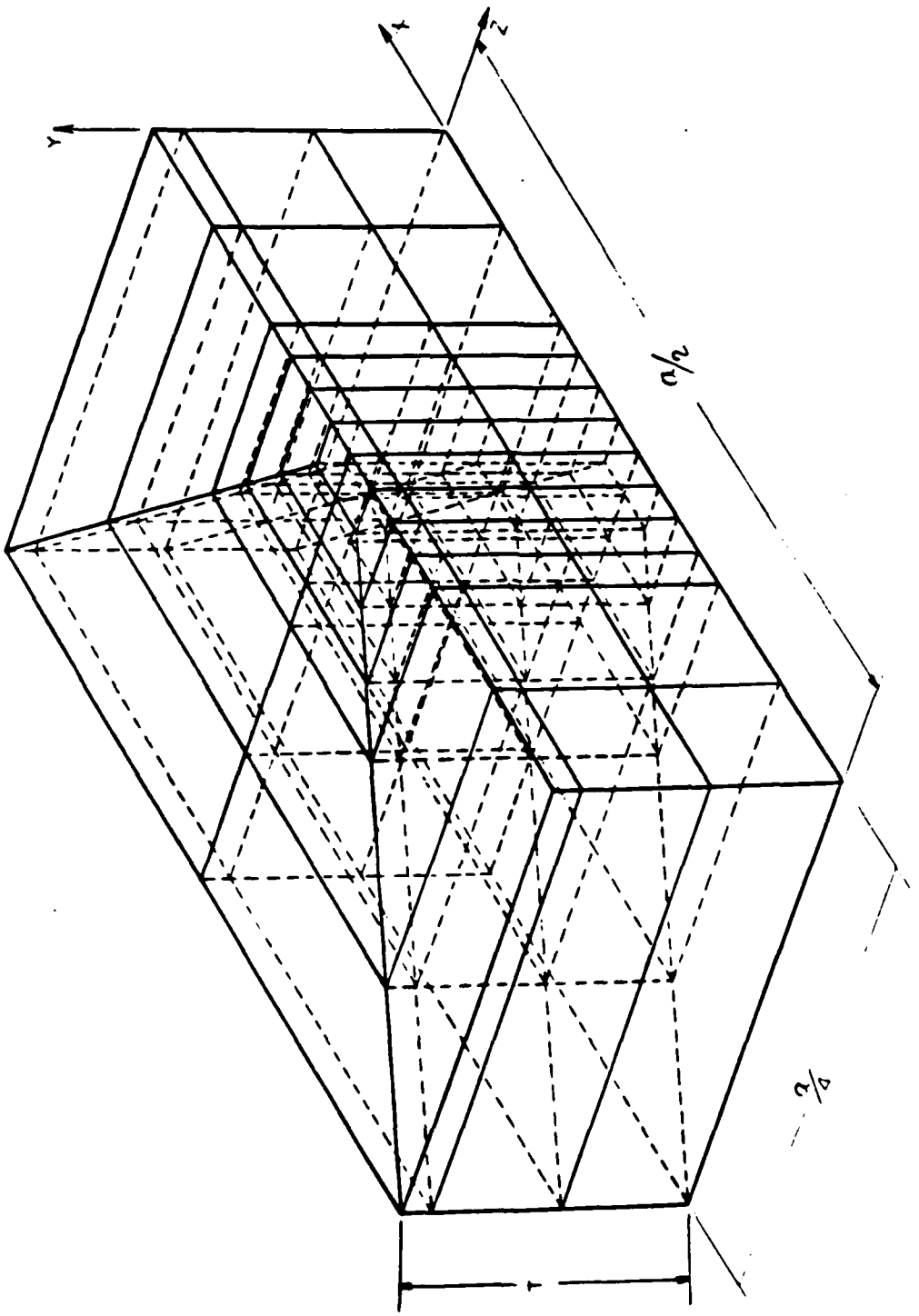

Figure 4c: Finite Element Grid - Near Tip Region B.

Typical runtimes for panels loaded to about 1/3 of the material yield stress converged in approximately 48 CPU hours. This is fairly consistent with existing benchmarks of computer codes which employ the frontal solution method for solution of the stiffness equations. Obviously it is preferable to run these types of problems on larger and faster computers if they are available. It should be appreciated, however, that even large problems can be run on fairly small machines using the frontal approach.

The elastic results presented in [18] demonstrate the convergence of the grid. It should be recognized at the outset that the grid employed in this study is the minimum required for convergence to the elastic solution. The next section demonstrates its ability to model elastic-plastic deformation realistically. While it is never possible for nonlinear problems without analytic solutions to establish optimal grid requirements, it is believed that little reduction in the discretization could be made without seriously compromising the accuracy of the solution. Studies which employ fewer degrees of freedom must be considered suspect.

COMPARISON WITH EXPERIMENT

A panel of overaged 7075 (T7651) aluminum was tested experimentally. The specimen was a center-cracked panel with width 8.89cm and crack length to width ratio of 0.5. The stress-strain curve for the material is shown in Figure 5. The specimen was loaded to the highest applied load precluding crack growth and subsequently unloaded. The residual surface deformations were measured using a special LVDT probe and measuring technique described in [19].

The same panel was analyzed using the finite element method using the procedure and discretization described previously. The panel was loaded incrementally and unloaded to a zero applied load state (the local plastic state, however, showed considerable residual deformation and stress as would be expected). Displacement contours near the intersection of the crack with the free surface were generated from the solution and compared with the average experimental results. The comparison is summarized in Figure 6. The solid lines are the numerically predicted contours and the discrete points are from the experimental data.

The average of the four sides was compared as the local inhomogeneity and lack of symmetry is virtually eliminated in the experimental average. The results demonstrate the accuracy of the finite element modeling and solution procedure being employed. The experimental data and predicted

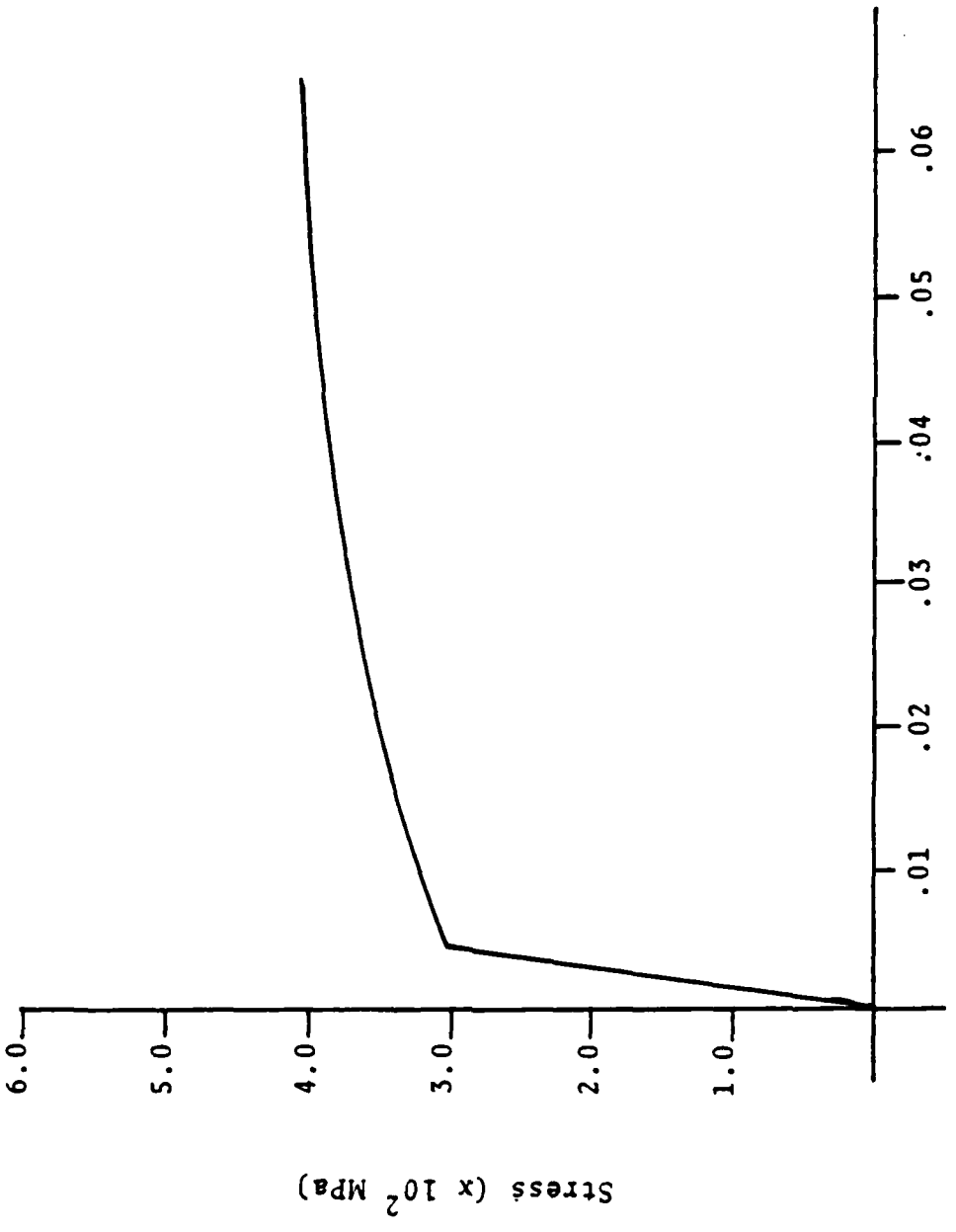

Figure 5: Uniaxial Stress-Strain Curve

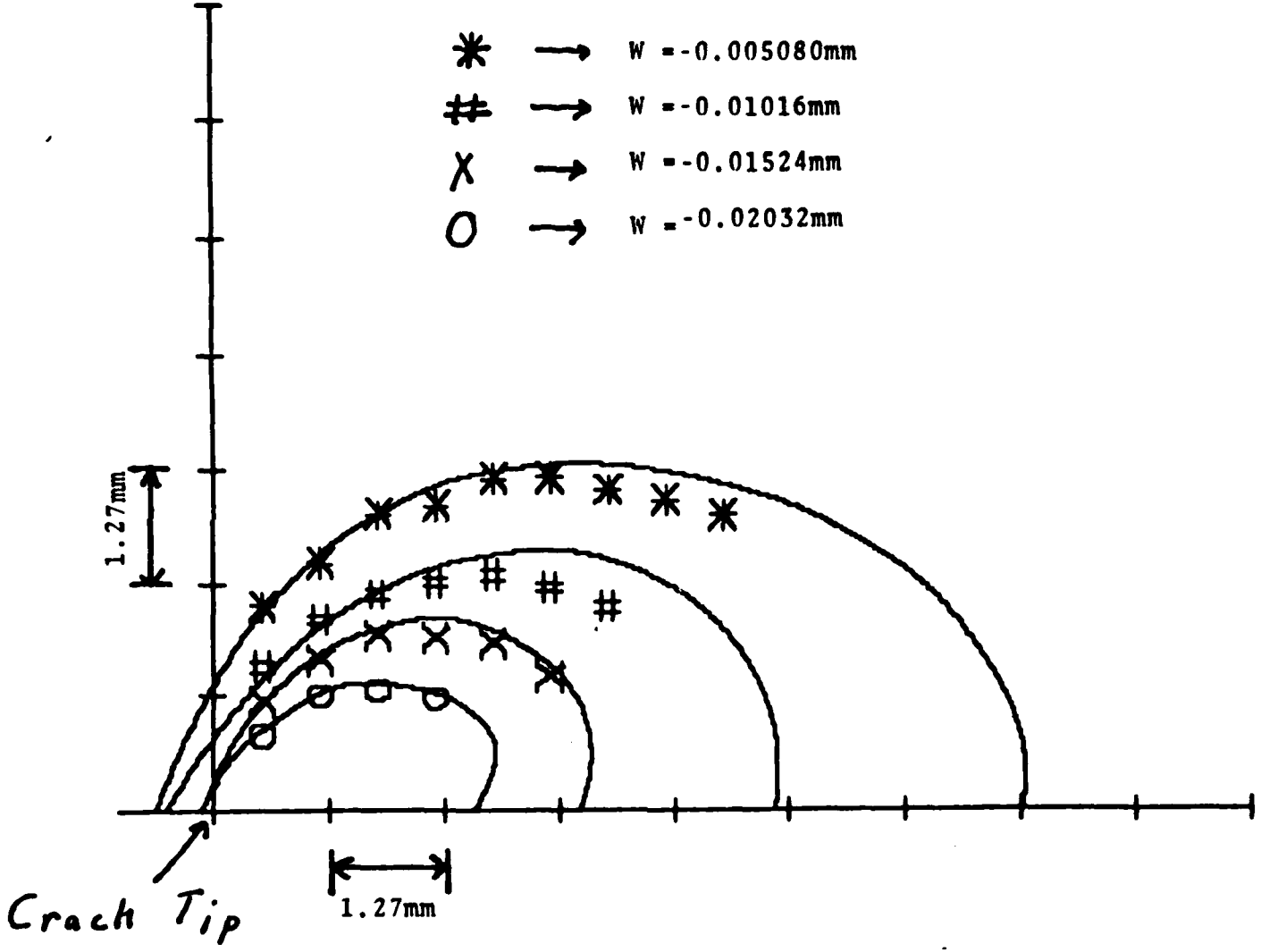

Figure 6: Comparison of Surface Displacements.

contours differ by less than 3%. This is more accurate than was expected comparing with claims made for the finite element solution of crack problems in two dimensions.

The comparison presented above and described fully in [19] demonstrates the accuracy of the current numerical approach and modeling. The results predicted subsequently would model fairly well the true deformation in engineering fracture specimens. The remainder of the problems to be discussed will qualitatively examine some of the more important aspect of fracture specimens and modeling.

MATERIAL HARDENING EFFECTS

To investigate the effect of material hardening model, a center cracked panel 8.89cm wide was studied. The crack length to width ratio is 0.5 and the specimen length to width ratio is 2.0. The idealization is the same as discussed previously. The loading is normal to the crack direction and reaches a maximum load equal to 1/3 for the material yield stress. The material is modeled as either exhibiting kinematic hardening behavior, isotropic hardening behavior or a mixed hardening behavior (as described previously). Since the global applied loading is monotonic, the three hardening modeles would predict identical response if the local deformation were truly proportional in nature (assuming no crack growth).

Figures 7, 8 and 9 show the yield zones on the surface of the specimen at maximum load for each of the hardening models. The local response is definitely non-proportional. The isotropic model predicts more yielding on the crack extent line than either or the other two models. This would suggest a more ductile response ahead of the crack (implying a greater tendency toward stable crack growth prior to final failure). The results with mixed hardening have proven to be the closest to what is observed experimentally. The others, therefore, should be viewed with that fact in mind.

The largest affect of hardening model is the yield

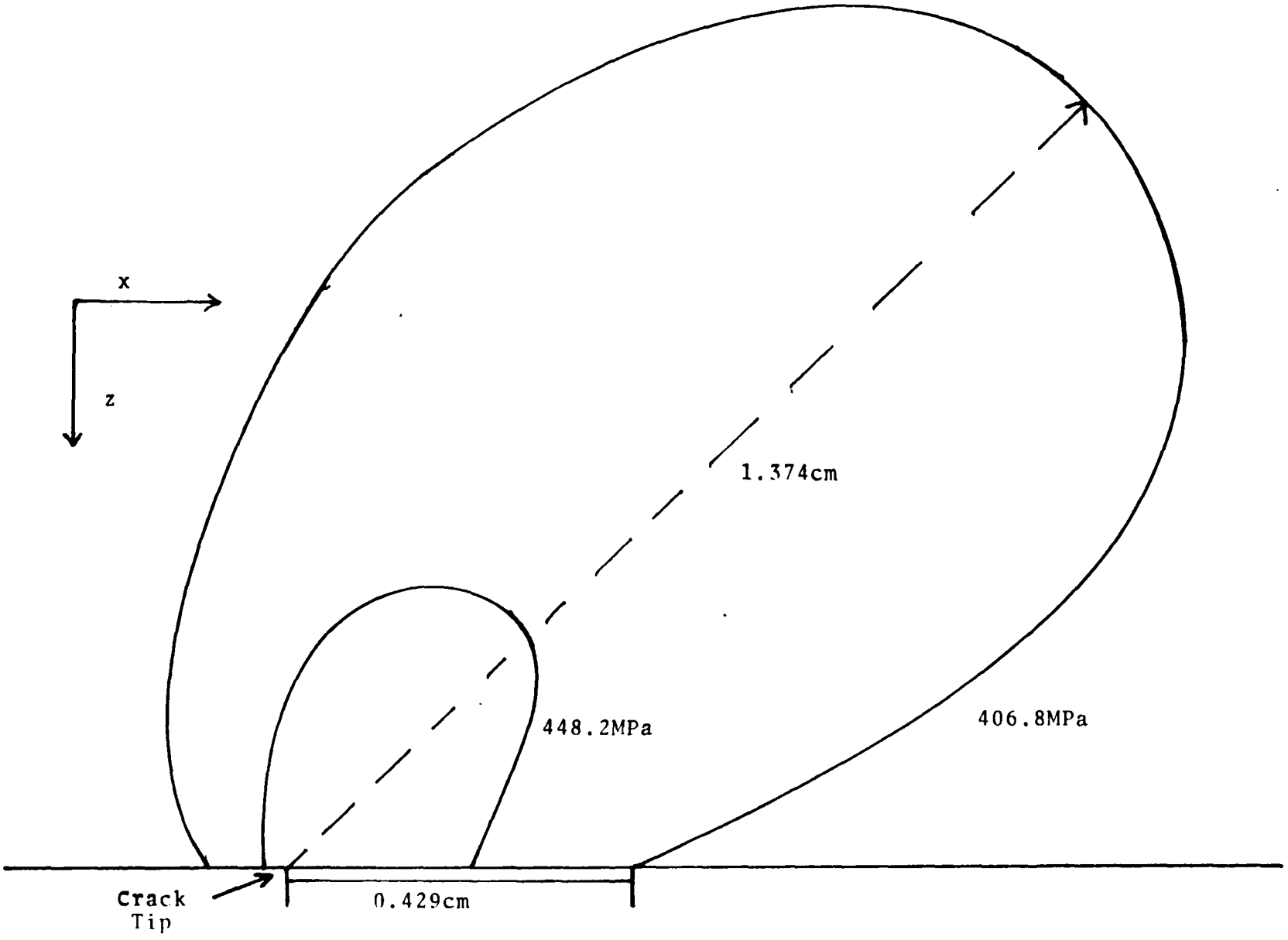

Figure 7: von Mises Stress Contours Near The Crack Tip On Specimen Surface At Maximum Load - Isotropic Hardening.

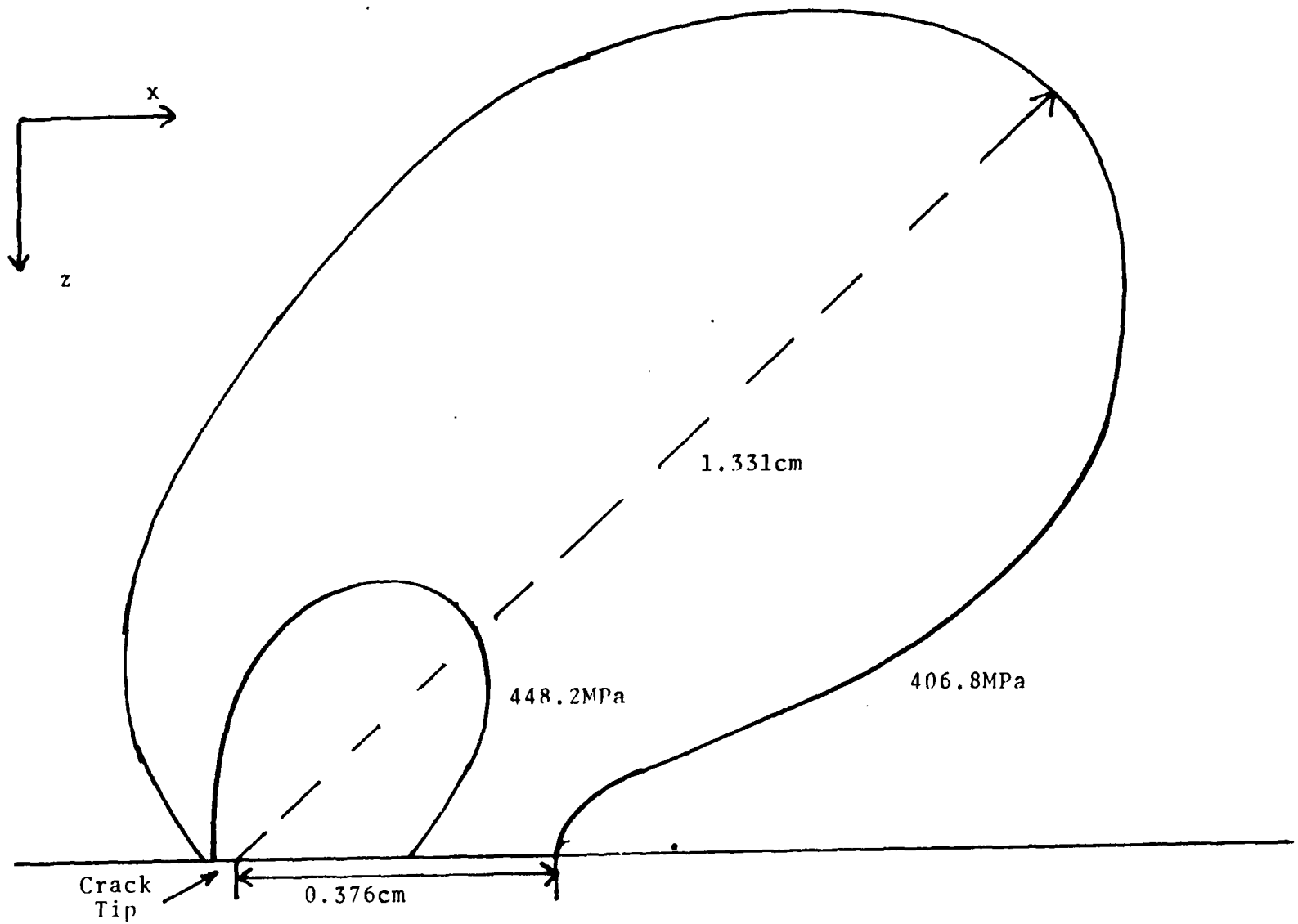

Figure 8: von Mises Stress Contours Near The Crack Tip On Specimen Surface At Maximum Load - Kinematic Hardening.

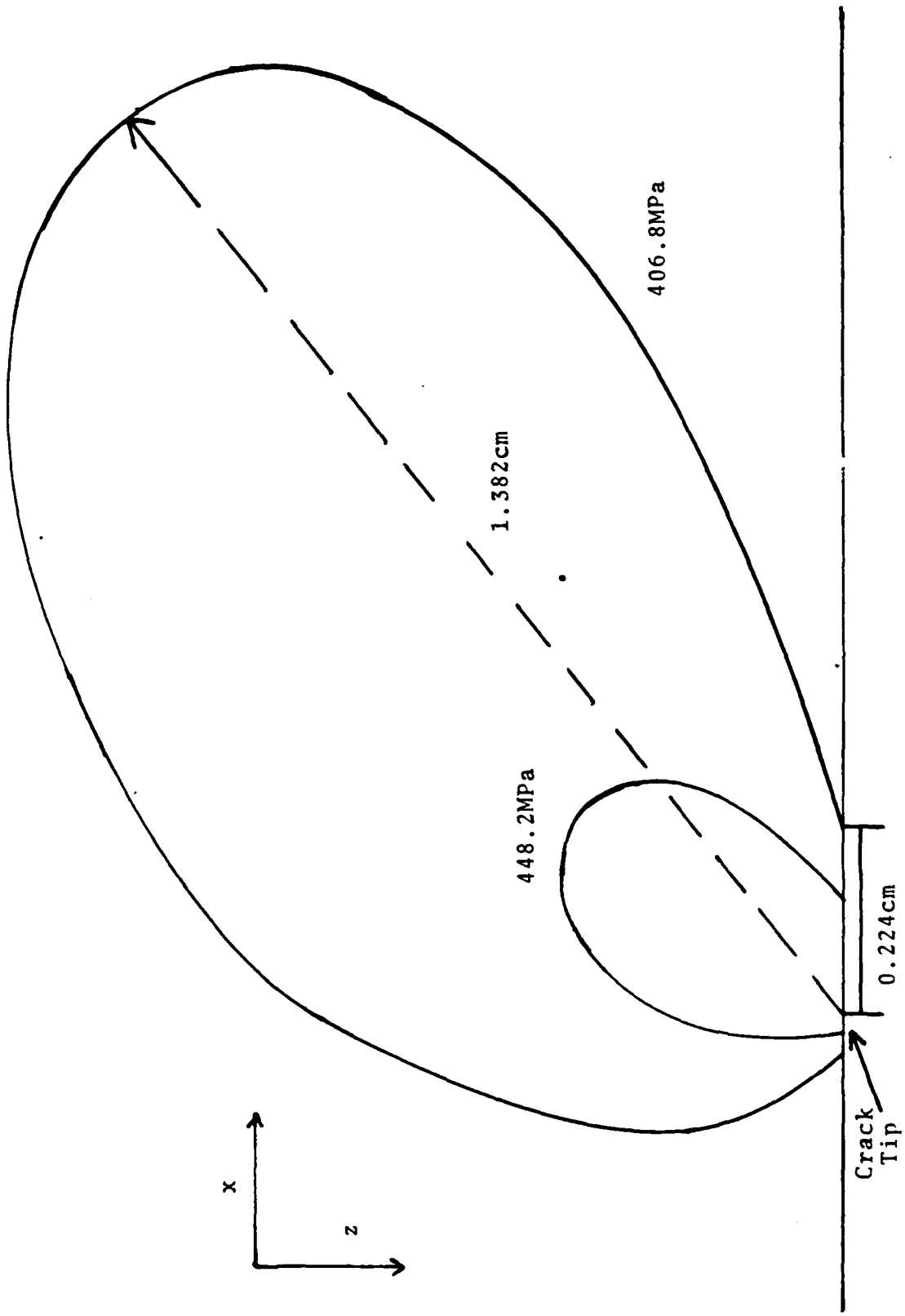

Figure 9: von Mises Stress Contours Near The Crack Tip On Specimen Surface At Maximum Load - Mixed Hardening.

characteristics on the crack extent line. The maximum yield radius and the "skewing" of the yield zones is fairly independent of the hardening model. It is important to emphasize, however, that the differences between the predictions are significant and the local response is highly non-proportional.

Figures 10, 11 and 12 show the yield zones on the midplane of the specimen. These zones demonstrate the same hardening effects as do the surface zones. The greatest influence of hardening model is seen on the line of crack extent. On the midplane of the specimen, a plane-strain type of zone would be expected (i.e., similar to zones predicted with a 2-dimensional plane-strain analysis). The mixed hardening model demonstrates the most realistic results (which is consistent with the surface observations).

The results demonstrate that the local response near a crack is not of the proportional type. This has significant implications with respect to valid failure criteria and analysis models (which will be discussed in the concluding section). The results presented also demonstrate that a mixed hardening rule is the most realistic for modeling the aluminum alloys investigated so far and is probably best for most engineering metals. A complete discussion of the hardening modeling effects and the implications of these findings can be found in [2].

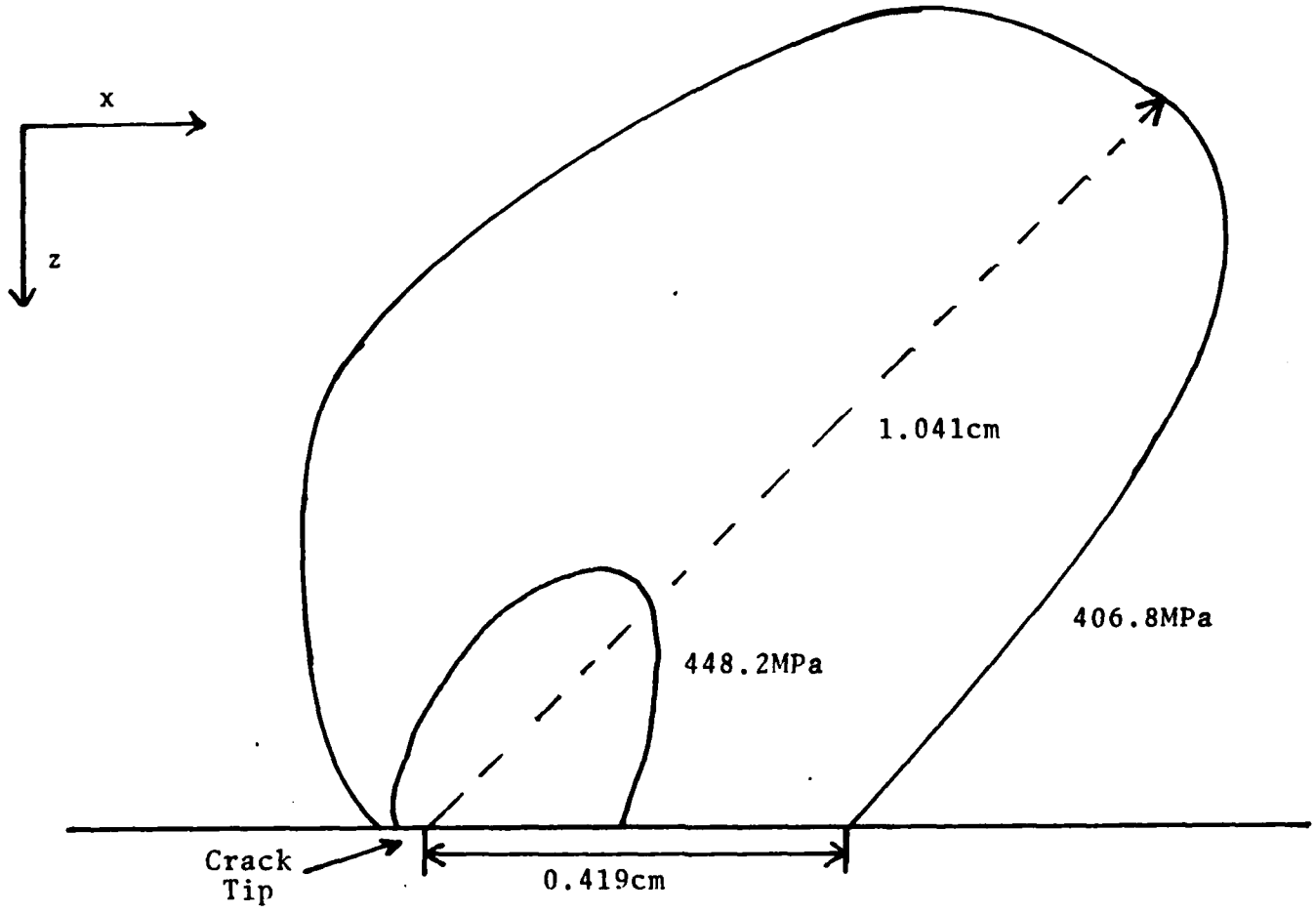

Figure 10: von Mises Stress Contours Near The Crack Tip On Specimen Midplane At Maximum Load - Isotropic Hardening.

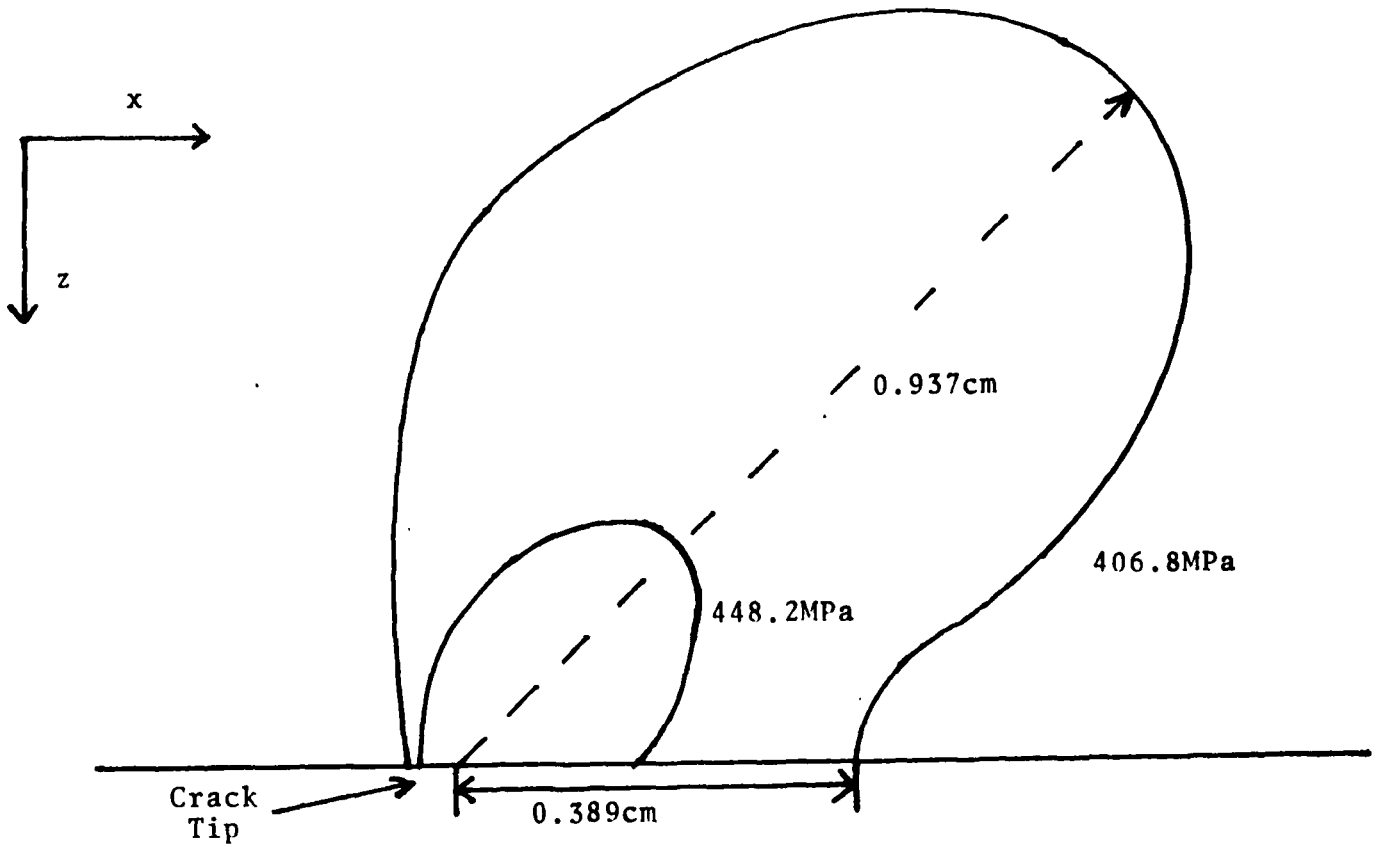

Figure 11: von Mises Stress Contours Near The Crack Tip On Specimen Midplane At Maximum Load - Kinematic Hardening.

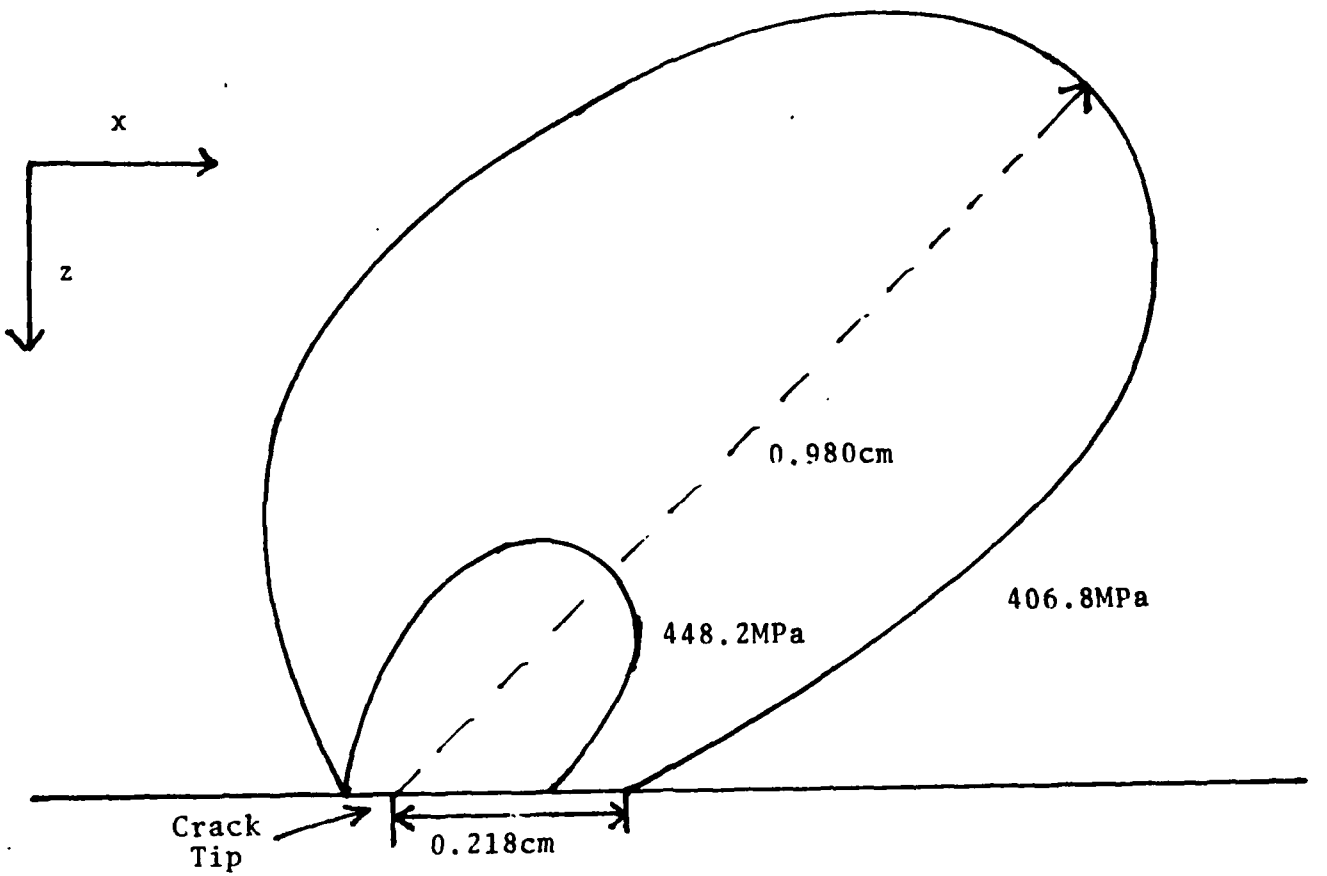

Figure 12: von Mises Stress Contours Near The Crack Tip On Specimen Midplane At Maximum Load - Mixed Hardening.

SPECIMEN THICKNESS EFFECTS

In this study, the specimen thickness is varied and the different zone sizes and shapes are reported (the same center cracked panel is used with mixed hardening assumptions). Figures 13a, 13b, 13c and 13d show the surface yield zones as a function of thickness. The thickness is varied from 1.5 times the ASTM plane strain requirement to a very thin panel dimensions (total thickness of about 3mm). Even for the thinnest specimens, the classical "plane stress" zones are not recovered demonstrating that the assumptions of 2-D plane stress are not valid for this specimen. Also, even for very thick specimens, the predicted zone does not conform to classical plane strain zones (the surface deformation will never conform to 2-D assumptions since not only is the surface normal stress zero but the strains required to produce plastic incompressibility require a nonuniform normal strain through the thickness which is incompatible with 2-D plane strain). It is important to remember that a state of stress with zero normal and anti-plane shear does not need to reduce to 2-D plane stress.

Figures 14a, 14b, 14c and 14d show the midplane zones for the four thicknesses. As the thickness increases, it is obvious that the zones approach plane strain zones (which they should). Even at the largest thickness, however, they show some skewing due to the finite geometry. From these

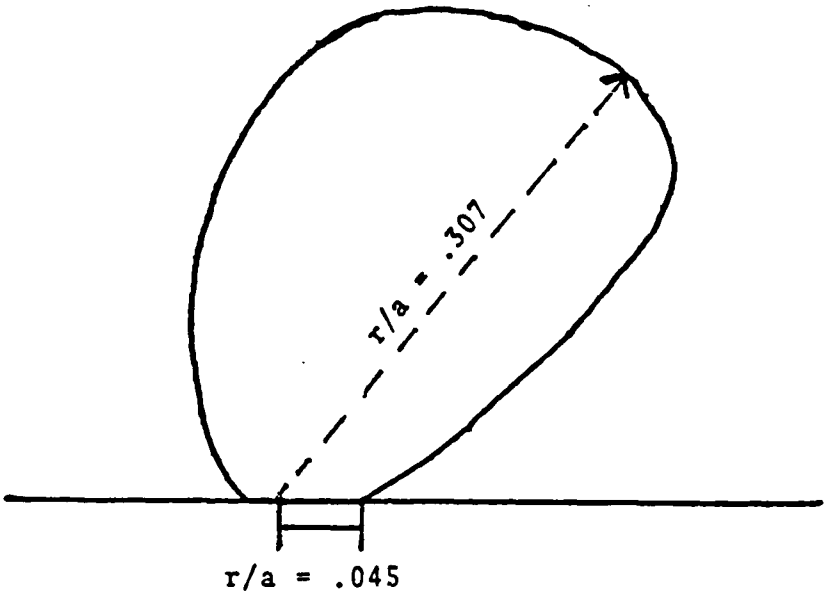

Figure 13a: Surface Yield Zones For Specimen With 2T = 2.54 cm.

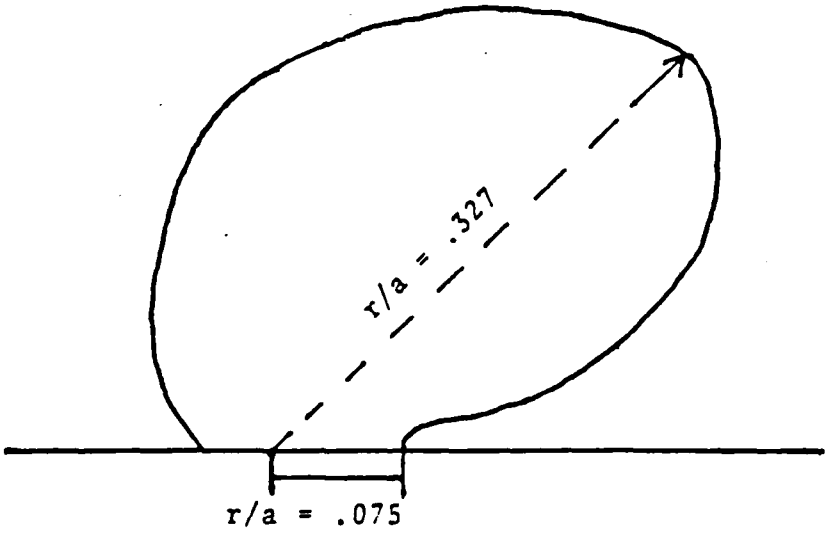

Figure 13b: Surface Yield Zones For Specimen With 2T = 1.27 cm.

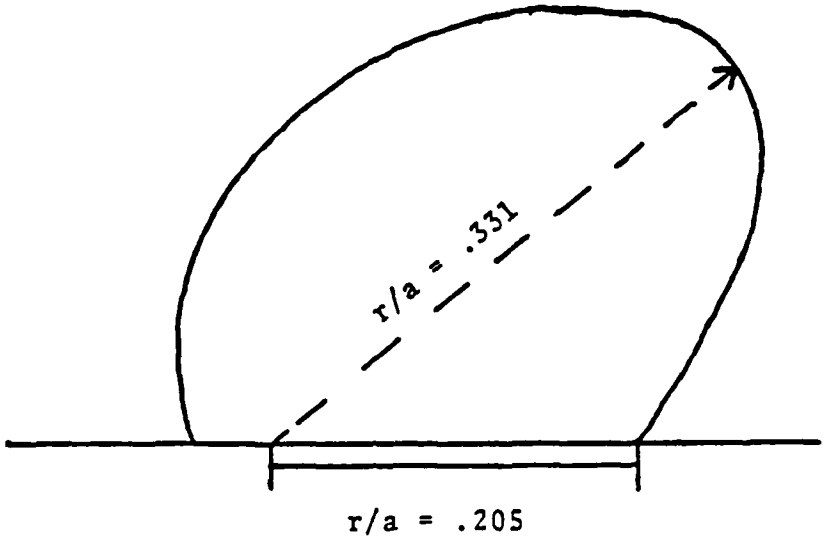

Figure 13c: Surface Yield Zones For Specimen With 2T = 6.35 mm.

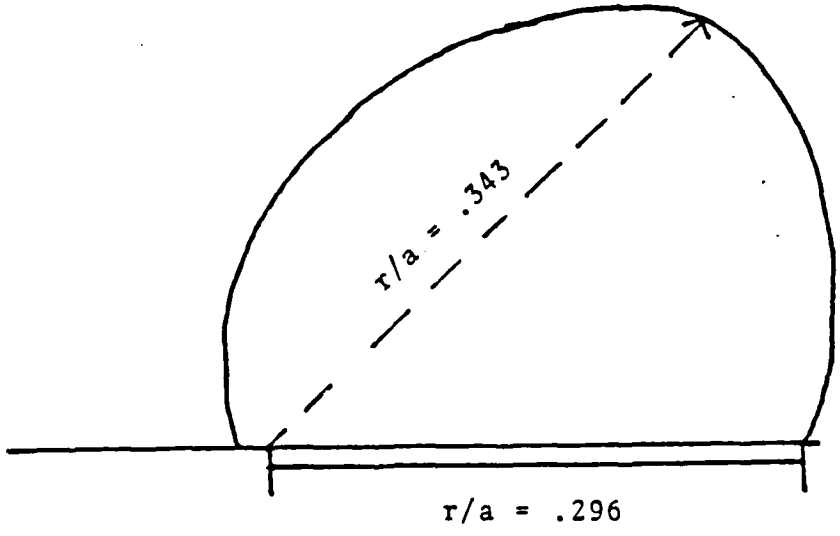

Figure 13d: Surface Yield Zones For Specimen With 2T = 3.175 mm.

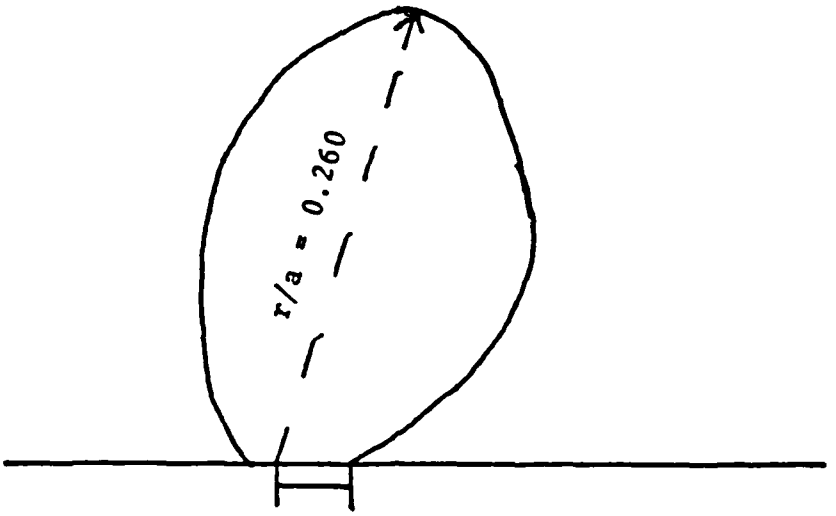

Figure 14a: Midplane Yield Zones For Specimen With 2T = 2.54 cm.

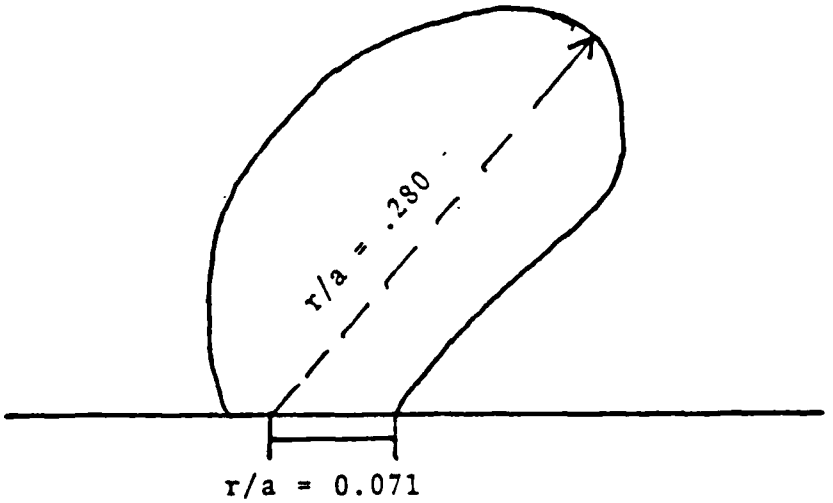

Figure 14b: Midplane Yield Zones For Specimen With 2T = 1.27 cm.

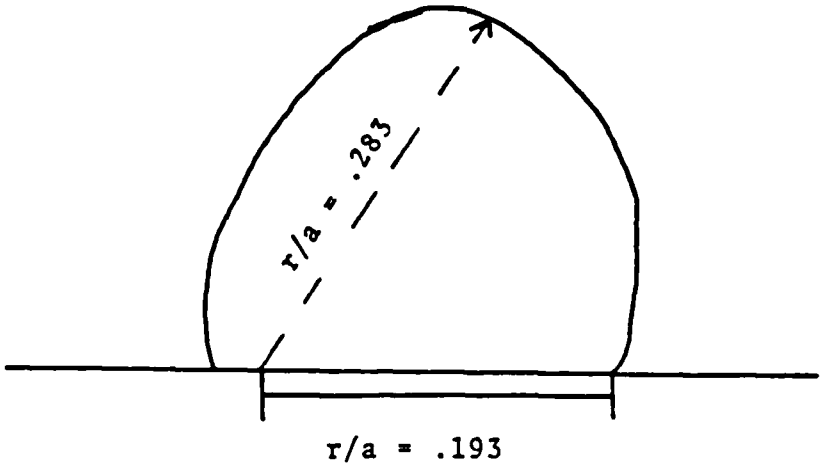

Figure 14c: Midplane Yield Zones For Specimen With 2T = 6.35 mm.

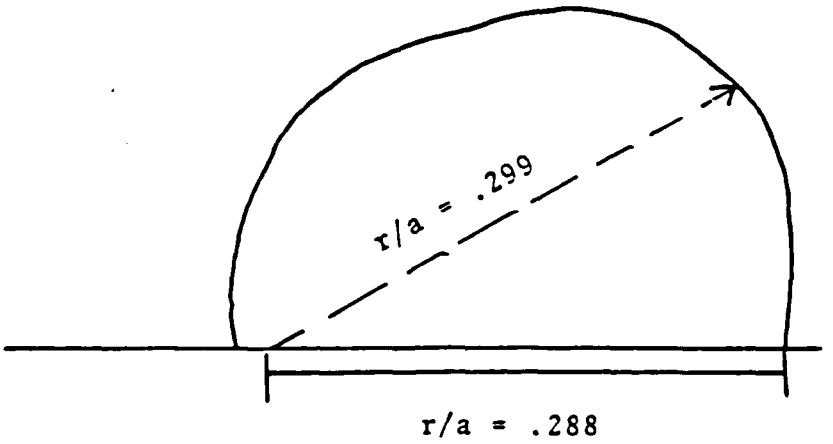

Figure 14d: Midplane Yield Zones For Specimen With 2T = 3.175 mm.

results, the ASTM criterion may not be good enough for ductile materials.

The yield radii and extent of yielding ahead of the crack tip are summarized in the tables. It is important to note that the yield radius changes by about 10% with thickness, however, the yielding ahead of the tip changes drastically and, thus, the plastic area changes. Since more energy is being dissipated with larger areas, the ductility and fracture properties are obviously dependent.

This study demonstrates the thickness effects on local yield characteristics and also mandates 3-D analysis for accurate quantitative predictions. A complete discussion on the effects of specimen thickness can be found in [3].

Thickness	$r_{max/a}$	$r_{o/a}$
T = 2.54 cm	0.307	0.045
T = 1.27 cm	0.327	0.075
T = 6.35 mm	0.331	0.205
T = 3.175 mm	0.343	0.296

r_{max} → maximum yield radius

r_o → yield radius along crack line

Table 1a: Yield Radii As A Function Of Thickness For Surface Yield Zones.

Thickness	$r_{max/a}$	$r_{o/a}$
T = 2.54 cm	0.260	0.039
T = 1.27 cm	0.280	0.071
T = 6.35 mm	0.283	0.193
T = 3.175 mm	0.299	0.288

Table 1b: Yield Radii As A Function Of Thickness For Midplane Yield Zones.

CONCLUSIONS

This paper presents a unified and complete computational approach to solving elastic-plastic engineering problems. The application of this approach to fracture specimens is presented including the mesh discretization necessary to produce accurate results. Several of the more important aspects of cracked specimens (i.e., material modeling, specimen thickness, accuracy requirements) are examined.

The results of the experimental study demonstrate that the current approach and discretization are extremely accurate for predicting detailed local deformations. This comparison is essential for establishing the validity of the computational procedure and discretization employed. Comparison of global parameters far from the crack (such as compliance, gauge displacement, mouth opening, etc.) are not sufficient to establish a given approach or modeling as accurate. The results of this study also demonstrate that the mixed hardening model is the most accurate for the material studied.

Initially, the effect of hardening parameter was examined to delineate the differences in local deformation during unloading. It was discovered, however, that significant local response differences are predicted during the loading segment also. This is in direct opposition to the assumption of proportional loading often made in the literature. Indeed, the assumption is imperative for "deformation"

theory plasticity studies to have any validity. The results presented (already established through experimental comparison) clearly demonstrate that the local response is distinctly non-proportional. This result also demonstrated that local fracture and failure criteria are the only criteria which are theoretically plausible (as proportional loading is essential for the validity of global criteria) are local criteria. This has been suggested by many authors in the past and has often been a point of argument in the fracture community. Global criteria such as J-integral, nonlinear compliance, crack mouth opening, etc., all require proportional local loading. These criteria, therefore, cannot validly be employed for nonlinear fracture problems.

The effect of specimen thickness was investigated to determine the range of validity for the assumptions of plane stress and plane strain near a crack tip. The results presented demonstrate that even for extremely thin specimens, the local response does not behave in a plane stress manner. These results also demonstrate that the local deformation does not approach plane strain behavior until the thickness is far beyond the ASTM requirement. While two dimensional studies need to be performed as preliminary qualitative investigations, they cannot be expected to produce results which predict local deformation quantitatively.

The extensions of the work presented needed to fully unravel the mysteries of fracture mechanics are endless. To

begin, however, several directions are clear. Computationally, it is important to extend the algorithms to account for crack growth in a consistent and accurate manner. The procedure, however, must be independent of any particular failure criterion and not require excessive computational requirements. Recent work has proposed one approach to the problem and demonstrated its efficiency and accuracy in two-dimensions. Further study is needed for the extension to three-dimensions.

The major theoretical area in which more research is needed is in the area of failure criteria. It is beyond the scope of this work to review all the criteria which have been proposed to address nonlinear fracture problems. The results of the work presented in this report, however, demonstrate that the global criteria presented must be abandoned as they rely on the assumption of propositional loading which is incorrect. The local criteria presented to date have not been sufficiently tested to establish any one as a truly valid fracture criteria. The most widely tested have all failed the critical requirements of geometry and specimen independence and consistency over a wide range of applications. Perhaps a new approach is needed. It is important to continue pursuing local fracture criteria. The ability to do large deformation, three-dimensional analysis without the a priori bias of a failure criterion should help in the development of a consistent and accurate approach to elastic-plastic fracture problems.

ACKNOWLEDGEMENT

The authors would like to thank Dr. Yapa Rajapakse for his support and encouragement of this work. This work was sponsored under the ONR Contract #N00014-84-K-0027 to The George Washington University.

REFERENCES

1] I.S. Raju and J.C. Newman, Jr., "Three-Dimensional Finite Element Analysis of Finite-Thickness Fracture Specimens." NASA TN-D-8414, NASA Langley Research Center, 1977.

2] E.T. Moyer, Jr. and H. Liebowitz, "Plastic Deformation and Hardening Characteristics in Three-Dimensional Fracture Specimens." Proceedings of ICF International Symposium on Fracture Mechanics, Science Press, Beijing, China, pp. 152-184, 1983.

3] E.T. Moyer, Jr. and H. Liebowitz, "Effect of Specimen Thickness on Crack Front Plasticity Characteristics in Three-Dimensions." Presented at the Sixth International Congress of Fracture Mechanics Conference, New Delhi, India, December, 1984.

4] D.G.H. Latzgo (ed.), Post Yield Fracture, Applied Science, Ltd., New York, 1979.

5] L.M. Kachanov, Foundations of the Theory of Plasticity, North Holland Publishing Co., 1971.

6] S.W. Key, "A Finite Element Procedure for Large Deformation Dynamic Response of Axisymmetric Solids." Computer Methods in Applied Mechanics and Engineering, Vol. 4, pp. 195-218, 1974.

7] S.W. Key, Z.E. Beisinger and R.D. Krieg, "HONDO-II A Finite Element Computer Program for the Large Deformation Dynamic Response of Axisymmetric Solids." SAND78-0422, Sandia National Laboratories, 1978.

8] L.N. Gifford and P.D. Hilton, "Preliminary Documentation of PAPST-Nonlinear Fracture and Stress Analysis by Finite Elements." DTSRDC Tech. Rept. M-43, 1981.

9] E.T. Moyer, Jr., "A Brief Note on the 'Local Least Squares' Stress Smoothing Technique." Computers and Structures, Vol. 15, 1982.

10] P.D. Hilton and L.N. Gifford, "Elastic-Plastic Finite Element Analysis for Two-Dimensional Crack Problems." ASTM Symposium on Elastic-Plastic Fracture Mechanics, October, 1981.

11] I.S. Raju and J.C. Newman, Jr., "Stress Intensity Factors for a Wide Range of Semi-Elliptical Surface Cracks in Finite Thickness Plates." Engineering Fracture Mechanics, Vol. 11, pp. 817-829, 1979.

12] R.D. Henshell and K.G. Shaw, "Crack-Tip Finite Elements are Unnecessary." International Journal of Numerical Methods in Engineering, Vol. 9, pp. 495-509, 1975.

13] R.S. Barsoum, "On the Use of Isoparametric Finite Elements in Linear Fracture Mechanics." International Journal of Numerical Methods in Engineering, Vol. 10, pp. 25-37, 1976.

14] S.N. Atluri and K. Kathiresan, "3-D Analysis of Surface Flaws in Thick-Walled Reactor Pressure-Vessels Using Displacement-Hybrid Finite Element Method." Nuclear Engineering and Design, Vol. 51, pp. 163-176, 1979.

15] I.S. Raju and J.C. Newman, Jr., "Analytical Methods for Cracks in Three-Dimensional Solids," To appear in the Special Issue on Fracture Mechanics of the Journal of the Aeronautical Society of India, 1985.

16] A.J. Fawkes, D.R.J. Owen and A.R. Luxmore, "An Assessment of Crack Tip Singularity Models for Use with Isoparametric Elements." Engineering Fracture Mechanics, Vol. 11, pp. 143-159, 1979.

17] G.C. Sih, Mechanics of Fracture, Vol. 2: Three-Dimensional Crack Problems, Noordhoff, Netherlands, 1975.

18] E.T. Moyer, Jr. and H. Liebowitz, "Comparative Study on Three-Dimensional Crack-Tip Modeling Methodology," in Application of Fracture Mechanics to Materials and Structures, Noordhoff, Netherlands, 1984.

19] E.T. Moyer, Jr., P.K. Poulose and H. Liebowitz, "Experimental Verification of Elastic Plastic Finite Element Modeling of Three-Dimensional Fracture Specimens." To be submitted to Engineering Fracture Mechanics, 1985.

APPENDIX H:

"Effect of Specimen Thickness on Crack Front Plasticity Characteristics in Three-Dimensions."

By: E. Thomas Moyer, Jr. and Harold Liebowitz.

Proceedings of the Sixth International Conference on Fracture, New Delhi, India, December 4-10, 1984.

EFFECT OF SPECIMEN THICKNESS ON CRACK FRONT PLASTICITY CHARACTERISTICS IN THREE-DIMENSIONS

E. Moyer, Jr. and H. Liebowitz

School of Engineering and Applied Science, The George Washington University, Washington, D.C.

ABSTRACT

A finite element investigation of the effect of thickness on plastic deformation and yielding characteristics in three-dimensional cracked bodies is presented. It is shown that the fundamental deformation modes and extent of plastic deformation are significantly influenced by the specimen thickness. The results show the transition from a local plane strain to plane stress response near the crack front as the specimen thickness is decreased. While the results are generated for a specific aluminum alloy (7075-T7651), the predictions for other hardening materials would be qualitatively the same.

KEYWORDS

Nonlinear finite-element calculations, plastic deformation, three-dimensional crack specimens, incremental analysis.

INTRODUCTION

Of fundamental importance to the accurate fracture assessment of components and structures made of metals is the study of ductile fracture processes and the plastic response near a crack. The basic deformation response near the crack front must be resolved accurately for reliable predictions. Fracture criteria have been proposed based on many controlling quantities (e.g., stress, strain, energy, displacements, etc.) both on global and local scale levels. Without exception, all of these criteria require accurate local deformation modeling.

To understand the scale shifting effects from the laboratory specimen to the structural component, it is imperative to discover the effects of specimen thickness on the deformation response. This problem is an essentially three-dimensional one and must be investigated accordingly.

The purpose of this investigation is to delineate the effect of specimen thickness on local crack front yielding characteristics in a cracked specimen. The three-dimensional elastic plastic finite element code developed in [1] is employed for the analysis. Specimen thicknesses investigated range

from well beyond ASTM plane-strain requirements to thin sheet dimensions. The yield zones calculated in this work demonstrate the transition from dilatational to distortional dominance ahead of the crack tip as a function of thickness (equivalent to a transition from plane strain to plane stress). The magnitude as well as the extent of yielding is shown to be highly thickness dependent. The results of this study also demonstrate that two-dimensional analysis based on plane strain (for thick specimens) or plane stress (for thin specimens) can fail to accurately model the local response when simple standards would dictate otherwise.

PLASTICITY FORMULATION

The incremental theory of plasticity employed in this work is based on the classical rate proportionality assumptions and J_2 flow theory. While the mathematical details vary with the choice of yield criteria, the salient features of all incremental theories are the same. This discussion will, therefore, be confined to the specific theory employed in this work.

Assuming stress strain rate proportionality and J_2 flow theory (which assumes the plastic deformations are incompressible) the stress-strain rate relations can be written as [2]

$$\dot{e}_{ij} = \begin{cases} \frac{1+\nu}{E}\dot{S}_{ij} + \frac{3}{2} f(\sigma_e)\, S'_{ij}\dot{\sigma}_e & \sigma_e = \sigma_y;\ \dot{\sigma}_e > 0 \\ \frac{1+\nu}{E}\dot{S}_{ij} & \text{Otherwise} \end{cases} \tag{1}$$

where:

$\dot{e}_{ij} = \dot{\varepsilon}_{ij} - \frac{1}{3}\dot{\varepsilon}_{pp}\,\delta_{ij}$ are the deviatoric strain rate components,

ν is Poisson's ratio,

E is Young's modulus,

$S_{ij} = \sigma_{ij} - \frac{1}{3}\sigma_{pp}\,\delta_{ij}$ are the deviatoric stress components,

a_{ij} are the coordinates in stress space of the yield surface center

$S'_{ij} = S_{ij} - a_{ij}$ are the deviatoric stress components measured relative to the current yield center,

$\sigma_e = \sqrt{\frac{3}{2} S_{ij}S_{ij}}$ is the effective stress,

$\sigma'_e = \sqrt{\frac{3}{2} S'_{ij}S'_{ij}}$ is the effective stress relative to the current yield center,

σ_y is the current yield stress, and

$\cdot$ denotes time differentiation.

Due to the incompressibility condition, the hydrostatic strain rate is proportional to the mean stress rate and is given by

$$\dot{\varepsilon}_{pp} = \frac{1-2\nu}{E}\dot{\sigma}_{pp} \tag{2}$$

The function $f(\sigma_e)$ is dependent on the uniaxial stress-strain curve and will be discussed subsequently. For a von Mises (J_2) material, the center of the yield surface moves at a rate proportional to the projection of the stress rate vector onto the local normal to the current yield surface and can be written as

$$a_{ij} = \begin{cases} \frac{3}{2}(1-\beta)\, S'_{k\ell}\dot{S}_{k\ell}S'_{ij}/\sigma'^{2}_{e} & \sigma_e = \sigma_y;\ \dot{\sigma}_e > 0 \\ 0 & \text{Otherwise} \end{cases} \tag{3}$$

where β varying from 0 to 1 will model hardening behavior from kinematic ($\beta = 0$) to isotropic ($\beta = 1$).

The function $f(\sigma_e)$ is derived from the uniaxial stress-strain curve. For a uniaxial specimen, equation (1) reduces to

$$\frac{3}{2}(\dot{\varepsilon}_{axial} - \dot{\varepsilon}_{transverse}) = \frac{2}{3}\left(\frac{1+\nu}{E}\right)\dot{\sigma}_e + f(\sigma_e)\,\sigma_e\dot{\sigma}_e \tag{4}$$

in the plastic range. Thus,

$$f(\sigma_e) = \frac{2}{3}(\dot{\varepsilon}_{axial} - \dot{\varepsilon}_{transverse})/\sigma_e\dot{\sigma}_e \tag{5}$$

Invoking incompressibility (i.e., $\dot{\varepsilon}_{transverse} = -\frac{1}{2}\dot{\varepsilon}_{axial}$), the function $f(\sigma_e)$ can be written as

$$f(\sigma_e) = \dot{\varepsilon}_{plastic}/\sigma_e\dot{\sigma}_e \tag{6}$$

If the uniaxial stress-strain curve is expressed in a multilinear fashion, the stress-strain relation is

$$\varepsilon = \frac{\sigma}{E} + \frac{\alpha_1}{E}(\sigma_1-\sigma_y) + \frac{\alpha_2}{E}(\sigma_2-\sigma_y) + \ldots + \frac{\alpha_m}{E}(\sigma-\sigma_m) \tag{7}$$

where $\sigma_{m-1} < \sigma < \sigma_m$ and α_m is given by

$$\alpha_m = \frac{E\Delta\varepsilon_m - \Delta\sigma_m}{\Delta\sigma_m} \tag{8}$$

From equation (7), the plastic strain rate is given by

$$\dot{\varepsilon}_{plastic} = \frac{\alpha_m\dot{\sigma}_e}{E} \tag{9}$$

and thus from (6)

$$f(\sigma_e) = \frac{\alpha_m}{E\sigma_e} \tag{10}$$

Equations (1), (2), (3) and (10) provide a complete set of elastic-plastic constitutive relations. Together with the equilibrium equations and the strain-displacement relations, a governing system will be formed. It is important to note that the constitutive formulation outlined above is acceptable for finite as well as infinitesimal strains. Also of importance is the fact that this formulation is strain-rate independent. This assumption appears to be realistic for most engineering metals at room temperature (or cooler). For high temperature problems a rate-independent formulation is dubious.

Equations (1), (2), (3) and (10) provide the fundamental relationships between stress and strain rates. The equilibrium conditions (governing equations) for a continuum body in the absence of body forces and inertia effects can be written as

$$\partial\dot{\sigma}_{ij}/\partial x_j = 0 \tag{11}$$

with the boundary conditions

$$\dot{\sigma}_{ij} n_j = \dot{T}_i \text{ on } S_T$$

and

$$\dot{u}_i = \dot{\hat{u}}_i \text{ on } S_u \tag{12}$$

where $\dot{T}$ are the specified loading rates on the boundary experiencing applied tractions (S_T) and $\dot{\hat{u}}_i$ are the velocities specified on the remainder of the boundary (S_u). Utilizing the standard infinitesimal strain-displacement relations

$$\varepsilon_{ij} = \frac{1}{2}(\partial u_i/\partial x_j + \partial u_j/\partial x_i) \tag{13}$$

and either employing the Principle of Virtual Work for increments of displacement or by performing the standard Galerkin technique on the governing equations, (11) and (12), the finite element equations governing the nodal velocities, $\underset{\sim}{\dot{U}}$ can be written in terms of the loading rate vector, $\underset{\sim}{\dot{R}}$, in the form

$$\underset{\sim}{K}(\underset{\sim}{U}) \cdot \underset{\sim}{\dot{U}} - \underset{\sim}{\dot{R}} = 0 \tag{14}$$

The standard finite element assumptions made are given by

$$\begin{aligned} \underset{\sim}{u} &= \underset{\sim}{N} \cdot \underset{\sim}{U} \\ \underset{\sim}{\dot{\varepsilon}} &= \underset{\sim}{B} \cdot \underset{\sim}{\dot{U}} \\ \underset{\sim}{\dot{\sigma}} &= \underset{\sim}{D}(\underset{\sim}{U}) \cdot \underset{\sim}{\dot{\varepsilon}} \end{aligned} \tag{15}$$

$$\underset{\sim}{K}(\underset{\sim}{U}) = \sum_{\text{elements}} \int_{\text{element volume}} \underset{\sim}{B}^T \underset{\sim}{D}(\underset{\sim}{U}) \underset{\sim}{B} \, dA$$

where N are the shape functions. The set of rate equations (14) will be integrated one load increment ($\Delta\underset{\sim}{R}$) at a given time to determine the corresponding new displacement increment, $\Delta\underset{\sim}{U}$. The Newton-Raphson or tangent stiffness solution procedure is employed as described in [3].

PROBLEM DESCRIPTION

To study the effects of specimen thickness on the yielding characteristics of typical fracture specimens, a finite center-cracked plate was chosen for investigation. The standard mode I configuration shown in Fig. 1 was analyzed for total thicknesses of

2T = 2.54 cm 2T = 1.27 cm
2T = 6.35 mm 2T = 3.175 mm

The material investigated was a 7075-T7651 aluminum alloy with elastic properties

$E = 7.24$ E+04 MPa

$\nu = 0.3$

$\sigma_y = 4.07$ E+02 MPa

The uniaxial stress-strain curve is shown in Fig. 2.

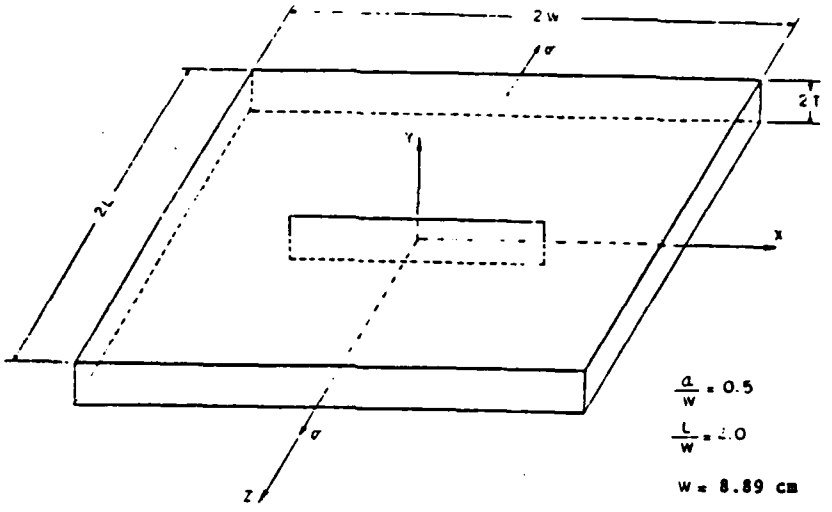

Fig. 1. Through crack geometry and loading.

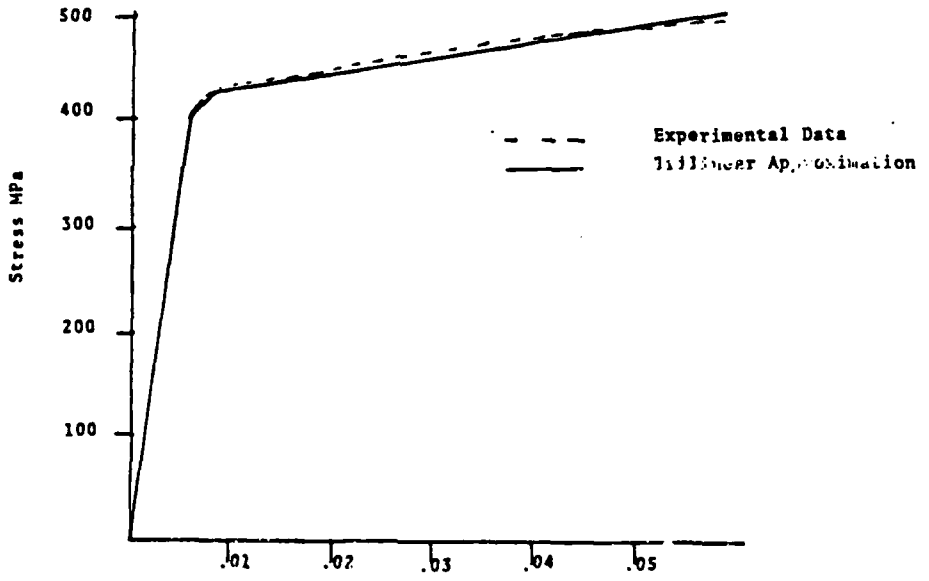

Fig. 2. Uniaxial stress-strain curve for 7075-T6751 aluminum.

The finite element discretization employed in the analysis utilizes 20-Node quadratic isoparametric elements exclusively. A fine mesh near the crack front is employed for accurate modeling. The grid characteristics and convergence properties are discussed in [1,4]. The maximum load applied was

$$\sigma_{max} = 1.77 \text{ E+02 MPa}$$

A hardening parameter of $\beta = 0.5$ was also assumed in the analysis.

RESULTS AND DISCUSSION

The yield zones predicted at the maximum load for each of the four thicknesses studied were calculated and plotted both on the surface and midplane of the specimen. The results demonstrate the significant influence thickness has both on the nature and extent of the yielding.

Figure 3a is a plot of the von Mises stress contour corresponding to the specimen yield stress calculated at the maximum load on the surface of the 2.54 cm thick specimen. As expected for a thick specimen, this zone has the characteristic form of a plane strain yield zone (i.e., minimal yielding ahead of the crack tip and a very upright yield zone). The maximum extent of yielding is 30.7% of the half crack length which is consistent with the small strain assumptions made in the analysis requiring contained yielding. Figure 3b is a plot of the surface zones for a specimen with total thickness of 1.27 cm. The yield zone is slightly wider (more rounded) with this thickness. The maximum radius is now 32.7% of the half crack length and the yielding ahead of the tip has increased (though it is still small). The zone still maintains the basic plane strain characteristics at this thickness.

Figure 3c shows the surface yield zone for a specimen with thickness of 6.35 mm. The zone is now much wider with a larger maximum radius and yield extent ahead of the tip. The zone no longer exhibits the plane strain characteristics but is in transition between plane strain and plane stress. Figure 3d is a plot of the surface yield zone for a specimen with total thickness of 3.175 mm. The zone is significantly more rounded than any of the previous zones with a larger maximum radius and yield extent. The maximum yield radii and extent of yielding ahead of the crack tip for the four thickness surface zones are given in Table 1a. These yield parameters both increase with decreasing thickness as was expected. The final zone at a thickness of 3.175 mm has the rounded characteristic of a plane stress yield zone. The direction of maximum yielding, however, is still a fairly large angle relative to the crack line suggesting some influence of dilatation. Though for this problem (with a relatively small amount of plastic deformation present) the difference between the maximum radii is not large, the nature and extent of yielding ahead of the crack tip show a large dependence on the specimen thickness.

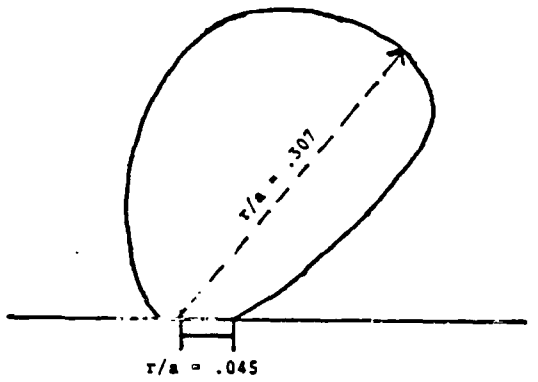

Fig. 3a. Surface yield zones for specimen with 2T = 2.54 cm.

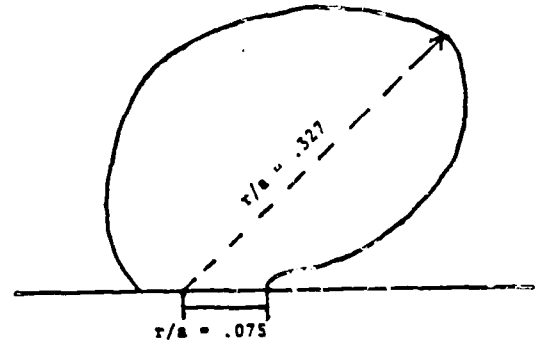

Fig. 3b. Surface yield zones for specimen with 2T = 1.27 cm.

Figure 4a is a plot of the von Mises stress contour corresponding to the material yield stress on the midplane of the 2.54 cmm thick specimen. The zone is typical of plane strain zones and is smaller than the surface zone for the same thickness specimen. The shape of the zone with a minimal extent of yielding ahead of the crack tip suggests high dilatation in that region. The midplane zone for the 1.27 cm thick specimen is shown in

Fig. 4b. The zone is larger than that of the thicker specimen, however, there is still minimal yielding ahead of the tip. The angle of maximum yielding is more acute than in the thicker specimen. The stress state, however, would still be characterized by plane strain.

Figure 4c shows the midplane yield zone for the 6.35 mm thick specimen. The zone is considerably wider and more rounded than for the thicker specimens. It shows characteristics of both plane strain and plane stress zones suggesting a region of transition. Figure 4d is a plot of the midplane yield zone for the 3.175 mm thick specimen. The zone is basically a plane stress zone and is larger than for the thicker specimens. The maximum yield radii and radius of yielding ahead of the crack tip on the specimen midplanes are given in Table 1b. Both increase with decreasing thickness as was expected. In all cases, the midplane yield zones are smaller than the surface zones.

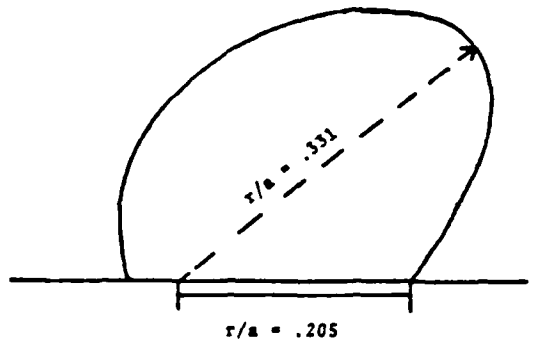

Fig. 3c. Surface yield zones for specimen with 2T = 6.35 mm.

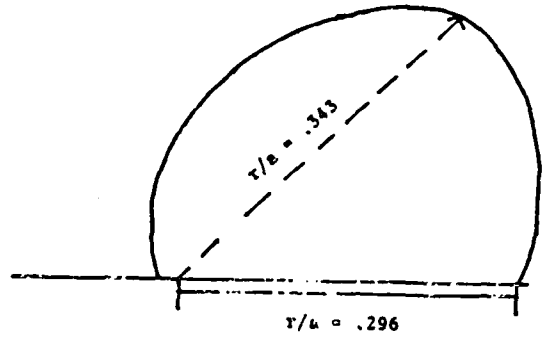

Fig. 3d. Surface yield zones for specimen with 2T = 3.175 mm.

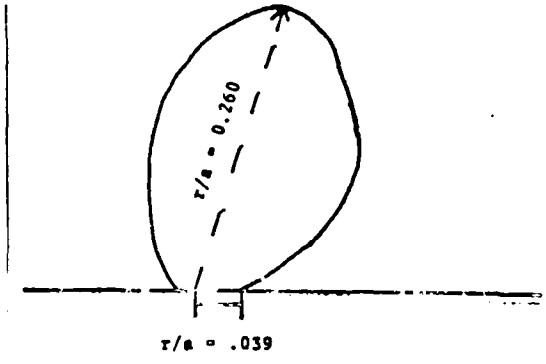

Fig. 4a. Midplane yield zones for specimen with 2T = 2.54 cm.

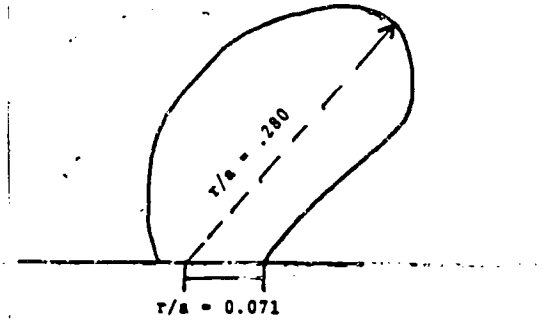

Fig. 4b. Midplane yield zones for specimen with 2T = 1.27 cm.

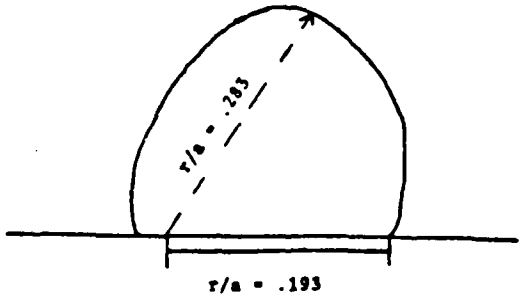

Fig. 4c. Midplane yield zones for specimen with 2T = 6.35 mm.

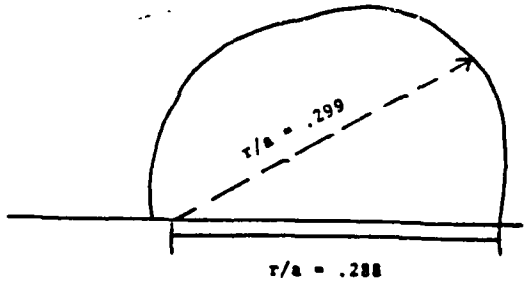

Fig. 4d. Midplane yield zones for specimen with 2T = 3.175 mm.

TABLE 1a Yield Radii as a function of Thickness for Surface Yield Zones.

Thickness	$r_{max/a}$	$r_{o/a}$
T = 2.54 cm	0.307	0.045
T = 1.27 cm	0.327	0.075
T = 6.35 mm	0.331	0.205
T = 3.175 mm	0.343	0.296

r_{max} → maximum yield radius

TABLE 1b Yield Radii as a Function of Thickness for Midplane Yield Zones.

Thickness	$r_{max/a}$	$r_{o/a}$
T = 2.54 cm	0.260	0.039
T = 1.27 cm	0.280	0.071
T = 6.35 mm	0.283	0.193
T = 3.175 mm	0.299	0.288

r_o → yield radius along crack line

CONCLUSIONS

The results of this study demonstrate the thickness dependence of the yield zones near a crack front on specimen thickness. It is shown that both the extent of plastic deformation and the dominance of deformation type (i.e., dilatation or distortion) are controlled by the thickness. The nature of the deformation is fundamental to the understanding of the incipient fracture processes. The delineation of the fundamental deformation response near a three-dimensional crack front is an imperative first step in the understanding and accurate prediction of ductile fracture processes.

To further the understanding of ductile fracture, it is necessary to compare theoretical and experimental deformation predictions local to the crack front. Only through such comparisons can an assessment be made of the accuracy and reliability of the numerical methods for plastic analysis. Toward this goal, it is proposed to measure the residual deformation on the surface of the specimen in the unloaded state. The theoretical study presented above demonstrates that the finite element predictions are qualitatively realistic and sensitive to specimen thickness. Comparison with experimental results will delineate the grid characteristics and hardening models which best model specific geometric and material applications. After successful "tuning" of the finite element model, a complete description of the stress and energy state in a cracked body can be predicted with confidence. Once fully three-dimensional stress fields are predicted, ductile failure theories can be tested and skeptically compared without the bias of unrealistic analytical approximations.

REFERENCES

Moyer, Jr., E. T. and H. Liebowitz (1983). Plastic deformation and hardening characteristics in three-dimensional fracture specimens. Presented at the ICF International Symposium on Fracture Mechanics, Beijing, China, November 22-25.

Kachanov, L. M. (1971). Foundations of the Theory of Plasticity, North-Holland Publishing Co.

Zienkiewicz, O. C. (1977). The Finite Element Method, McGraw-Hill, New York.

Moyer, Jr., E. T. and H. Liebowitz (1983). Comparative study on three-dimensional crack tip modeling methodology. Presented at the International Conference on Application of Fracture Mechanics to Materials and Structures, Freiburg, Germany, June 20-24.

ACKNOWLEDGMENT

This work was sponsored by the Office of Naval Research under Contract Number: N00014-75-C-0946.

APPENDIX I:

ONR Distribution List.

MS/432/86/180

ONR SOLID MECHANICS PROGRAM
(Code 1132SM)
DISTRIBUTION LIST - FAILURE MECHANICS
Revised 21 February, 1986

Office of Naval Research
800 N. Quincy Street
Arlington, VA 22217-5000
Attn: Code 1132SM (4 copies)
Code 1131

Defense Documentation Center (4 copies)
Cameron Station
Alexandria, VA 22314

Naval Research Laboratory
Washington, DC 20375
Attn: Code 6000
Code 6300
Code 6380
Code 5830
Code 6390
Code 2620

David W. Taylor Naval Ship Research
and Development Center
Annapolis, MD 21402
Attn: Code 28
Code 2812
Code 2814

David W. Taylor Naval Ship Research
and Development Center
Bethesda, MD 20084
Attn: Code 1700
Code 1720
Code 1720.4

Naval Air Development Center
Warminister, PA 18974
Attn: Code 6043
Code 6063

Naval Surface Weapons Center
White Oak, MD 20910
Attn: Code R30
Technical Library

Naval Surface Weapons Center
Dahlgren, VA 22448
Attn: Technical Library

Naval Civil Engineering Laboratory
Port Hueneme, CA 93043
Attn: Technical Library

Naval Underwater Systems Center
New London, CT 06320
Attn: Code 44
Technical Library

Naval Underwater Systems Center
Newport, RI 02841
Attn: Technical Library

Naval Weapons Center
China Lake, CA 93555
Attn: Technical Library

NRL/Underwater Sound Reference Detachment
Orlando, FL 32856
Attn: Technical Library

Chief of Naval Operations
Department of the Navy
Washington, DC 20350
Attn: Code OP-098

Commander
Naval Sea Systems Command
Washington, DC 20362
Attn: Code 05R25
Code 05R26
Code 09B31
Code 55Y
Code 55Y2

Commander
Naval Air Systems Command
Washington, DC 20361
Attn: Code 03D
Code 7226
Code 310A
Code 310B

U.S. Naval Academy
Mechanical Engineering Department
Annapolis, MD 21402

Naval Postgraduate School
Monterey, CA 93940
Attn: Technical Library

Mr. Jerome Persh
Staff Specialist for Materials
and Structures
OUSDE&E, The Pentagon
Room 3D1089
Washington, DC 20301

Prof. J. Hutchinson
Harvard University
Division of Applied Sciences
Cambridge, MA 02138

Prof. R.H. Gallagher
Worcester Polytechnic Institute
Worcester, MA 01609

* *

Prof. Albert S. Kobayashi
University of Washington
Dept. of Mechanical Engineering
Seattle, WA 98195

Dr. Harold Liebowitz, Dean
School of Engineering and Applied Science
George Washington University
Washington, DC 20052

Professor G.T. Hahn
Vanderbilt University
Department of Mechanical & Materials Eng.
Nashville, TN 37235

Professor L.B. Freund
Brown University
Division of Engineering
Providence, RI 02912

Professor B. Budiansky
Harvard University
Division of Applied Sciences
Cambridge, MA 02138

Professor S.N. Atluri
Georgia Institute of Technology
School of Civil Engineering
Atlanta, GA 30332

Professor J. Duffy
Brown University
Division of Engineering
Providence, RI 02912

Professor J.D. Achenbach
Northwestern University
Department of Civil Engineering
Evanston, IL 60201

Professor F.A. McClintock
Massachusetts Institute of Technology
Department of Mechanical Engineering
Cambridge, MA 02139

Professor D.M. Parks
Massachusetts Institute of Technology
Department of Mechanical Engineering
Cambridge, MA 02139

Dr. M.F. Kanninen
Southwest Research Institute
Post Office Drawer 28510
6220 Culebra Road
San Antonio, TX 78284

Prof. F.P. Chiang
State Univ. of New York at Stony Brook
Dept. of Mechanical Engineering
Stony Brook, NY 11794

Prof. S.S. Wang
University of Illinois
Dept. of Theoretical & Applied Mechanics
Urbana, IL 61801

Prof. Y. Weitsman
Texas A&M University
Civil Engineering Department
College Station, TX 77843

Prof. I.M. Daniel
Illinois Institute of Technology
Dept. of Mechanical Engineering
Chicago, IL 60616

Prof. C.T. Sun
Purdue University
School of Aeronautics & Astronautics
W. Lafayette, IN 47907

Prof. J. Awerbuch
Drexel University
Dept. of Mechanical Engr. & Mechanics
Philadelphia, PA 19104

Prof. T.H. Lin
University of California
Civil Engineering Department
Los Angeles, CA 90024

Prof. J. R. Rice
Harvard University
Division of Applied Science
Cambridge, MA 02138

Prof. W.N. Sharpe
The Johns Hopkins University
Department of Mechanics
Baltimore, MD 21218

Prof. C.F. Shih
Brown University
Division of Engineering
Providence, RI 02912

Prof. A. Rosakis
California Institute of Technology
Graduate Aeronautical Laboratories
Pasadena, CA 91125

Prof. D. Post
VA Polytechnic & State University
Dept. of Engineering Science & Mechanics
Blacksburg, VA 24061

Prof. G. J. Dvorak
Rensselaer Polytechnic Institute
Department of Civil Engineering
Troy, NY 12180

Prof. W. Sachse
Cornell University
Dept. of Theoretical & Applied Mechanics
Ithaca, NY 14853

Prof. G.S. Springer
Stanford University
Dept. of Aeronautics & Astronautics
Stanford, CA 94305

Prof. H.T. Hahn
Washington University
Center for Composites Research
St. Louis, MO 63130

Prof. S.K. Datta
University of Colorado
Dept. of Mechanical Engineering
Boulder, CO 80309

* *

Dr. R.M. Christensen
Lawrence Livermore National Laboratory
Chemistry & Material Science Department
P.O. Box 80P
Livermore, CA 94550

Prof. M.L. Williams
University of Pittsburgh
School of Engineering
Pittsburgh, PA 15261

Prof. D.C. Drucker
University of Florida
Dept. of Aerospace Engineering & Mechanics
Tallahassee, FL 32611

Prof. B.A. Boley
Northwestern University
Department of Civil Engineering
Evanston, IL 60201

END

FILMED

5-86

DTIC